Modeling morphogenesis in living matter

Valentina Balbi

THÈSE DE DOCTORAT
DE L'UNIVERSITÉ PIERRE ET MARIE CURIE (UPMC - PARIS VI)

Spécialité

MÉCANIQUE DES SOLIDES
(Ecole doctorale SMAER 391)

Présentée par

Valentina BALBI

pour obtenir le grade de

DOCTEUR DE L'UNIVERSITÉ PIERRE ET MARIE CURIE

Sujet de la thèse

Modeling morphogenesis in living matter

Soutenue à l'UPMC le 4 Septembre 2015 devant le jury composé de :

Michel DESTRADE	NUI Galway	Rapporteur
Yibin FU	Keele University	Rapporteur
Rachele ALLENA	ENSAM Paris	Examinateur
Jean-François GANGHOFFER	Université de Lorraine	Examinateur
Djimédo KONDO	UPMC	Examinateur
Sébastien NEUKIRCH	UPMC	Examinateur
Vittorio SANSALONE	Université Paris Est Créteil	Examinateur
Pasquale CIARLETTA	UPMC	Directeur de thèse

Contents

List of Figures

Page

List of Tables

Page

Abstract

Among the fundamental processes involved in the development of an organism, morphogenesis is one of the most complex. During the past centuries, an amount of experimental studies have improved our actual knowledge of the mechanisms which drive many morphogenetic processes in living organisms. Only recently, experiments have been complemented with mathematical modeling as a tool for proving novel insights on morphogenesis in soft tissues. In this context, this thesis aims at developing new mathematical models for the formation of patterns and forms in soft tubular organs. A macroscopic approach is adopted, where the tissue is considered as a continuum body undergoing growth and remodeling. The main idea behind the proposed models is that during growth and remodeling, residual stresses can arise and once they exceed a critical value, an elastic instability can occur in the tissue and lead to a morphological change. Therefore, the morphoelastic models are developed integrating the modern theories of growth and remodeling within the framework of the thermo-mechanics of open systems. The occurrence of the elastic instability is investigated using the method of incremental deformations superposed on finite deformations. The critical thresholds for the onset of the instability are determined together with the modes of the associated instability pattern. The morphoelastic theory is applied to the modeling of different morphogenetic processes occurring in soft tubular organs and gives useful insights in two interesting problems: the formation of the wide range of patterns in the gastro-intestinal system and the occurrence of torsional instabilities in pre-stressed tubular organs.

Résumé

Parmi les processus fondamentaux qui ont lieu pendant le développement d'un organisme, la morphogenèse est un des plus complexes. De nombreuses études expérimentales ont contribué à mieux comprendre les mécanismes morphogénétiques dans les organismes vivants. Cependant peu de modèles mathmatiques ont été proposés afin d'étudier la morphogenèse dans les tissus vivants. Dans ce contexte, la thèse se propose de développer de nouveaux modèles mathématiques pour étudier les changements de forme dans les tissus mous tubulaires. L'approche adoptée est macroscopique o le tissu biologique est considéré comme un milieu continu déformable. L'hypothèse principale sur laquelle se basent les modèles proposés est la suivante : pendant les processus de croissance et remodelage, des contraintes résiduelles peuvent s'accumuler dans le tissu et, une fois une valeur critique dépassée, le mener à un changement morphologique sous la forme d'une instabilité élastique. Pour cela, les modèles développés intègrent les théories modernes de croissance et remodelage, dans le cadre de la thermomécanique des systèmes ouverts. Ensuite, l'analyse de stabilité linéaire permet de calculer les seuils et modes de l'instabilité élastique en utilisant la méthode des déformations incrémentales superposées aux déformations finies. L'ensemble de ces techniques (théorie morpho-élastique) est utilisé dans cette thèse afin de modéliser deux différents processus morphogénétiques ayant lieu dans les tissus mous tubulaires : la formation dune variété des formes dans le système gastro-intestinal et le flambage hélicoïdal dans les organes tubulaires avec précontraintes.

Riassunto

Tra i processi fondamentali che contribuiscono allo sviluppo embrionale di un organismo, la morfogenesi è uno dei più complessi. In passato, molti studi sperimentali hanno contribuito ad arricchire le conoscenze che abbiamo oggi circa i meccanismi coinvolti durante la morfogenesi negli organismi viventi. Solo ultimamente, parallelamente agli esperimenti, i modelli matematici hanno iniziato ad essere utilizzati come strumenti per studiare tali meccanismi nei tessuti biologici. In tale contesto, la tesi si propone di formulare nuovi modelli matematici per la formazione di pattern e forme nei tessuti molli tubolari. Un approccio macroscopico è utilizzato, dove il tessuto è considerato come un corpo continuo elastico che cresce e si rimodella. L'idea principale che sta dietro ai modelli proposti si basa sul fatto che, durante la crescita ed il rimodellamento, possano insorgere degli stress residui e, accumulatisi oltre un certo valore critico, possano dare origine ad un'instabilità elastica nel tessuto e indurvi un cambiamento di forma. Pertanto, i modelli morfoelastici sono sviluppati integrando le teorie moderne di crescita e rimodellamento nel contesto della termomeccanica dei sistemi aperti. L'insorgenza dell'instabilità è studiata utilizzando il metodo delle deformazioni incrementali sovrapposte alle deformazioni finite. Le soglie critiche dei parametri dell'instabilità e i corrispondenti modi critici associati al pattern geometrico, sono calcolati. La teoria morfoelastica è applicata alla modellizzazione di diversi processi morfogenetici che coinvolgono gli organi tubolari, permettendo di studiare due interessanti problemi: la formazione dei diversi pattern che si sviluppano sulla parete interna del sistema gastro-intestinale nei vertebrati e l'insorgenza di instabilità in organi tubolari con stress residui sottoposti a torsione.

Chapter 1

Introduction to morphogenetic theories in living matter

Contents

Morphogenesis is the ensemble of the coordinates processes which lead to the formation of shapes and structures in living organisms. From a biomechanical point of view,

together with growth and remodeling, morphogenesis is one of the main processes underlying biological development. As defined by Taber in a seminal biomechanical review [11], growth can be defined as the change of mass in a material. It can occur by change of volume or by surface deposition, the former is called *volumetric growth*, the latter is defined as *surface growth*. Remodeling is considered as an alteration of the microstructure in the tissue. Material properties such as stiffness, orientation of fibers, density, strength can change in response of some external stimuli such as stress, pressure, chemical concentration. If changes in the microstructure of the tissue occur without involving variation of mass, they are referred to as *remodeling processes*.
Therefore, morphogenesis includes growth and remodeling, but it is a much more complex phenomenon. First of all, it is the result of a chain of developmental events which are not independent one from another. Second, it is a multi-scale process involving aspects from the molecular, cellular and tissue levels. Third, it is a four-dimensional problem (three-dimensional in space and dependent of time). This first Chapter aims to provide an historical overview on the morphogenetic theories in living matter which built our current knowledge on this fascinating branch of research. First, the main discoveries and ideas behind them will be presented following a chronological order. Then, the modern biomechanical approaches to morphogenesis will be presented, with particular attention on the link between mechanical stimuli and generation of form.

1.1 Early mechanistic vision

The first speculations on morphogenesis date back to ancient Greece time. In order to explain how shapes and structures originate in living organisms, in his book Historia Animalium, **Aristotle** introduced the *epigenetic hypothesis*. Although his approach was mainly philosophical, it was based on the idea that structures and shapes gradually develop and are not pre-existent from the beginning. By contrast, this latter vision called *preformationism*, became predominant in the years when theology was having a strong influence on the society and persisted until the 17th Century. **Malpighi** even claimed that a miniature of the human body (a *homunculus*) was present in the head of each sperm, completely avoiding the problem of generation of shapes in developing organisms. Besides these very early attempts, mostly based on intuition and theological preconceptions, the first approach to morphogenesis based on mechanical and geometrical arguments came from **Galileo Galilei**. After having started his studies in medicine, Galileo followed his

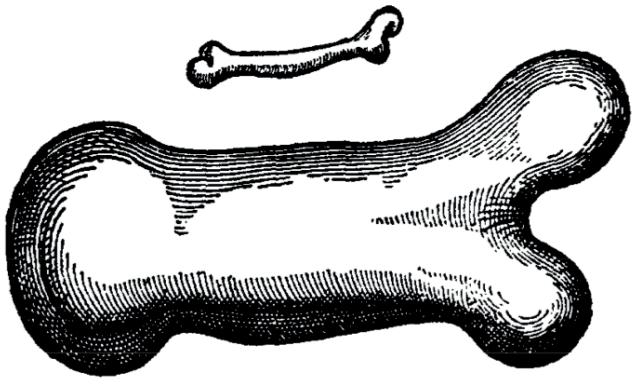

Figure 1.1: Galileo sketch of bones for a small animal (top) and a large animal (down) based on allometric arguments, taken from [1]. The natural length of the small bone has been increased three times and the thickness multiplied until, for a correspondingly large animal, the large bone would have the same strength of the small one.

passion for mathematics and physics and he devoted his entire life to investigate mechanical problems. His method was based on the idea that "*mathematics is the best way of supplying physics with the finest rules of logics*" [1]. The wide interests of Galileo covered some aspects of biomechanics such as allometric studies on vertebrates. He showed that most organisms change their shape in function of the loads that they have to hold, according to a scaling law in the form:

$$y = a_0 x^{\alpha}$$

where a_0 is a constant depending on the organism, α is the scaling exponent, x the reference variable and y is the dependent variable. If an animal increases its length l, then its mass M, being proportional to the volume, would increase by a power $\alpha = 3$ and its strength S, being proportional to the area, by $\alpha = 2$. Therefore, in the case of isometric growth, its mass would have increased more than its strength and thus the animal would have been subjected to a higher load while having a lower strength to support it. Thus, Galileo proved that the changes in size are actually governed by allometric scaling (see Figure 1.1).

The 19th century was the era of Darwinism and evolutionary theories, but also of the discovery of the cell and of the birth of experimental embryology. In particular, a

school of thought which established itself in the second half of the 19th century was the *Recapitulation theory* of Ernst Haeckel [12]. Supported by Darwinism, he claimed that steps of embryonic development of a species correspond to adult stages of their ancestors. Haeckel's school was very influential in the scientific community of the time and every attempt to show that the theory was unfounded and not able to provide a through description of morphogenesis was brutally suppressed.

1.1.1 Wilhelm His and the "constrained expansion" model

The recapitulation theory was particularly rejected by the German scientist **Wilhelm His**. He rather supported a mechanical causation behind embryonic development. He performed several experiments to prove the **constrained expansion principle**, i.e. expansion of a spherical or cylindrical tissue surrounded by inelastic tissue [13]. He performed several experiments on rubber tubes under constrained compression and tension, in order to model the gut tube, the brain formation and other changes of shape during embryogenesis. Among the most relevant results, His showed that the gut tube morphogenesis could be modeled by a rubber tube under tension. In Figure 1.2 a sketch of His's mechanical explanation for gut shaping is depicted. Because of Haeckel scientific influence, His's work had to wait some decades to be diffused. The input came right from one of Haeckel's students, Wilhelm Roux.

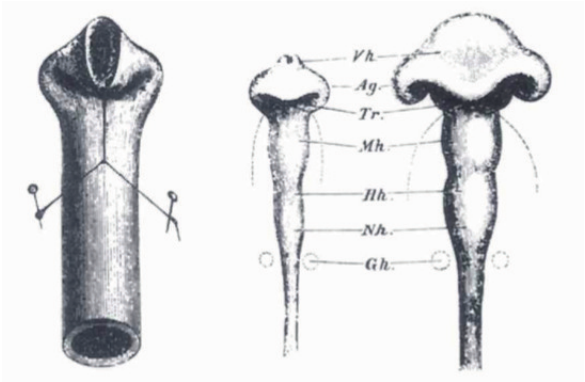

Figure 1.2: Sketch of His's model for gut tube morphogenesis, adapted from [2].

1.1.2 Wilhelm Roux and developmental mechanics

At the end of the 19th century, **Wilhelm Roux** shifted the attention from evolution (final purpose) to mechanisms (cause) in developmental biology. As well as being a promoter of His's work, he was interested into two aspects of development: first, the role of *self-differentiation* and second, the role of *dependent-differentiation*. He investigated self-differentiation by performing a lot of experiments on embryos, which eventually opened the way to the discovery of regulation and induction. *Regulation* is the property by which the embryo develops normally even if a part of it is removed. *Induction* is the ability of a cell or a tissue to influence the development of another.
The experiments to test the role of self-differentiation in the embryo where based on the analysis of the first cleavage of the embryo. Roux separated the two blastomeres which resulted after the first cleavage, killing one of the two, and he observed that from the surviving blastomere, a half-embryo still developed. He erroneously explained the result in the context of the *mosaic theory*, first introduced by **August Weismann** in the 1880s [3]. According to Weismann's theory, the nucleus of the egg contains a number of factors which determinate the cell fate, as shown in Figure 1.3. During cleavage these determinants are asymmetrically distributed between the daughter cells in the embryo. As cleavage proceeds, the potentiality of each daughter cell decreases while the cells become more and more specialized. Roux thought that killing one of the two blastomeres corresponded to remove part of the cell determinants, which resulted in the development of a half-embryo.

Some years later, **Hans Driesch**, another of Haeckel's students, explained Roux's

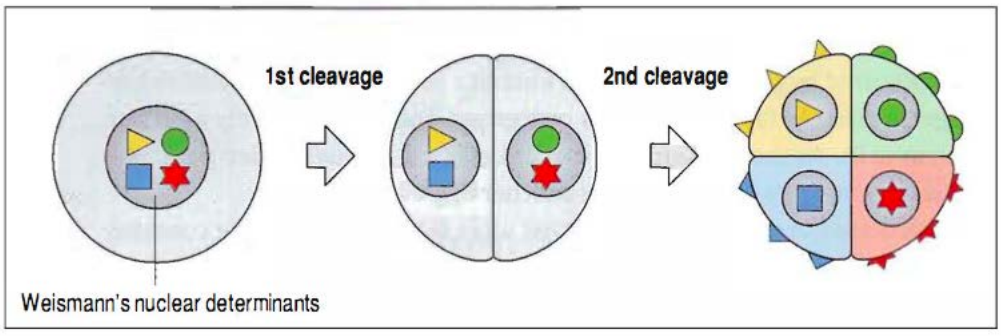

Figure 1.3: Mosaic theory: during cell division, the cell fate determinants are unequally distributed among the daughter cells, adapted from [3].

results with the discovery of regulation. Driesch repeated the experiment done by Roux using frog embryos. Unlike in Roux's experiment, after having killed one of the two blastomeres, he removed the killed cell. As a result, he observed that a whole, but smaller embryo developed from the one-cell fertilized egg because the killed cell didn't prevent the other cell from regulating and forming a complete embryo [14].

The discovery of induction had to wait some more years. Following the methodic experimental approach of Roux, in 1924 **Spemann** and **Mangold** transplanted part of the embryonic tissue from a amphibian into an embryo of a different amphibian species [15]. They observed that a partial second embryo developed from the transplanted tissue: the hosting tissue induced the development of the hosted tissue.

Roux is also remembered for establishing the concept of *functional adaptation* as a principle for dependent-differentiation: cells and tissues respond to change in external conditions in order to preserve their global organization and functions. He applied the principle of functional adaptation to the study of development of bone, cartilage and muscle. Pauwels [16] summarized Roux principle of functional adaptation as follows:

> *The formation of the different types of tissue should be considered as an adaptation of the formative tissue to the function demanded of it.*

According to Roux, the bone would be built with the minimum amount of tissue, in order to support the stresses which it undergoes. Moreover, it would adapt under the action of external forces, through growth in width in order to preserve the lightness.

1.2 The 20th century

The 20th century has been a century rich in crucial discoveries and scientific contributions to the understanding of morphogenesis. This period can be split into two phases. The first half of the century was characterized by the statical point of view of D'Arcy Thompson on the relation between physical forces and generation of shapes. The second half was the era of genetics and molecular biology which shifted the focus to the dynamical aspects of morphogenesis.

1.2.1 D'Arcy Thompson: a first mathematical approach to morphogenesis

In 1917, **D'Arcy Thompson** published his only scientific book, entitled "On growth and form" [17]. While other contemporary scientists focused on experimental analysis, D'Arcy Thompson's investigations were based on a mathematical approach. As Wilhelm His, D'Arcy Thompson was skeptical about evolution theories and natural selection, which were dominant during the 19th century. His idea of morphogenesis was based on the role of physical forces in shaping organisms. Therefore, the book has a purely mechanical approach where living organisms are treated as material bodies subjected to physical forces, obeying to simple physical and geometrical laws. An example of D'Arcy Thompson's approach can be found in the second chapter of his book, where he focused on the effect of external forces on animals of different sizes. He stated that big animals are subjected to inertial forces while small animals are subjected to surface tension. It follows that big animals have strong and heavy structures in order to support the gravitational force, while small animals need lighter structures in response to the weaker surface tension.

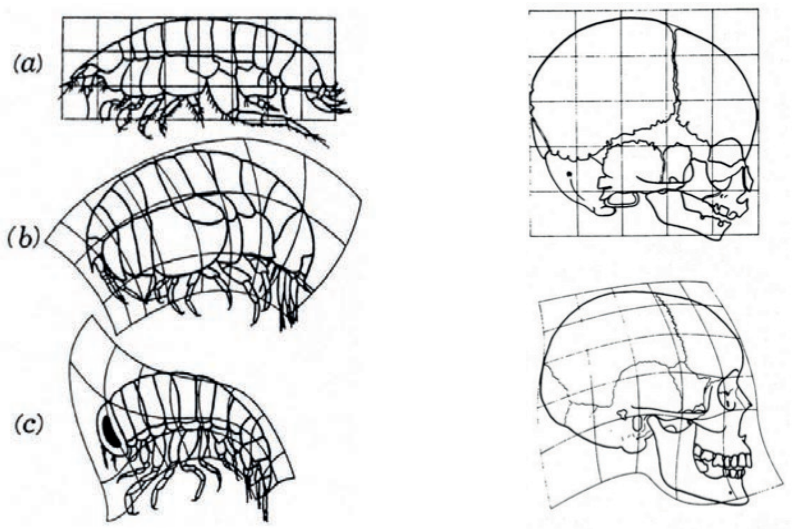

Figure 1.4: Left: Transformation grid applied to the transformation of the shape of a small amphiopod (a) *Harpinia Plumosa* into the shapes of two other genera belonging to the same family (b) *Stegocephalus Inflatus*, and (c) *Hyperia Galba*), adapted from [4]. Right: Transformation grid applied to the growth of a skull in human foetus. In both examples the transformation is achieved by applying physical forces on the considered structure, during evolution and growth respectively.

Furthermore, he proposed a grid transformation method, aimed at showing that physical forces can shape a living organism during growth and even evolution, see Figure 1.4. As highlighted by Ulett [18], "On growth and form" had a great influence on modern biomechanics and is still read and published in reduced and revised versions. D'Arcy Thompson's book inspired the work of Julian Huxley on allometric growth [19] and of Gould in his attempt to deal with such a mechanistic theory of shape in evolutionary theories [20].

1.2.2 Genetics

The origins of genetics date back to the second half of the 19th Century when **Gregor Mendel** discovered the inheritance of biological traits [3]. His theory was based on the idea that the hereditary package is transmitted from parents to offspring through a set of discrete hereditary factors. Each factor is a potential expression of a biological trait. For any biological feature, a child receives one factor from the mother and one from the father. The effective expression of a biological trait is given by the combined action of the two related factors. When the two factors combine, they are not affected by each other, but they just influence the potentiality of the fertilized egg. Mendel proved his theory by performing experiments on pea plants, but his results remained mostly unappreciated until the first half of the 20th century. One of the main problems of Mendel's theory was that it couldn't give a concrete description of the nature of these factors. At that time, genetics was considered the study of transmission of heredity properties in the embryo, while embryology was seen as the science investigating how the organisms develop. But there wasn't any link between the two disciplines, which finally merged only in the second half of the 20th Century. The main steps leading to the fusion of the two fields are basically the discovery that the DNA carries the genetic information and that genes encode proteins. The properties of a cell are determined by the proteins they contain, genes control and act on proteins in order to drive the cell fate and consequently, the development of the embryo. Right after these discoveries, a lot of experiments focused on finding the genes responsible for several morphogenetic events in the embryo. The strategy adopted was to introduce changes in the molecular organization of the DNA in order to observe abnormal changes in a final structure. In this way, it has been possible to identify which genes play an active role in the formation of an emerging pattern.

1.2.3 Pattern Formation

The fast development of genetics in the years following the 50s also promoted an increasing attention to the chemical and molecular mechanisms which might underpin morphogenetic processes. The concept of pattern formation in morphogenesis originated from that period. *Pattern formation* can be defined as the emergence of organized structures in space and time. The main contributions to the development of this concept were given by Alan Turing and Lewis Wolpert.

1.2.3.1 Alan Turing: chemical basis of morphogenesis

In 1952 **Alan Turing**, published his paper on the chemical bases of morphogenesis, which later became another milestone in biomathematics [21]. This was his only contribution on morphogenesis, but it represents the first reaction-diffusion model for pattern formation. The main ingredients of Turing's model are:

- The presence of at least two chemical species which undergo chemical reaction. Turing called them *morphogens*, in order to underline their role in generating a new pattern. The concentration of the two morphogens in the cell drives the cell activity. (In this sense genes can be considered indirectly as morphogens).

- In absence of diffusion, the system is in a stable state, defined by homogeneous concentrations of the two reactants. Under certain conditions, diffusion can destabilize the homogeneous state and a new non-homogenous pattern arises. This is counter-intuitive because generally diffusion would rather be thought to introduce chaos in a system, instead of generating an organized pattern [22].

Turing's model predicted the existence of six possible steady-states as shown in Figure 1.5. The *uniform* stationary (I) and oscillatory (II) states, the *short wavelengths* stationary (III) and oscillatory (IV) states and the *finite wavelength* stationary (V) and oscillatory (VI) states. Of particular interest is the Case VI, which occurs when the diffusion coefficients of the two morphogens differ substantially and initiate the so-called *short range activation long range inhibition* [23] mechanism. The two morphogens are seen as an activator and an inhibitor, respectively, which can act on themselves as well as on the other. A small perturbation in the homogeneous concentration can induce an increase in the activator concentration and initiate the feedback which lead to the formation of one of the Turing's patterns in Figure 1.5 (b).

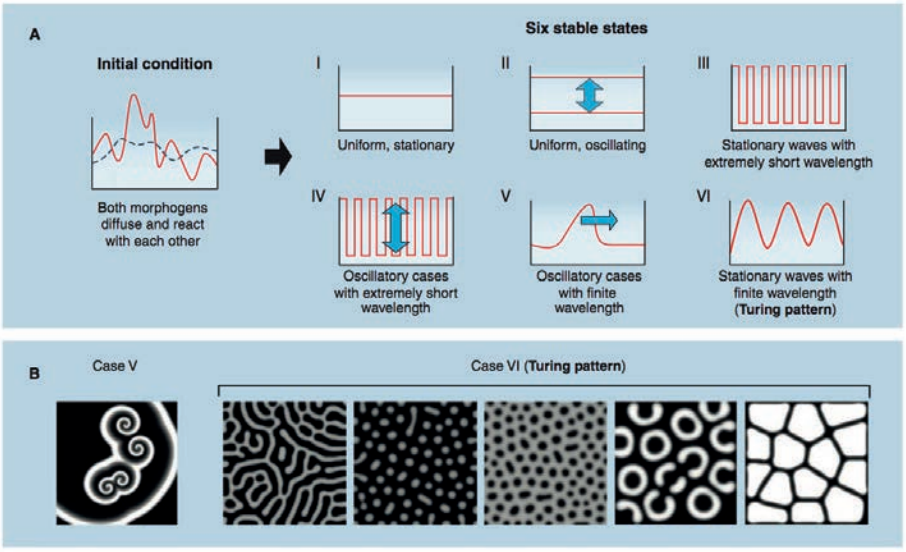

Figure 1.5: Turing's reaction-diffusion model: (a) Examples of the six stable states solutions of Turing's model. (b) The so-called Turing's pattern is depicted as the Case VI where a stationary wave of finite wavelength develops, adapted from [5].

Turing's model has later been largely employed for modeling the emergence of several patterns in vertebrates such as the stripes in the zebra-fish pigmentation [24], the branching pattern in feathers [25], but also the fabulous seashell patterns [26] and the mechanism of plant phyllotaxis, i.e. the arrangement of leaves on a plant stem [27].

1.2.3.2 Positional Information: molecular basis of morphogenesis

In the years right after its publication, Turing's work didn't receive a great attention. The problem of emergence of organized cellular patterns in the tissue was brought back to the attention of developmental biologists some years later in the 70s. In fact, **Lewis Wolpert** introduced the concept of *Positional Information* (PI) in order to explain how complex patterns could arise from initial asymmetries in the tissue [28]. The main idea of Wolpert is that the position of a cell in the tissue specifies the information about the molecular changes the cell will undergo. The key elements of Wolpert's theory can be summarized in the definition of:

- A mechanism which specifies the *polarity* in the tissue. Polarity is the direction in which PI is specified and is defined with respect to one or more reference points.
- A mechanism for specifying the different responses of the cell.

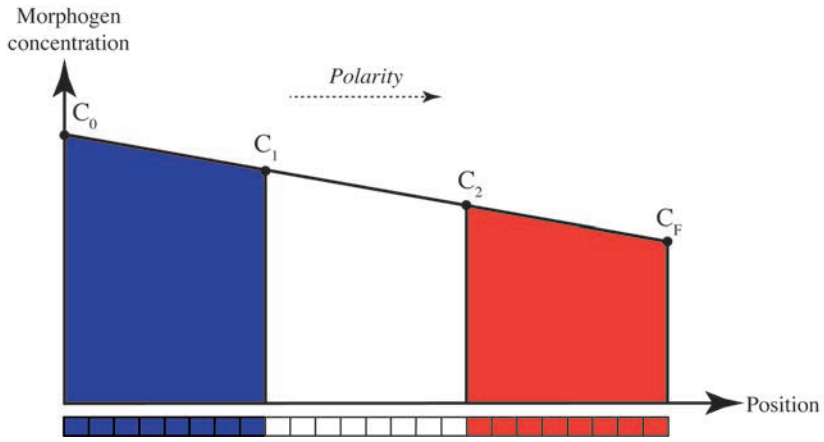

Figure 1.6: The french flag model: positional information is specified by the gradient of a morphogen concentration, the dotted line identifies the direction of the polarity.

PI can be specified by a quantitative variation of some factor such as the concentration, or a qualitative variation of some cell parameters such as a combination of genes or enzymes. A set of cells which have their PI specified with respect to the same reference points constitutes a field. *Interpretation* of PI is the process by which PI specifies the cell state and *conversion* is the mechanism by which PI is translated in a particular cellular activity. Furthermore, PI is universal in organisms and size invariant, meaning that if a part of the tissue is removed, the tissue is still able to pattern and interpret the PI.
The concept of positional information is well clarified in the French Flag Model depicted in Figure 1.6. In this example, the mechanism which specifies polarity is the monotonic variation of the morphogen concentration C, in respect to the reference values C_0 and C_F. The thresholds C_1 and C_2 identify the mechanism for the differential response of the cells. The interpretation acts according to the following rule: cells with position in the region where $C_0 < C < C_1$ express the blue pigment, a cell in the region where $C_1 < C < C_2$ expresses the white pigment and cells in the region where $C_2 < C < C_F$ express the red pigment. The molecular patterning in the early Drosophila embryo has been explained using positional information [29].

The models proposed by Turing and Wolpert offer two different points of view on pattern formation. A first difference comes from the fact that Turing aimed at modeling spontaneous formation of a pattern, while Wolpert asked how a more complex pattern can arise from an asymmetry (polarity) in the tissue. Furthermore, in Turing's model the concentration of morphogens is directly related to the spatial pattern, in this sense

it is a "pre-pattern". Conversely, Wolpert introduced an interpretation step where the cell activity is specified by the concentration gradient. On the other hand, in their recent paper Green and Sharpe have proposed a different mechanism through which the two models can cooperate in pattern formation [30]. For example, in the mouse limb bud a periodic pattern develops with different wavelengths depending on the position along a polarity gradient.

1.3 Modern approaches to morphogenesis

In the previous sections, the main discoveries and theories which have contributed to our current understanding of morphogenesis have been presented. The research field rapidly expanded in the last decades. In particular, modern approaches focused on the effect of external stimuli, such as mechanical, chemical, molecular on the generation of patterns and on the structural organization in living organisms.
In the following, the modern approaches to morphogenesis from a biomechanical viewpoint will be summarized.

1.3.1 Volumetric Growth and Remodeling

At the beginning of the 80s, Skalak and coworkers gave the first analytical description of finite volumetric and surface growth [31,32] in a continuum mechanics framework. They introduced the idea that growth can induce incompatibilities in the geometry of a body. According to the authors, the growing body can pass from an unloaded stress-free configuration to a pre-stressed reference configuration arising due to incompatibilities in the growth process. Conversely, if the growth strains are *compatible*, then no internal stresses will be generated in the tissue.
The seminal work of Skalak opened the door to a number of experimental studies which aimed at characterizing the residual stress distribution in biological tissues. Residual stresses have been found in blood vessels (arteries [10, 33] and veins [34]), heart [35], airways [36]. On the theoretical side, Skalak's formulation of volumetric growth prepared the ground for the paper of Rodriguez and colleagues [37] in which they formalized, in an elegant mathematical formulation, the relation between growth and remodeling on one side and residual stresses on the other side. In their fundamental contribution, they use the *multiplicative decomposition* of the deformation gradient associated to the growth/remodeling process, into a purely growth/remodeling and an elastic component.

The growth/remodeling deformation introduces the incompatibility in the tissue and the elastic deformation restores the compatibility, while residual stresses arise. As highlighted by Ambrosi et al. [38], the main advantage of this type of representation is that it allows to account for the effects of growth and remodeling. On the other hand, the mechanisms underlying these processes are neglected.
The multiplicative decomposition was first introduced in the theory of elasto-plasticity by Kröner [39] and Lee [40] in order to split the inelastic and the elastic components and it has been widely employed in continuum mechanics models. In this framework, the growth and remodeling processes are basically modeled as deformations from a stress-free configuration to a residually stressed state, where the body has grown or remodeled and changed its natural state. The relation between the variation of mass and changes in shapes is given by a volumetric growth. For remodeling, the micro-structural reorganization of the tissue can be linked for example to the changes in density, stiffness, orientation of fibers. Therefore, the thermo-mechanics of open systems has been used to describe the evolution of growth or remodeling parameters in time, as well as the constitutive relations for the material.

1.3.1.1 Extended theories and applications

In the years following Skalak's and Rodriguez's papers, a lot of work has been done both at the theoretical level and for experimental purposes. From the theoretical viewpoint, the attention has been pointed to develop constitutive theories for growth and remodeling. Accounting for mass volumetric sources and fluxes, Epstein and Maugin derived constitutive and evolution laws using the thermomechanical principles [41]. Ganghoffer et al. developed a constitutive framework for volumetric and surface growth involving the Eshelby stress [42]. Following the work of Di Carlo and Quiligotti [43] where accretive forces for growth are included in the system, Ambrosi and Guana derived the evolution laws for mass production which involves a direct link between stress and growth [44].
In parallel, another part of the biomechanical community has focussed on the application of the growth and remodeling theory to determine the onset of pattern formation after an elastic instability. This branch is called *morpho-elasticity*. A number of studies have employed the growth theory of Skalak and of Rodriguez et al. in order to model the emergence of geometrical patterns in tissues as an elastic instability due to excessive accumulation of residual stresses in the tissue. Among the main contributions, Ben Amar and Goriely studied the stability of elastic growing shells of different geometries [45], Li

et al. modeled the formation of mucosal pattern in the oesophagus of pigs [46], Moulton and Goriely modeled the mucosal folding mechanism in growing airways [47].

1.3.2 Mixture theory

The approaches described so far consider the growing tissue as an open system of a single constituent with an internal source of mass. Soft tissues are composed by several constituents such as collagen, elastin, ground substance. In *mixture theory*, the tissue is considered as a sum of different constituents. Each of them obeys some constitutive laws, and it exchanges mass with the other constituents. The mixture theory allows for a more realistic growth considered as exchange of mass between constituents. But, on the other hand, it introduces some controversial issues, such as the constitutive modeling of the partial stresses which act on each constituent and the definition of their physical meaningful boundary conditions.

From a theoretical viewpoint, one of the early contributions came at the end of the 70s from Bowen. He proposed a thermo-mechanical theory for mixtures, which gave the bases for modeling diffusing mixtures of elastic materials [48]. Later in the 90s, Cowin proposed *poroelasticity*, i.e the theory of interactions between deformation and fluid flow in a porous medium, as theoretical framework to study the bone [49]. Humphrey and Rajagopal proposed one of the first mixture models [50] for living materials. The main idea in their model was that each constituent has its own natural configuration. Therefore, the state of stress of each constituent might not be compatible with that of the surrounding tissue and residual stresses arise.
Loret and Simòes developed a theoretical framework for growth within mixture theory [51]. They considered a biphasic tissue composed by a solid and a liquid phase. Using the multiplicative decomposition on the solid phase they split the growth and the elastic effects and they derived the constitutive laws for growth from the second law of thermodynamics. A similar approach has been applied by Garikipati et al. to the growth of artificial tendon [52] and by Baek et al. for modeling aneurysm in brain [53].

Ambrosi et al. used the mixture theory in order to investigate the emergence of residual stresses during growth and remodeling of soft tissues [54]. The mixture framework has also been used for modeling tumor growth. Byrne and Preziosi modeled the tumor as a multicellular spheroid constituted by cells, considered as an elastic fluid, and extracellular space filled by the organic liquid [55]. Such a biphasic model was later extended by Ambrosi and Preziosi to a triphasic mixture which also accounted for the effect of the

extracellular matrix [56]. Finally, Athesian modeled growth and remodeling of a reactive mixture including electrical charged solid and fluid constituents which are typical of cartilage tissue [57].

1.3.3 Morphomechanics: hyper-restoration principle

Another modern approach to morphogenesis comes from the work of Lev Beloussov. During the 70s he performed several experiments on embryos in order to investigate the effects of mechanical stresses on early morphogenetic events [58, 59]. Beloussov in-

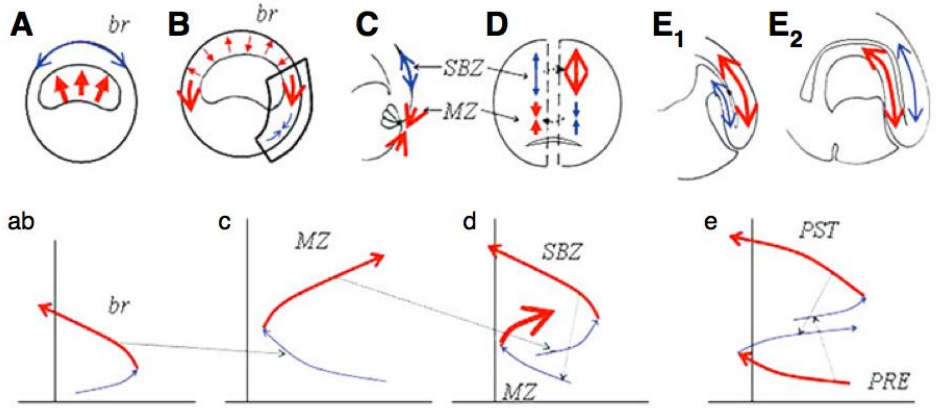

Figure 1.7: Hyper-restoration principle: Beloussov's illustration of the mechanical feedbacks acting in the embryo during gastrulation, adapted from [6]. Active stresses (red curves) overshoot passive ones (blue curves). Horizontal and vertical axes represent stress and time, respectively.

troduced the idea that the changes in shape during gastrulation occur according to a *hyper-restoration principle* [6, 60]. Cells tend to restore the original stress distribution in the embryo by responding to the external forces with generation of active forces inside the embryo and which overshoot the original stress. Therefore, gastrulation is seen as a chain of events driven by mechanical feedbacks. In Figure 1.7, a graphical interpretation of Beloussov's results is depicted. For example, during the early stages of gastrulation (A and B) the passive stretching of the roof of the blastocoel induces an active increase of the blastocoel internal pressure (red curve in Figure 1.7ab), which in turn affects the stress distribution in the neighboring marginal zone (MZ).

1.3.4 Mechanotransduction

The generation of shapes can be initiated by the chemical response of the tissue to some mechanical stimulus. Models which account for this mechanism belong to the class of *mechanotransduction models*. Mechanical stimuli are sensed by the cell through mechanotransducers, such as transmembrane proteins (e.g. cadherins and integrins). They respond to a mechanical stimulus by generating a transduction current which in turn changes the membrane potential and activates a cascade of processes. For example during embryogenesis, changes in the membrane potential induce the contraction of the actomyosin in order to maintain tensional homeostasis in the cell. This process is called mechanoreciprocity and is fundamental during embryogenesis, when the stiffness of the external environment of the cell is translated into contraction forces which in turn drive morphogenetic movements in the embryo [61]. Furthermore, the conversion of physical forces into biochemical information has been demonstrated to play a crucial role in the formation of left-right asymmetry in mammal embryos [62] and during the embryonic development of the heart [63], where the mechanical stimulus is represented by the blood flow.
Mechanotransductors can directly act on gene activation and inhibition, or indirectly, altering morphogen gradients [64]. During tumor growth for example, the stiffness increase of the extra-cellular matrix induces an increase in the cytoskeletal tension which in turn activates the expression of a malignant phenotype through regulation of integrins [65]. Ciarletta et al. recently proposed an analytical mechano-transduction model of avascular tumor growth [66]. Paszek et al. develop a numerical model to investigate how a cluster of integrin responds to chemical and mechanical changes in the extra-cellular matrix [67]. In their review, Mitchell and King provide examples of both experimental and computational methods to model and predict how cancer cells respond to fluid shear forces [68].

1.4 Summary and conclusions

In the first part of this chapter, an historical overview on the evolution of the concept of morphogenesis from ancient to modern times has been presented. Our actual knowledge on morphogenesis has been built over the centuries through the work of many scientists which contributed on several levels and fields. The early mechanistic vision of Galileo, who showed that most organisms change their shape in function of the loads that they have to hold, later inspired D'Arcy Thompson in developing a first mathematical approach to morphogenesis. The methodic experimental approach of Roux to the investigation of the

early steps of embryogenesis opened the way to understand the fascinating properties of the embryo and of the cells. The evolutionary theories developed during the 19th Century gave the basis for the development of the modern genetics.
Since the research field has rapidly expanded in the last decades, in the second part of the chapter the focus has been pointed to the modern theories which consider the effect of external stimuli, such as mechanical, chemical, molecular on the generation of forms in living organisms. In particular, this thesis is based on the recent theory of volumetric growth and remodeling which have been proposed at the end of the 90s. The next chapter is intended to give a comprehensive description of the method adopted in this work to model morphogenesis in tubular organs.

Chapter 2

Morphoelasticity: theory and methods

Contents

In this thesis a macroscopic approach for modeling morphogenesis in living matter is adopted. In particular, the focus is on tubular organs. This chapter is intended to give a description of the methodology used.

2.1 The thermo-mechanics of open systems

There are few main issues one has to deal with, when modeling morphogenetic processes involving soft tissues. First, biological tissues undergo **large deformations**. Thus undeformed and deformed configurations can substantially differ and classical infinitesimal elastic theories cannot be used. A second issue is that biological tissues exhibit **residual stresses**. This means that even when all external loads have been removed, a self-equilibrated distribution of internal stresses persists in the tissue. Residual stresses can be introduced in the tissue by addition of mass (growth) or either from changes in tissue properties (remodeling). They may accumulate in the tissue and, once exceeded a critical value, residual stresses may provoke an elastic instability, thus guiding the transition to a morphological change. Residual stresses have been found in several tubular organs such as arteries [69,70], airways [36,71] and the gastro-intestinal system [72,73]. In arteries for instance, their presence is revealed when radially (i.e. on a plan parallel to the longitudinal axis) cutting a ring of the blood vessel. The arterial ring opens up releasing the circumferential residual stress. Lastly, soft tissues exhibit a **nonlinear mechanical behavior** and this has to be taken into account when making constitutive assumptions. In view of these considerations, thermo-mechanics of open systems is a natural framework for a macroscopic modeling of morphogenesis in living tissues. The kinematics of finite deformations allows for the mathematical description of the morphogenetic process. The balance of mass and linear momentum governs the physical problem and the second law of thermodynamics dictates the restrictions for the evolution of the growth and for the constitutive equations for the material.

2.1.1 Kinematics

Let the soft tissue be an elastic body and let $\mathcal{E} \subset \mathbb{R}^3$ be a three-dimensional Euclidean space. Let $\mathcal{B}_0, \mathcal{B}_a \subset \mathcal{E}$ be two regions occupied by the tissue in two different instants of time. Let $\boldsymbol{\chi}$ be the deformation which transforms the tissue from its initial unstressed configuration $\mathcal{B}_0$ to its final residually stressed configuration $\mathcal{B}_a$. It is defined as the

following $\mathcal{C}^1$-diffeomorphism:

$$\boldsymbol{\chi} : \mathcal{B}_0 \to \mathcal{B}_a \qquad \mathbf{x} = \boldsymbol{\chi}(\mathbf{X}), \qquad \text{with inverse} \quad \mathbf{X} = \boldsymbol{\chi}^{-1}(\mathbf{x}) \tag{2.1}$$

where $\mathbf{X}$, $\mathbf{x}$ are the position vectors in the reference and actual configurations $\mathcal{B}_0$ and $\mathcal{B}_a$, respectively. The deformation gradient, associated to the deformation in Eq.(2.1), is the second order two-point tensor defined as:

$$\mathbf{F} : T\mathcal{B}_0 \to T\mathcal{B}_a \qquad \mathbf{F} = \operatorname{Grad} \mathbf{x} = \frac{\partial \boldsymbol{\chi}(\mathbf{X})}{\partial \mathbf{X}} = \frac{\partial x_i}{\partial X_j} \mathbf{e}_i \otimes \mathbf{E}_j, \tag{2.2}$$

where $\mathbf{E}_j, \mathbf{e}_i$ (with $i, j \in \{1, 2, 3\}$) are the basis unit vectors in the reference and actual configurations, respectively, and $T\mathcal{B}_0, T\mathcal{B}_a$ are the collections of all tangent spaces on $\mathcal{B}_0$ and $\mathcal{B}_a$, respectively. A tangent space is the set of all line elements attached to a body point. The capital notation Grad in Eq.(2.2) indicates the gradient operator with respect to the material position X_j in the reference configuration $\mathcal{B}_0$ and the symbol $\otimes$ indicates the dyadic product between two vectors ($(\mathbf{a} \otimes \mathbf{b})_{\alpha\beta} = (\mathbf{a}\mathbf{b}^T)_{\alpha\beta} = a_\alpha b_\beta$).
According to Eq. (2.2), the following relations for the transformation of line, surface and volume elements, respectively, hold:

$$\mathbf{dx} = \mathbf{F}\mathbf{dX} \tag{2.3}$$

$$\mathbf{n}\mathrm{ds} = J\mathbf{F}^{-T}\mathbf{N}\mathrm{dS} \tag{2.4}$$

$$\mathrm{d}v = J\mathrm{d}V \tag{2.5}$$

where $J = \det \mathbf{F}$ and the quantities $\mathbf{dX}, \mathbf{N}\mathrm{dS}, \mathrm{d}V$ and $\mathbf{dx}, \mathbf{n}\mathrm{ds}, \mathrm{d}v$ are defined in the reference and actual configurations, respectively, with $\mathbf{N}$ and $\mathbf{n}$ being the unit normal vectors to dS and ds, respectively. Eq. (2.5) can be directly derived from Eq. (2.3), while Eq (2.4) is also known as *Nanson's Formula*.

2.1.2 Mathematical theory of growth and remodeling

The aim of this section is to give a mathematical description of growth and remodeling in soft tissues.
The mathematical theory for volumetric growth and remodeling adopted in this thesis, has been first proposed by Skalak [31] and later formalized by Rodriguez et al. [37]. As noted in the first chapter, it has its origins in the plasticity theory.

According to these authors, the mapping $\boldsymbol{\chi}$ introduced in Eq.(2.1) can be split into two parts. One component is associated to the growth (remodeling) and it transforms the tissue from its initial stress free configuration $\mathcal{B}_0$ into a new stress-free grown (remodeled) state, denoted as $\mathcal{B}_g$ in Figure 2.1. This may not be an observable physical state and the tissue can never reach it *in vivo*. Indeed, the grown (remodeled) state $\mathcal{B}_g$ is a collection of local grown (remodeled) states of the body parts, which may not be geometrically compatible with each other, meaning that they can overlap and intersect. The second component restores the global compatibility of the tissue and transforms it from the grown (remodeled) state $\mathcal{B}_g$ into the final compatible and residually stressed configuration $\mathcal{B}_a$. According to this decomposition, the deformation gradient $\mathbf{F}$ defined in Eq.(2.2), can be split into two components, as follows:

$$\mathbf{F} = \mathbf{F}_e \mathbf{F}_g \tag{2.6}$$

where $\mathbf{F}_g$ represents the volumetric growth (remodeling) tensor and $\mathbf{F}_e$ is the elastic tensor. According to the definition given in Chapter 1, remodeling occurs without changes in mass, thus in this case $\det \mathbf{F}_g = 1$. The decomposition in Eq.(2.6) is called *multiplicative decomposition* of the deformation gradient. It is worth noting that even if $\mathbf{F}$ is a gradient of a deformation, this is not the case for its components $\mathbf{F}_g$ and $\mathbf{F}_e$ which are defined as tangent maps as follows:

$$\mathbf{F}_g : T\mathcal{B}_0 \to T\mathcal{B}_g \qquad \mathbf{F}_e : T\mathcal{B}_g \to T\mathcal{B}_a. \tag{2.7}$$

In order to clarify the meaning of the multiplicative decomposition, one can think of cutting an unloaded tissue which is in its residually stressed configuration $\mathcal{B}_a$, into small pieces until all the residual stresses are released. The collection of these stress-free parts defines the natural grown state of the tissue $\mathcal{B}_g$. The natural state is the result of volumetric growth of its body parts, which has occurred over a certain time.
The multiplicative decomposition in Eq.(2.6) implies that the growth (remodeling) and the elastic deformations can be separated. This assumption resides on the physical observation that the typical time-scales involving elasticity and growth (remodeling) are very different.
Let $\tau_g, \tau_v, \tau_l, \tau_e$ be the four characteristic times of the growth problem, namely the growth, the viscoelastic, the loading and the elastic time scales. The characteristic time of growth τ_g can range from hours to days, e.g. being characterized by the typical doubling time of

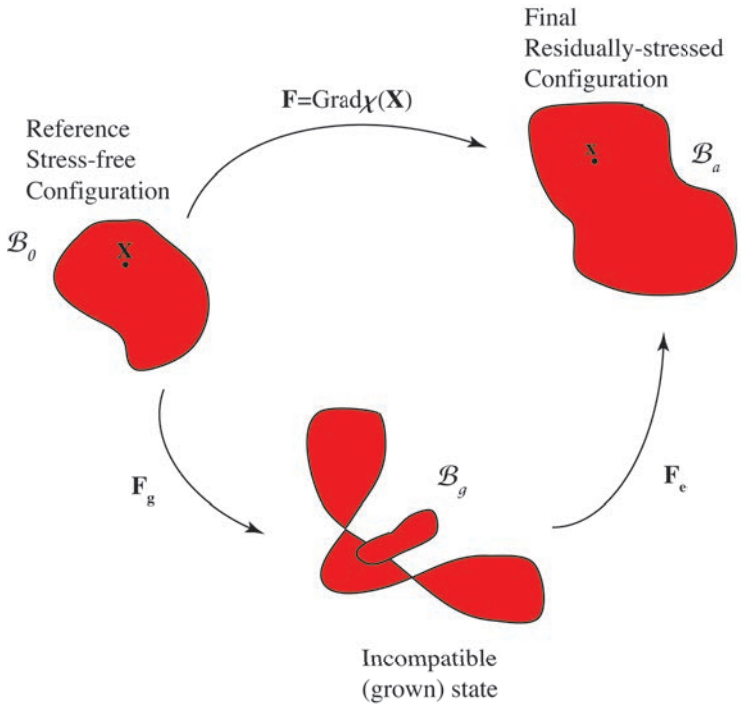

Figure 2.1: The multiplicative decomposition of the deformation gradient $\mathbf{F}$: the growth (remodeling) component $\mathbf{F}_g$ defines a natural grown (remodeled) state $\mathcal{B}_g$ in which geometrical incompatibilities are allowed, and the elastic component $\mathbf{F}_e$ restores the physical compatibility of the tissue deformation.

living cells. The viscoelastic characteristic time τ_v is of the order of hundreds of seconds and is considered as the relaxation time of the tissue [74]. The elastic time τ_e is associated to the characteristic propagation time of elastic waves and the loading time τ_l to the external loading. Therefore the growth time scale is much bigger than the others. This allows for the growth to be separated from the elastic deformations and for τ_g to be the only relevant time in the process. Furthermore, since the elastic response is much faster than the growth, the soft tissue is in elastic static equilibrium at times comparable to τ_g [75].

In the next section, the governing equations for a soft elastic continuum body which undergoes volumetric growth will be derived. The theory can be adapted to the case of remodeling by considering that no change of mass occurs, but instead the microstructure of the tissue varies with time according to an internal parameter, such as for example the density, the stiffness, the symmetry or the orientation of fibers within the tissue.

2.1.3 Governing equations

Before deriving the thermo-mechanical laws for a growing biological tissue, it is useful to introduce some relations that will be used in the following.
Let $\mathbf{f}(\mathbf{x},t)$ be a continuously differentiable spatial vector field, its total time derivative writes as:

$$\dot{\mathbf{f}}(\mathbf{x},t) = \frac{D\mathbf{f}(\mathbf{x},t)}{Dt} = \frac{\partial \mathbf{f}(\mathbf{x},t)}{\partial t} + \mathbf{v}(\mathbf{x},t)\,\mathrm{grad}\,\mathbf{f}(\mathbf{x},t), \tag{2.8}$$

Moreover, considering the integral of the spatial field $\mathbf{f}$ on a volume changing with time, the Reynolds theorem allows for the time derivative to be calculated as:

$$\frac{D}{Dt}\int_{\mathcal{B}_a} \mathbf{f}(\mathbf{x},t)\ \mathrm{d}v = \int_{\mathcal{B}_a} [\dot{\mathbf{f}}(\mathbf{x},t) + \mathbf{f}(\mathbf{x},t)\,\mathrm{div}\,\mathbf{v}(\mathbf{x},t)]\ \mathrm{d}v, \tag{2.9}$$

where $\mathbf{v}(\mathbf{x},t)$ is the spatial velocity. Furthermore, the divergence theorem writes:

$$\int_{\partial\mathcal{B}_a} \mathbf{n}\cdot\mathbf{f}(\mathbf{x},t)\ \mathrm{d}s = \int_{\mathcal{B}_a} \mathrm{div}\,\mathbf{f}(\mathbf{x},t)\ \mathrm{d}v, \tag{2.10}$$

where, in both Eqs.(2.9,2.10), div is the divergence operator with respect to $\mathbf{x}$. If $\mathbf{f}$ is a tensor field, the divergence operates as $\mathrm{div}(\mathbf{f}) = \mathrm{f}_{ih,i}$

2.1.3.1 Balance of mass

In the following, it will be assumed, for the sake of brevity, that body forces and inertial contributions can be neglected, and that there is no flux of mass. Under these assumptions, **the global form of the mass balance** for a growing body writes **in spatial coordinates**:

$$\frac{D}{Dt}\int_{\mathcal{B}_a} \rho\ \mathrm{d}v = \int_{\mathcal{B}_a} \omega\ \mathrm{d}v \tag{2.11}$$

where ρ is the mass density per unit current volume, D/Dt denotes the total time material derivative, and ω is the internal mass production rate per unit current volume. Applying the Reynolds theorem in Eq.(2.9) to the l.h.s of Eq.(2.11), it follows that:

$$\int_{\mathcal{B}_a} [\dot{\rho} + \rho\,\mathrm{div}\,\mathbf{v}]\ \mathrm{d}v = \int_{\mathcal{B}_a} \omega\ \mathrm{d}v. \tag{2.12}$$

In order to derive the material counterpart of Eq.(2.12), it is useful to write the mass element change:

$$\mathrm{dm} = \rho_0 \mathrm{dV} = \rho \mathrm{dv}, \tag{2.13}$$

where ρ_0 is the mass density per unit reference volume. Using Eq.(2.5), it follows that:

$$\rho_0 = J\rho. \tag{2.14}$$

Therefore, using Eq.(2.14), Eq.(2.11) rewrites:

$$\frac{D}{Dt}\int_{\mathcal{B}_0} \rho_0 \ \mathrm{dV} = \int_{\mathcal{B}_0} \Omega \ \mathrm{dV} \tag{2.15}$$

where ρ_0 is the density mass per unit reference volume and, by means of Eq.(2.5), the spatial rate of mass production ω is related to Ω as follows:

$$J\omega = \Omega. \tag{2.16}$$

The local forms of Eqs.(2.12,2.15), can now be easily derived. From Eq.(2.12), **the local form of the mass balance in spatial coordinates** writes:

$$\dot{\rho} + \rho \,\mathrm{div}\, \mathbf{v} = \omega, \tag{2.17}$$

where the dot symbol $\dot{}$ operates as the total time derivative defined in Eq.(2.8). Permuting integration and differentiation in Eq.(2.15), **the local form of the mass balance in material coordinates** reads:

$$\dot{\rho}_0 = \Omega. \tag{2.18}$$

Now, with the aim of deriving a relation between the rate of mass production ω (thus Ω) and the growth tensor $\mathbf{F}_g$, it is assumed that all the mass production takes place in the transformation from $\mathcal{B}_0$ to $\mathcal{B}_g$. Accordingly, a mass element $\mathrm{dM} = \rho_0 \mathrm{dV}$ in $\mathcal{B}_0$ transforms into:

$$\mathrm{dm} = \rho_g \ \mathrm{dV}_g = \rho J_e \ \mathrm{dV}_g = \rho \ \mathrm{d}v \tag{2.19}$$

in $\mathcal{B}_a$, where ρ_g and dV_g are the mass density and the volume element, respectively in $\mathcal{B}_g$ and $J_e = \det \mathbf{F}_e$. Substituting Eqs.(2.14) and (2.16) into Eq. (2.18) and assuming ρ

constant, the material mass balance in Eq.(2.18) reads:

$$\rho \dot{J} = \omega J. \tag{2.20}$$

Now, soft tissues are mostly made of water. This feature characterizes them as incompressible materials, i.e. they deform at constant volume. The incompressibility constraint implies that the elastic deformation is isochoric in the transformation from $\mathcal{B}_g$ to $\mathcal{B}_a$, so that:

$$J_e = \mathrm{d}v/\mathrm{dV}_g = 1 \quad \Rightarrow \quad \det \mathbf{F}_e = 1. \tag{2.21}$$

According to the multiplicative decomposition, which implies the following relation:

$$J = \det \mathbf{F} = \det \mathbf{F}_e \det \mathbf{F}_g = J_e J_g, \tag{2.22}$$

Eq.(2.20) rewrites:

$$\rho \frac{\dot{J}_g}{J_g} = \omega. \tag{2.23}$$

The l.h.s. of Eq. (2.23) is given by:

$$\dot{J}_g = \frac{D}{Dt}(\det \mathbf{F}_g) = J_g \mathbf{F}_g^{-T} : \dot{\mathbf{F}}_g, \tag{2.24}$$

where the symbol : operates as $\mathbf{A}$:$\mathbf{B}$=tr($\mathbf{B}\mathbf{A}^T$)=$B_{ij}A_{ij}$ and tr is the trace operator. Substituting Eq.(2.24) into Eq.(2.23), the relation between the rate of mass production ω and the growth tensor $\mathbf{F}_g$ is given by:

$$\omega = \rho \ \mathbf{F}_g^{-T} : \dot{\mathbf{F}}_g = \rho \ \mathbf{I} : \dot{\mathbf{F}}_g \mathbf{F}_g^{-1} = \rho \, \mathrm{tr}(\dot{\mathbf{F}}_g \mathbf{F}_g^{-1}), \tag{2.25}$$

where $\mathbf{I}$ is the identity matrix. Then, either ω is assigned from constitutive argument, or a form of the growth tensor $\mathbf{F}_g$ must be chosen.

2.1.3.2 Balance of linear momentum

Under the assumption that the body forces can be neglected and there is no flux of mass, **the global form of the linear momentum balance** in presence of volumetric growth can be written **in spatial coordinates** as:

$$\frac{D}{Dt} \int_{\mathcal{B}_a} \rho \mathbf{v} \ \mathrm{d}v = \int_{\partial \mathcal{B}_a} \boldsymbol{\sigma}^T \mathbf{n} \ \mathrm{d}s + \int_{\mathcal{B}_a} \omega \mathbf{v} \ \mathrm{d}v \tag{2.26}$$

where $\boldsymbol{\sigma}$ is the Cauchy stress tensor and $\mathbf{v}$ is the spatial velocity. Applying the material time derivative of a spatial field rule in Eq.(2.9) on the l.h.s, the divergence theorem in Eq.(2.10) on the first term of the r.h.s and substituting the local mass balance in Eq.(2.17) into the second term of the r.h.s, Eq.(2.26) rewrites:

$$\int_{\mathcal{B}_a} \rho\ \dot{\mathbf{v}}\ \mathrm{d}v = \int_{\mathcal{B}_a} \operatorname{div} \boldsymbol{\sigma}\ \mathrm{d}v. \tag{2.27}$$

Eq.(2.27) is **the global form of the balance of linear momentum in spatial coordinates**.

The aim now is to derive the material counterpart of Eq.(2.27). Applying the Nanson's formula in Eq.(2.4) to the first term of the r.h.s of Eq.(2.26), it follows that:

$$\frac{D}{Dt}\int_{\mathcal{B}_0} \rho_0 \mathbf{v}\ \mathrm{dV} = \int_{\partial\mathcal{B}_0} \mathbf{S}^T\mathbf{N}\ \mathrm{dS} + \int_{\mathcal{B}_0} \Omega\mathbf{v}\ \mathrm{dV} \tag{2.28}$$

where the volume element transformation in Eq.(2.5) and the relation in Eq.(2.16) have been used. The stress tensor $\mathbf{S}$ in Eq.(2.28) is called the Nominal stress and is related to the Cauchy stress by $\mathbf{S} = J\mathbf{F}^{-1}\boldsymbol{\sigma}$.

Using the material form of the mass balance in Eq.(2.18) and the divergence theorem, Eq.(2.28) reduces to **the global form of the linear momentum balance in material coordinates**:

$$\int_{\mathcal{B}_0} \rho_0 \dot{\mathbf{v}}\ \mathrm{dV} = \int_{\mathcal{B}_0} \operatorname{Div} \mathbf{S}\ \mathrm{dV}, \tag{2.29}$$

where Div operates as $\operatorname{Div}(\bullet) = (\bullet)_{ij,i}$. The **local forms of the material and spatial balance of linear momentum** in Eqs.(2.27,2.29) respectively, write:

$$\rho\ \dot{\mathbf{v}}\ = \operatorname{div} \boldsymbol{\sigma} \tag{2.30}$$

$$\rho_0 \dot{\mathbf{v}} = \operatorname{Div} \mathbf{S}. \tag{2.31}$$

Eqs. (2.17,2.21,2.30) and (2.18,2.21,2.31) are the governing equations for a body undergoing finite growth in spatial and material coordinates, respectively.

In order to solve the governing equations, appropriate boundary conditions need to be assigned. Before giving a brief overview on the type and form of the boundary conditions, the balance of angular momentum will be presented in the next section, in order to derive the symmetry property of the Cauchy stress tensor.

2.1.3.3 Balance of angular momentum

Under the assumption that the body forces can be neglected and there is no flux of mass, **the global form of the angular momentum balance** in presence of volumetric growth can be written **in spatial coordinates** as:

$$\frac{D}{Dt}\int_{\mathcal{B}_a}\mathbf{y}\times\rho\mathbf{v}\ \mathrm{d}v=\int_{\partial\mathcal{B}_a}\mathbf{y}\times\boldsymbol{\sigma}\mathbf{n}\ \mathrm{d}s+\int_{\mathcal{B}_a}\mathbf{y}\times\omega\mathbf{v}\ \mathrm{d}v \tag{2.32}$$

where $\times$ is the cross product and the position vector $\mathbf{y}$ has been introduced as $\mathbf{y}=\mathbf{x}-\mathbf{x}_0$ with $\mathbf{x}_0$ being a fixed vector position. Using the Reynolds theorem in Eq.(2.9), the l.h.s of Eq.(2.32), rewrites:

$$\frac{D}{Dt}\int_{\mathcal{B}_a}\mathbf{y}\times\rho\mathbf{v}\ \mathrm{d}v=\int_{\mathcal{B}_a}[\dot{\overline{(\mathbf{y}\times\rho\mathbf{v})}}+(\mathbf{y}\times\rho\mathbf{v})\,\mathrm{div}\,\mathbf{v}]\ \mathrm{d}v=\int_{\mathcal{B}_a}[\mathbf{y}\times(\dot{\rho}\mathbf{v}+\rho\dot{\mathbf{v}})+(\mathbf{y}\times\rho\mathbf{v})\,\mathrm{div}\,\mathbf{v}]\ \mathrm{d}v \tag{2.33}$$

where the second equality follows from $\dot{\mathbf{y}}=\dot{\mathbf{x}}=\mathbf{v}$ and the product differentiation rule of the cross product.
Using the divergence theorem in Eq.(2.10) and the properties of the cross product, the first term in the r.h.s of Eq.(2.32) transforms into the volume integral:

$$\int_{\partial\mathcal{B}_a}\mathbf{y}\times\boldsymbol{\sigma}\mathbf{n}\ \mathrm{d}s=\int_{\mathcal{B}_a}[\mathbf{y}\times\mathrm{div}\,\boldsymbol{\sigma}+\boldsymbol{\mathcal{E}}:\boldsymbol{\sigma}^T]\ \mathrm{dV} \tag{2.34}$$

where $\boldsymbol{\mathcal{E}}=\epsilon_{jkl}\mathbf{e}_j\otimes\mathbf{e}_k\otimes\mathbf{e}_l$ is the third-order permutation tensor with components $\epsilon_{jkl}=(\mathbf{e}_j\times\mathbf{e}_k)\cdot\mathbf{e}_l$. Now, using the mass balance in Eq.(2.17), the balance of linear momentum in Eq.(2.30) and substituting Eqs.(2.33,2.34) into Eq.(2.32), it follows that:

$$\int_{\mathcal{B}_a}\boldsymbol{\mathcal{E}}:\boldsymbol{\sigma}^T\ \mathrm{dV}=\mathbf{0} \tag{2.35}$$

The local form of Eq.(2.35) rewrites in index notation:

$$\boldsymbol{\mathcal{E}}:\boldsymbol{\sigma}^T=\epsilon_{jkl}\sigma_{mn}(\mathbf{e}_j\otimes\mathbf{e}_k\otimes\mathbf{e}_l):(\mathbf{e}_n\otimes\mathbf{e}_m)=\epsilon_{jkl}\sigma_{mn}(\mathbf{e}_k\cdot\mathbf{e}_n)(\mathbf{e}_l\cdot\mathbf{e}_m)\mathbf{e}_j=\epsilon_{jkl}\sigma_{lk}\mathbf{e}_j=\mathbf{0}. \tag{2.36}$$

Recalling the property of ϵ_{jkl}, the Cauchy stress tensor $\boldsymbol{\sigma}$ must satisfy:

$$\boldsymbol{\sigma}=\boldsymbol{\sigma}^T \tag{2.37}$$

which implies that:

$$\mathbf{FS} = \mathbf{S}^T\mathbf{F}^T \tag{2.38}$$

hence, the Nominal stress $\mathbf{S}$ is not symmetric.
In the following, a brief description of the type of boundary conditions which can be assigned to the governing equations will be given.

2.1.4 Boundary conditions

Let $\partial\mathcal{B}_0, \partial\mathcal{B}_0^{\mathbf{x}}, \partial\mathcal{B}_0^{\boldsymbol{\sigma}}$ be the boundary in the reference configuration and two portions of the boundary, respectively, such that $\partial\mathcal{B}_0 = \partial\mathcal{B}_0^{\mathbf{x}} \cup \mathcal{B}_0^{\boldsymbol{\sigma}}$. Let $\partial\mathcal{B}_a, \partial\mathcal{B}_a^{\mathbf{x}}, \partial\mathcal{B}_a^{\boldsymbol{\sigma}}$ the associated quantities in the actual configuration, where $\partial\mathcal{B}_a = \partial\mathcal{B}_a^{\mathbf{x}} \cup \mathcal{B}_a^{\boldsymbol{\sigma}}$. In the following three possible categories of boundary conditions are listed:

- **Dirichlet boundary conditions**: the displacements at all points in $\partial\mathcal{B}_0$ and $\partial\mathcal{B}_a$ are specified in the following forms, respectively:

$$\mathbf{u}_0(\mathbf{X}) = \mathbf{x}(\mathbf{X}) - \mathbf{X} = \mathbf{u}_0^* \qquad \text{on } \partial\mathcal{B}_0 \tag{2.39}$$

$$\mathbf{u}_a(\mathbf{x}) = \mathbf{x} - \mathbf{X}(\mathbf{x}) = \mathbf{u}_0^* \qquad \text{on } \partial\mathcal{B}_a \tag{2.40}$$

  where $\mathbf{u}_0, \mathbf{u}_a$ are the displacements in material and spacial form, respectively and $\mathbf{u}_0^*$ is the displacement vector to be assigned at the boundaries.

- **Neumann boundary conditions**: the tractions at all points of $\partial\mathcal{B}_0$ and $\partial\mathcal{B}_a$ are given in the following forms, respectively:

$$\mathbf{S}^T\mathbf{N} = \mathbf{t}_0^* \qquad \text{on } \partial\mathcal{B}_0 \tag{2.41}$$

$$\boldsymbol{\sigma}\mathbf{n} = \mathbf{t}^* \qquad \text{on } \partial\mathcal{B}_a, \tag{2.42}$$

  where $\mathbf{S}, \boldsymbol{\sigma}$ are the Nominal and Cauchy stress respectively and $\mathbf{t}_0^*, \mathbf{t}^*$ are traction vectors to be assigned.

- **Mixed boundary conditions**: displacements are specified on a portion of the boundary $\partial\mathcal{B}_0^{\mathbf{x}}$, $\partial\mathcal{B}_a^{\mathbf{x}}$ and tractions are given on the remaining subset $\partial\mathcal{B}_0^{\boldsymbol{\sigma}}$,$\partial\mathcal{B}_a^{\boldsymbol{\sigma}}$, in

the following forms:

$$\mathbf{u}_0(\mathbf{X}) = \mathbf{u}_0^* \qquad \text{on } \partial\mathcal{B}_0^{\mathbf{x}} \tag{2.43}$$

$$\mathbf{S}^T\mathbf{N} = \mathbf{t}_0^* \qquad \text{on } \partial\mathcal{B}_0^{\boldsymbol{\sigma}}, \tag{2.44}$$

in the reference configuration or:

$$\mathbf{u}_a(\mathbf{X}) = \mathbf{u}_0^* \qquad \text{on } \partial\mathcal{B}_a^{\mathbf{x}} \tag{2.45}$$

$$\boldsymbol{\sigma}\mathbf{n} = \mathbf{t}^* \qquad \text{on } \partial\mathcal{B}_a^{\boldsymbol{\sigma}}, \tag{2.46}$$

in the actual configuration.

2.1.5 Constitutive relations

This section deals with the derivation of the constitutive equations for the elastic stress and the evolution laws for the growth tensor. Following the approach proposed in [41], the first law of thermo-dynamics for an open system with an internal source of growth will be derived. Then, the Clausius-Duhem form of the second law of thermodynamics will be used to impose the restrictions on the constitutive relations for the stress tensors and the evolution law for the growth tensor.

2.1.5.1 First law of thermodynamics

Assuming no heat flux and that the process occurs at constant temperature, the first law of thermodynamics for an open system writes:

$$\frac{D}{Dt}\mathcal{K}(t) + \frac{D}{Dt}\mathcal{E}_{int}(t) = \mathcal{P}_{int}(t) + \mathcal{P}_g(t). \tag{2.47}$$

where $\mathcal{K}(t)$ is the kinetic energy, $\mathcal{E}_{int}(t)$ is the internal energy, $\mathcal{P}_{int}(t)$ is the internal mechanical power and $\mathcal{P}_g(t)$ is the power associated to the generation of mass. The kinetic energy $\mathcal{K}(t)$ is given by:

$$\frac{D}{Dt}\mathcal{K}(t) = \frac{D}{Dt}\int_{\mathcal{B}_0} \frac{1}{2}\rho_0\mathbf{v}^2 \, \mathrm{dV} \tag{2.48}$$

Let ε_0 be the internal energy per unit mass in the reference configuration $\mathcal{B}_0$, then the variation of the internal energy $\mathcal{E}_{int}(t)$ writes:

$$\frac{D}{Dt}\mathcal{E}_{int}(t) = \frac{D}{Dt}\int_{\mathcal{B}_0} \rho_0\varepsilon_0 \ \mathrm{dV}, \tag{2.49}$$

The power $\mathcal{P}_{int}(t)$ associated to the work done by internal forces is given by:

$$\mathcal{P}_{int}(t) = \int_{\partial\mathcal{B}_0} \mathbf{S}^T\mathbf{N}\cdot\mathbf{v} \ \mathrm{dS}. \tag{2.50}$$

and the power due to the internal production of growth reads:

$$\mathcal{P}_g(t) = \int_{\mathcal{B}_0} \frac{1}{2}\Omega\mathbf{v}^2 \ \mathrm{dV} + \int_{\mathcal{B}_0} \Omega\varepsilon_0 \ \mathrm{dV}. \tag{2.51}$$

Now, Ω can be eliminated substituting the mass balance in Eq.(2.18) into Eq.(2.51). Applying the product differentiation rule to Eqs.(2.48) and (2.49) and substituting Eq.(2.51), the variation of kinetic and internal energy rewrite respectively:

$$\frac{D}{Dt}\mathcal{K}(t) = \int_{\mathcal{B}_0} \rho_0\dot{\mathbf{v}}\cdot\mathbf{v} \ \mathrm{dV} \tag{2.52}$$

$$\frac{D}{Dt}\mathcal{E}_{int}(t) = \int_{\mathcal{B}_0} \rho_0\dot{\varepsilon}_0 \ \mathrm{dV} \tag{2.53}$$

Using the divergence theorem in Eq.(2.10), Eq.(2.50) expands as:

$$\mathcal{P}_{int}(t) = \int_{\mathcal{B}_0} [\mathrm{Div}\,\mathbf{S}\cdot\mathbf{v} + \mathbf{S}^T : \dot{\mathbf{F}}] \ \mathrm{dV} = \int_{\mathcal{B}_0} [\rho_0\dot{\mathbf{v}}\cdot\mathbf{v} + \mathbf{S}^T : \dot{\mathbf{F}}] \ \mathrm{dV}. \tag{2.54}$$

Now, substituting Eqs.(2.52,2.53,2.54) into Eq.(2.47), the first law of thermodynamics writes for a growing body:

$$\int_{\mathcal{B}_0} \rho_0\dot{\varepsilon}_0 \ \mathrm{dV} = \int_{\mathcal{B}_0} \mathbf{S}^T : \dot{\mathbf{F}} \ \mathrm{dV}. \tag{2.55}$$

Eq.(2.55) defines how the energy is transformed in the physical system.

2.1.5.2 Second law of thermodynamics

While the energy balance in Eq.(2.55) governs the energy transfer, the Clausius-Duhem form of the second law of thermodynamics defines the direction in which the energy transfer takes place in a physical system. In this section, the second law of the thermodynamics will be used in order to obtain some restrictions on the constitutive relations for the stress tensors $\mathbf{S}$ and $\boldsymbol{\sigma}$ and to derive the evolution law for the growth tensor $\mathbf{F}_g$.

The second law of thermodynamics states that the total production of entropy is never negative:

$$\frac{D}{Dt}\int_{\mathcal{B}_0}\rho_0\eta_0\ \mathrm{dV} - \int_{\mathcal{B}_0}\Omega\eta_0\ \mathrm{dV} \geq 0, \tag{2.56}$$

where η_0 is the entropy per unit reference mass; thus the first term is the rate of entropy change and the second term is the rate of entropy production due to the internal production of mass. Differentiating the first term in Eq.(2.56) and using the mass balance in Eq.(2.18), the inequality in Eq.(2.56) rewrites:

$$\int_{\mathcal{B}_0}\rho_0\dot{\eta}_0\ \mathrm{dV} \geq 0. \tag{2.57}$$

Now, let the **free energy per unit mass** ψ_0 in the reference configuration be introduced as follows:

$$\psi_0 = \varepsilon_0 - \eta_0 T. \tag{2.58}$$

The r.h.s of Eq.(2.58) has a **conservative** contribution, which comes from the internal energy ε_0 and is the amount of available work, and a **dissipative** term $\eta_0 T$, where T is the absolute temperature. Multiplying Eq.(2.57) by T and then substituting the differentiated form of Eq.(2.58), into Eq.(2.57), it follows:

$$\int_{\mathcal{B}_0}\rho_0[\dot{\varepsilon}_0 - \dot{\psi}_0]\ \mathrm{dV} \geq 0. \tag{2.59}$$

Using the first law of thermodynamics in Eq.(2.55), the inequality in Eq.(2.59) transforms into:

$$\int_{\mathcal{B}_0}[\mathbf{S}^T : \dot{\mathbf{F}} - \rho_0\dot{\psi}_0]\ \mathrm{dV} \geq 0. \tag{2.60}$$

By means of the multiplicative decomposition in Eq.(2.6), the first term in Eq.(2.60) can

be derived as follows:

$$\mathbf{S}^T : \dot{\mathbf{F}} = \mathbf{S}^T : (\dot{\mathbf{F}}_e\mathbf{F}_g + \mathbf{F}_e\dot{\mathbf{F}}_g) = \mathbf{S}^T\mathbf{F}_g^T : \dot{\mathbf{F}}_e + \mathbf{F}_e^T\mathbf{S}^T\mathbf{F}_g^T : \dot{\mathbf{F}}_g\mathbf{F}_g^{-1} \tag{2.61}$$

where the properties of the double contraction $(\mathbf{A} : (\mathbf{BC}) = (\mathbf{B}^T\mathbf{A}) : \mathbf{C} = (\mathbf{AC}^T) : \mathbf{B})$ have been used. Assuming that the free energy ψ_0 only depends on the elastic part $\mathbf{F}_e$ of the deformation gradient, the second term in Eq.(2.60) rewrites:

$$\rho_0\dot{\psi_0} = \rho_0\frac{D\psi_0}{Dt} = \rho_0\Big(\frac{\partial\psi_0}{\partial\mathbf{F}_e}\Big)^T : \dot{\mathbf{F}}_e \tag{2.62}$$

Now, substituting Eqs.(2.61) and (2.62) into Eq.(2.57), the inequality in Eq.(2.60) rewrites in the local form:

$$[\mathbf{S}^T\mathbf{F}_g^T - \rho_0\Big(\frac{\partial\psi_0}{\partial\mathbf{F}_e}\Big)^T] : \dot{\mathbf{F}}_e + [\mathbf{F}_e^T\mathbf{S}^T] : \dot{\mathbf{F}}_g \geq 0. \tag{2.63}$$

Eq.(2.63) has to hold for every choice of $\dot{\mathbf{F}}_e$ and $\dot{\mathbf{F}}_g$. Thus, from the first term of Eq.(2.63), follows **the constitutive equation for the Nominal stress tensor**:

$$\mathbf{S} = \rho_0\mathbf{F}_g^{-1}\frac{\partial\psi_0}{\partial\mathbf{F}_e}, \tag{2.64}$$

In the case of an incompressible material, the constitutive equation in Eq.(2.64) takes the following form:

$$\mathbf{S} = \rho_0\mathbf{F}_g^{-1}(\frac{\partial\psi_0}{\partial\mathbf{F}_e} - p\mathbf{F}_e^{-1}), \tag{2.65}$$

where the Lagrange multiplier p has been introduced in order to enforce the incompressibility condition. From Eq.(2.65), **the constitutive relation for the Cauchy stress tensor** writes in the form:

$$\boldsymbol{\sigma} = \rho\mathbf{F}_e\frac{\partial\psi_0}{\partial\mathbf{F}_e} - p\mathbf{I}, \tag{2.66}$$

where $\mathbf{I}$ is the identity matrix. Substituting Eq.(2.64) into Eq.(2.63), the Clausius-Duhem inequality reduces to:

$$[\mathbf{F}_e^T\mathbf{S}^T\mathbf{F}_g^T] : \dot{\mathbf{F}}_g\mathbf{F}_g^{-1} = \rho_0[\mathbf{F}_e^T\Big(\frac{\partial\psi_0}{\partial\mathbf{F}_e}\Big)^T] : \dot{\mathbf{F}}_g\mathbf{F}_g^{-1} = \mathbf{M} : \dot{\mathbf{F}}_g\mathbf{F}_g^{-1} \geq 0, \tag{2.67}$$

where the so called Mandel stress tensor $\mathbf{M} = \rho_0\mathbf{F}_e^T\Big(\frac{\partial\psi_0}{\partial\mathbf{F}_e}\Big)^T$ appears as the work conjugate of $\dot{\mathbf{F}}_g\mathbf{F}_g^{-1}$, thus it is defined in the grown state $\mathcal{B}_g$. Its counterpart expressed in the

reference configuration $\mathcal{B}_0$ can be derived rewriting the reduced inequality in Eq.(2.67), in the equivalent form:

$$\mathbf{M} : \dot{\mathbf{F}}_g \mathbf{F}_g^{-1} = [\mathbf{F}_g^T \mathbf{M} \mathbf{F}_g^{-T}] : \mathbf{F}_g^{-1} \dot{\mathbf{F}}_g \geq 0. \tag{2.68}$$

The term in the square brackets of Eq.(2.68) can be rearranged as follows:

$$\begin{aligned} \mathbf{F}_g^T \mathbf{M} \mathbf{F}_g^{-T} &= \rho_0 [\mathbf{F}_g^T \mathbf{F}_e^T \Big(\frac{\partial \psi_0}{\partial \mathbf{F}_e}\Big)^T \mathbf{F}_g^{-T}] = \rho_0 [\mathbf{F}_g^T \mathbf{F}_e^T \Big(\frac{\partial \psi_0}{\partial \mathbf{F}_e}\Big)^T \mathbf{F}_e^T \mathbf{F}_e^{-T} \mathbf{F}_g^{-T}] = \\ &= [\mathbf{F}^T \boldsymbol{\sigma}^T \mathbf{F}^{-T}] = \mathbf{T}_s^T, \end{aligned} \tag{2.69}$$

where the tensor $\mathbf{T}_s$ is the Mandel tensor in the material configuration, which is symmetric. This implies that $\mathbf{F}_g^{-1} \dot{\mathbf{F}}_g$ is also symmetric, having at most six independent components.

The inequality in Eq.(2.67) has to hold for all $\dot{\mathbf{F}}_g \mathbf{F}_g^{-1}$, thus the evolution law for $\mathbf{F}_g$ can be derived by making appropriate assumptions and would usually write as function of $\mathbf{F}_g, \mathbf{F}_e$ and the stress, in the general form:

$$\dot{\mathbf{F}}_g = \mathcal{H}(\mathbf{F}_g, \mathbf{F}_e, \mathbf{S}, \boldsymbol{\sigma}). \tag{2.70}$$

As proposed in [44], one simple possible assumption could be:

$$\boldsymbol{\mathcal{K}} \mathbf{F}_e^T \Big(\frac{\partial \psi_0}{\partial \mathbf{F}_e}\Big)^T = \dot{\mathbf{F}}_g \mathbf{F}_g^{-1} \tag{2.71}$$

where $\boldsymbol{\mathcal{K}}$ is a constant symmetric positive-definite second order tensor. Under the hypothesis in Eq.(2.71), the inequality in Eq.(2.67) is automatically satisfied (because of the quadratic form) and the evolution law for the growth would be given by:

$$\dot{\mathbf{F}}_g = \boldsymbol{\mathcal{K}} \mathbf{F}_e^T \Big(\frac{\partial \psi_0}{\partial \mathbf{F}_e}\Big)^T \mathbf{F}_g. \tag{2.72}$$

The Eq.(2.72), also represents a constitutive equation for the mass production term ω in Eq.(2.25), in the case where the grown matter is produced at a given constant density.

2.1.6 Summary of the key equations and some comments

In this section, it has been shown how continuum mechanics can provide a useful framework in order to model the problem of volumetric growth and remodeling of an elastic

body. The growth process has been described as a motion from an initial configuration $\mathcal{B}_0$ where the body is stress-free, into a current residually stressed configuration $\mathcal{B}_a$. Following the theory of volumetric growth developed by Skalak and by Rodriguez et al. in the 90s, the gradient associated to the deformation has been split into a pure volumetric growth component and a pure elastic one. Following the approach proposed by Epstein and Maugin [41], the classic mechanical balance laws for closed systems have been adapted to a physical system in which an internal production of mass takes place and the governing equations for the equilibrium problem have been derived from the balance of mass and linear momentum. The two thermodynamic laws have provided the tools for deriving the constitutive relations for the elastic body and the evolution law for the growth tensor.
The elastic problem is thus completely described in the current configuration $\mathcal{B}_a$ by the following set of equations:

$$\rho\dot{\mathbf{v}} - \operatorname{div}\boldsymbol{\sigma} = \mathbf{0} \tag{2.73}$$

$$\omega = \rho\ \mathbf{I} : \dot{\mathbf{F}}_g\mathbf{F}_g^{-1} \tag{2.74}$$

$$\det\mathbf{F}_e = 1 \tag{2.75}$$

$$\boldsymbol{\sigma} = \rho\mathbf{F}_e\frac{\partial\psi_0}{\partial\mathbf{F}_e} - p\mathbf{I} \tag{2.76}$$

$$\dot{\mathbf{F}}_g\mathbf{F}_g^{-1} = \mathcal{H}(\mathbf{F}_e, \mathbf{F}_g, \boldsymbol{\sigma}) \tag{2.77}$$

which are the balance of momentum and mass in absence of body forces and fluxes of mass, the incompressibility constraint, the constitutive equation for the Cauchy stress tensor and the evolution law for the growth tensor, respectively.
In the case of a quasi-static growth process the time doesn't enter in the governing equations as a variable. It follows that the evolution law for the growth and the mass balance are not needed, and in this case, it is sufficient to specify a form for the growth tensor $\mathbf{F}_g$. Therefore, for a quasi-static growth problem, the governing equations reduce to the spatial form:

$$\operatorname{div}\boldsymbol{\sigma} = \mathbf{0} \tag{2.78}$$

$$\det\mathbf{F}_e = 1. \tag{2.79}$$

$$\boldsymbol{\sigma} = \rho(\mathbf{F}_e\frac{\partial\psi_0}{\partial\mathbf{F}_e} - p\mathbf{I}), \tag{2.80}$$

or equivalently to the material form:

$$\operatorname{Div} \mathbf{S} = \mathbf{0} \tag{2.81}$$

$$\det \mathbf{F}_e = 1 \tag{2.82}$$

$$\mathbf{S} = \rho_0 \mathbf{F}_g^{-1} \left(\frac{\partial \psi_0}{\partial \mathbf{F}_e} - p\mathbf{F}_e^{-1}\right). \tag{2.83}$$

The basic solution $\mathbf{x}^{(0)} = \boldsymbol{\chi}^{(0)}(\mathbf{X})$ to the quasi-static problem defines an equilibrium configuration for the elastic body. Moreover, the solution $\mathbf{x}^{(0)}$ depends on a control parameter which is related to the volumetric growth or remodeling. It might happen that the solution is stable for certain values of the control parameter but it becomes unstable when the parameter reaches a critical value and a bifurcation in the solution path occurs. In the next section, the method used to perform the linear stability analysis of the basic solution will be outlined.

2.2 Method of incremental deformations superposed on finite deformations

An accumulation of residual stresses during growth and remodeling can trigger elastic instabilities in the tissue. Morpho-elasticity investigates the emergence of complex patterns in living matter after the occurrence of an elastic instability. Therefore, *the method of incremental deformations superposed on finite deformations* will be introduced in the following.

Following Ogden [76], the fundamental idea is to perturb the basic solution $\mathbf{x}^{(0)}$ to the elastic problem, with a small incremental deformation so that, the perturbed solution can be written as a series expansion to the first order around the basic solution. The zeroth order term is in the form of a finite deformation, representing the basic solution with the initial shape of the material. The first order term is in the form of an incremental deformation, defining the morphology of the material after a possible bifurcation.

In the following, the method of incremental deformation will be introduced and the first-order constitutive and governing equations will be derived.

2.2.1 Incremental deformation

Let $\mathbf{x}^{(0)}$ be the *basic* position vector in $\mathcal{B}_a$ identified by the basic finite deformation $\boldsymbol{\chi}^{(0)}$ and let $\varepsilon\hat{\mathbf{x}}$ be a small displacement from $\mathbf{x}^{(0)}$. It follows that the perturbed position $\bar{\mathbf{x}}$ can be written as:

$$\bar{\mathbf{x}} = \mathbf{x}^{(0)} + \varepsilon\hat{\mathbf{x}} = \boldsymbol{\chi}^{(0)}(\mathbf{X}) + \varepsilon\boldsymbol{\chi}^{(1)}(\mathbf{x}^{(0)}) \tag{2.84}$$

where $|\varepsilon| \ll 1$ and $\varepsilon\boldsymbol{\chi}^{(1)}(\mathbf{x}^{(0)})$ is a small deformation which in the following will be referred to as the *incremental* deformation. Note that $\boldsymbol{\chi}^{(1)}$ maps the basic position vector $\mathbf{x}^{(0)}$ into its incremental displacement $\hat{\mathbf{x}}$ in the perturbed actual configuration $\hat{\mathcal{B}}_a$. Adopting the convention of summation on repeated indexes, the incremental deformation can be written:

$$\boldsymbol{\chi}^{(1)}(\mathbf{x}) = u_j(\mathbf{x})\mathbf{e}_j \tag{2.85}$$

where the components u_j $(j = 1, 2, 3)$ are the displacements along the principal directions $\mathbf{e}_j$ $(j = 1, 2, 3)$, respectively. Figure 2.2 gives a graphical representation of the basic and

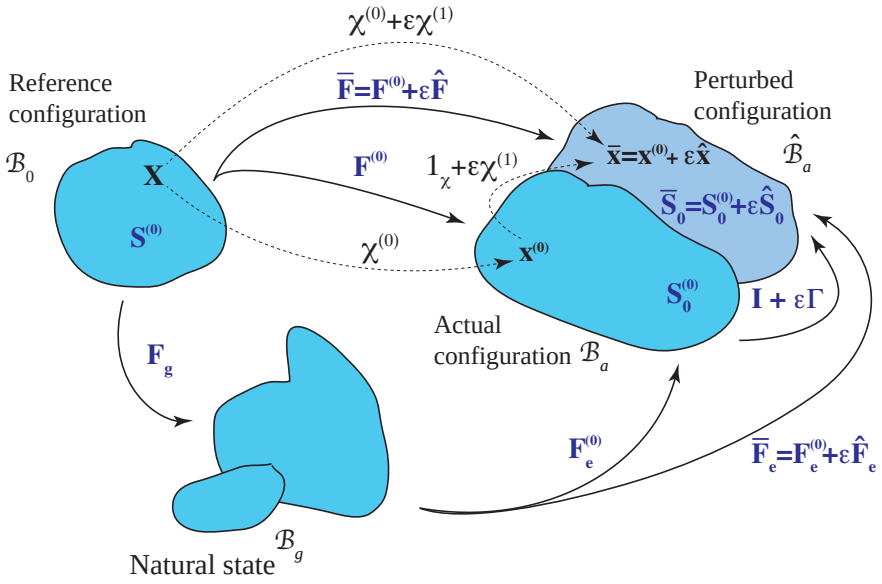

Figure 2.2: Scheme of the basic and perturbed variables. The basic finite deformation $\boldsymbol{\chi}^{(0)}$, the basic position vector $\mathbf{x}^{(0)}$, the basic deformation gradient $\mathbf{F}^{(0)}$ and its elastic component $\mathbf{F}_e^{(0)}$, the basic Nominal stress $\mathbf{S}^{(0)}$ and its push-forward $\mathbf{S}_0^{(0)}$. The variables after the introduction of the incremental deformation $\boldsymbol{\chi}^{(1)}$: the perturbed position vector $\bar{\mathbf{x}}$, the perturbed deformation gradient $\bar{\mathbf{F}}$ and its elastic component $\bar{\mathbf{F}}_e$, the push forward of the perturbed Nominal stress $\bar{\mathbf{S}}^{(0)}$.

perturbed quantities introduced in this section.

2.2.2 Incremental boundary value problem

With the final purpose of writing the first-order boundary value problem (BVP), first the deformation gradient $\mathbf{F}$ and the stress tensors $\mathbf{S}$ and $\boldsymbol{\sigma}$ will be rewritten in the perturbed form. Then, the incremental equilibrium equations and the incompressibility condition will be derived, together with the incremental boundary conditions. In the following, the variables after perturbation will be indicated with the symbol $\bar{(\bullet)}$, and the incremental variables with the symbol $\hat{(\bullet)}$.

2.2.2.1 Perturbed deformation gradient

Using the definition of deformation gradient in Eq.(2.2), the **perturbed deformation gradient** $\bar{\mathbf{F}}$ rewrites:

$$\begin{aligned}\bar{\mathbf{F}} = \mathbf{F}^{(0)} + \varepsilon\hat{\mathbf{F}} = \frac{\partial \boldsymbol{\chi}^{(0)}(\mathbf{X})}{\partial \mathbf{X}} + \varepsilon\frac{\partial \boldsymbol{\chi}^{(1)}(\mathbf{x}^{(0)})}{\partial \mathbf{X}} = \\ = \frac{\partial \boldsymbol{\chi}^{(0)}(\mathbf{x}^{(0)})}{\partial \mathbf{X}} + \varepsilon\frac{\partial \boldsymbol{\chi}^{(1)}(\mathbf{x}^{(0)})}{\partial \mathbf{x}^{(0)}}\frac{\partial \mathbf{x}^{(0)}}{\partial \mathbf{X}} = \mathbf{F}^{(0)} + \varepsilon\boldsymbol{\Gamma}\mathbf{F}^{(0)}\end{aligned} \tag{2.86}$$

where the material and the spatial displacement gradient $\hat{\mathbf{F}} = \mathrm{Grad}(\boldsymbol{\chi}^{(1)}(\mathbf{x}^{(0)}))$ and $\boldsymbol{\Gamma} = \mathrm{grad}(\boldsymbol{\chi}^{(1)}(\mathbf{x}^{(0)}))$ respectively, have been introduced and are related by:

$$\hat{\mathbf{F}} = \boldsymbol{\Gamma}\mathbf{F}^{(0)}. \tag{2.87}$$

2.2.2.2 Perturbed stresses

The **perturbed Nominal stress** $\bar{\mathbf{S}}$ is given by:

$$\bar{\mathbf{S}} = \underbrace{\mathbf{S}^{(0)}}_{\text{zeroth-order term}} + \underbrace{\varepsilon\hat{\mathbf{S}},}_{\text{first-order term}} \tag{2.88}$$

where the $\mathbf{S}^{(0)}$ is the zeroth order term of the series expansion of the Nominal stress in Eq.(2.65). The first order increment $\hat{\mathbf{S}}$ can be derived by differentiating the constitutive equation in Eq. (2.65) and it reads:

$$\hat{\mathbf{S}} = \boldsymbol{\mathcal{A}}^1\hat{\mathbf{F}} + p(\mathbf{F}^{(0)})^{-1}\hat{\mathbf{F}}(\mathbf{F}^{(0)})^{-1} - q(\mathbf{F}^{(0)})^{-1}. \tag{2.89}$$

In Eq. (2.89), the term $q = \hat{p}$ is the increment in p and $\boldsymbol{\mathcal{A}}^1$ is the fourth-order tensor of the elastic moduli, defined as:

$$\boldsymbol{\mathcal{A}}^1 = \frac{\partial \psi_0}{\partial \mathbf{F} \partial \mathbf{F}}, \quad \mathcal{A}^1_{\gamma k \beta j} = \frac{\partial^2 \psi_0}{\partial F_{k\gamma} \partial F_{j\beta}}. \tag{2.90}$$

The **perturbed Cauchy stress** tensor in the perturbed configuration $\hat{\mathcal{B}}_a$, is given by $\bar{\boldsymbol{\sigma}} = \bar{\mathbf{F}}\bar{\mathbf{S}}$, but since $\hat{\mathcal{B}}_a$ is unknown, in the following it will not be convenient to use $\bar{\boldsymbol{\sigma}}$. Therefore, let **the push-forward of the perturbed Nominal stress** be defined as:

$$\bar{\mathbf{S}}_0 = \mathbf{F}^{(0)}\bar{\mathbf{S}} = \mathbf{S}_0^{(0)} + \varepsilon \hat{\mathbf{S}}_0 \tag{2.91}$$

where, $\mathbf{S}_0^{(0)} = \mathbf{F}^{(0)}\mathbf{S}^{(0)}$ is the push forward of the zeroth-order term $\mathbf{S}^{(0)}$. Using Eq.(2.87) the push-forward $\hat{\mathbf{S}}_0$ of the first order term $\hat{\mathbf{S}}$ is given by:

$$\hat{\mathbf{S}}_0 = \mathbf{F}^{(0)}\hat{\mathbf{S}} = \boldsymbol{\mathcal{A}}_0^1 \boldsymbol{\Gamma} + p\boldsymbol{\Gamma} - q\mathbf{I} \tag{2.92}$$

and $\boldsymbol{\mathcal{A}}_0^1$, i.e. the push-forward of $\boldsymbol{\mathcal{A}}^1$ has been introduced. Its components read:

$$\mathcal{A}^1_{0hklj} = F^{(0)}_{h\gamma} F^{(0)}_{l\beta} \mathcal{A}^1_{\gamma k \beta j}. \tag{2.93}$$

The fourth-order tensor $\mathcal{A}_0^1$ is also known as *the tensor of instantaneous moduli*.

2.2.2.3 Incremental governing equations

The equilibrium equations after introducing the perturbation write in the reference configuration $\mathcal{B}_0$:

$$\mathrm{Div}(\bar{\mathbf{S}}) = \mathrm{Div}(\mathbf{S}^{(0)} + \varepsilon \hat{\mathbf{S}}) = \mathrm{Div}(\mathbf{S}^{(0)}) + \varepsilon \,\mathrm{Div}(\hat{\mathbf{S}}) = \mathbf{0} \tag{2.94}$$

Recalling that the zeroth order term $\mathbf{S}^{(0)}$ is solution of Eq.(2.81), the **incremental equilibrium equations in the reference configuration** $\mathcal{B}_0$ rewrite:

$$\mathrm{Div}\, \hat{\mathbf{S}} = \mathbf{0}, \tag{2.95}$$

where $\hat{\mathbf{S}}$ is given by Eq.(2.89).
Using the properties of the Piola transformation and Eq.(2.91), the equilibrium equations

in Eq. (2.95) can be written in $\mathcal{B}_a$ as:

$$\mathrm{Div}(\bar{\mathbf{S}}) = \mathrm{div}(\mathbf{F}^{(0)}\bar{\mathbf{S}}) = \mathrm{div}(\mathbf{F}^{(0)}\mathbf{S}^{(0)} + \varepsilon\mathbf{F}^{(0)}\hat{\mathbf{S}}) = \mathrm{Div}(\mathbf{S}^{(0)}) + \varepsilon\,\mathrm{div}(\hat{\mathbf{S}}_0) = \mathbf{0}. \tag{2.96}$$

Recalling that the zeroth order $\mathbf{S}^{(0)}$ is solution of Eq.(2.81), the **incremental equilibrium equations in the actual configuration** $\mathcal{B}_a$ rewrite:

$$\mathrm{div}\,\hat{\mathbf{S}}_0 = \mathbf{0}, \tag{2.97}$$

where $\hat{\mathbf{S}}_0$ is given by Eq.(2.92).
Furthermore, the **incompressibility condition** in Eq.(2.21) linearized at the first order reads:

$$\mathrm{tr}\,\boldsymbol{\Gamma} = \mathbf{0}. \tag{2.98}$$

In the following section, the first order incremental boundary conditions will be derived.

2.2.2.4 Incremental boundary conditions

Let $\hat{\mathbf{u}}_0^*$ and $\hat{\mathbf{t}}_0^*$ be the increments of the assigned displacement and traction vectors $\mathbf{u}_0^*$ and $\mathbf{t}_0^*$ respectively and $\hat{\mathbf{t}}^*$ the increment of the assigned traction vector $\mathbf{t}^*$.
The boundary conditions on displacements, introduced in Section 2.1.4, rewrite in the first order incremental form:

$$\hat{\mathbf{x}}(\mathbf{X}) = \hat{\mathbf{u}}_0^* \qquad \text{on } \partial\mathcal{B}_0^{\mathbf{x}} \tag{2.99}$$

$$\hat{\mathbf{x}}(\mathbf{x}) = \boldsymbol{\chi}^{(1)}(\mathbf{x}) = \hat{\mathbf{u}}_0^* \qquad \text{on } \partial\mathcal{B}_a^{\mathbf{x}} \tag{2.100}$$

and the incremental boundary conditions on tractions read:

$$\hat{\mathbf{S}}^T\mathbf{N} = \hat{\mathbf{t}}_0^* \qquad \text{on } \partial\mathcal{B}_0^{\boldsymbol{\sigma}} \tag{2.101}$$

$$\hat{\mathbf{S}}_0^T\mathbf{n} = \hat{\mathbf{t}}^* \qquad \text{on } \partial\mathcal{B}_a^{\boldsymbol{\sigma}}. \tag{2.102}$$

2.2.3 Summary of the key incremental equations

Before proceeding to illustrate the resolution methods of the incremental problem, a brief summary of the main equations derived so far is presented.
In Section 2.1, the governing equations for a body undergoing volumetric growth and remodeling have been derived together with the constitutive equations for the material,

both in spatial (Eqs.(2.81,2.82,2.83)) and material coordinates (Eqs.(2.78,2.79,2.80)). The basic solution to these equations defines an equilibrium configuration for the elastic body. With the aim of investigating the emergence of complex patterns in living materials after the occurrence of an elastic instability, *the method of incremental deformations superposed on finite deformations* has been introduced in Section 2.2. The solution to the elastic problem has been written as series expansion to the first order, where the zeroth order term is in the form of a finite deformation and represents the basic solution, and the first order term is in the form of an incremental deformation. The constitutive equations after the introduction of the perturbation have been derived together with the first order incremental equilibrium equations and read:

$$\operatorname{div} \hat{\mathbf{S}}_0 = \mathbf{0} \tag{2.103}$$

$$\operatorname{tr} \boldsymbol{\Gamma} = 0 \tag{2.104}$$

$$\hat{\mathbf{S}}_0 = \mathbf{F}^{(0)}\hat{\mathbf{S}} = \boldsymbol{\mathcal{A}}_0^1\boldsymbol{\Gamma} + p\boldsymbol{\Gamma} - q\mathbf{I} \tag{2.105}$$

with boundary conditions in the general mixed form:

$$\boldsymbol{\chi}^{(1)}(\mathbf{x}) = \hat{\mathbf{u}}_0^* \qquad \text{on } \partial\mathcal{B}_a^{\mathbf{x}} \tag{2.106}$$

$$\hat{\mathbf{S}}_0^T\mathbf{n} = \hat{\mathbf{t}}^* \qquad \text{on } \partial\mathcal{B}_a^{\boldsymbol{\sigma}}. \tag{2.107}$$

Eqs.(2.103-2.107) represent the **incremental boundary value problem** (BVP) and define a system of four partial differential equations (PDEs), where the four unknowns are the three incremental displacements $u_1(\mathbf{x}), u_2(\mathbf{x}), u_3(\mathbf{x})$ in Eq.(2.85) and the increment q of the Lagrange multiplier. In the following section the methods for solving the incremental problem will be presented.

2.3 Theories and methods for solving the incremental problem

In the previous section, the first order incremental equilibrium problem has been derived for a body undergoing volumetric growth and remodeling. As already mentioned, the problem is a system of four PDEs with boundary conditions. In this section, the focus will be on the analytical techniques that can be used in order to transform the problem in a more suitable form for implementing an efficient numerical solution procedure.

First, the Stroh formalism will be introduced. It will allow to transform the system of PDEs with boundary conditions into a system of first order ordinary differential equations (ODEs) with initial conditions. It will be shown that the Stroh formalism provides an optimal form for building a numerical solution procedure when the problem has a Dirichlet boundary condition. Second, the surface impedance method will be illustrated. It will allow to further transform the Stroh form of the incremental problem into a matrix Riccati equation, which in the case of Neumann boundary conditions, allows to build a more efficient numerical solution algorithm.

2.3.1 Stroh formulation

The Stroh formalism was originally developed by Stroh [77] for a steady state elastic problem and allows the set of four PDEs in Eqs.(2.103,2.104) with the associated boundary conditions to be transformed into a set of six ODEs of first order with initial conditions. In the following, the Stroh formulation will be first derived for a general three-dimensional problem in Cartesian coordinates. Then it will be extended to a problem in cylindrical coordinates, and lastly the formulation will be adapted to incompressible materials.
First, the governing equation of the problem are rewritten in the more suitable index notation. The equilibrium equations in Eq.(2.103) rewrite:

$$\hat{S}_{0hj,h} = 0, \qquad \text{with} \quad h, j = \{1, 2, 3\} \tag{2.108}$$

where summation applies to repeated indexes and the comma indicates the derivative with respect to the variables which follows. The components of the incremental nominal stress $\hat{S}_{0hj}$ from Eq.(2.92) are given by:

$$\hat{S}_{0hj} = \mathcal{A}^1_{0hjkl}\Gamma_{lk} + p\Gamma_{hj} - q\delta_{hj}. \tag{2.109}$$

Let the traction vector in the direction $\mathbf{e}_1$ be:

$$\mathbf{t} = \hat{\mathbf{S}}_0^T \mathbf{e}_1 = \hat{S}_{01h}. \tag{2.110}$$

The incompressibility condition in Eq.(2.98), rewrites:

$$\Gamma_{hh} = 0, \tag{2.111}$$

where the incremental displacement gradient $\mathbf{\Gamma}$ is given by:

$$\mathbf{\Gamma} = \begin{pmatrix} u_{1,1} & u_{1,2} & u_{1,3} \\ u_{2,1} & u_{2,2} & u_{2,3} \\ u_{3,1} & u_{3,2} & u_{3,3} \end{pmatrix}. \tag{2.112}$$

Recalling that the fourth order tensor $\boldsymbol{\mathcal{A}}_0^1$ has the major symmetry $\mathcal{A}^1_{0hjkl} = \mathcal{A}^1_{0klhj}$, it is useful to introduce the following 3x3 matrices:

$$\begin{aligned} &\mathbf{A}_{33} = \mathcal{A}^1_{03j3l}, \qquad \mathbf{A}_{22} = \mathcal{A}^1_{02j2l}, \qquad \mathbf{A}_{11} = \mathcal{A}^1_{01j1l}, \\ &\mathbf{A}_{32} = \mathcal{A}^1_{03j2l}, \qquad \mathbf{A}_{31} = \mathcal{A}^1_{03j1l}, \qquad \mathbf{A}_{21} = \mathcal{A}^1_{02j1l}. \end{aligned} \tag{2.113}$$

In order to briefly illustrates the usefulness of the Stroh formalism, first the most general three-dimensional case without accounting for the incompressibility constraint is considered and the compact form of the problem is derived.

Example 1. Stroh formulation in Cartesian coordinates Let $\mathbf{t}_2 = \hat{S}_{02h}$ and $\mathbf{t}_3 = \hat{S}_{03h}$, using the matrices in Eq.(2.113), it follows:

$$\mathbf{t} = \mathbf{A}_{11}\mathbf{u}_{,1} + \mathbf{A}_{21}^T\mathbf{u}_{,2} + \mathbf{A}_{31}^T\mathbf{u}_{,3} \tag{2.114}$$

$$\mathbf{t}_2 = \mathbf{A}_{21}\mathbf{u}_{,1} + \mathbf{A}_{22}\mathbf{u}_{,2} + \mathbf{A}_{32}^T\mathbf{u}_{,3} \tag{2.115}$$

$$\mathbf{t}_3 = \mathbf{A}_{31}\mathbf{u}_{,1} + \mathbf{A}_{32}\mathbf{u}_{,2} + \mathbf{A}_{33}\mathbf{u}_{,3} \tag{2.116}$$

and the divergence in Eq.(2.108) rewrites in the following compact form:

$$\mathbf{t}_{,1} + \mathbf{t}_{2,2} + \mathbf{t}_{3,3} = \mathbf{0}. \tag{2.117}$$

Now, substituting Eq.(2.115) and (2.116) into Eq.(2.117):

$$\mathbf{t}_{,1} + \mathbf{A}_{21}\mathbf{u}_{,12} + \mathbf{A}_{22}\mathbf{u}_{,22} + (\mathbf{A}_{32} + \mathbf{A}_{32}^T)\mathbf{u}_{,32} + \mathbf{A}_{31}\mathbf{u}_{,13} + \mathbf{A}_{33}\mathbf{u}_{,33} = \mathbf{0}. \tag{2.118}$$

From Eq.(2.114) $\mathbf{u}_{,1}$ can be calculated as:

$$\mathbf{u}_{,1} = \mathbf{A}_{11}^{-1}(\mathbf{t} - \mathbf{A}_{21}^T\mathbf{u}_{,2} - \mathbf{A}_{31}^T\mathbf{u}_{,3}) \tag{2.119}$$

where the invertibility of $\mathbf{A}_{11}$ is guaranteed by the strong convexity of $\mathcal{A}_0^1$. Differentiating Eq.(2.119):

$$\mathbf{u}_{,12} = \mathbf{A}_{11}^{-1}(\mathbf{t}_{,2} - \mathbf{A}_{21}^T\mathbf{u}_{,22} - \mathbf{A}_{31}^T\mathbf{u}_{,32}) \tag{2.120}$$

$$\mathbf{u}_{,13} = \mathbf{A}_{11}^{-1}(\mathbf{t}_{,3} - \mathbf{A}_{21}^T\mathbf{u}_{,23} - \mathbf{A}_{31}^T\mathbf{u}_{,33}) \tag{2.121}$$

substituting into Eq.(2.118) and rearranging terms:

$$\begin{aligned}\mathbf{t}_{,1} = &-\mathbf{A}_{21}\mathbf{A}_{11}^{-1}\mathbf{t}_{,2} - \mathbf{A}_{31}\mathbf{A}_{11}^{-1}\mathbf{t}_{,3} + (\mathbf{A}_{21}\mathbf{A}_{11}^{-1}\mathbf{A}_{21}^T - \mathbf{A}_{22})\mathbf{u}_{,22} + (\mathbf{A}_{31}\mathbf{A}_{11}^{-1}\mathbf{A}_{31}^T - \mathbf{A}_{33})\mathbf{u}_{,33} + \\ &+(\mathbf{A}_{21}\mathbf{A}_{11}^{-1}\mathbf{A}_{31}^T - (\mathbf{A}_{32} + \mathbf{A}_{32}^T) + \mathbf{A}_{31}\mathbf{A}_{11}^{-1}\mathbf{A}_{21}^T)\mathbf{u}_{,23}.\end{aligned} \tag{2.122}$$

Assuming that separation of variables holds, solutions are sought in the form:

$$\begin{aligned}\mathbf{u} &= \mathbf{U}(x_1)\, e^{i(k_2x_2+k_3x_3)} \\ \mathbf{t} &= \mathbf{S}(x_1)\, e^{i(k_2x_2+k_3x_3)},\end{aligned} \tag{2.123}$$

where k_2 and k_3, are the wavenumber in the x_2 and x_3 direction respectively, i is the imaginary unit and $\mathbf{U}(x_1), \mathbf{S}(x_1)$ are the amplitude of the incremental displacement and traction vectors, respectively. Using Eq.(2.123) and substituting the vectors $\mathbf{u}$ and $\mathbf{t}$, Eqs.(2.119) and (2.122) rewrite, respectively:

$$\frac{d}{dx_1}\mathbf{U}(x_1) = -\Big\{\mathbf{A}_{11}^{-1}[\mathbf{A}_{21}^T(ik_2) + \mathbf{A}_{31}^T(ik_3)]\Big\}\mathbf{U}(x_1) + \mathbf{A}_{11}^{-1}\mathbf{S}(x_1) \tag{2.124}$$

$$\begin{aligned}\frac{d}{dx_1}\mathbf{S}(x_1) = &\Big\{[\mathbf{A}_{21}\mathbf{A}_{11}^{-1}\mathbf{A}_{31}^T - (\mathbf{A}_{32} + \mathbf{A}_{32}^T) + \mathbf{A}_{31}\mathbf{A}_{11}^{-1}\mathbf{A}_{21}^T](-k_2k_3) + \\ &+[\mathbf{A}_{21}\mathbf{A}_{11}^{-1}\mathbf{A}_{21}^T - \mathbf{A}_{22}](-k_2^2) + [\mathbf{A}_{31}\mathbf{A}_{11}^{-1}\mathbf{A}_{31}^T - \mathbf{A}_{33}](-k_3^2)\Big\}\mathbf{U}(x_1) + \\ &-\Big\{[\mathbf{A}_{21}(ik_2) + \mathbf{A}_{31}(ik_3)]\mathbf{A}_{11}^{-1}\Big\}\mathbf{S}(x_1)\end{aligned} \tag{2.125}$$

or, equivalently:

$$\frac{d}{dx_1}\boldsymbol{\eta}(x_1) = i\mathbf{G}\boldsymbol{\eta}(x_1) \qquad \text{with} \qquad \boldsymbol{\eta}(x_1) = \begin{bmatrix} \mathbf{U}(x_1) \\ i\mathbf{S}(x_1) \end{bmatrix} \tag{2.126}$$

The vector $\boldsymbol{\eta}(x_1)$ is the six-component displacement-traction vector and $\mathbf{G}$ is the so-called Stroh matrix, which was first introduced by Stroh [77] and has the following block-type

structure:

$$\mathbf{G} = \begin{bmatrix} \mathbf{G}_1 & \mathbf{G}_2 \\ \mathbf{G}_3 & \mathbf{G}_1^+ \end{bmatrix} \tag{2.127}$$

where

$$\begin{aligned} \mathbf{G}_1 =& -\mathbf{A}_{11}^{-1}[\mathbf{A}_{21}^T(k_2) + \mathbf{A}_{31}^T(k_3)] \\ \mathbf{G}_2 =& -\mathbf{A}_{11}^{-1} \\ \mathbf{G}_3 =& \quad [\mathbf{A}_{21}\mathbf{A}_{11}^{-1}\mathbf{A}_{31}^T - (\mathbf{A}_{32} + \mathbf{A}_{32}^T) + \mathbf{A}_{31}\mathbf{A}_{11}^{-1}\mathbf{A}_{21}^T](-k_2k_3) \\ & +[\mathbf{A}_{21}\mathbf{A}_{11}^{-1}\mathbf{A}_{21}^T - \mathbf{A}_{22}](-k_2^2) + [\mathbf{A}_{31}\mathbf{A}_{11}^{-1}\mathbf{A}_{31}^T - \mathbf{A}_{33}](-k_3^2) \\ \mathbf{G}_4 =& \quad \mathbf{G}_4 \end{aligned} \tag{2.128}$$

In particular, the Hermitian property $\mathbf{G}_4 = \mathbf{G}_1^+$, where the apex $^+$ indicates the transpose conjugate, leads to a great simplification in solving the problem associated to the compact formulation in Eq.(2.126).

Example 2. Stroh formulation in cylindrical coordinates This section deals with the derivation of the Stroh formalism in a system of cylindrical coordinates. In the following, the variables x_1, x_2, x_3 will be substituted with r, θ, z.
Following the notation adopted in [78], the incremental displacement gradient $\mathbf{\Gamma}_{\text{cyl}}$ has the form:

$$\mathbf{\Gamma}_{\text{cyl}} = \begin{pmatrix} u_{r,r} & \dfrac{u_{r,\theta} - u_\theta}{r} & u_{r,z} \\ u_{\theta,r} & \dfrac{u_{\theta,\theta} + u_r}{r} & u_{\theta,z} \\ u_{z,r} & \dfrac{u_{z,\theta}}{r} & u_{z,z} \end{pmatrix} \tag{2.129}$$

The traction vectors in Eqs.(2.114,2.115,2.116) take the following form:

$$\mathbf{t} = \mathbf{A}_{11}\mathbf{u}_{,r} + \frac{1}{r}\mathbf{A}_{21}^T(\mathbf{u}_{,\theta} + \mathbf{K}\mathbf{u}) + \mathbf{A}_{31}^T\mathbf{u}_{,z} \tag{2.130}$$

$$\mathbf{t}_\theta = \mathbf{A}_{21}\mathbf{u}_{,r} + \frac{1}{r}\mathbf{A}_{22}(\mathbf{u}_{,\theta} + \mathbf{K}\mathbf{u}) + \mathbf{A}_{32}^T\mathbf{u}_{,z} \tag{2.131}$$

$$\mathbf{t}_{,}z = \mathbf{A}_{31}\mathbf{u}_{,r} + \frac{1}{r}\mathbf{A}_{32}(\mathbf{u}_{,\theta} + \mathbf{K}\mathbf{u}) + \mathbf{A}_{33}\mathbf{u}_{,z} \tag{2.132}$$

where the matrix $\mathbf{K}$ is given by:

$$\mathbf{K} = \begin{pmatrix} 0 & -1 & 0 \\ 1 & 0 & 0 \\ 0 & 0 & 0 \end{pmatrix}, \tag{2.133}$$

and the equilibrium equations in cylindrical coordinates rewrite:

$$(r\mathbf{t})_{,r} + \mathbf{t}_{\theta,\theta} + \mathbf{K}\mathbf{t}_{\theta} + r\mathbf{t}_{z,z} = \mathbf{0}. \tag{2.134}$$

Substituting Eq.(2.131) and (2.132) into Eq.(2.134), the equilibrium equations rewrite:

$$\begin{aligned}(r\mathbf{t})_{,r} &+\mathbf{A}_{21}\mathbf{u}_{,r\theta} + \frac{1}{r}\mathbf{A}_{22}(\mathbf{u}_{,\theta\theta} + \mathbf{K}\mathbf{u}_{,\theta}) + \mathbf{K}\big[\mathbf{A}_{21}\mathbf{u}_{,r} + \frac{1}{r}\mathbf{A}_{22}(\mathbf{u}_{,\theta} + \mathbf{K}\mathbf{u})\big] \\ &+r\big[\mathbf{A}_{31}\mathbf{u}_{,rz} + \frac{1}{r}\mathbf{A}_{32}(\mathbf{u}_{,\theta z} + \mathbf{K}\mathbf{u}_{,z}) + \mathbf{A}_{33}\mathbf{u}_{,zz}\big] = \mathbf{0}.\end{aligned} \tag{2.135}$$

Now, from Eq.(2.130) $\mathbf{u}_{,r}$ can be calculated as:

$$\mathbf{u}_{,r} = \mathbf{A}_{11}^{-1}(\mathbf{t} - \frac{1}{r}\mathbf{A}_{21}^{T}(\mathbf{u}_{,\theta} + \mathbf{K}\mathbf{u}) - \mathbf{A}_{31}^{T}\mathbf{u}_{,z}) \tag{2.136}$$

Deriving Eq.(2.136), it follows:

$$\mathbf{u}_{,r\theta} = \mathbf{A}_{11}^{-1}\big[\mathbf{t}_{,\theta} - \frac{1}{r}\mathbf{A}_{21}^{T}(\mathbf{u}_{,\theta\theta} + \mathbf{K}\mathbf{u}_{,\theta}) - \mathbf{A}_{31}^{T}\mathbf{u}_{,z\theta}\big] \tag{2.137}$$

$$\mathbf{u}_{,rz} = \mathbf{A}_{11}^{-1}\big[\mathbf{t}_{,z} - \frac{1}{r}\mathbf{A}_{21}^{T}(\mathbf{u}_{,\theta z} + \mathbf{K}\mathbf{u}_{,z}) - \mathbf{A}_{31}^{T}\mathbf{u}_{,zz}\big] \tag{2.138}$$

Substituting Eqs.(2.137) and (2.138) and replacing the vector $\mathbf{u}$ and $\mathbf{t}$ with Eq.(2.123), Eqs.(2.136) and (2.135) rewrite, respectively:

$$\frac{d}{dr}\mathbf{U}(r) = -\frac{1}{r}\Big\{\mathbf{A}_{11}^{-1}[\mathbf{A}_{21}^{T}\boldsymbol{\kappa} + r\mathbf{A}_{31}^{T}(ik_3)]\Big\}\mathbf{U}(r) + \frac{1}{r}\mathbf{A}_{11}^{-1}\Big(r\mathbf{S}(r)\Big) \tag{2.139}$$

$$\begin{aligned}\frac{d}{dr}\Big(r\mathbf{S}(r)\Big) = \frac{1}{r}\Big\{&\boldsymbol{\kappa}(\mathbf{A}_{22} - \mathbf{A}_{21}\mathbf{A}_{11}^{-1}\mathbf{A}_{21}^{T})\boldsymbol{\kappa} + (k_3 r)^2[\mathbf{A}_{33} - \mathbf{A}_{31}\mathbf{A}_{11}^{-1}\mathbf{A}_{31}^{T}] + \\ &-irk_3[\boldsymbol{\kappa}(\mathbf{A}_{32}^{T} - \mathbf{A}_{21}\mathbf{A}_{11}^{-1}\mathbf{A}_{31}^{T}) + (\mathbf{A}_{32} - \mathbf{A}_{31}\mathbf{A}_{11}^{-1}\mathbf{A}_{21}^{T})\boldsymbol{\kappa}]\Big\}\mathbf{U}(r) + \\ &-\frac{1}{r}\Big\{[\boldsymbol{\kappa}\mathbf{A}_{21} + r\mathbf{A}_{31}(ik_3)]\mathbf{A}_{11}^{-1}\Big\}\Big(r\mathbf{S}(r)\Big)\end{aligned} \tag{2.140}$$

where the matrix $\boldsymbol{\kappa} = ik_2\mathbf{I} + \mathbf{K}$ has been introduced.
Therefore, the compact form of the the problem in Eqs.(2.139) and (2.140) writes:

$$\frac{d}{dr}\boldsymbol{\eta}(r) = \frac{i}{r}\mathbf{G}\boldsymbol{\eta}(r) \qquad \text{with} \qquad \boldsymbol{\eta}(r) = \begin{bmatrix} \mathbf{U}(r) \\ ir\mathbf{S}(r) \end{bmatrix} \tag{2.141}$$

where the four blocks of the Stroh matrix have the form:

$$\begin{aligned}
\mathbf{G}_1 &= i\mathbf{A}_{11}^{-1}[\mathbf{A}_{21}^T\boldsymbol{\kappa} + (irk_3)\mathbf{A}_{31}^T] \\
\mathbf{G}_2 &= -\mathbf{A}_{11}^{-1} \\
\mathbf{G}_3 &= \boldsymbol{\kappa}(\mathbf{A}_{22} - \mathbf{A}_{21}\mathbf{A}_{11}^{-1}\mathbf{A}_{21}^T)\boldsymbol{\kappa} + (k_3r)^2[\mathbf{A}_{33} - \mathbf{A}_{31}\mathbf{A}_{11}^{-1}\mathbf{A}_{31}^T] + \\
&\quad -irk_3[\boldsymbol{\kappa}(\mathbf{A}_{32}^T - \mathbf{A}_{21}\mathbf{A}_{11}^{-1}\mathbf{A}_{31}^T) + (\mathbf{A}_{32} - \mathbf{A}_{31}\mathbf{A}_{11}^{-1}\mathbf{A}_{21}^T)\boldsymbol{\kappa}] \\
\mathbf{G}_4 &= i[\boldsymbol{\kappa}\mathbf{A}_{21} + (irk_3)\mathbf{A}_{31}]\mathbf{A}_{11}^{-1} = \mathbf{G}_1^+.
\end{aligned} \tag{2.142}$$

Recalling that $\boldsymbol{\kappa}^+ = -\boldsymbol{\kappa}$ the identity Hermitian property $\mathbf{G}_4 = \mathbf{G}_1^+$ holds, but in this case the blocks of the Stroh matrix are complex.

Example 3. Stroh formulation for incompressible materials So far, the Stroh compact form has been derived for material without internal constraint. In the following, the case of an incompressible material will be considered. In a Cartesian reference system, the traction vectors in Eqs.(2.114,2.115,2.116) write:

$$\mathbf{t} = \tilde{\mathbf{A}}_{11}\mathbf{u}_{,1} + \tilde{\mathbf{A}}_{21}^T\mathbf{u}_{,2} + \tilde{\mathbf{A}}_{31}^T\mathbf{u}_{,3} - q\ \mathbf{e}_1 \tag{2.143}$$

$$\mathbf{t}_2 = \tilde{\mathbf{A}}_{21}\mathbf{u}_{,1} + \tilde{\mathbf{A}}_{22}\mathbf{u}_{,2} + \tilde{\mathbf{A}}_{32}^T\mathbf{u}_{,3} - q\ \mathbf{e}_2 \tag{2.144}$$

$$\mathbf{t}_3 = \tilde{\mathbf{A}}_{31}\mathbf{u}_{,1} + \tilde{\mathbf{A}}_{32}\mathbf{u}_{,2} + \tilde{\mathbf{A}}_{33}\mathbf{u}_{,3} - q\ \mathbf{e}_3, \tag{2.145}$$

where the following matrices have been introduced:

$$\begin{aligned}
&\tilde{\mathbf{A}}_{33} = \mathcal{A}^1_{03j3l} + p\ \mathbf{e}_3 \otimes \mathbf{e}_3, \quad \tilde{\mathbf{A}}_{22} = \mathcal{A}^1_{02j2l} + p\ \mathbf{e}_2 \otimes \mathbf{e}_2, \quad \tilde{\mathbf{A}}_{11} = \mathcal{A}^1_{01j1l} + p\ \mathbf{e}_1 \otimes \mathbf{e}_1, \\
&\tilde{\mathbf{A}}_{32} = \mathcal{A}^1_{03j2l} + p\ \mathbf{e}_3 \otimes \mathbf{e}_2, \quad \tilde{\mathbf{A}}_{31} = \mathcal{A}^1_{03j1l} + p\ \mathbf{e}_3 \otimes \mathbf{e}_1, \quad \tilde{\mathbf{A}}_{21} = \mathcal{A}^1_{02j1l} + p\ \mathbf{e}_2 \otimes \mathbf{e}_1.
\end{aligned} \tag{2.146}$$

The incompressibility condition in Eq.(2.111) writes:

$$\mathbf{e}_1 \cdot \mathbf{u}_{,1} + \mathbf{e}_2 \cdot \mathbf{u}_{,2} + \mathbf{e}_3 \cdot \mathbf{u}_{,3} = 0. \tag{2.147}$$

Substituting Eq.(2.144) and (2.145) into Eq.(2.117), the equilibrium equations rewrite:

$$\mathbf{t}_{,1}+\tilde{\mathbf{A}}_{21}\mathbf{u}_{,12}+\tilde{\mathbf{A}}_{22}\mathbf{u}_{,22}+(\tilde{\mathbf{A}}_{32}+\tilde{\mathbf{A}}_{32}^{T})\mathbf{u}_{,32}+\tilde{\mathbf{A}}_{31}\mathbf{u}_{,13}+\tilde{\mathbf{A}}_{33}\mathbf{u}_{,33}-q_{,2}\ \mathbf{e}_2-q_{,3}\ \mathbf{e}_3=\mathbf{0}. \quad (2.148)$$

Now, as in the case of material without internal constraints, from Eq.(2.143) $\mathbf{u}_{,1}$ can be calculated as:

$$\mathbf{u}_{,1}=\tilde{\mathbf{A}}_{11}^{-1}(\mathbf{t}-\tilde{\mathbf{A}}_{21}^{T}\mathbf{u}_{,2}-\tilde{\mathbf{A}}_{31}^{T}\mathbf{u}_{,3}+q\ \mathbf{e}_1) \quad (2.149)$$

Deriving Eq.(2.149), it follows:

$$\mathbf{u}_{,12}=\tilde{\mathbf{A}}_{11}^{-1}(\mathbf{t}_{,2}-\tilde{\mathbf{A}}_{21}^{T}\mathbf{u}_{,22}-\tilde{\mathbf{A}}_{31}^{T}\mathbf{u}_{,32}+q_{,2}\ \mathbf{e}_1) \quad (2.150)$$

$$\mathbf{u}_{,13}=\tilde{\mathbf{A}}_{11}^{-1}(\mathbf{t}_{,3}-\tilde{\mathbf{A}}_{21}^{T}\mathbf{u}_{,23}-\tilde{\mathbf{A}}_{31}^{T}\mathbf{u}_{,33}+q_{,3}\ \mathbf{e}_1) \quad (2.151)$$

Substituting Eqs.(2.150) and (2.151) into Eq.(2.148), the equilibrium equations in Eq.(2.148) rewrite:

$$\begin{aligned}\mathbf{t}_{,1}&+\tilde{\mathbf{A}}_{21}\tilde{\mathbf{A}}_{11}^{-1}(\mathbf{t}_{,2}-\tilde{\mathbf{A}}_{21}^{T}\mathbf{u}_{,22}-\tilde{\mathbf{A}}_{31}^{T}\mathbf{u}_{,32}+q_{,2}\ \mathbf{e}_1)+\\&+\tilde{\mathbf{A}}_{31}\tilde{\mathbf{A}}_{11}^{-1}(\mathbf{t}_{,3}-\tilde{\mathbf{A}}_{21}^{T}\mathbf{u}_{,23}-\tilde{\mathbf{A}}_{31}^{T}\mathbf{u}_{,33}+q_{,3}\ \mathbf{e}_1)+\\&+(\tilde{\mathbf{A}}_{32}+\tilde{\mathbf{A}}_{32}^{T})\mathbf{u}_{,32}+\tilde{\mathbf{A}}_{22}\mathbf{u}_{,22}+\tilde{\mathbf{A}}_{33}\mathbf{u}_{,33}-q_{,2}\ \mathbf{e}_2-q_{,3}\ \mathbf{e}_3=\mathbf{0}.\end{aligned} \quad (2.152)$$

Now, the aim is to eliminate the unknown q from Eq.(2.152).
Therefore, the scalar product $\mathbf{e}_1\cdot$ is applied to Eq.(2.149). Then, using the incompressibility condition in Eq.(2.147) the term $\mathbf{e}_1\cdot\mathbf{u}_{,1}$ can be eliminated and after some rearrangements the expression for q can be derived as follows:

$$q=\xi\Big(\mathbf{e}_1\cdot\tilde{\mathbf{A}}_{11}^{-1}\mathbf{A}_{21}^{T}\mathbf{u}_{,2}-\mathbf{e}_2\cdot\mathbf{u}_{,2}+\mathbf{e}_1\cdot\tilde{\mathbf{A}}_{11}^{-1}\mathbf{A}_{31}^{T}\mathbf{u}_{,3}-\mathbf{e}_3\cdot\mathbf{u}_{,3}-\mathbf{e}_1\cdot\tilde{\mathbf{A}}_{11}^{-1}\mathbf{t}\Big), \quad (2.153)$$

where $\xi=1/(\mathbf{e}_1\cdot\tilde{\mathbf{A}}_{11}^{-1}\mathbf{e}_1)$.

Using Eqs.(2.123) and (2.153), Eq.(2.149) and Eq.(2.152) rewrite:

$$\begin{aligned}\frac{d}{dx_1}\mathbf{U}(x_1)=&-i\Big\{\tilde{\mathbf{A}}_{11}^{-1}\big[\tilde{\mathbf{A}}_{21}^{T}(k_2)+\tilde{\mathbf{A}}_{31}^{T}(k_3)+\xi\mathbf{e}_1\otimes(k_2\boldsymbol{\alpha}+k_3\boldsymbol{\beta})\big]\Big\}\mathbf{U}(x_1)+\\&-i\Big\{\tilde{\mathbf{A}}_{11}^{-1}-\xi\mathbf{e}_1\otimes\mathbf{e}_1\tilde{\mathbf{A}}_{11}^{-1}\Big\}(i\mathbf{S}(x_1))\end{aligned} \quad (2.154)$$

$$\begin{aligned}\frac{d}{dx_1}(i\mathbf{S}(x_1)) = i\Big\{ &\big[\tilde{\mathbf{A}}_{21}\tilde{\mathbf{A}}_{11}^{-1}\tilde{\mathbf{A}}_{31}^{T} - (\tilde{\mathbf{A}}_{32} + \tilde{\mathbf{A}}_{32}^{T}) + \tilde{\mathbf{A}}_{31}\tilde{\mathbf{A}}_{11}^{-1}\tilde{\mathbf{A}}_{21}^{T} - \xi(\boldsymbol{\alpha}\otimes\boldsymbol{\beta} + \boldsymbol{\beta}\otimes\boldsymbol{\alpha})\big](-k_2k_3) + \\ &+\big[\tilde{\mathbf{A}}_{21}\tilde{\mathbf{A}}_{11}^{-1}\tilde{\mathbf{A}}_{21}^{T} - \tilde{\mathbf{A}}_{22} - \xi\boldsymbol{\alpha}\otimes\boldsymbol{\alpha}\big](-k_2^2) + \\ &+\big[\tilde{\mathbf{A}}_{31}\tilde{\mathbf{A}}_{11}^{-1}\tilde{\mathbf{A}}_{31}^{T} - \tilde{\mathbf{A}}_{33} - \xi\boldsymbol{\beta}\otimes\boldsymbol{\beta}\big](-k_3^2)\Big\}\mathbf{U}(x_1) + \\ &-i\Big\{\big[\tilde{\mathbf{A}}_{21}(k_2) + \tilde{\mathbf{A}}_{31}(k_3) + \xi(k_2\boldsymbol{\alpha} + k_3\boldsymbol{\beta})\otimes\mathbf{e}_1\big]\tilde{\mathbf{A}}_{11}^{-1}\Big\}(i\mathbf{S}(x_1))\end{aligned} \tag{2.155}$$

respectively, where $\boldsymbol{\alpha} = (\mathbf{e}_2 - \tilde{\mathbf{A}}_{21}\tilde{\mathbf{A}}_{11}^{-1}\mathbf{e}_1)$ and $\boldsymbol{\beta} = (\mathbf{e}_3 - \tilde{\mathbf{A}}_{31}\tilde{\mathbf{A}}_{11}^{-1}\mathbf{e}_1)$. Therefore the blocks which constitute the Stroh matrix in the case of incompressible materials take the form:

$$\begin{aligned}\mathbf{G}_1 =& -\tilde{\mathbf{A}}_{11}^{-1}\big[\tilde{\mathbf{A}}_{21}^{T}(k_2) + \tilde{\mathbf{A}}_{31}^{T}(k_3) + \xi\mathbf{e}_1\otimes(k_2\boldsymbol{\alpha} + k_3\boldsymbol{\beta})\big] \\ \mathbf{G}_2 =& -\tilde{\mathbf{A}}_{11}^{-1} + \xi\mathbf{e}_1\otimes\mathbf{e}_1\tilde{\mathbf{A}}_{11}^{-1} \\ \mathbf{G}_3 =& \big[\tilde{\mathbf{A}}_{21}\tilde{\mathbf{A}}_{11}^{-1}\tilde{\mathbf{A}}_{31}^{T} - (\tilde{\mathbf{A}}_{32} + \tilde{\mathbf{A}}_{32}^{T}) + \tilde{\mathbf{A}}_{31}\tilde{\mathbf{A}}_{11}^{-1}\tilde{\mathbf{A}}_{21}^{T} - \xi(\boldsymbol{\alpha}\otimes\boldsymbol{\beta} + \boldsymbol{\beta}\otimes\boldsymbol{\alpha})\big](-k_2k_3) + \\ &+\big[\tilde{\mathbf{A}}_{21}\tilde{\mathbf{A}}_{11}^{-1}\tilde{\mathbf{A}}_{21}^{T} - \tilde{\mathbf{A}}_{22} - \xi\boldsymbol{\alpha}\otimes\boldsymbol{\alpha}\big](-k_2^2) + \\ &+\big[\tilde{\mathbf{A}}_{31}\tilde{\mathbf{A}}_{11}^{-1}\tilde{\mathbf{A}}_{31}^{T} - \tilde{\mathbf{A}}_{33} - \xi\boldsymbol{\beta}\otimes\boldsymbol{\beta}\big](-k_3^2) \\ \mathbf{G}_4 =& \mathbf{G}_1^{+},\end{aligned} \tag{2.156}$$

where the Hermitian property $\mathbf{G}_4 = \mathbf{G}_1^{+}$ holds.

2.3.1.1 Some comments on the Stroh formalism

The compact Stroh form of the incremental problem has been derived in both Cartesian and cylindrical coordinates and in the case of incompressible materials. In all the examples presented, the hermitian property $\mathbf{G}_4 = \mathbf{G}_1^{+}$ holds. This property is crucial for the Stroh formalism to provide an optimal form in a great variety of elasticity problems. Optimal here is used in the sense that an efficient numerical procedure can be implemented in order to solve the incremental problem. The hermitian property, also implies that the matrix $i\hat{\mathbf{I}}\mathbf{G}$ is symmetric, where $\hat{\mathbf{I}}$ is defined as the block matrix with 0-blocks on the diagonal and identity blocks elsewhere. This property can be used to derive the orthogonality and closure relations which provide useful informations on the nature of the blocks of the Stroh matrix [79]. Furthermore, Fu et al. pointed out that the hermitian property is a direct consequence of the Hamiltonian nature of the Stroh formalism. In particular, every Hamiltonian system in which the variables $\mathbf{u}$ and $\mathbf{t}$ are work conjugates owns the fundamental property [80, 81].

In the following section, another compact representation of the incremental problem, based on the surface impedance method, will be presented.

2.3.2 The surface impedance method

The surface impedance method is largely used for studying waves propagation in inhomogeneous solids. It was first introduced by Biryukov [82] and developed for cylindrical geometries by Destrade et al. [83] and Norris and Shuvalov [84]. The method is presented in the case both of Cartesian an cylindrical coordinates.

Case 1. Surface impedance method in Cartesian coordinates The Stroh formulation for a general three-dimensional problem in Cartesian coordinates reads:

$$\frac{d}{dx_1}\boldsymbol{\eta}(x_1) = i\mathbf{G}\boldsymbol{\eta}(x_1) \qquad \text{with} \qquad \boldsymbol{\eta}(x_1) = \begin{bmatrix} \mathbf{U}(x_1) \\ i\mathbf{S}(x_1) \end{bmatrix} \tag{2.157}$$

With $\mathbf{G}$ having the property $\mathbf{G}_4 = \mathbf{G}_1^+$. Now, let $\boldsymbol{\eta}_n$, $n = \{1, \ldots, 6\}$ be a set of independent solutions of the system in Eq. (2.157) and the 6×6 *matricant* $\mathbf{M}(x_1, x^*_{ini})$ be the following block matrix:

$$\mathbf{M}(x_1, x^*_{ini}) = \begin{pmatrix} \mathbf{M}_1(x_1, x^*_{ini}) & \mathbf{M}_2(x_1, x^*_{ini}) \\ \mathbf{M}_3(x_1, x^*_{ini}) & \mathbf{M}_4(x_1, x^*_{ini}) \end{pmatrix} = \boldsymbol{\mathcal{N}}(x_1)\boldsymbol{\mathcal{N}}^{-1}(x^*_{ini}), \tag{2.158}$$

where x^*_{ini} is the point where the initial condition is assigned and $\boldsymbol{\mathcal{N}}$ is the integral matrix, defined as:

$$\boldsymbol{\mathcal{N}}(x_1) = [\,\boldsymbol{\eta}_1, \ldots, \boldsymbol{\eta}_6\,]\,. \tag{2.159}$$

The matricant in Eq.(2.158), is the solution of the initial value problem :

$$\frac{d\mathbf{M}}{dx_1}(x_1, x^*_{ini}) = i\mathbf{G}(x_1)\mathbf{M}(x_1, x^*_{ini}) \qquad \text{with} \qquad \mathbf{M}(x^*_{ini}, x^*_{ini}) = \mathbf{I}_{(6)}, \tag{2.160}$$

where $\mathbf{I}_{(6)}$ is the 6×6 identity matrix. Now, let $\mathbf{z} = \mathbf{z}(x_1)$ be the conditional impedance matrix defined as the 3×3 matrix, such that:

$$\Big(i\,\mathbf{S}(x_1)\Big) = -i\mathbf{z}(x_1)\,\mathbf{U}(x_1). \tag{2.161}$$

The impedance matrix $\mathbf{z}$ is called *conditional* because of its dependence on the auxiliary value at x_{ini}. Now, the matricant in Eq.(2.158) can be alternatively written in the form:

$$\boldsymbol{\eta}(x_1) = \mathbf{M}(x_1, x^*_{ini})\boldsymbol{\eta}(x^*_{ini}), \tag{2.162}$$

which rewrites:

$$\mathbf{U}(x_1) = [\mathbf{M}_1 - i\mathbf{M}_2\mathbf{z}(x^*_{ini})]\mathbf{U}(x^*_{ini}) \tag{2.163}$$

$$i\,\mathbf{S}(x_1) = [\mathbf{M}_3 - i\mathbf{M}_4\mathbf{z}(x^*_{ini})]\mathbf{U}(x^*_{ini}), \tag{2.164}$$

where $\mathbf{z}(x^*_{ini})$ is the conditional impedance matrix at x^*_{ini}. Now, substituting Eq.(2.161) into Eq.(2.164), it follows:

$$\mathbf{z}(x_1) = i[\mathbf{M}_1 + \mathbf{M}_2\mathbf{z}(x^*_{ini})][\mathbf{M}_3 + \mathbf{M}_4\mathbf{z}(x^*_{ini})]^{-1} \tag{2.165}$$

Therefore, in the case of Neumann and Dirichlet boundary conditions, respectively, the impedance matrix $\mathbf{z}$ reads:

$$\mathbf{z}(x_1) = i\mathbf{M}_3\mathbf{M}_1^{-1} \qquad \text{for } \mathbf{S}(x_{ini}) = \mathbf{0} \tag{2.166}$$

$$\mathbf{z}(x_1) = i\mathbf{M}_4\mathbf{M}_2^{-1} \qquad \text{for } \mathbf{U}(x_{ini}) = \mathbf{0}. \tag{2.167}$$

Now, substituting Eq.(2.161) in Eq.(2.157), the Stroh form of the incremental problem rewrites in term of the impedance matrix:

$$\begin{aligned} \frac{d}{dx_1}\mathbf{U} \quad &= i\mathbf{G}_1\mathbf{U} \;\; + \mathbf{G}_2\mathbf{z}\mathbf{U} \\ \frac{d}{dx_1}(\mathbf{z}\,\mathbf{U}) &= -\mathbf{G}_3\mathbf{U} + i\mathbf{G}_1^{+}\mathbf{z}\mathbf{U} \end{aligned} \tag{2.168}$$

and substituting the first of Eq.(2.168) into the second of Eq. (2.168) it follows **the differential matrix Riccati equation**:

$$\frac{d\mathbf{z}}{dx_1} = i(\mathbf{G}_1^{+}\mathbf{z} + i\mathbf{G}_3 + i\mathbf{z}\mathbf{G}_2\mathbf{z} - \mathbf{z}\mathbf{G}_1). \tag{2.169}$$

The conditional impedance matrix $\mathbf{z}(x^*_{ini})$ can be used as initial value condition for the Riccati Eq.(2.169) and can be calculated using the relation between $\mathbf{z}$ and the traction-displacement vectors in Eq.(2.161).

Case 2. Surface impedance method in cylindrical coordinates In the following, the Stroh form in Eq(2.141), introduced in the previous section will be rewritten in the case of a cylindrical system of coordinates. The matricant $\mathbf{M}(r, r^*_{ini})$ is now solution of

the system:

$$\frac{d\mathbf{M}}{dr}(r, r^*_{ini}) = \frac{i}{r}\mathbf{G}(r)\mathbf{M}(r, r^*_{ini}) \qquad \text{with} \qquad \mathbf{M}(r^*_{ini}, r^*_{ini}) = \mathbf{I}_{(6)}, \tag{2.170}$$

The impedance matrix $\mathbf{z}(r)$ is defined such that:

$$i\, r\, \mathbf{S}(r) = \mathbf{z}(r)\, \mathbf{U}(r). \tag{2.171}$$

Substituting Eq.(2.171) into the Stroh form in Eq.(2.141), the matrix Riccati equation reads in cylindrical coordinates:

$$\frac{d\mathbf{z}}{dr} = \frac{i}{r}\left(\mathbf{G}_1^+\mathbf{z} + i\mathbf{G}_3 + i\mathbf{z}\mathbf{G}_2\mathbf{z} - \mathbf{z}\mathbf{G}_1\right). \tag{2.172}$$

In the following, the Stroh formalism and the Surface Impedance method will be employed in two examples, in order to numerically solve the incremental problem in Eqs.(2.103,2.104) in the case of Dirichlet and Neumann boundary conditions.

2.3.3 Mixed boundary conditions

One of the advantages of the Stroh formulation is that it allows for a stable numerical resolution of the incremental problem with a Dirichlet boundary condition. In this section, an example will be illustrated.
The incremental problem introduced in Section 2.2.2.3 writes:

$$\operatorname{div}\hat{\mathbf{S}}_0 = \mathbf{0} \tag{2.173}$$

$$\operatorname{tr}\boldsymbol{\Gamma} = 0 \tag{2.174}$$

$$\hat{\mathbf{S}}_0 = \mathbf{F}^{(0)}\hat{\mathbf{S}} = \boldsymbol{\mathcal{A}}_0^1\boldsymbol{\Gamma} + p\boldsymbol{\Gamma} - q\mathbf{I} \tag{2.175}$$

with boundary conditions in the mixed form:

$$\boldsymbol{\chi}^{(1)}(\mathbf{x}^{(0)}) = \{0,0,0\} \qquad \text{on } \partial\mathcal{B}_a^{\mathbf{x}} \tag{2.176}$$

$$\hat{\mathbf{S}}_0^T\mathbf{n} = \{0,0,0\} \qquad \text{on } \partial\mathcal{B}_a^{\boldsymbol{\sigma}}. \tag{2.177}$$

It is a set of four PDEs where the unknowns are the components of the incremental deformation $\boldsymbol{\chi}^{(1)}(\mathbf{x}^{(0)})$, namely u_1, u_2, u_3 and the increment of the Lagrange multiplier q

introduced to enforce incompressibility. The problem rewrites in the compact Stroh form:

$$\frac{d}{dx_1}\boldsymbol{\eta}(x_1) = i\mathbf{G}\boldsymbol{\eta}(x_1) \qquad \text{with} \qquad \boldsymbol{\eta}(x_1) = \begin{bmatrix} \mathbf{U}(x_1) \\ i\mathbf{S}(x_1) \end{bmatrix} \tag{2.178}$$

where the blocks of the Stroh matrix $\mathbf{G}$ are in the form of Eq.(2.156), $\mathbf{U}(x_1) = U_j$ {j=1,2,3} and $\mathbf{S}(x_1) = s_{01j}$ {j=1,2,3}. The problem is now a set of six ODEs in the six unknowns: the three incremental displacements $U_1(x_1)$, $U_2(x_1)$, $U_3(x_1)$ and the three incremental stresses $s_{011}(x_1)$, $s_{012}(x_1)$, $s_{013}(x_1)$. Using the Dirichlet boundary condition in Eq.(2.176), an initial condition for Eq.(2.178) can be written in the following form:

$$\eta_0(x_1) = \{\hat{\mathbf{u}}_0^*, \hat{\mathbf{t}}^*\} = \{0, 0, 0, t_1^*, t_2^*, t_3^*\} \qquad \text{at } x_1 = x_{ini}^*, \tag{2.179}$$

where the values $\{t_1^*, t_2^*, t_3^*\}$ are the initial values of the incremental stress vector to be assigned. In order to numerically solve Eqs.(2.178) and (2.179), the *determinantal method* can be used [45, 85]. The idea is to express the solution $\boldsymbol{\eta}$ of Eq.(2.178), as a linear combination of three scalar functions $\boldsymbol{\eta}_1, \boldsymbol{\eta}_2, \boldsymbol{\eta}_3$, being:

$$\boldsymbol{\eta} = \nu_1\boldsymbol{\eta_1} + \nu_2\boldsymbol{\eta_2} + \nu_3\boldsymbol{\eta_3} \tag{2.180}$$

where ν_1, ν_2, ν_3 are constant coefficients. The scalar functions $\boldsymbol{\eta}_k$, $k = \{1, 2, 3\}$, in Eq.(2.180) are three linearly independent copies of the solution, obtained numerically integrating the system of Eq.(2.178) between $x_1 = x_{ini}$ and $x_1 = x_{fin}$ and imposing three linearly independent sets $\boldsymbol{\eta_{0}}_k$ of initial conditions, expressed as:

$$\boldsymbol{\eta}_{0k}(x_1 = x_{ini}) = \{0, 0, 0, (t_1^*)_k, (t_2^*)_k, (t_3^*)_k\}, \quad \text{with} \quad k = \{1, 2, 3\} \tag{2.181}$$

with arbitrary linearly independent incremental stress components $(t_1^*)_k, (t_2^*)_k, (t_3^*)_k$ at $x_1 = x_{fin}$. Then, the solution in Eq.(2.180) must satisfy the other boundary conditions in Eq.(2.177) at $x_1 = x_{fin}$, which rewrites:

$$\det \begin{pmatrix} (s_{011}(x_{fin}))_1 & (s_{012}(x_{fin}))_1 & (s_{013}(x_{fin}))_1 \\ (s_{011}(x_{fin}))_2 & (s_{012}(x_{fin}))_2 & (s_{013}(x_{fin}))_2 \\ (s_{011}(x_{fin}))_3 & (s_{012}(x_{fin}))_3 & (s_{013}(x_{fin}))_3 \end{pmatrix} = 0 \tag{2.182}$$

where $(s_{01l})_k$, $l, k = \{1, 2, 3\}$ are the incremental stresses numerically calculated at $x_1 = x_{fin}$ from the initial value $\boldsymbol{\eta}_{0k}$. At this point the numerical solution to the determinant

condition in Eq.(2.182) can be easily calculated using standard root-finding algorithms. In this example, the matrix in Eq.(2.182) doesn't exhibit specific numerical problems. However, it might happen that the matrix is sparse and thus, rigidity problem might arise when numerically solving Eq.(2.182). A typical example is when Neumann boundary conditions are associated to the incremental problem. In this case the Stroh form of the incremental problem cannot be directly solved, and an alternative method must be used.

2.3.4 Neumann boundary conditions

The surface impedance method introduced in Section 2.3.2 can be used to implement a fast and efficient procedure to numerically solve the problem in Eqs.(2.173,2.174,2.175) with Neumann boundary conditions in the form:

$$\hat{\mathbf{S}}_0^T \mathbf{n} = \{0,0,0\} \qquad \text{on } \partial\mathcal{B}_a^{\boldsymbol{\sigma}1} \tag{2.183}$$

$$\hat{\mathbf{S}}_0^T \mathbf{n} = \{0,0,0\} \qquad \text{on } \partial\mathcal{B}_a^{\boldsymbol{\sigma}2}. \tag{2.184}$$

The Stroh formulation of the problem writes in the form of Eq.(2.178). As anticipated in the previous section, in this case the Stroh form does not provide the most suitable form of the problem for implementing an efficient numerical resolution procedure. Therefore, Eqs.(2.178) is rewritten in the form of the Riccati equation (2.169), where the impedance matrix $\mathbf{z}$ has the form of Eq.(2.166). Using Eq.(2.161), the boundary conditions in Eq.(2.183) can be transformed in the following initial condition for the differential matrix Riccati equation:

$$\mathbf{z}(x^*_{ini}) = \mathbf{0}. \tag{2.185}$$

From the boundary conditions in Eq.(2.184), the following stop condition is derived:

$$\det \mathbf{z}(x_{fin}) = 0 \tag{2.186}$$

Then, Eq.2.169 is numerically integrated using the initial conditions in Eq.(2.185) until the stop condition in Eq.(2.186) is satisfied. This procedure allows to calculate the critical thresholds of the instability i.e. the bifurcation parameter, and the wavenumbers k_2^{cr} and k_3^{cr} of the associated instability pattern. Furthermore, it is possible to calculate the displacement fields at the onset of the instability by integrating the Riccati equation in

Eq.(2.169) together with the first of Eqs.(2.168) and using the following initial conditions:

$$\mathbf{U}(x_{fin}) = \mathbf{U}_{fin} = \{u0, v0, w0\} \tag{2.187}$$

$$\mathbf{z}(x_{fin}) = \mathbf{z}_{fin}. \tag{2.188}$$

The value $\mathbf{z}_{fin}$ is calculated by substituting the critical value of the bifurcation parameter and the critical wavenumbers k_2^{cr}, k_3^{cr} into the Riccati equation and integrating Eq.(2.169) using Eq.(2.185) as initial condition. The solution is then evaluated at $x = x_{fin}$. The value $\mathbf{U}_{fin}$ is calculated as follows. By means of Eq.(2.161), the condition in Eq.(2.184) rewrites:

$$\mathbf{z}(x_{fin})\,\mathbf{U}(x_{fin}) = 0 \tag{2.189}$$

Substituting Eqs.(2.187) and (2.188) into Eq.(2.189) and setting $u0 = 1$, the components $v0$ and $w0$ are calculated solving the two linearly independent equations of Eq.(2.189).

2.4 Concluding remarks

In this chapter, a morphoelastic theory for the modeling of morphogenesis in living tissues has been presented. The theory stands in the framework of the thermo-mechanics of open systems and addresses all the main issues related to the modeling of soft tissues. It accounts for the large deformations, the presence of residual stresses and the nonlinear behavior of soft tissues. The main points of the theory can be summarized as follows:

- The kinematics of finite deformations allows for the mathematical description of the morphogenetic process.
- The theory of volumetric growth and remodeling allows to account for the emergence of residual stresses in the tissue.
- The thermo-mechanics of open systems provides the governing equations for the physical problem and dictates the restrictions for both the evolution of the growth (remodeling) and the constitutive equations of the tissue.
- The method of incremental deformations superposed on finite deformations allows to derive the governing equations of the perturbed problem linearized at the first order.

- The Stroh formalism and the surface impedance method allow to transform the incremental problem into a compact form, more suitable for numerical resolution.
- The numerical methods for solving the incremental problem allow to calculate the thresholds for the instability and determine the associated instability pattern.

In the next chapter, the morpho-elastic theory will be applied to two biological problems: the gastro-intestinal morphogenesis and the helical buckling of pre-stressed remodeled tubular tissues.

Chapter 3

Morphoelastic modeling of gastro-intestinal organogenesis

Contents

In the following, the morphoelastic theory presented in Chapter 2 will be applied to the modeling of the gastro-intestinal (GI) organogenesis. In fact, a rich collection of fascinating patterns can be found when observing the internal lumen of the GI system in different vertebrates. These patterns arise during the early stages of the embryonic development, just few days after fertilization. The aim of this chapter is to employ the morphoelastic theory to give insight on the morphogenetic mechanisms which drive the emergence of these patterns. Two possible mechanisms will be considered: the first one is related to the spatially constrained volumetric growth and the second one is based on the hypothesis of spatially unconstrained differential volumetric growth of the intestinal embryonic tissues. In the first model, the main idea is that the geometrical constraint, imposed by the outer surrounding tissue will introduce incompatibilities in the growing embryonic tissue, thus residual stresses will arise and eventually provoke buckling. In the second example, the incompatible differential growth of the two constituting layers of the GI tissue will be assumed to be the driving effect of the instability.
Following the layout of Chapter 2, the corresponding morphoelastic models will be built step by step according to the main assumptions.
Before starting with the modeling aspects, a brief overview on the GI anatomy and physiology and on what is currently known about its embryonic development will be presented.

3.1 Introduction to intestinal morphogenesis

The GI tissue originates from the embryonic differentiation of two primary matrices, the endoderm and the mesoderm. In later stages of development, the endoderm gives rise to the mucosa, while the mesoderm differentiates into several tissues including the submucosa, the sereosa (or adventitia) and the smooth muscle layers [86, 87]. As shown

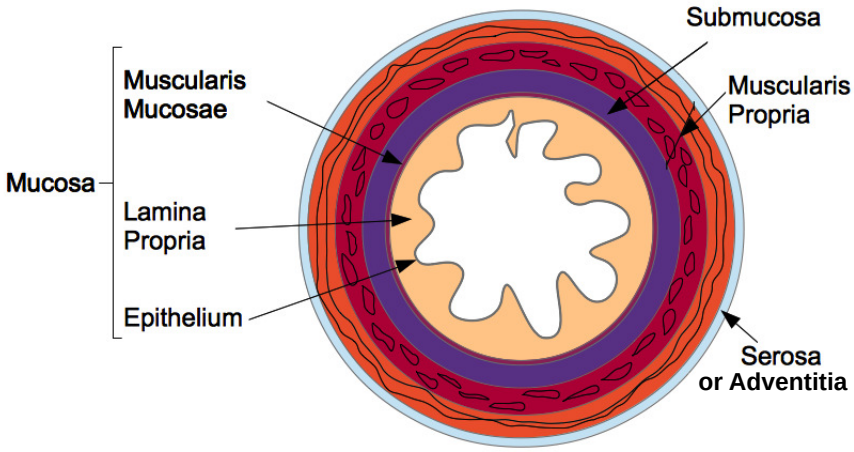

Figure 3.1: Schematic structure of the GI wall in adult vertebrates: the inner layer called mucosa (in which concur the epithelium, the lamina propria and the muscularis mucosae), the submucosa (made of dense irregular connective tissue), the muscularis propria (oriented smooth muscles) and the outer serosa (or adventitia) layer are evidenced.

in Figure 3.1, the typical GI mucosa in adult vertebrates is made of three layers: the epithelium, the lamina propria and the muscularis mucosae. Epithelial cells constitute the epithelial layer and cover the inner part of the mucosa. The lamina propria is the layer which is most specific to the anatomical origin. In particular, the lamina propria of the GI mucosa includes blood-vessels, lymph nodes and connective tissue composed by cells and an extracellular matrix made of ground substances (fluids) and fibers (collagen and elastin). Finally, the lamina muscularis mucosae is a continuous thin sheet of smooth muscle cells.

The inner mucosal surface in the intestine of all vertebrates is characterized by fascinating structures such as the crypts of Lieberkuhn, and finger-like projections, called villi. Intestinal villi contain the majority of differentiated absorptive cells, possessing a peculiar morphology which allows to increase the surface area of the intestine as well as its capacity to absorb liquids and nutrients from food. In fact, an increased surface area decreases the average distance traveled by nutrient molecules, thus improving the effectiveness of the diffusion process.

Since the pioneering experimental works of Hilton [88] and Johnson [89], it is well known that these structures can emerge in vertebrates from the embryonic development of either

plain circumferential folds or a more complex epithelial network of folds.
A recent study on the development of intestine in vertebrates has shown that the morphogenesis of the intestinal mucosa is strictly related to the muscle layer differentiation in the gut [90]. In the chick, for instance, muscle layers form between Days 8 and 16 after

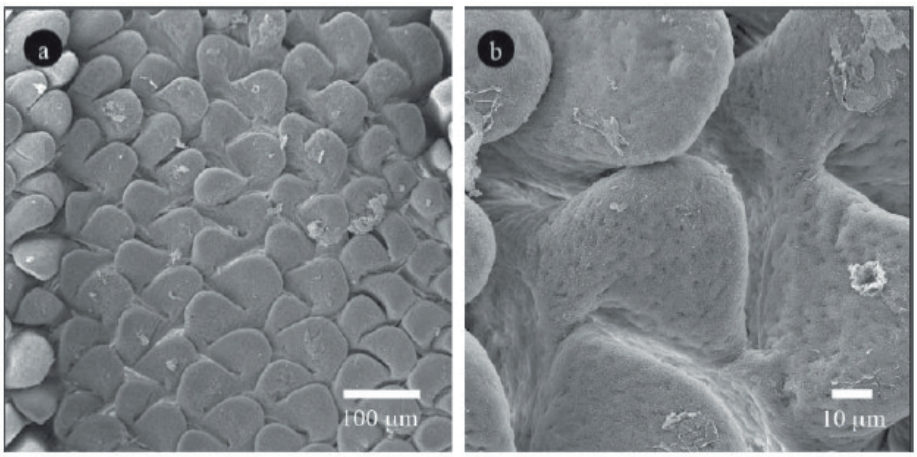

Figure 3.2: Scanning electron micrographs of emerging villi in the jejunum of turkey embryos (from [7]). The micrographs are taken at 21 days of incubations, and shown using scales of 100μm (a) and 10μm (b) for outlining of the morphology of the two-dimensional undulated pattern at the free surface of the mucosa.

incubation, passing through three stage of differentiation. At Day 8, a circumferentially oriented muscle forms, which corresponds to the onset of longitudinal ridges at the free surface of the epithelium. Around Day 13, a second exterior muscular layer starts forming longitudinally and the longitudinal ridges transition into zigzag patterns. Finally, at Day 16, a third longitudinally oriented muscle layer forms, interior to the first one, and simultaneously bulges arise from the zigzags, giving rise to the final villi. In the mouse gut, the muscle layer differentiates much faster than in the chick and develops in only 48 hours, without requiring the formation of an inner longitudinal layer (in the chick the same process takes 8 days). As a consequence, villi directly start forming from a two-dimensional pattern at the luminal surface, as shown in Figure 3.2, without passing through folding and zigzags.

3.2 State of the art of biomechanical modeling

Some morphoelastic models have been proposed in the last years to study some of the instability patterns which can occur at the inner surface of the mucosal tissue. In the following, a brief review of the main contributions is presented.

3.2.1 Spatially constrained growth models

Based on the hypothesis of spatially constrained growth, Li et al. studied the circumferential buckling of the mucosa considered as a one-layered cylinder made of a hyperelastic isotropic material [46]. Moulton and Goriely performed a linear stability analysis for studying the circumferential buckling of a growing cylinder under external pressure [91]. More recently Ciarletta and Ben Amar proposed a variational method for studying how the spatially constrained growth of thick-walled cylinders can induce the occurrence of either circumferential or longitudinal folds. In their model, they also accounted for the anisotropic distribution of collagen fibers inside the tissue [8, 85]. However, none of these analytical models considered the simultaneous occurrence of circumferential and longitudinal instabilities.

3.2.2 Differential growth models

Accounting for the anisotropic differential growth between epithelium and mesenchyme, Ben Amar and Jia proposed a weakly nonlinear stability analysis for studying the emergence of the zigzag pattern, which typically develops in the chick embryo in the later stages of villi formations [92]. Li et al. studied the occurrence of wrinkling in a two-layered cylinder with fixed outer boundaries, modeling mucosal-submucosal differential volumetric growth [93]. A similar approach has also been used for modeling surface patterns emerging in other soft tissues. Papastavrou et al. studied the non-linear stability of the skin epithelium also including the finite element implementation of surface growth [94]. Furthermore, Eskandari et al. investigated the role of volumetric growth in lung disease, where circumferential folding characterizes the pathologic state of the airway mucosa [95]. All these models assume that the muscle surrounding the differentially growing tissue is rigid, implying that the tissue cannot move outward while it grows.

3.3 Homogeneous growth model with spatial constraints

In order to model the early stages of intestinal morphogenesis in vertebrates species such as mouses where villi originate from a two-dimensional network of folds, the embryonic intestine is modeled as a one-layered cylinder composed by embryonic mucosal tissue which undergoes volumetric growth. Since the surrounding tissues, in particular the muscularis propria and the serosa are much stiffer, they are included in the model by introducing a rigid confinement at the outer radius of the cylinder. Although being simplificative, this hypothesis may be a valid approximation in the very early stages of embryogenesis when the displacements at the outer radius of the mucosal tissue can be neglected [96]. According to the morphoelastic theory presented in Chapter 2, first the geometry of the model will be sketched and the kinematics of the morphogenetic process will be described. Then, the constitutive laws for the embryonic tissue will be assigned and the equations governing the morphoelastic problem will be derived. In order to investigate the emergence of the two-dimensional network of folds, the linear stability analysis will be performed. First the basic solution to the governing problem, which represents the axial-symmetric shape of the embryonic mucosa prior to instability, will be calculated. Then, a small perturbation in the form of an incremental deformation, which describes a two-dimensional undulated pattern will be superposed on the basic axial-symmetric deformation. The incremental problem associated to the perturbed state will be derived using the Stroh formalism. A numerical procedure will be implemented in order to calculate the thresholds of the instability in term of the volumetric growth ratio and the effect of the geometrical and mechanical parameters on the onset of the instability will be investigated.

3.3.1 Kinematics

Let (R, Θ, Z) be the cylindrical coordinates in the initial reference configuration $\mathcal{B}_0$, with orthonormal basis vectors $(\mathbf{E}_R, \mathbf{E}_\Theta, \mathbf{E}_Z)$ and (r, θ, z) the cylindrical coordinates in the actual configuration $\mathcal{B}_a$, with orthonormal basis vectors $(\mathbf{e}_r, \mathbf{e}_\theta, \mathbf{e}_z)$. The mucosa is described as a thick-walled tube, as sketched in Figure 3.3, whose geometry in $\mathcal{B}_0$ is defined by

$$R_i \leq R \leq R_0, \quad 0 \leq \Theta \leq 2\pi, \quad 0 \leq Z \leq L, \tag{3.1}$$

where R_i and R_0 are the internal and external radii, respectively, and $L \gg R_0$ is the axial length of the cylinder.

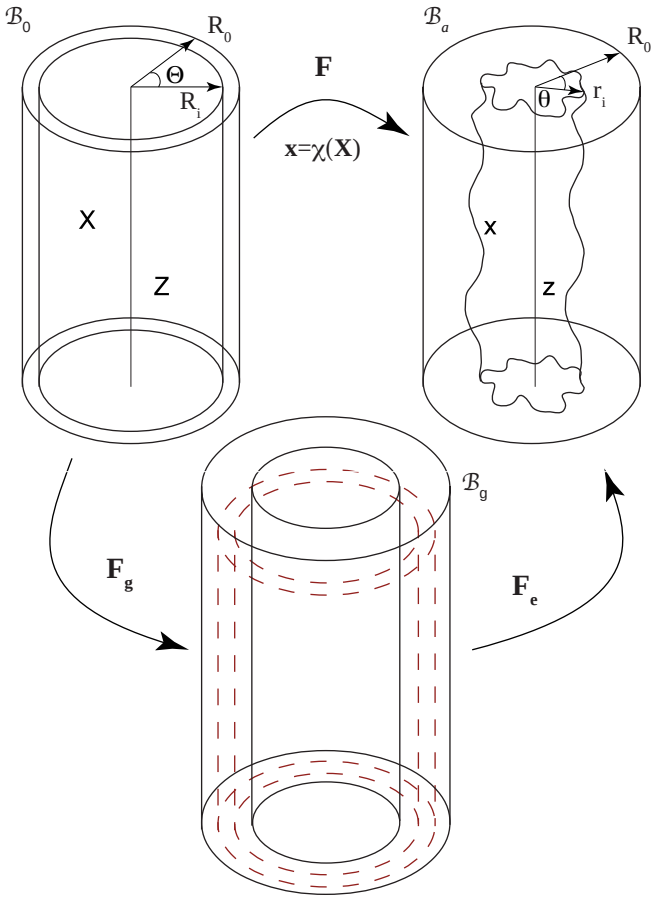

Figure 3.3: Geometrical model of the mucosal growth process: the mapping $\boldsymbol{\chi}$ transforms the point $\mathbf{X}$ from the reference configuration $\mathcal{B}_0$ into the point $\mathbf{x}$ in the actual configuration $\mathcal{B}_a$. The intermediate incompatible grown state $\mathcal{B}_g$ is depicted. The dotted cylinder indicates the geometrical constraint.

Let the morpho-elastic deformation $\boldsymbol{\chi}$, defined as in Eq.(2.1), be in the axial-symmetric form:

$$\boldsymbol{\chi}(r,\theta,z) = \begin{cases} r(R,\Theta,Z) = r(R) \\ \theta(R,\Theta,Z) = \Theta \\ z(R,\Theta,Z) = Z. \end{cases} \tag{3.2}$$

As introduced in Chapter 2, the growth time scale is much larger than the one associated to the elastic deformation. Therefore, the multiplicative decomposition in Eq.(2.6) can be applied to the deformation gradient $\mathbf{F}$, associated to the morphoelastic deformation $\boldsymbol{\chi}$ in Eq.(3.2), and reads $\mathbf{F} = \mathbf{F}_e\mathbf{F}_g$. Accordingly, the growth component $\mathbf{F}_g$ identifies an intermediate grown stress-free state $\mathcal{B}_g$ where the spatial constrained growth has intro-

duced a geometrical incompatibility in the tissue. The elastic part $\mathbf{F}_e$ is associated to the elastic deformation from the grown state $\mathcal{B}_g$ to the final configuration $\mathcal{B}_a$ and restores the geometrical compatibility of the tissue, whilst residual stresses arise.
Now, since the total process is quasi-static, an evolution law for the growth tensor is not needed. It is sufficient to specify a growth tensor $\mathbf{F}_g$ which identifies the grown stress-free state $\mathcal{B}_g$ after growth occurred. For the sake of simplicity, a homogeneous growth tensor is considered in the form:

$$\mathbf{F}_g = \mathrm{diag}(g_r, g_r, g_z) \qquad \text{with} \qquad J_g = \det \mathbf{F}_g = g_r^2 g_z \tag{3.3}$$

where the operator diag indicates that the growth tensor is diagonal. The growth rates in the radial and longitudinal directions are expressed as g_r and g_z, respectively, and they are assumed constant and positive definite. Accordingly, the elastic part of the deformation gradient $\mathbf{F}_e = \mathbf{F}\mathbf{F}_g^{-1}$ writes:

$$\mathbf{F}_e = \mathrm{diag}(\lambda_r, \lambda_\theta, \lambda_z), \tag{3.4}$$

where λ_r, λ_θ and λ_z are the principal stretches and from Eq.(3.2) are calculated as:

$$\lambda_r = \frac{r_{,R}}{g_r} \quad \lambda_\theta = \frac{r}{g_r R} \quad \lambda_z = \frac{1}{g_z}, \tag{3.5}$$

so that the left Cauchy-Green tensor $\mathbf{B}_e$ is defined as $\mathbf{B}_e = \mathbf{F}_e\mathbf{F}_e^T = \mathrm{diag}(\lambda_r^2, \lambda_\theta^2, \lambda_z^2)$. Since the cells and extra-cellular matrix constituting the mucosa are prevalently composed by water, the tissue can be considered incompressible. The incompressibility constraint writes according to Eq.(2.21).

3.3.2 Constitutive equations

The mucosa is modeled as a one-layered, hyperelastic, homogeneous, incompressible tissue, composed by a cross-ply continuous distribution of collagen and elastin fibers (anisotropic component), immersed into a homogeneous ground substance (isotropic component). It is assumed that collagen and fibers are distributed along the two principal directions $\mathbf{m}_\alpha$ and $\mathbf{m}_{-\alpha}$, defined as:

$$\begin{aligned} \mathbf{m}_\alpha &= (\sin\alpha)\mathbf{e}_\theta + (\cos\alpha)\mathbf{e}_z \\ \mathbf{m}_{-\alpha} &= -(\sin\alpha)\mathbf{e}_\theta + (\cos\alpha)\mathbf{e}_z \end{aligned} \tag{3.6}$$

where α is the cross-ply fiber angle in respect to the longitudinal direction $\mathbf{e}_z$. Hence, neglecting the mutual interaction between fibers and ground substance, and adopting the additive decomposition proposed by Holzapfel and Ogden [97], the strain energy function can be expressed as a sum of two terms:

$$\psi_0(\mathbf{C}_e, \mathbf{m}_{\pm\alpha}) = \psi_{Iso}(\mathbf{C}_e) + \psi_{Aniso}(\mathbf{C}_e, \mathbf{m}_{\pm\alpha}) \tag{3.7}$$

where ψ_{Iso} is the isotropic component, a scalar function of the right Cauchy-Green tensor $\mathbf{C}_e = \mathbf{F}_e\mathbf{F}_e^T$, and ψ_{Aniso} is the anisotropic component, which also depends on the orientation of the fibers through the vectors $\mathbf{m}_{\pm\alpha}$. Let the ground substance have a Neo-Hookean behavior, so that the isotropic contribution $\psi_{Iso}(\mathbf{C}_e)$ in Eq. (3.7) reads:

$$\psi_{Iso}(\mathbf{C}_e) = \frac{\mu}{2}(I_1 - 3) = \frac{\mu}{2}(\lambda_r^2 + \lambda_\theta^2 + \lambda_z^2 - 3) \tag{3.8}$$

where μ is the shear modulus, λ_l are the principal stretches, with $l \in \{r, \theta, z\}$, and $I_1 = \mathrm{tr}[\mathbf{C}_e]$ is the first principal invariant of $\mathbf{C}_e$. The structural tensors are defined as $\mathbf{M}_{\pm\alpha} = \mathbf{m}_{\pm\alpha} \otimes \mathbf{m}_{\pm\alpha}$. The anisotropic strain energy function $\psi_{Aniso}(\mathbf{C}_e, \mathbf{m}_{\pm\alpha})$ can be defined as [98]:

$$\psi_{Aniso}(\mathbf{C}_e, \mathbf{m}_{\pm\alpha}) = k_1 I_4, \tag{3.9}$$

where k_1 is the anisotropic stiffness of the material, and I_4 is a structural pseudo-invariant, which reads:

$$\begin{aligned} I_4 &= \frac{1}{4}(\mathbf{C}_e + \mathbf{C}_e^{-1} - 2\mathbf{I}) : (\mathbf{M}_\alpha + \mathbf{M}_{-\alpha}) = \\ &= \frac{1}{2}\left[\left(\frac{1}{\lambda_z^2} + \lambda_z^2 - 2\right)\cos(\alpha)^2 + \left(\frac{1}{\lambda_\theta^2} + \lambda_\theta^2 - 2\right)\sin(\alpha)^2\right] \end{aligned} \tag{3.10}$$

Note that the strain energy in Eq. (3.9) is polyconvex and physically consistent both with the compression and the extension of fibers. The **Nominal stress tensor S** of the mucosa defined in Eq.(2.65) can be then expressed as:

$$\mathbf{S} = 2\psi_1\mathbf{F}_e^T + \sum_{j=\pm\alpha}\frac{1}{2}\psi_4(\mathbf{m}_j \otimes \mathbf{m}_j)\mathbf{F}_e^T - \sum_{j=\pm\alpha}\frac{1}{2}\psi_4(\mathbf{C}_e^{-1}\mathbf{m}_j \otimes \mathbf{m}_j\mathbf{F}_e^{-1}) - p\mathbf{F}_e^{-1}, \tag{3.11}$$

where p is the Lagrange multiplier introduced to enforce the incompressibility constraint. Note that the Nominal stress tensor in Eq.(3.11) is obtained by multiplying Eq.(2.65) by a factor $\mathbf{F}_g$, thus has one basis in $\mathcal{B}_g$ and one basis in $\mathcal{B}_a$. The **Cauchy stress tensor**

$\boldsymbol{\sigma} = \mathbf{F}_e\mathbf{S}$ reads:

$$\boldsymbol{\sigma} = 2\psi_1\mathbf{B}_e + \sum_{j=\pm\alpha}\frac{1}{2}\psi_4(\mathbf{F}_e\mathbf{m}_j \otimes \mathbf{F}_e\mathbf{m}_j - \mathbf{F}_e^{-T}\mathbf{m}_j \otimes \mathbf{F}_e^{-T}\mathbf{m}_j) - p\mathbf{I} = \boldsymbol{\Sigma} - p\mathbf{I} \tag{3.12}$$

where $\psi_1 = \partial\psi_0/\partial I_1$, $\psi_4 = \partial\psi_0/\partial I_4$ and $\boldsymbol{\Sigma} = \mu\mathbf{B}_e + \sum_{j=\pm\alpha}\frac{1}{2}k_1(\mathbf{F}_e\mathbf{m}_j \otimes \mathbf{F}_e\mathbf{m}_j - \mathbf{F}_e^{-T}\mathbf{m}_j \otimes \mathbf{F}_e^{-T}\mathbf{m}_j)$. The principal components of the Cauchy stress $\boldsymbol{\sigma}$ read:

$$\begin{aligned}
\sigma_{rr}(r) &= \Sigma_r(r) - p(r) = \mu\lambda_r^2 - p(r) \\
\sigma_{\theta\theta}(r) &= \Sigma_\theta(r) - p(r) = \mu\lambda_\theta^2 + \frac{k1}{2}\left(\lambda_\theta^2 - \frac{1}{\lambda_\theta^2}\right)\sin^2(\alpha) - p(r) \\
\sigma_{zz}(r) &= \Sigma_z(r) - p(r) = \mu\lambda_z^2 + \frac{k1}{2}\left(\lambda_z^2 - \frac{1}{\lambda_z^2}\right)\cos^2(\alpha) - p(r)
\end{aligned} \tag{3.13}$$

where Σ_k, $k = \{r, \theta, z\}$ are the diagonal components of $\boldsymbol{\Sigma}$ in Eq. (3.12) and $\lambda_r, \lambda_\theta, \lambda_z$ are the principal stretches in Eq.(3.5).

3.3.3 Governing equations and basic axial-symmetric solution

The following aim is to write the governing equations of the elastic problem and calculate the basic solution.

According to the hypothesis of spatially constrained growth, the external radius is fixed during the entire process ($r_0 = r(R_0) = R(r_0) = R_0$). Moreover, the free annular surfaces cannot slide longitudinally ($z(0) = 0$ and $l = z(L) = L$) and, since the inner intestinal pressure in embryos is negligible, the mucosal internal surface is free of external traction. Therefore the elastic problem is governed by Eqs.(2.78,2.79) in $\mathcal{B}_a$ with mixed boundary conditions in Eqs.(2.43,2.44). Now, the deformation $\boldsymbol{\chi}$ has been assumed in the axial-symmetric form of Eq.(3.2), thus **the governing equations** reduce to:

$$\frac{d\sigma_{rr}(r)}{dr} + \frac{1}{r}(\sigma_{rr}(r) - \sigma_{\theta\theta}(r)) = 0 \qquad \text{in} \quad \mathcal{B}_a \tag{3.14}$$

$$\frac{r\, r_{,R}}{R\, g_r^2 g_z} = 1 \qquad \text{in} \quad \mathcal{B}_a \tag{3.15}$$

$$r_0 - R(r_0) = 0 \qquad \text{at} \quad r = r_0 \tag{3.16}$$

$$\sigma_{rr}(r_i) = 0 \qquad \text{at} \quad r = r_i. \tag{3.17}$$

where Eq.(3.14) is the first component of Eq.(2.78) written in cylindrical coordinates, Eq.(3.15) is the incompressibility condition in Eq.(2.79), rewritten after substituting

Eqs.(3.4) and (3.5), Eq.(3.16) is the Dirichlet boundary condition coming from the assumption of rigid outer boundary and Eq.(3.17) is the Neumann boundary condition following from the stress-free assumption at the inner surface.
The aim now is to calculate the basic solution of the governing problem. From integrating Eq.(3.15) follows the relation between the initial and the deformed radii r and R, respectively:

$$r = \sqrt{g_r^2 g_z R^2 + a} \tag{3.18}$$

where the constant $a = (1 - g_r^2 g_z) R_0^2$ follows from the condition in Eq.(3.16). Using Eq.(3.18), the **basic deformation** in Eq.(3.2) rewrites in the following form:

$$\mathbf{x}^{(0)}(r,\theta,z) = \boldsymbol{\chi}^{(0)}(r,\theta,z) = \begin{cases} r(R,\Theta,Z) = \sqrt{g_r^2 g_z R^2 + a} \\ \theta(R,\Theta,Z) = \Theta \\ z(R,\Theta,Z) = Z, \end{cases} \tag{3.19}$$

which is the basic solution of the problem in Eqs.(3.14-3.17). The elastic part of the associated deformation gradient reads:

$$\mathbf{F}_e^{(0)} = \mathrm{diag}(\lambda_r^{(0)}, \lambda_\theta^{(0)}, \lambda_z^{(0)}). \tag{3.20}$$

where $\lambda_r^{(0)}$, $\lambda_\theta^{(0)}$ and $\lambda_z^{(0)}$ are calculated substituting Eq.(3.19) into Eq.(3.5). Finally, substituting σ_{rr} and $\sigma_{\theta\theta}$ from Eq.(3.13) into Eq.(3.14) the only unknown is the Lagrange multiplier p. By imposing the boundary condition in Eq. (3.17), p can be obtained by solving Eq. (3.14) as:

$$p(r) = \Sigma_r(r) + \int_{r_i}^{r} \frac{\Sigma_r(s) - \Sigma_\theta(s)}{s} ds. \tag{3.21}$$

Substituting Eq.(4.23) in Eq.(3.13), the spatial distribution of the residual stresses inside the mucosa can be calculated as a function of the growth rates. In the following, the linear stability analysis of the basic solution in Eq.(3.19) will be performed.

3.3.4 Incremental boundary value problem

According to the method of incremental deformations superposed on finite deformations, introduced in Section 2.2, let the incremental deformation $\boldsymbol{\chi}^{(1)}(\mathbf{x}^{(0)})$ be defined in the following form:

$$\boldsymbol{\chi}^{(1)}(r,\theta,z) = u(r,\theta,z)\mathbf{e}_r + v(r,\theta,z)\mathbf{e}_\theta + w(r,\theta,z)\mathbf{e}_z \tag{3.22}$$

where (u, v, w) are scalar functions representing the incremental displacements. The associated displacement gradient $\mathbf{\Gamma}$ reads:

$$\mathbf{\Gamma} = \begin{pmatrix} u_{,r} & (u_{,\theta} - v)/r & u_{,z} \\ v_{,r} & (u_{,\theta} + v)/r & v_{,z} \\ w_{,r} & (v_{,\theta})/r & w_{,z} \end{pmatrix}. \tag{3.23}$$

Following the theory presented in Section 2.2, the perturbed deformation gradient rewrites in the form of Eq.(2.86) and the perturbed Nominal stress in the form of Eq.(2.88). The first-order increment $\hat{\mathbf{S}}$ of the Nominal stress tensor $\mathbf{S}$ is in the form of Eq.(2.89) and its push forward $\hat{\mathbf{S}}_0 = \mathbf{F}_e^{(0)}\hat{\mathbf{S}}$ is given by Eq.(2.92) and writes:

$$\hat{\mathbf{S}}_0 = \boldsymbol{\mathcal{A}}_0^1 \mathbf{\Gamma} + p\mathbf{\Gamma} - q\mathbf{I}. \tag{3.24}$$

From Eq.(3.20) and from the definition of the instantaneous moduli $\boldsymbol{\mathcal{A}}_0^1$ given in Eq.(2.93) it follows that the non-zero components of $\boldsymbol{\mathcal{A}}_0^1$ are:

$$\begin{aligned} \mathcal{A}^1_{0kkjj} &= \lambda_k \lambda_j \psi_{0kj} \\ \mathcal{A}^1_{0kjkj} &= (\lambda_k \psi_{0k} - \lambda_j \psi_{0j}) \frac{\lambda_k^2}{\lambda_k^2 - \lambda_j^2}, \quad k \neq j \\ \mathcal{A}^1_{0kjjk} &= \mathcal{A}^1_{0jkkj} = \mathcal{A}^1_{0kjkj} - \lambda_k \psi_{0k}, \quad k \neq j \end{aligned} \tag{3.25}$$

where $\psi_{0k} = \partial\psi_0/\partial\lambda_k$, $\psi_{0kj} = \partial^2\psi_0/\partial\lambda_k\partial\lambda_j$ and with k and j running over r, θ and z [99]. Therefore **the incremental BVP**, rewrites:

$$\frac{\partial(r\hat{S}_{0rr})}{\partial r} + \frac{\partial \hat{S}_{0\theta r}}{\partial \theta} + r\frac{\partial \hat{S}_{0zr}}{\partial z} - \hat{S}_{0\theta\theta} = 0 \qquad \text{in } \mathcal{B}_a \tag{3.26}$$

$$\frac{\partial(r\hat{S}_{0r\theta})}{\partial r} + \frac{\partial \hat{S}_{0\theta\theta}}{\partial \theta} + r\frac{\partial \hat{S}_{0z\theta}}{\partial z} + \hat{S}_{0\theta r} = 0 \qquad \text{in } \mathcal{B}_a \tag{3.27}$$

$$\frac{\partial(r\hat{S}_{0rz})}{\partial r} + \frac{\partial \hat{S}_{0\theta z}}{\partial \theta} + r\frac{\partial \hat{S}_{0zz}}{\partial z} = 0 \qquad \text{in } \mathcal{B}_a \tag{3.28}$$

$$u_{,r} + \frac{u + v_{,\theta}}{r} + w_{,z} = 0 \qquad \text{in } \mathcal{B}_a \tag{3.29}$$

$$u(r,\theta,z) = 0, v(r,\theta,z) = 0, w(r,\theta,z) = 0 \qquad \text{at } r = r_0 \tag{3.30}$$

$$\hat{S}_{0rr} = 0, \hat{S}_{0r\theta} = 0, \hat{S}_{0rz} = 0 \qquad \text{at } r = r_i \tag{3.31}$$

where Eqs.(3.26-3.28) are the first order incremental equilibrium equations in Eq.(2.103), Eq.(3.29) is the incremental incompressibility condition in Eq.(2.104), and Eqs.(3.30) and

(3.31) are the first-order increments of the boundary conditions in Eqs.(3.16) and (3.17), respectively. Eqs.(3.26-3.29) define a system of four partial differential equations, where the four unknowns are the three incremental displacements in Eq.(3.22) and the increment q of the Lagrange multiplier. In the next section, a compact form of the incremental problem will be derived, using the Stroh formalism introduced in Section 2.3.1.

3.3.5 Stroh formulation of the BVP and numerical solution

In order to solve Eqs.(3.26-3.29), the system of PDEs is transformed into a system of ODEs of the first order.
According to the separation of variables, the solution is sought in the form:

$$(u, v, w, q) = (U(r), V(r), W(r), Q(r))e^{i(m\theta+k_z z)} \tag{3.32}$$

where m (resp. $k_z = \frac{2n\pi}{L}$) is the circumferential (resp. longitudinal) wavenumber of the perturbation, with m and n positive integers, and i is the imaginary unit. Using the perturbation defined in Eq. (3.32), the deformed mucosa is depicted in Figure 3.4, showing a characteristic two-dimensional undulated pattern at the inner surface emerging at the initial stages of intestinal villi formation.
From Eqs.3.24 it follows that the incremental stress components have the similar form:

$$\hat{S}_{0kj} = S_{0kj}(r)e^{i(m\theta+k_z z)} \tag{3.33}$$

where S_{0kj} is a function of r, with indices $\{k, j\}$ running over $\{r, \theta, z\}$. Substituting Eqs. (3.25,3.32,3.33) in the incremental constitutive equations for $\hat{S}_{0rr}$, given by Eq. (3.24), it follows that:

$$Q = \left(\mathcal{A}^1_{0rrrr} + p\right) U' + \mathcal{A}^1_{0rr\theta\theta}\frac{imU + V}{r} + \mathcal{A}^1_{0rrzz} ik_z W - \left(S_{0rr}\right). \tag{3.34}$$

Similarly, from the constitutive equations for the incremental components $\hat{S}_{0r\theta}$ and $\hat{S}_{0rz}$, V' and W' can expressed as:

$$V' = \frac{S_{0r\theta}}{\mathcal{A}^1_{0r\theta r\theta}} - \left(\mathcal{A}^1_{0r\theta\theta r} + p\right)\frac{imU - V}{r\mathcal{A}^1_{0r\theta r\theta}} \tag{3.35}$$

$$W' = \frac{S_{0rz}}{\mathcal{A}^1_{0rzrz}} - \frac{\left(\mathcal{A}^1_{0rzzr} + p\right) ik_z U}{\mathcal{A}^1_{0rzrz}}. \tag{3.36}$$

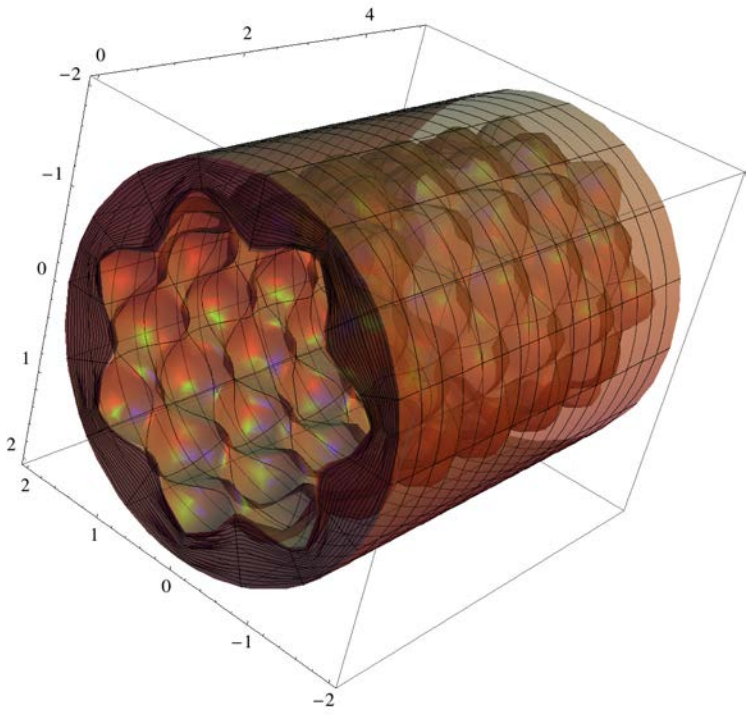

Figure 3.4: Morphology of the intestinal mucosa after imposing a perturbation of the axial-symmetric solution of the elastic problem, having the form of Eq. (3.32). The geometrical parameters are $r_0 = 2$, $r_i = 1.5$, $L = 5$, $m = 7$, $k_z = 5$ and $\epsilon = 0.15$.

Furthermore, the incremental incompressibility condition in Eq. (3.29) yields:

$$U' = -\frac{U + imV}{r} - ik_z W. \tag{3.37}$$

Now, first the components $\hat{S}_{0rr}, \hat{S}_{0r\theta}, \hat{S}_{0rz}$ are replaced in Eqs.(3.26-3.28) using Eq. (3.33) and setting $s_{0kj} = (irS_{0kj})$ for $(k, j) = \{r, \theta, z\}$. Using Eqs. (3.24,3.25,3.32), the incremental equilibrium equations take the following expressions:

$$\begin{aligned}
&\frac{1}{ir}\left(s_{0rr}\right)' + m\frac{1}{r}\left(-\mathcal{A}^1_{0\theta r\theta r}\frac{mU + iV}{r} + i\left(\mathcal{A}^1_{0\theta rr\theta} + p\right)V'\right) + \\
&+k_z^2\mathcal{A}^1_{0zrzr}U + k_z i\left(\mathcal{A}^1_{0zrrz} + p\right)W' + \\
&-\tfrac{1}{r}\left(\mathcal{A}^1_{0\theta\theta rr}U' + \mathcal{A}^1_{0\theta\theta\theta}\tfrac{miU+V}{r} + k_z i\mathcal{A}^1_{0\theta\theta zz}W + p\tfrac{miU+V}{r} - Q\right) = 0
\end{aligned} \tag{3.38}$$

$$\begin{aligned}&\frac{1}{ir}\left(s_{0r\theta}\right)' - k_z^2\mathcal{A}^1_{0z\theta z}V - mk_z\mathcal{A}^1_{0z\theta\theta z}\frac{V}{r} - mk_z\frac{V}{r}p+\\&+\tfrac{1}{r}\left(\mathcal{A}^1_{0\theta rr\theta}V' + \mathcal{A}^1_{0\theta r\theta r}\tfrac{miU-V}{r} + pV'\right)+\\&+\tfrac{m}{r}\left(i\mathcal{A}^1_{0\theta\theta rr}U' - \mathcal{A}^1_{0\theta\theta\theta}\tfrac{mU-iV}{r} - mk_z\mathcal{A}^1_{0\theta\theta zz}W - p\tfrac{mU-iV}{r} - iQ\right) = 0\end{aligned} \tag{3.39}$$

$$\begin{aligned}&\frac{1}{ri}\left(s_{0rz}\right)' - \frac{m}{r}\left(\frac{1}{r}\mathcal{A}^1_{0\theta z\theta z} + k_z\left(\mathcal{A}^1_{0\theta zz\theta} + p\right)\right)V+\\&+k_z\left(\mathcal{A}^1_{0zzrr}iU' - \mathcal{A}^1_{0zz\theta\theta} - k_z\left(\mathcal{A}^1_{0zzzz} + p\right)W - iQ\right) = 0\end{aligned} \tag{3.40}$$

where prime denotes the differentiation with respect to the variable r. Then, the displacement-traction vector $\boldsymbol{\eta}$ is defined as:

$$\boldsymbol{\eta} = \{U, V, W, s_{0rr}, s_{0r\theta}, s_{0rz}\}^T. \tag{3.41}$$

Substituting Eqs.(3.34-3.37) in Eqs.(3.38-3.40), the unknown Q is eliminated and three ODEs of first order that depend only on (U, V, W) and $(s_{0rr}, s_{0r\theta}, s_{0rz})$ are obtained. Accordingly, Eqs.(3.35-3.40) can be written in a more compact formulation as follows:

$$\frac{d\boldsymbol{\eta}(\boldsymbol{r})}{dr} = \frac{i}{r}\mathbf{G}(r)\boldsymbol{\eta}(r), \tag{3.42}$$

where **the Stroh matrix G** has the form:

$$\mathbf{G} = \begin{pmatrix} \mathbf{G}_1 & \mathbf{G}_2 \\ \mathbf{G}_3 & \mathbf{G}_4 \end{pmatrix}. \tag{3.43}$$

In particular, the four blocks of $\mathbf{G}$ read:

$$\mathbf{G}_1 = \begin{pmatrix} i & -m & -k_z r \\ -m(1-\sigma_1) & -i(1-\sigma_1) & 0 \\ -k_z r(1-\sigma_2) & 0 & 0 \end{pmatrix}, \quad \mathbf{G}_2 = \begin{pmatrix} 0 & 0 & 0 \\ 0 & -1/\alpha_1 & 0 \\ 0 & 0 & -1/\alpha_2 \end{pmatrix}, \tag{3.44}$$

$$\mathbf{G}_3 = \begin{pmatrix} \kappa_{11} & i\kappa_{12} & i\kappa_{13} \\ -i\kappa_{12} & \kappa_{22} & \kappa_{23} \\ -i\kappa_{13} & \kappa_{23} & \kappa_{33} \end{pmatrix}, \quad \mathbf{G}_4 = \mathbf{G}_1^+ \tag{3.45}$$

where $\mathbf{G}_1^+$ is the adjugate (transpose conjugate) of $\mathbf{G}_1$ and

$$\begin{aligned}
\kappa_{11} &= m^2[\gamma_1 - \alpha_1(1-\sigma_1)^2] + k_z^2 r^2[\gamma_2 - \alpha_2(1-\sigma_2)^2] + 2[\beta_1 + \alpha_1(1-\sigma_1)] \\
\kappa_{12} &= m[2\beta_1 + \gamma_1 + \alpha_1(1-\sigma_1^2)] \\
\kappa_{13} &= k_z r[2\beta_2 + \alpha_3(1-\sigma_3)^2] \\
\kappa_{22} &= 2m^2[\beta_1 + \alpha_1(1-\sigma_1)] + \gamma_1 - \alpha_1(1-\sigma_1)^2 + k_z^2 r^2 \gamma_3 \\
\kappa_{23} &= 2mk_z r[\beta_2 + \alpha_3(1-\sigma_3)] \\
\kappa_{33} &= m^2\alpha_3 + 2k_z^2 r^2[\beta_3 + \alpha_2(1-\sigma_2)]
\end{aligned} \tag{3.46}$$

with:

$$\begin{aligned}
&\gamma_1 = \mathcal{A}^1_{0\theta r\theta r}, \qquad \alpha_1 = \mathcal{A}^1_{0r\theta r\theta}, \qquad \sigma_1 = \sigma_{rr}/\alpha_1, \\
&\gamma_2 = \mathcal{A}^1_{0zrzr}, \qquad \alpha_2 = \mathcal{A}^1_{0rzrz}, \qquad \sigma_2 = \sigma_{rr}/\alpha_2, \\
&\gamma_3 = \mathcal{A}^1_{0z\theta z\theta}, \qquad \alpha_3 = \mathcal{A}^1_{0\theta z\theta z}, \qquad \sigma_3 = \sigma_{\theta\theta}/\alpha_3, \\
&2\beta_1 = \mathcal{A}^1_{0rrrr} + \mathcal{A}^1_{0\theta\theta\theta} - 2\mathcal{A}^1_{0rr\theta\theta} - 2\mathcal{A}^1_{0r\theta\theta r}, \\
&2\beta_2 = \mathcal{A}^1_{0rrrr} - \mathcal{A}^1_{0rr\theta\theta} - \mathcal{A}^1_{0rrzz} + \mathcal{A}^1_{0\theta\theta zz} - \mathcal{A}^1_{0z\theta\theta z}, \\
&2\beta_3 = \mathcal{A}^1_{0rrrr} + \mathcal{A}^1_{0zzzz} - 2\mathcal{A}^1_{0rrzz} - 2\mathcal{A}^1_{0rzzr}.
\end{aligned} \tag{3.47}$$

Using the Dirichlet boundary condition in Eq.(3.16), the following initial conditions are associated to the Stroh form of the incremental problem in Eq.(3.42):

$$\boldsymbol{\eta}_0(R_0) = \{0, 0, 0, s^*_{0rr}, s^*_{0r\theta}, s^*_{0rz}\} \tag{3.48}$$

$$\boldsymbol{\eta}_0(r_i) = \{U^*, V^*, W^*, 0, 0, 0\} \tag{3.49}$$

where the values $\{U^*, V^*, W^*\}$ and $\{s^*_{0rr}, s^*_{0r\theta}, s^*_{0rz}\}$ are the initial values of the incremental displacement and stress vectors, respectively, to be determined. In the following, the numerical procedure for solving Eq. (3.93) will be presented.

3.3.5.1 Numerical resolution procedure

The aim of this section is to find the critical values of a control parameter solving Eq.(3.42) with initial conditions given by Eqs.(3.48,3.49). The growth has been considered homogeneous, thus the growth rates g_r and g_z can be considered as the control parameters of the elastic instability for the mucosa.
Since the incremental BVP has a Dirichlet boundary condition, the Stroh form in Eq.(3.42) allows for a safe and efficient implementation of a numerical resolution algorithm. Therefore, as motivated in Section 2.3.3, the determinantal method is used to implement the numerical procedure. The following numerical procedure is implemented in Mathemat-

ica [100].
The solution $\boldsymbol{\eta}$ of Eq.(3.42) is expressed as a linear combination of three scalar functions $\boldsymbol{\eta}_1, \boldsymbol{\eta}_2, \boldsymbol{\eta}_3$, being:

$$\boldsymbol{\eta} = \nu_1 \boldsymbol{\eta_1} + \nu_2 \boldsymbol{\eta_2} + \nu_3 \boldsymbol{\eta_3} \tag{3.50}$$

with ν_1, ν_2, ν_3 constant coefficients. The scalar functions $\boldsymbol{\eta}_k$, $k = \{1, 2, 3\}$, in Eq.(3.50) are three linearly independent copies of the solution. Using the function `NSolve`, the three copies are obtained numerically integrating the system of Eq.(3.42) between $r = R_0$ and $r = r_i$ and imposing three linearly independent sets $\boldsymbol{\eta}_{0k}$ of initial conditions, from Eq.(3.48), expressed as:

$$\boldsymbol{\eta}_{0k}(r = R_0) = \{0, 0, 0, (s_{0rr})_k, (s_{0r\theta})_k, (s_{0rz})_k\}, \quad \text{with} \quad k = \{1, 2, 3\} \tag{3.51}$$

with appropriately chosen incremental stress components $(s_{0rr})_k, (s_{0r\theta})_k, (s_{0rz})_k$ at $r = R_0$. Then, the solution in Eq. (3.50) must satisfy the other initial condition in Eq. (3.49) at $r = r_i$, which rewrites:

$$D(g_\tau(r = r_i)) = \det \begin{pmatrix} (s_{0rr}(r_i))_1 & (s_{0r\theta}(r_i))_1 & (s_{0rz}(r_i))_1 \\ (s_{0rr}(r_i))_2 & (s_{0r\theta}(r_i))_2 & (s_{0rz}(r_i))_2 \\ (s_{0rr}(r_i))_3 & (s_{0r\theta}(r_i))_3 & (s_{0rz}(r_i))_3 \end{pmatrix} = 0 \tag{3.52}$$

where $(s_{0jl})_k$, $jl = \{r, \theta, z\}$, $k = \{1, 2, 3\}$ are the incremental stresses numerically calculated at $r = r_i$ from the initial value $\boldsymbol{\eta}_{0k}$. As shown in Figure 3.5, the bifurcation threshold $g_\tau(H)$, $\tau = \{r, z\}$ are calculated with the help of two cycles of iteration: a first iteration is on the aspect ratio $H = R_0/R_i$, followed by a second cycle in which the bifurcation parameter is iterated until the stop condition in Eq. (3.52) is reached.

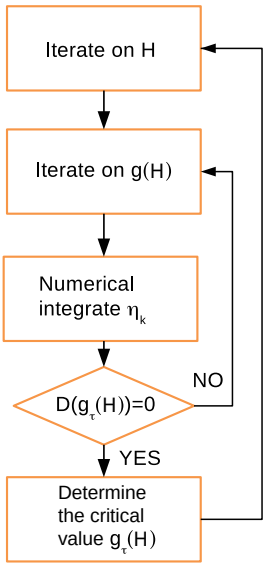

Figure 3.5: Implementation of the numerical scheme: after a first iteration on the aspect ratio H, it follows a second iteration on the bifurcation parameter $g(H)$. In this second cycle, the solution is numerically integrated until the condition $D((g_\tau(r = r_i))$ is satisfied and the threshold value for the parameter g_τ is obtained.

3.3.6 Results

The numerical results obtained from the linear stability analysis of the growing intestinal mucosa are presented in the following. First, the mucosa is considered as an isotropic material, with the aim to investigate the effect of the volumetric growth on the onset of instability. The volume increase is considered resulting from both isotropic ($g_r = g_z$) and anisotropic ($g_r \neq g_z$) growth processes. The curves of marginal stability depict the growth thresholds at which a bifurcation occurs in function of the aspect ratio H, and are shown for different perturbation modes. Second, the mucosa is considered as a fiber-reinforced tissue according to Eq. (3.7). The numerical results are shown with the aim of investigating the effect of the material anisotropy on the bifurcation thresholds for g_r and g_z, in order to study the effects of the stiffness and the orientation of the reinforcing fibers on the onset of instability.

3.3.6.1 Isotropic behavior of the mucosa

First, the mucosa is considered as an isotropic material (i.e. setting $k_1 = 0$ in Eq. (3.7)). The marginal stability curves obtained assuming an isotropic growth process (g_r $=g_z$) with $m = k_z$ are plotted in Figure 3.6 within the range of $1 < H \leq 2$. An increase of

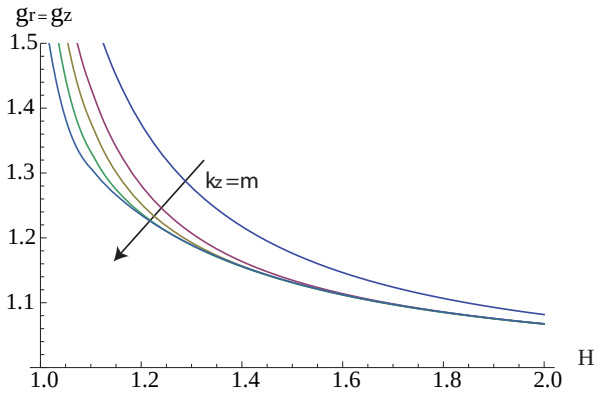

Figure 3.6: Marginal stability curves for isotropic growth showing the isotropic growth rate $g_r = g_z$ at different modes $k_z = m = 2, 5, 10, 15$.

the value of the perturbation modes results in a decrease of the growth thresholds, highlighting the occurrence of a surface instability at very short wavelengths. The same instability mechanism occurs when considering anisotropic growth processes. The marginal stability curves are plotted in Figure 3.7, referring to a volume increase completely due to a radial ($g_z = 1$, left) or to a longitudinal ($g_r = 1$, right) growth process. In Figure 3.8,

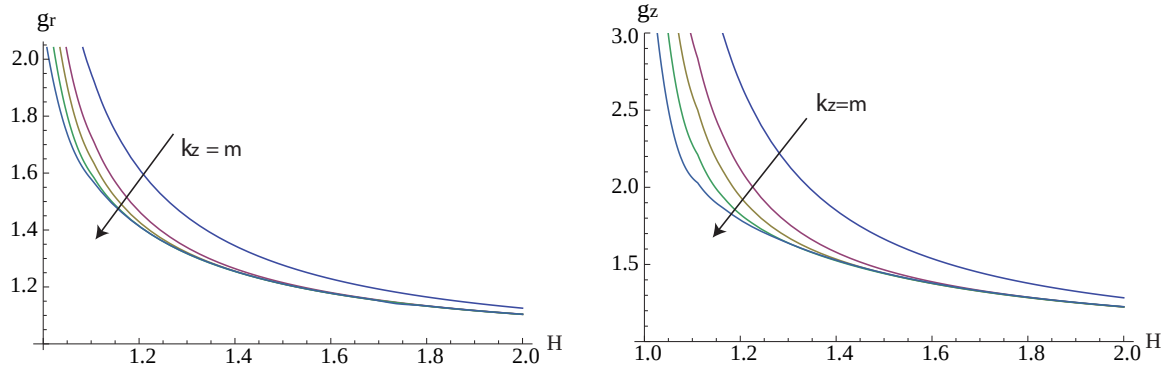

Figure 3.7: Marginal stability curves for anisotropic growth showing the radial growth g_r (left, setting $g_z = 1$) and the longitudinal growth g_z (right, setting $g_r = 1$) thresholds, calculated at different modes $m = k_z = 2, 5, 7, 10, 15$.

the marginal stability curves are shown for different circumferential perturbation modes m, at fixed the perturbation mode in the longitudinal direction, $k_z = 10$. In the same way, fixing the circumferential perturbation mode at $m = 10$, the instability thresholds are depicted in Figure 3.9, for different longitudinal modes k_z. These results confirm the occurrence of a surface instability mechanism: the growth thresholds for high values of

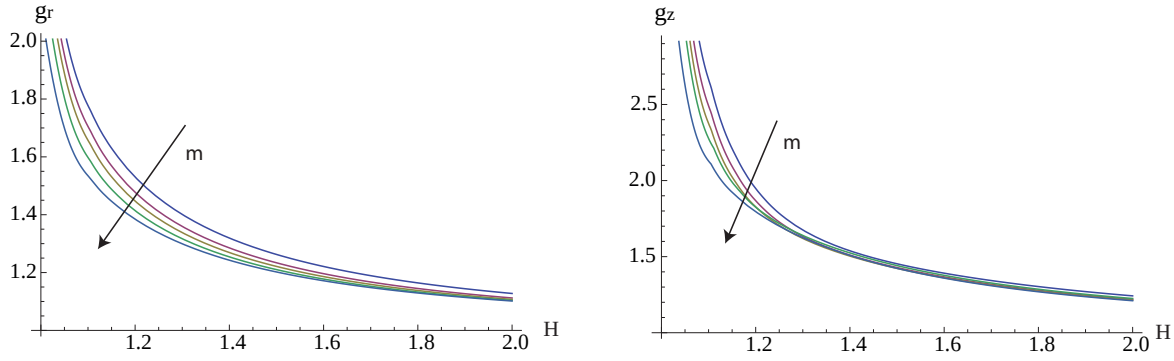

Figure 3.8: Marginal stability curves for anisotropic growth showing the radial growth g_r (left, setting $g_z = 1$) and the longitudinal growth g_z (right, setting $g_r = 1$) thresholds, calculated at different modes $m = 2, 5, 7, 10, 15$ and fixed $k_z = 10$.

m, k_z collapse to a single master curve in the case of thick tissues ($H > 1.5$), while a large variability on the perturbation mode appear as the aspect ratio decreases. Even if the instability is predicted for $(m, k_z) \to \infty$, the biological system will select a finite wavelength because of the existence of boundary energies penalizing the increase in the surface area of the mucosa. Although such correction of the wavelength can be calculated following the method proposed by Ben Amar and Ciarletta for a soft layer attached to a rigid substrate [101], it will be neglected in here for the sake of simplicity. Finally, it is useful to compare the instability thresholds for the three different growth processes investigated in terms of the total volume increase, given by $J_g = g_r^2 g_z$. In Figure 3.10, the

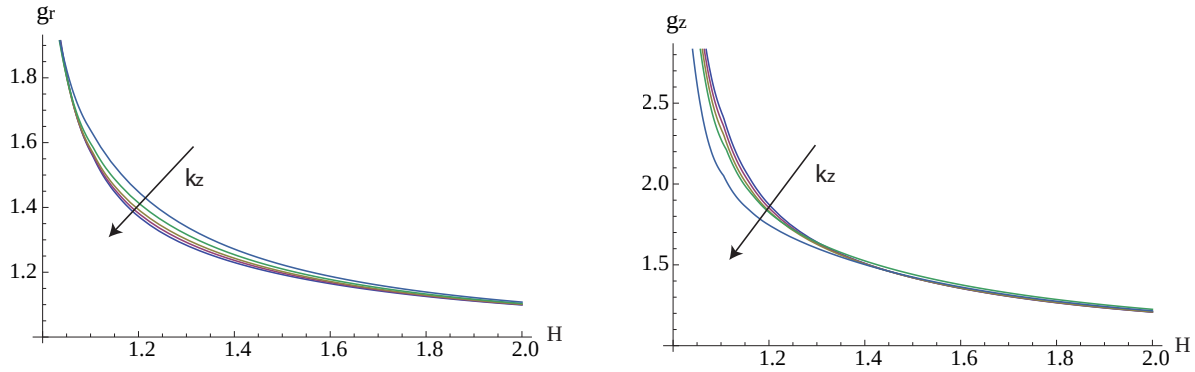

Figure 3.9: Marginal stability curves for anisotropic growth showing the radial growth g_r (left, setting $g_z = 1$) and the longitudinal growth g_z (right, setting $g_r = 1$) thresholds, calculated at different modes $k_z = 2, 5, 7, 10, 15$ and fixed $m = 10$.

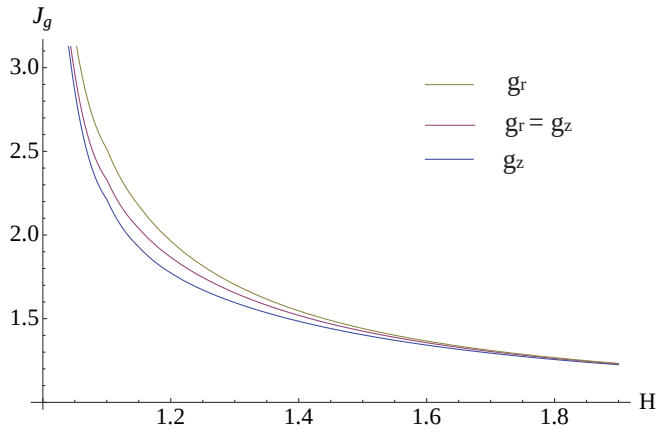

Figure 3.10: Marginal stability curves showing the critical volume increase J_g at modes $k_z = m = 10$ for isotropic ($g_r = g_z$, magenta) and anisotropic ($g_r = 1$, yellow and $g_z = 1$, blue) growth processes.

marginal stability curves are depicted for J_g in the cases $g_r = g_z$, $g_r = 1$ and $g_z = 1$, predicting that the two-dimensional surface undulations occur first when the mucosal growth is uniquely longitudinal.

3.3.6.2 Anisotropic behavior of the mucosa

In this paragraph, the material anisotropy of the mucosa is taken into account, and

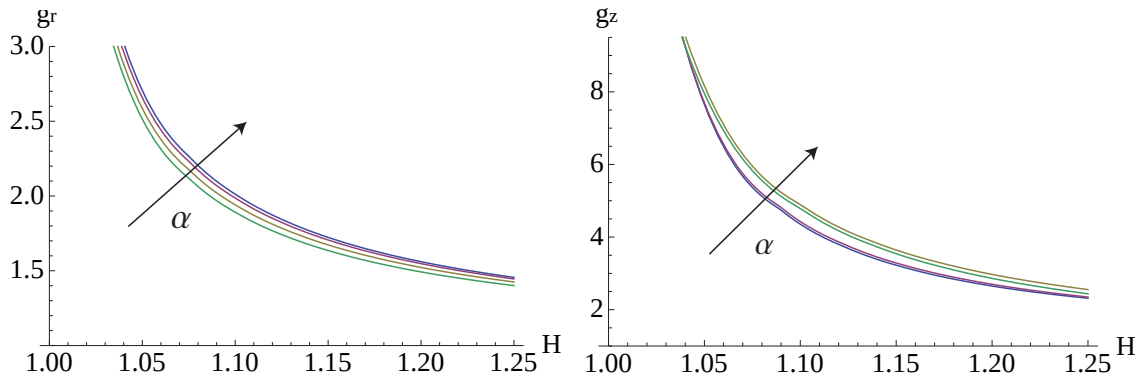

Figure 3.11: Marginal stability curves for anisotropic growth showing the radial growth g_r (left, setting $g_z = 1$) and the longitudinal growth g_z (right, setting $g_r = 1$) thresholds at modes $k_z = m = 5$. The material anisotropy ratio is fixed at $k_1/\mu = 10$, while the curves are shown at different cross-ply fiber angles $\alpha = (0, \pi/6, \pi/4, \pi/3)$.

the numerical results are calculated for different cross-ply fiber angles α (Figure 3.11) and

for different material anisotropy ratios k_1/μ (Figure 3.12).

The curves plotted in Figure 3.11 show how increasing the cross-ply angle α increases the instability thresholds increase, both for the radial and longitudinal growth processes.

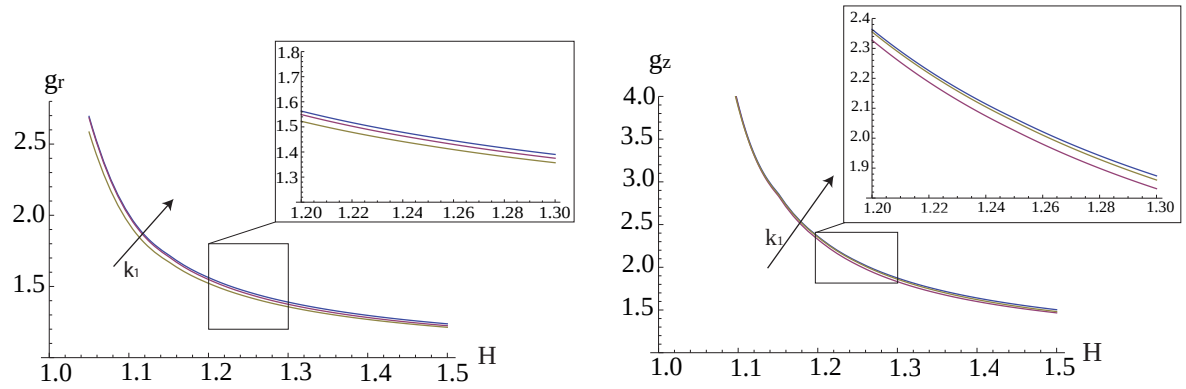

Figure 3.12: Marginal stability curves for anisotropic growth showing the radial growth g_r (left, setting $g_z = 1$) and the longitudinal growth g_z (right, setting $g_r = 1$) thresholds at modes $k_z = m = 5$. The cross-ply fiber angle is fixed at $\alpha = \dfrac{\pi}{4}$, while the curves are shown at different material anisotropy ratios $k_1/\mu = (0.1, 1, 10)$.

Hence, a surface instability first occurs when the fiber orientation angle is $\alpha = 0$. Moreover, the curves of marginal stability in Figure 3.12 show that the presence of a material anisotropy is a stabilizing factor, as increasing k_1/μ increases the growth thresholds of the instability. The results in Figure 3.11 (resp. Figure 3.12) are shown for $1 < H < 1.25$ (resp. 1.5) as the equation system became stiff for thicker tissues.

3.3.7 Discussion of the results

In the first part of this chapter, the morphoelastic theory presented in Chapter 2 has been applied in order to investigate the occurrence of undulated two-dimensional patterns during the initial stages of villi morphogenesis. The main idea behind the model is that epithelial patterns originate from an elastic instability which arise as consequence of the spatially constrained volumetric growth of the embryonic mucosa. Therefore, in order to test this hypothesis the intestinal mucosa has been modeled as a thick-walled cylinder with an outer spatial confinement. Its deformation gradient has been decomposed into a homogeneous growth component and an incompressible elastic deformation, in order to account for the spatial distribution of residual stresses arising during the spatially constrained growth process. The mechanical behavior of the mucosa has been described

using the hyperelastic model presented in Section 3.3.2. The nonlinear mechanical behavior accounts for the anisotropy of the tissue, including a polyconvex energy term that depends on both the orientation and the stiffness of the collagen and elastin fibers lying under the epithelial layer. The linear stability analysis has been performed perturbing the basic axial-symmetric solution in Eq.(3.19) with an incremental deformation. With the aim of describing the undulated morphology at the free surface of the mucosa, a two-dimensional perturbation has been considered in the form of Eq.(3.32). The incremental BVP has been derived using the Stroh formulation, and it has been solved with the help of the determinantal method. The numerical results have been presented in Section 3.3.6. The growth rate thresholds for the onset of instability have been depicted in function of the aspect ratio $H = R_0/R_i$, considering isotropic and anisotropic growth processes in Figures 3.6 and 3.7, respectively. The marginal stability curves show that a short-wavelength two-dimensional undulation occurs. An increase in the perturbation modes results in decreasing instability thresholds, showing the occurrence of a surface instability on the internal surface of the mucosal wall, as depicted in Figure 3.8 and Figure 3.9. The calculated volume increase thresholds are smaller when considering an anisotropic growth process, with the most unstable scenario being the mucosa growing only along the longitudinal direction, as shown in Figure 3.10. In Section 3.3.6.2, the role played by the material anisotropy of the mucosa on the onset of the surface instability has been investigated. The results in Figures 3.11 and 3.12 show that an increase of both the cross-ply angle and the stiffness of the reinforcing fibers provokes an increase of the growth instability thresholds, highlighting that the material anisotropy is a stabilizing effect.

The aim is now to compare the growth thresholds obtained from the linear stability analysis for the occurrence of undulated two-dimensional patterns with those reported in [8] for prismatic deformations, representing both circumferential folding and longitudinal segmentation. This comparison shows how the instability thresholds for the two-dimensional perturbations are smaller than those required for folding and segmentation, both for isotropic (Figure 3.13, left) and anisotropic (Figure 3.13, right) growth processes. This also prove that a two-dimensional undulation always occurs first for a thin mucosa (i.e. H $<$ 1.15), while for thicker tubes the growth threshold is roughly the same as the one reported for circumferential folding. In the last case, the emerging kind of instability will be selected by nonlinear effects.

Using the experimental curves reported by Sbarbati [9], the aspect ratio of the mucosa in mouse embryos are calculated within the range $H = 1.75 - 1.93$ (duodenum) and $H = 1.51 - 1.72$ (large intestine), whilst the external radius is about $R_0 = 20 - 40\ \mu m$ between 12

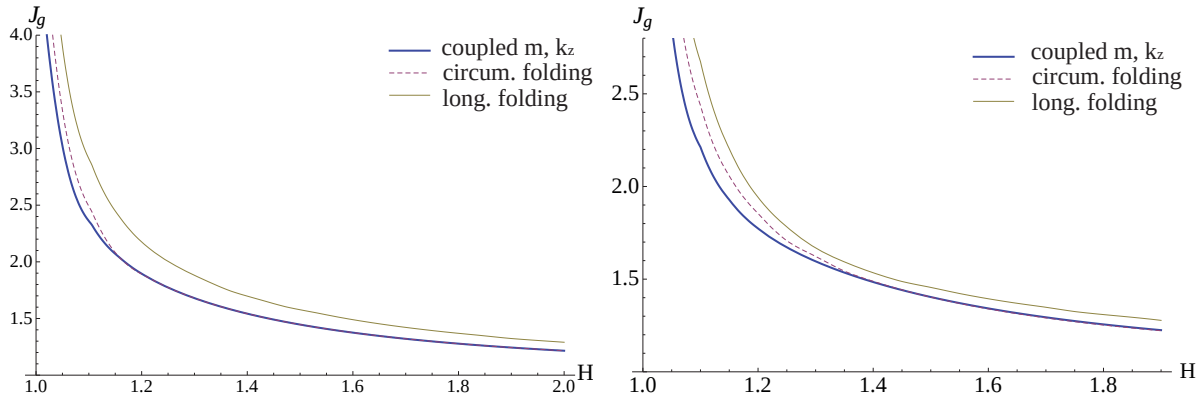

Figure 3.13: Instability thresholds in terms of volume increase due to isotropic (left) and anisotropic (right, $g_r = 1$) growth processes. The curves referring to the circumferential and longitudinal folding are taken from [8].

and 16 days after incubation. The predictions of the proposed model using such values of aspect ratio are consistent with the experimental observations of circumferential folding preceding the villi elongation mouse embryos. In conclusion, the model demonstrates that the villi morphogenesis can start directly from a two-dimensional undulation of the mucosa when the tissue grows subjected to an outer rigid constrain. The theoretical analysis predicts that the selected previllous structure on the mucosa is mainly driven by the initial aspect ratio of the tubular tissue, with thinner tubes not requiring any preceding mucosal folding. The proposed morphoelastic model highlights that both the geometrical and the mechanical properties of the mucosa strongly influence the formation of previllous structures in embryos, providing useful suggestions for interpreting the dynamics of villi morphogenesis in living organisms. Nonetheless, the proposed model is unable to identify the critical wavelength of the emerging surface pattern. Accordingly, it will be refined in the following in order to take into account a differential growth between the layers removing the outer spatial constraint.

3.4 Differential growth model without spatial constraints

In the previous section, a morphoelastic model for the morphogenesis of the GI mucosa has been presented. Assuming the GI tissue composed by a single embryonic layer, spatially constrained by the surrounding tissues, the emergence of a two-dimensional network of folds have been investigated using the morphoelastic theory presented in Chapter 2. It has been shown that the proposed model well reproduces the early formation of villi in vertebrates species such as mouses, but it doesn't allow for the prediction of the finite wavelength of the pattern.

Now, with the aim of modeling the formation of the wider range of patterns observed in the human GI system, a second morphoelastic model will be presented in the following. The embryonic GI tube will be modeled as a two-layered cylinder. The inner and outer layers, respectively represent the primary endodermal layer from which the embryonic mucosa develops and the primary mesoderm matrix from which the mesenchyme and the muscles originate. The model is based on the idea that the differential growth between the two primary matrices induces geometrical incompatibilities in the tissue. As consequence, the residual stresses accumulate in the tissue and eventually they result in the onset of an instability pattern. The factors which can be involved in the selection of the specific pattern will also be investigated. Furthermore, the nonlinear regime of the instability will be investigated using numerical simulations, in order to study the evolution of the pattern as the growth proceeds. As experimentally shown in [90], during the mature stages of intestinal embryogenesis, the tissues surrounding the mucosal layers allow for the intestine to move outward, thus the hypothesis of fixed outer boundary is no more realistic. Instead, it is assumed that the differential growth process evolves without spatial constraints.

The section is organized as follows. The geometry of the model will be first presented, together with the kinematics of the morphoelastic deformation associated to the volumetric growth process. The constitutive equations for the two layers will be assigned using a Neo-Hookean model to account for the nonlinear, hyperelastic and isotropic behavior of the embryonic tissues. The linear stability analysis will be performed and the instability thresholds will be calculated in term of the ratio between the volumetric growth of the endoderm and that of the mesoderm. The wavelength of the associated instability pattern will also be determined for different values of the geometrical and mechanical parameters

of the model. Then, the nonlinear regime of the instability will be studied using a finite element method implemented in Abaqus [102]. Finally the numerical and analytical results will be validated with the experimental data available in the literature.

3.4.1 Kinematics

Let $\mathcal{E} \subset \mathbb{R}^3$ be the three-dimensional Euclidean space, so that $\mathcal{B}_0, \mathcal{B}_a \subset \mathcal{E}$ are two regions occupied by the cylinder at two different instants of time. Let $\mathcal{B}_0$ be the reference configuration with orthonormal basis $\{\mathbf{E}_R, \mathbf{E}_\Theta, \mathbf{E}_Z\}$ and $\mathcal{B}_a$ the spatial or deformed configuration at time t, with orthonormal basis $\{\mathbf{e}_r, \mathbf{e}_\theta, \mathbf{e}_z\}$. Let R_i and R_0 be the initial internal and external radii, respectively, R_m be the initial contact radius at the interface of the two layers and L the initial length of the tube. The internal, the contact, and the external radii are denoted by r_i, r_m and r_0, respectively, and the length of the tube in the deformed state is indicated as l. Figure 3.14 depicts the geometric representation of the

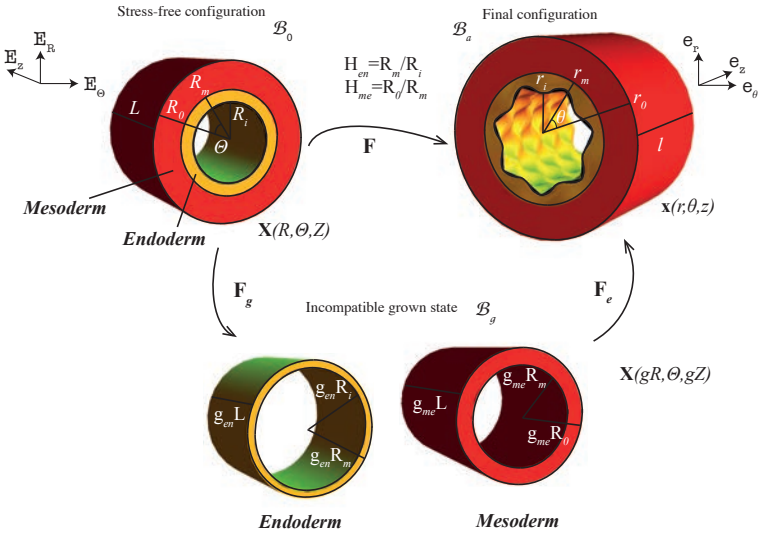

Figure 3.14: Kinematics of the two-layered embryonic gut and representation of the deformation $\boldsymbol{\chi}$ from the stress free reference configuration $\mathcal{B}_0$, to the deformed residually stressed configuration $\mathcal{B}_a$, with the use of cylindrical coordinates.

model.

The growth process of the GI wall is modeled as a deformation $\boldsymbol{\chi}$ from the reference configuration $\mathcal{B}_0$ to the spatial configuration $\mathcal{B}_a$, defined as in Eq.(2.1). For each layer the

finite deformation $\boldsymbol{\chi}$ has the axial-symmetric form:

$$\boldsymbol{\chi}(r,\theta,z) = \begin{cases} r(R,\Theta,Z) = r(R) \\ \theta(R,\Theta,Z) = \Theta \\ z(R,\Theta,Z) = Z \end{cases} \tag{3.53}$$

The deformation in Eq.(3.53) identifies the morphology of the GI tube prior to the occurrence of any instability pattern.

Following the volumetric growth theory presented in Chapter 2, the multiplicative decomposition in Eq.(2.6) can be applied to the deformation gradient $\mathbf{F}$ associated to the morphoelastic deformation $\boldsymbol{\chi}$ in Eq.(3.53), and reads $\mathbf{F} = \mathbf{F}_e\mathbf{F}_g$. Accordingly, the growth component $\mathbf{F}_g$ identifies an intermediate grown stress-free state $\mathcal{B}_g$. In this case, a geometrical incompatibility is introduced in the tissue by the differential growth between the two layers (see Figure 3.14). The elastic part $\mathbf{F}_e$, associated to the deformation from the grown state $\mathcal{B}_g$ to the final configuration $\mathcal{B}_a$, restores the geometrical compatibility of the tissue, whilst residual stresses arise.

Now, since the total process is quasi-static, an evolution law for the growth tensor is not needed. It is sufficient to specify a growth tensor $\mathbf{F}_g$ which identifies the grown stress-free state $\mathcal{B}_g$ after growth occurred. For the sake of simplicity, a homogeneous growth tensor is considered in the form:

$$\mathbf{F}_g = g\mathbf{I} \qquad \text{with} \qquad J_g = \det \mathbf{F}_g = g^3 \tag{3.54}$$

where g denotes the volumetric growth factor of each layer (constant and positive definite) and $\mathbf{I}$ is the identity tensor. Accordingly, the deformation gradient $\mathbf{F}_e = \mathbf{F}\mathbf{F}_g^{-1}$ writes:

$$\mathbf{F}_e = \mathrm{diag}(\lambda_r, \lambda_\theta, \lambda_z). \tag{3.55}$$

where λ_r, λ_θ and λ_z are the principal stretches and from Eq.(3.53) are calculated as:

$$\lambda_r = \frac{r_{,R}}{g} \quad \lambda_\theta = \frac{r}{gR} \quad \lambda_z = \frac{1}{g}. \tag{3.56}$$

Accounting for the incompressibility constraint, it follows that:

$$\det \mathbf{F}_e = \lambda_r\lambda_\theta\lambda_z = 1 \tag{3.57}$$

The left and right Cauchy-Green tensors $\mathbf{B}_e$ and $\mathbf{C}_e$, respectively are defined as $\mathbf{B}_e = \mathbf{F}_e\mathbf{F}_e^T = \mathrm{diag}(\lambda_r^2, \lambda_\theta^2, \lambda_z^2)$ and $\mathbf{C}_e = \mathbf{F}_e^T\mathbf{F}_e = \mathrm{diag}(\lambda_r^2, \lambda_\theta^2, \lambda_z^2)$.
In the following the constitutive relations for the two embryonic layers will be assigned.

3.4.2 Constitutive equations

Since the cellular components of the embryonic tissue are mostly composed of water, the intestine is modeled as an incompressible, hyperelastic, isotropic, two-layered tube. In order to account for the typical nonlinear behavior of the tissues, a Neo-Hookean model is used, so that the elastic strain energy function of each layer can be defined as:

$$\psi_0(\mathbf{F}_e) = \frac{1}{2}\mu(\mathrm{tr}\,\mathbf{C}_e - 3) \tag{3.58}$$

where μ is the shear modulus of each layers. From Eq. (3.58) the nominal stress defined in Eq.(2.65) can be calculated as:

$$\mathbf{S} = \mu\mathbf{F}_e^T - p\mathbf{F}_e^{-1}, \tag{3.59}$$

where p is the Lagrange multiplier of each layer. The Cauchy stress $\boldsymbol{\sigma} = \mathbf{F}_e\mathbf{S}$ follows as:

$$\boldsymbol{\sigma} = \mu\mathbf{B}_e - p\mathbf{I}. \tag{3.60}$$

Since the deformation $\boldsymbol{\chi}$ has been considered axial-symmetric, the only non-zero components of the Cauchy stress are the principal stresses:

$$\begin{aligned}
\sigma_{rr}(r) &= \mu\lambda_r^2(r) - p(r) \\
\sigma_{\theta\theta}(r) &= \mu\lambda_\theta^2(r) - p(r) \\
\sigma_{zz}(r) &= \mu\lambda_z^2 - p(r),
\end{aligned} \tag{3.61}$$

The aim of the next section is to write the governing equations of the elastic problem and to derive the basic solution.

3.4.3 Governing equations and axial-symmetric solution

It has been assumed that no tractions are acting on the internal and external surfaces of the embryonic GI tube. Moreover, recalling that the pressure due to embryonic fluids

acting at the internal wall of the forming gut can be neglected, a zero-traction condition is assigned at the internal surface. Therefore, the elastic problem is governed by Eqs.(2.78) and (2.79) with Neumann boundary conditions in the form of Eq.(2.46) at both the inner and outer surfaces. Moreover, the continuity of the radial displacement and of the radial component of the stress must be ensured at the contact radius between the two layer. Accordingly, **the governing equations** reduce to:

$$\frac{d\sigma_{rr}(r)}{dr} + \frac{1}{r}(\sigma_{rr}(r) - \sigma_{\theta\theta}(r)) = 0 \qquad \text{in} \quad \mathcal{B}_a \tag{3.62}$$

$$\frac{r\, r_{,R}}{R\, g^3} = 1 \qquad \text{in} \quad \mathcal{B}_a \tag{3.63}$$

$$\sigma_{rr}(r_0) = 0 \qquad \text{at} \quad r = r_0 \tag{3.64}$$

$$\sigma_{rr}(r_i) = 0 \qquad \text{at} \quad r = r_i \tag{3.65}$$

$$\sigma_{rr}(r_m^{en}) = \sigma_{rr}(r_m^{me}) \qquad \text{at} \quad r = r_m \tag{3.66}$$

$$r_m^{en} - R(r_m^{en}) = r_m^{me} - R(r_m^{me}) \qquad \text{at} \quad r = r_m. \tag{3.67}$$

Eq.(3.62) is the equilibrium equation in Eq.(2.78) reduced to the first component because of the axial-symmetric property of the deformation $\boldsymbol{\chi}$ in Eq.(3.53). Eq.(3.63) is the incompressibility condition which follows substituting Eqs.(3.55) and (3.56) in Eq.(2.79). Eqs.(3.64) and (3.65) are the Neumann boundary conditions at the outer and inner surfaces, respectively. Eq.(3.66) and (3.67) are the continuity conditions of the displacements and of the radial stress components at the interface between the two embryonic layers.

The aim is now to calculate the basic solution to the equilibrium problem. Integrating Eq.(3.63), the relation between the undeformed and the deformed radii, r and R respectively is calculated as:

$$r = \sqrt{g_l^3 R^2 + a_l} \tag{3.68}$$

where $l = \{en, me\}$ such that g_{en} and g_{me} are the volumetric growth factors of the endodermal and mesodermal layers and $a_{en} = (r_i^2 - g_{en}^3 R_i^2)$ and $a_{me} = (r_m^2 - g_{me}^3 R_m^2)$ follow from the global incompressibility condition. For the sake of notation simplicity, unless explicitly stated, from now on the sub- and superscript l, which refers to the individual layers, will be omitted. Using Eq.(3.68), **the basic axial-symmetric deformation** in

Eq.(3.53) rewrites in the following form:

$$\mathbf{x}^{(0)}(r,\theta,z) = \boldsymbol{\chi}^{(0)}(r,\theta,z) = \begin{cases} r(R,\Theta,Z) = \sqrt{g_l^3 R^2 + a_l} \\ \theta(R,\Theta,Z) = \Theta \\ z(R,\Theta,Z) = Z, \end{cases} \tag{3.69}$$

which is the basic solution of the equilibrium problem in Eqs.(3.62-3.67). The elastic component $\mathbf{F}_e^{(0)}$ of the associated deformation gradient reads:

$$\mathbf{F}_e^{(0)} = \text{diag}\left(\lambda_r^{(0)}(r), \lambda_\theta^{(0)}(r), \lambda_z^{(0)}\right), \tag{3.70}$$

where $\lambda_r^{(0)}(r), \lambda_\theta^{(0)}(r), \lambda_z^{(0)}$ are calculated using Eqs.(3.69) and (3.56). The two unknowns of the problem are now the two Lagrange multipliers p_l with $l = \{en, me\}$ in Eqs.(3.61). They are calculated by integrating Eq.(3.62) with the boundary conditions in Eqs.(3.64) and (3.65) as follows:

$$\begin{aligned} p_{en}(r) &= \mu_{en}(\lambda_r^{(0)})^2(r) + \mu_{en}\int_{r_i}^{r} \frac{(\lambda_r^{(0)})^2(s) - (\lambda_\theta^{(0)})^2(s)}{s}\, ds \\ p_{me}(r) &= \mu_{me}(\lambda_r^{(0)})^2(r) - \mu_{me}\int_{r}^{r_0} \frac{(\lambda_r^{(0)})^2(s) - (\lambda_\theta^{(0)})^2(s)}{s}\, ds, \end{aligned} \tag{3.71}$$

where the internal and external radii follow from the global form of the incompressibility in Eq.(3.63):

$$r_i = \sqrt{\left(\frac{g_{en}}{g_{me}}\right)^3\left(\frac{1}{H_{en}^2} - \frac{1}{H_{me}^2}\right) + r_m^2} \qquad \text{and} \qquad r_0 = \sqrt{1 - \frac{1}{H_{me}^2} + r_m^2}. \tag{3.72}$$

Here $H_{en} = R_m/R_i$ and $H_{me} = R_0/R_m$ denote the geometric aspect ratios of the internal and external layers, respectively. Using the continuity condition in Eq.(3.66), Eq.(3.62)

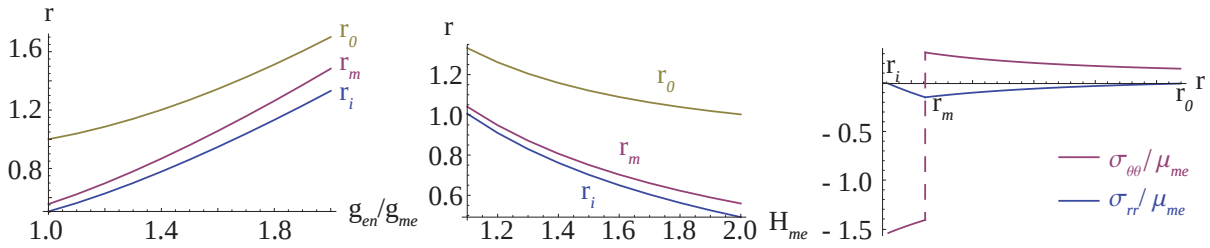

(a) (b) (c)

Figure 3.15: Deformed internal, external, and contact radii, r_i, r_0, r_m as functions of the growth ratio g_{en}/g_{me} at fixed $H_{en} = 1.1$ and $H_{me} = 1.8$ (a), and as function of the mesoderm aspect ratio H_{me}, at fixed $H_{en} = 1.1$ (b), and $g_{en}/g_{me} = 1.1$, setting $\mu_{me}/\mu_{en} = 10$. Radial and circumferential components of the Cauchy stress $\boldsymbol{\sigma}$ plotted with respect to r at fixed $g_{en}/g_{me} = 1.1$ with $g_{me} = 1$, $\mu_{me}/\mu_{en} = 10$, $R_0 = 1$, $H_{en} = 1.1$ and $H_{me} = 1.8$ (c).

can be solved with the boundary conditions in Eqs.(3.64) and (3.65):

$$\frac{g_{me}}{H_{me}^2}\left(\frac{1}{r_m^2} - \frac{H_{me}^4}{H_{me}^2(1+r_m^2)-1}\right) + \frac{\mu_{me}}{\mu_{en}}\frac{g_{en}^4}{g_{me}^3}\left(\frac{1}{\left(\frac{g_{en}}{g_{me}}\right)^3(1-H_{en}^2)+H_{en}^2H_{me}^2r_m^2} - \frac{1}{H_{me}^2r_m^2}\right)$$

$$+g_{me}\log\left(\frac{\left(H_{me}^2(r_m^2+1)-1\right)}{r_m^2H_{me}^4}\right) - g_{en}\frac{\mu_{me}}{\mu_{en}}\log\left(\frac{\left(\frac{g_{en}}{g_{me}}\right)^3(1-H_{en}^2)+r_m^2(H_{en}^2H_{me}^2)}{r_m^2H_{me}^2}\right) = 0. \tag{3.73}$$

Finally, the deformed radius is calculated at the interface between the two layers r_m by numerically solving Eq.(3.73) using the function `NSolve` in Mathematica [100]. In Figure 3.15, the deformed internal, external, and contact radii, r_i, r_0, r_m are plotted against H_{en} (a) and H_{me} (b), and the radial and circumferential components of the Cauchy stress in Eq.(3.60) are depicted as a function of r.

3.4.4 Incremental boundary value problem

Now, the method of incremental deformations superposed on finite deformations will be applied in order to perform the linear stability analysis of the basic solution calculated in Section 3.4.3. Let the basic solution $\boldsymbol{\chi}^{(0)}$ be perturbed by superposing a small incremental deformation $\boldsymbol{\chi}^{(1)}$ to the finite deformation in Eq.(3.69). Let $\boldsymbol{\chi}^{(1)}$ be expressed as:

$$\boldsymbol{\chi}^1(r,\theta,z) = u(r,\theta,z)\mathbf{e}_r + v(r,\theta,z)\mathbf{e}_\theta + w(r,\theta,z)\mathbf{e}_z, \tag{3.74}$$

where u, v, w are three scalar functions. The displacement gradient $\mathbf{\Gamma}$, associated to the incremental deformation has the form:

$$\mathbf{\Gamma} = \begin{pmatrix} u_{,r} & (u_{,\theta} - v)/r & u_{,z} \\ v_{,r} & (v_{,\theta} + u)/r & v_{,z} \\ w_{,r} & (v_{,\theta})/r & w_{,z} \end{pmatrix}, \tag{3.75}$$

According to the theory presented in Section 2.2, the perturbed deformation gradient $\bar{\mathbf{F}}$ rewrites in the form of Eq.(2.86) and the perturbed Nominal stress $\bar{\mathbf{S}}$ in the form of Eq.(2.88). The first-order increment $\hat{\mathbf{S}}$ of the Nominal stress tensor $\mathbf{S}$ is in the form of Eq.(2.89) and its push forward $\hat{\mathbf{S}}_0 = \mathbf{F}_e^{(0)}\hat{\mathbf{S}}$ is given by Eq.(2.92) and writes:

$$\hat{\mathbf{S}}_0 = \boldsymbol{\mathcal{A}}_0^1 \mathbf{\Gamma} + p\mathbf{\Gamma} - q\mathbf{I}. \tag{3.76}$$

where $\boldsymbol{\mathcal{A}}_0^1$ is the tensor of instantaneous moduli, defined in Eq.(2.93), p is the Lagrange multiplier and q its first-order increment. The **incremental BVP** rewrites:

$$\frac{\partial(r\hat{S}_{0rr})}{\partial r} + \frac{\partial \hat{S}_{0\theta r}}{\partial \theta} + r\frac{\partial \hat{S}_{0zr}}{\partial z} - \hat{S}_{0\theta\theta} = 0 \qquad \text{in } \mathcal{B}_a \tag{3.77}$$

$$\frac{\partial(r\hat{S}_{0r\theta})}{\partial r} + \frac{\partial \hat{S}_{0\theta\theta}}{\partial \theta} + r\frac{\partial \hat{S}_{0z\theta}}{\partial z} + \hat{S}_{0\theta r} = 0 \qquad \text{in } \mathcal{B}_a \tag{3.78}$$

$$\frac{\partial(r\hat{S}_{0rz})}{\partial r} + \frac{\partial \hat{S}_{0\theta z}}{\partial \theta} + r\frac{\partial \hat{S}_{0zz}}{\partial z} = 0 \qquad \text{in } \mathcal{B}_a \tag{3.79}$$

$$u_{,r} + \frac{u + v_{,\theta}}{r} + w_{,z} = 0 \qquad \text{in } \mathcal{B}_a \tag{3.80}$$

$$\hat{S}_{0rr}(r_0) = 0,\ \hat{S}_{0r\theta}(r_0) = 0,\ \hat{S}_{0rz}(r_0) = 0 \qquad \text{at } r = r_0 \tag{3.81}$$

$$\hat{S}_{0rr}(r_i) = 0,\ \hat{S}_{0r\theta}(r_i) = 0,\ \hat{S}_{0rz}(r_i) = 0 \qquad \text{at } r = r_i \tag{3.82}$$

$$\hat{S}_{0rr}(r_m^{en}) = \hat{S}_{0rr}(r_m^{me}),\ \hat{S}_{0r\theta}(r_m^{en}) = \hat{S}_{0r\theta}(r_m^{me}),\ \hat{S}_{0rz}(r_m^{en}) = \hat{S}_{0rz}(r_m^{me}) \qquad \text{at } r = r_m \tag{3.83}$$

$$u(r_m^{en}) = u(r_m^{me}),\ v(r_m^{en}) = v(r_m^{me}),\ w(r_m^{en}) = w(r_m^{me}) \qquad \text{at } r = r_m \tag{3.84}$$

where Eqs.(3.77-3.79) are the first-order incremental equilibrium equations in Eq.(2.103). Eq.(3.80) is the incremental incompressibility condition in Eq.(2.104). Eqs.(3.81) and (3.82) are the first-order increments of the boundary conditions in Eqs.(3.64) and (3.65), respectively. Eqs.(3.83) and (3.84) are the continuity incremental conditions for the radial components of the stress and for the displacements, at the interface between the two layers. Eqs.(3.77-3.80) define a system of four partial differential equations, where the four unknowns are the three incremental displacements in Eq.(3.74) and the increment

q of the Lagrange multiplier. In the next section, a compact form of the incremental problem will be derived, using the Stroh formalism introduced in Section 2.3.1.

3.4.5 Stroh formulation of the BVP

In order to solve the incremental problem the Stroh formalism is used in the following. The set of four PDEs in Eqs.(3.77-3.80) is transformed into a set of six ODEs of first order with initial conditions for both layers, $l = \{en, me\}$.

Assuming the separation of variables, the components in Eq. (3.74) and the increment of the Lagrange multiplier in Eq. (3.76) can be expressed in the following form:

$$\begin{aligned} u &= U(r)\cos(m\theta)\cos(k_z z) \\ v &= V(r)\sin(m\theta)\cos(k_z z) \\ w &= W(r)\cos(m\theta)\sin(k_z z) \\ q &= Q(r)\cos(m\theta)\cos(k_z z), \end{aligned} \tag{3.85}$$

where m and $k_z = 2\pi n/L$ (with $m, n \in \mathbb{N}$), are the circumferential and longitudinal modes respectively, and $U(r), V(r), W(r), Q(r)$ are four scalar functions. Similarly, the incremental stress components $\hat{S}_{0rr}, \hat{S}_{0r\theta}, \hat{S}_{0rz}$ can be written as follows:

$$\begin{aligned} \hat{S}_{0rr} &= s_{0rr}(r)\cos(m\theta)\cos(k_z z) \\ \hat{S}_{0r\theta} &= s_{0r\theta}(r)\sin(m\theta)\cos(k_z z) \\ \hat{S}_{0rz} &= s_{0rz}(r)\cos(m\theta)\sin(k_z z), \end{aligned} \tag{3.86}$$

where $s_{0rr}(r), s_{0r\theta}(r), s_{0rz}(r)$ are three scalar functions. Substituting Eqs. (3.85) and Eq. (3.86) into Eqs. (3.80) and (3.76) gives:

$$U' = -\frac{U + mV}{r} - k_z W, \quad V' = \frac{s_{0r\theta} + mUp + Vp}{\mathcal{A}^1_{0r\theta r\theta} r}, \quad W' = \frac{s_{0rz} + rk_z Up}{A^1_{0rzrz} r}, \tag{3.87}$$

and

$$Q = -\frac{s_{0rr}}{r} + (A^1_{0rrrr} + p)U'\,. \tag{3.88}$$

Finally, by substituting Eqs.(3.85,3.86) into the three incremental equilibrium equations in Eqs.(3.77-3.79) and by using Eq.(3.88) to eliminate the variable Q, the following equations

are obtained:

$$\begin{aligned}&\Big(\mathcal{A}^1_{0\theta\theta\theta\theta}+\mathcal{A}^1_{0\theta r\theta r}m^2+p+\mathcal{A}^1_{0zrzr}k_z^2r^2\Big)U+m\Big(\mathcal{A}^1_{0\theta r\theta r}+\mathcal{A}^1_{0\theta\theta\theta\theta}+p\Big)V\\&+s_{0rr}-r\Big((\mathcal{A}^1_{0rrrr}+p)U'+p(mV'+k_zrW')+s'_{0rr}\Big)=0,\end{aligned}\tag{3.89}$$

$$\begin{aligned}&m\Big(\mathcal{A}^1_{0\theta r\theta r}+\mathcal{A}^1_{0\theta\theta\theta\theta}+p\Big)U+\Big(\mathcal{A}^1_{0\theta r\theta r}+m^2(\mathcal{A}^1_{0\theta\theta\theta\theta}+p)+\mathcal{A}^1_{0z\theta z\theta}k_z^2r^2\Big)V\\&+\Big(mk_zrp\Big)W+ms_{0rr}-mr\Big(\mathcal{A}^1_{0rrrr}+p\Big)U'-prV'-rs'_{0r\theta}=0,\end{aligned}\tag{3.90}$$

$$\begin{aligned}&rs'_{0rz}+k_zrs_{0rr}-\Big(k_zmrp\Big)V+\Big(\mathcal{A}^1_{0\theta z\theta z}m^2-k_z^2r^2(\mathcal{A}^1_{0zzzz}+p)\Big)W\\&-k_z\Big(\mathcal{A}^1_{0rrrr}+p\Big)r^2U'=0.\end{aligned}\tag{3.91}$$

In order to write the set of six first ODEs in Eqs.(3.87) and Eqs.(3.89-3.91) in the compact form, the displacement-traction vector $\boldsymbol{\eta}$ is defined as follows:

$$\boldsymbol{\eta}(r)=\begin{bmatrix}\mathbf{U}(r)\\ r\,\mathbf{S}(r)\end{bmatrix}\quad\text{with}\quad\begin{aligned}\mathbf{U}\ (r)&=[\,U(r),V(r),W(r)\,]^T\\ \mathbf{S}\ (r)&=[\,s_{0rr}(r),s_{0r\theta}(r),s_{0rz}(r)\,]^T.\end{aligned}\tag{3.92}$$

It follows that Eqs.(3.87) and Eqs.(3.89-3.91) rewrite in the Stroh compact form:

$$\frac{d\boldsymbol{\eta}(r)}{dr}=\frac{1}{r}\mathbf{G}(r)\boldsymbol{\eta}(r),\tag{3.93}$$

where $\mathbf{G}$ is the so-called **Stroh matrix**, which takes the following block form:

$$\mathbf{G}=\begin{pmatrix}\mathbf{G}_1&\mathbf{G}_2\\ \mathbf{G}_3&\mathbf{G}_4\end{pmatrix},\tag{3.94}$$

The four blocks in Eq. (3.94) are given by:

$$\begin{aligned}\mathbf{G}_1&=\begin{pmatrix}-1&-m&-k_zr\\ m\sigma_1&\sigma_1&0\\ k_zr\sigma_2&0&0\end{pmatrix}\quad\mathbf{G}_2=\begin{pmatrix}0&0&0\\ 0&1/\alpha_1&0\\ 0&0&1/\alpha_2\end{pmatrix}\\ \mathbf{G}_3&=\begin{pmatrix}\kappa_{11}&\kappa_{12}&\kappa_{13}\\ \kappa_{12}&\kappa_{22}&\kappa_{23}\\ \kappa_{13}&\kappa_{23}&\kappa_{33}\end{pmatrix}\qquad\mathbf{G}_4=\begin{pmatrix}1&-m\sigma_1&-k_zr\sigma_2\\ m&-\sigma_1&0\\ k_zr&0&0\end{pmatrix}\end{aligned}\tag{3.95}$$

with $\mathbf{G}_4 = -\mathbf{G}_1^T$ and:

$$\begin{aligned}
\kappa_{11} &= m^2(\nu_1 - \alpha_1\sigma_1^2) + k_z^2 r^2(\nu_2 - \alpha_2\sigma_2^2) + \mathcal{A}^1_{0rrrr} + \mathcal{A}^1_{0\theta\theta\theta\theta} + 2\alpha_1\sigma_1 \\
\kappa_{12} &= m(\mathcal{A}^1_{0rrrr} + \mathcal{A}^1_{0\theta\theta\theta} + 2\alpha_1\sigma_{1l} + \nu_1 - \alpha_1\sigma_1^2) \\
\kappa_{13} &= k_z r(\mathcal{A}^1_{0rrrr} + \alpha_1\sigma_1) \\
\kappa_{22} &= m^2\left[\mathcal{A}^1_{0rrrr} + \mathcal{A}^1_{0\theta\theta\theta} + 2\alpha_1\sigma_1\right] + k_z^2 r^2\nu_3 + \nu_1 - \alpha_1\sigma_1^2 \\
\kappa_{23} &= mk_z r(\mathcal{A}^1_{0rrrr} + 2\alpha_1\sigma_1) \\
\kappa_{33} &= m^2\alpha_3 + k_z^2 r^2(\mathcal{A}^1_{0rrrr} + \mathcal{A}^1_{0zzzz} + 2\alpha_3\sigma_3),
\end{aligned} \tag{3.96}$$

and:

$$\begin{aligned}
&\nu_1 = \mathcal{A}^1_{0\theta r\theta r}, \qquad \alpha_1 = \mathcal{A}^1_{0r\theta r\theta}, \qquad \sigma_1 = p/\alpha_1, \\
&\nu_2 = \mathcal{A}^1_{0zrzr}, \qquad \alpha_2 = \mathcal{A}^1_{0rzrz}, \qquad \sigma_2 = p/\alpha_2 \\
&\nu_3 = \mathcal{A}^1_{0z\theta z\theta}, \qquad \alpha_3 = \mathcal{A}^1_{0\theta z\theta z}, \qquad \sigma_3 = p/\alpha_3.
\end{aligned} \tag{3.97}$$

Note that, since the perturbation in Eq.(3.85) has real components, the four blocks of the Stroh matrix are real.

As mentioned in Section 2.3.3, the Stroh form of the incremental BVP doesn't provide the best form of the problem to be solved when Neumann boundary conditions are assigned. Therefore, the surface impedance method will be used in order to obtain a compact form which will allow for the implementation of a stable numerical solving procedure.

3.4.6 Surface impedance method and numerical solution

Following Section 2.3.2, a set of independent solutions $\boldsymbol{\eta}_n$, $n = \{1, \ldots, 6\}$ of the system in Eq. (3.93) is defined. Then the 6×6 matricant $\mathbf{M}(r, r_k)$ is introduced as in Eq.(2.113) for the inner and outer layers $k = (i, o)$. The matricant in Eq. (2.113), is the solution of the initial value problem for the inner and outer layers, $k = (i, o)$:

$$\frac{d\mathbf{M}}{dr}(r, r_k) = \frac{1}{r}\mathbf{G}(r)\mathbf{M}(r, r_k) \qquad \text{with} \qquad \mathbf{M}(r_k, r_k) = \mathbf{I}_{(6)}, \tag{3.98}$$

where $\mathbf{I}_{(6)}$ is the 6×6 identity matrix. Now, since the components of the incremental deformation in Eq.(3.85) are real, the conditional impedance matrix $\mathbf{z} = \mathbf{z}(r, r_k)$ is defined as the 3×3 matrix, such that:

$$r\,\mathbf{S} = \mathbf{z}\,\mathbf{U}, \qquad \text{with} \qquad \mathbf{z} = \mathbf{M}_3\mathbf{M}_1^{-1} \tag{3.99}$$

Substituting Eq. (3.92) and Eq. (3.99) in Eq. (3.93), the following equations are obtained:

$$\begin{aligned} \frac{d}{dr}\mathbf{U} &= \frac{1}{r}\mathbf{G}_1\mathbf{U} + \frac{1}{r}\mathbf{G}_2\mathbf{z}\mathbf{U} \\ \frac{d}{dr}(\mathbf{z}\,\mathbf{U}) &= \frac{1}{r}\mathbf{G}_3\mathbf{U} - \frac{1}{r}\mathbf{G}_1^T\mathbf{z}\mathbf{U} \end{aligned} \tag{3.100}$$

and substituting Eq.(3.100).1 into Eq. (3.100).2, **the matrix Riccati equation** is derived:

$$\frac{d\mathbf{z}}{dr} = \frac{1}{r}\left(\mathbf{G}_3 - \mathbf{G}_1^T\mathbf{z} - \mathbf{z}\mathbf{G}_1 - \mathbf{z}\mathbf{G}_2\mathbf{z}\right). \tag{3.101}$$

From the boundary condition at the inner layer in Eq.(3.82) and using Eq.(3.99), the initial condition of zero traction at the inner surface r_i writes:

$$\mathbf{z}^{en}(r_i) = \mathbf{0}, \tag{3.102}$$

The initial conditions of zero traction at the outer surface in Eq.(3.81) are used to derive the following stop condition:

$$\det \mathbf{z}^{me}(r_0) = 0 \tag{3.103}$$

and the continuity conditions at the interface of the two layers in Eqs.(3.83,3.84) read:

$$\mathbf{z}^{en}(r_m^{en}) = \mathbf{z}^{me}(r_m^{me}). \tag{3.104}$$

The matrix Riccati equation (3.101) for the endoderm is integrated from $r = r_i$ to $r = r_m^{en}$ using the initial condition in Eq.(3.102). Using this solution and the continuity condition in Eq. (3.104) the initial condition for the mesoderm at $r = r_m^{me}$ is derived and the Riccati equation is integrated again, now from $r = r_m^{me}$ to $r = r_0$, until the convergence criterion in Eq.(3.103) is satisfied.

The numerical resolution algorithm is implemented in Mathematica and the function `NSolve` is used to numerically integrate the Riccati Equation. The function automatically uses the most suitable numerical method to solve the system of equations. In Figure 3.16 the algorithm flowchart is sketched.

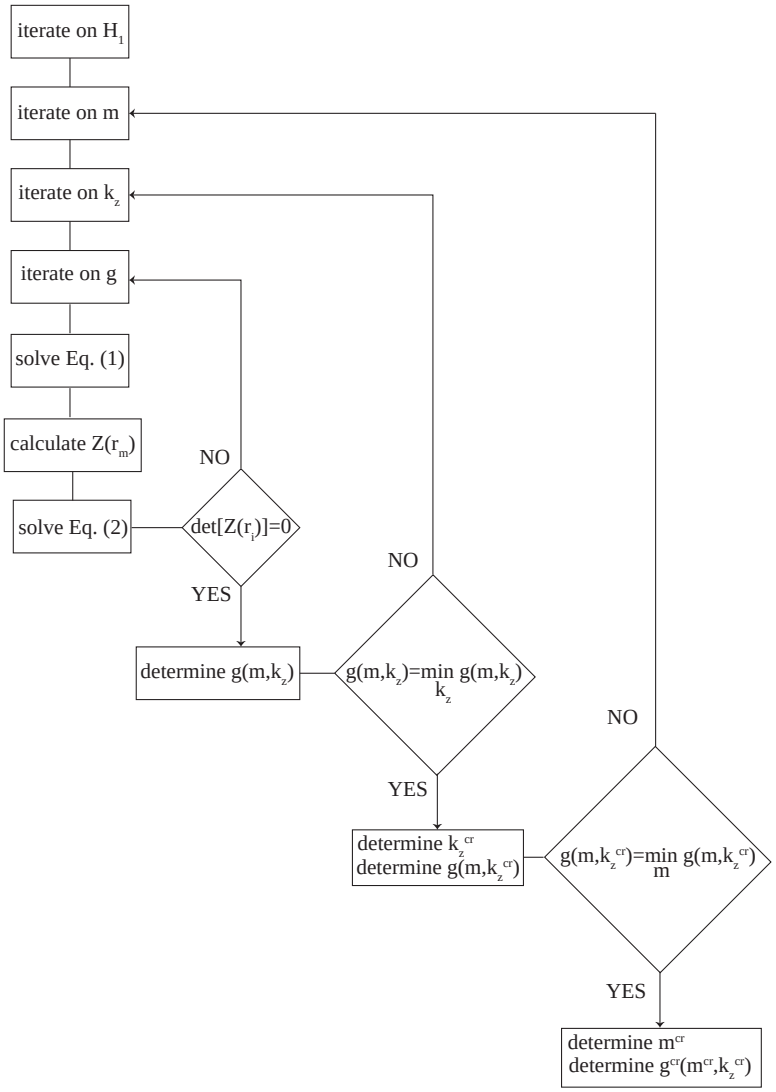

Figure 3.16: Algorithmic flowchart to solve the differential Riccati equation in Eq.(3.101).

3.4.7 Theoretical results of the linear stability analysis

In this section, the analytical results obtained from the linear stability analysis performed in Section 3.4.4 will be presented. In particular, the role played by the aspect ratios H_{en} and H_{me} of the endodermal and mesodermal layers on the onset of the instability is analyzed. Furthermore, it will be investigated in the following how the stiffness ratio μ_{me}/μ_{en} affects the morphology of the emerging pattern.

3.4.7.1 Effect of the aspect ratios of the layers on the pattern selection

First, the effect that the geometric aspect ratios of the two layers have on the onset of the mechanical instabilities of the growing tube is investigated. Since the mesoderm is physiologically stiffer than the endoderm, the stiffness ratio is fixed to $\mu_{me}/\mu_{en} = 5$ in Figures 3.17 and $\mu_{me}/\mu_{en} = 10$ in Figure 3.18. In both cases the initial external radius is $R_0 = 1$ and the initial aspect ratio of the mesodermal layer H_{me} ranges between 1.8 and 2. In Figures 3.17(a) and 3.18(a) the critical growth ratio $(g_{en}/g_{me})^{cr}$ is plotted against the

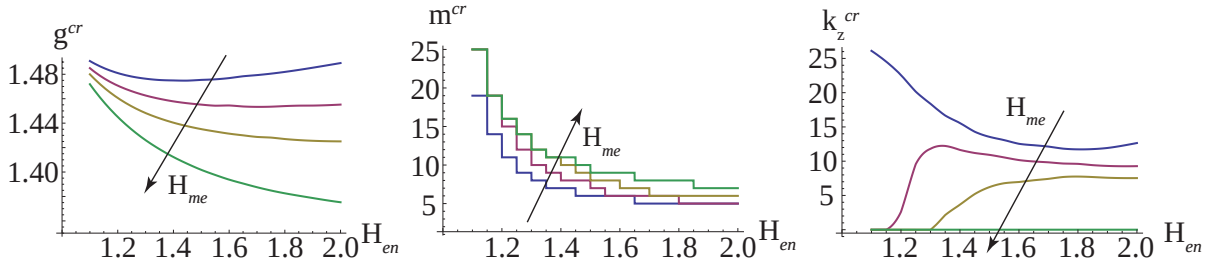

Figure 3.17: Critical growth ratios $(g_{en}/g_{me})^{cr}$ (a), with the corresponding critical circumferential modes m^{cr} (b) and longitudinal modes k_z^{cr} (c), plotted against the initial aspect ratio of the endoderm H_{en}, at different initial aspect ratios of the mesoderm $H_{me} = \{1.8, 1.85, 1.9, 2\}$ for constant $\mu_{me}/\mu_{en} = 5$.

initial aspect ratio of the endodermal layer H_{en} at different ratios of H_{me}. The corresponding critical circumferential modes m^{cr} and the critical longitudinal wavenumber k_z^{cr} are depicted in Figures 3.17(b), 3.18(b) and Figures 3.17(c), 3.18(c), respectively. The curves

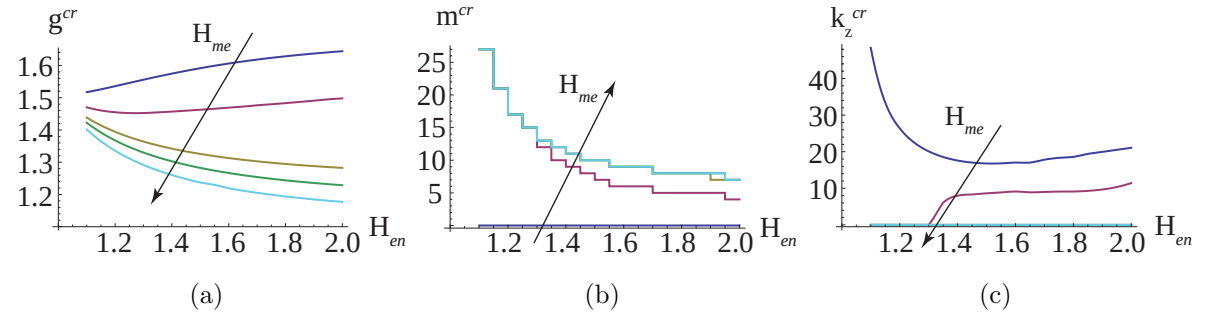

Figure 3.18: Critical growth ratio $(g_{en}/g_{me})^{cr}$ (a), with the corresponding critical circumferential and longitudinal modes m^{cr} (b) and k_z^{cr} (c), at different mesodermal aspect ratios $H_{me} = 1.2, 1.3, 1.4, 1.5, 1.8$, fixing $\mu_{me}/\mu_{en} = 10$.

show how increasing either H_{en} or H_{me} decreases the critical growth ratio $(g_{en}/g_{me})^{cr}$. A different trend can be observed in Figure 3.17(b): the critical circumferential modes m^{cr} increase as the initial aspect ratio H_{me} of the external layer increases, but the critical modes m^{cr} decrease as the initial aspect ratio H_{en} of the internal layer increases. The critical longitudinal wavenumber k_z^{cr}, in Figure 3.17(c), decreases as H_{me} increases. When the internal layer is thin, i.e., $H_{en} \leq 1.3$, the following trends can be observed: low longitudinal wavelengths emerge for cylinders with thick external layers, i.e., $H_{me} \geq 2$, whereas high longitudinal wavelengths emerge for cylinders with thinner external layer, i.e., $H_{me} \leq 1.9$. In order to explore the behavior of the tissue when the mesodermal layer is thin, the stiffness ratio is fixed to $\mu_{me}/\mu_{en} = 10$ and the focus is pointed to the range $H_{me} = 1.2 - 1.8$. In the following, the effect of the stiffness ratio between the two layer on the onset and the morphology of the instability is investigated.

3.4.7.2 Effect of the stiffness ratio on the pattern selection

Now, fixed the initial aspect ratio of the mesoderm $H_{me} = 1.8$ and the initial external radius $R_0 = 1$, different values of the stiffness ratio μ_{me}/μ_{en} between mesoderm and endoderm are considered.
In Figure 3.19(a) the critical growth ratio $(g_{en}/g_{me})^{cr}$ are plotted against the initial aspect ratio of the endodermal layer H_{en} at different stiffness ratios μ_{me}/μ_{en}. In Figure 3.19(b) and Figure 3.19(c), the corresponding critical circumferential modes m^{cr} and the longitudinal wavenumber k_z^{cr} are plotted against H_{en} at different μ_{me}/μ_{en}. Figure 3.19(a) highlights how the critical growth factor g_{en}/g_{me} decreases as the stiffness ratio μ_{me}/μ_{en}

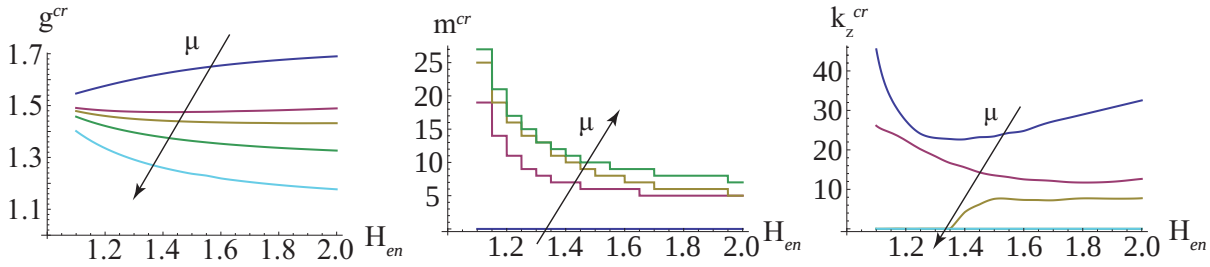

Figure 3.19: Critical growth ratios $(g_{en}/g_{me})^{cr}$ (a), with the corresponding critical circumferential modes m^{cr} (b) and longitudinal modes k_z^{cr} (c), plotted against the initial aspect ratio of the endoderm H_{en}, at different stiffness ratios $\mu_{me}/\mu_{en} = \{3, 5, 5.3, 6, 10\}$ for constant $H_{me} = 1.8$.

increases. The stiffer the external layer, the lower the critical growth required to induce the instability. The curves in Figure 3.19(b) and 3.19(c) show how an increase in the stiffness ratio corresponds to an increasing critical circumferential mode and a decreasing longitudinal wavenumber k_z^{cr}. In the following, the implementation of the numerical model for investigating the evolution of the instability patterns will be described.

3.4.8 Finite element simulations in the post-buckling regime

The linear stability analysis performed in Section 3.4.4 allows to calculate the thresholds for the onset of the instability and the associated patterns, but does not allow to study the evolution of the patterns beyond the linear threshold. A more complete analysis would require the resolution of Eqs.(3.77-3.80) and Eqs.(3.81-3.83), including the terms of higher orders in ε. For the elastic problem considered in this work, this strategy leads to a form of the equations which is not analytically treatable. Therefore, a numerical solution will be derived using the finite element method.
To explore the behavior of the system in the post-critical regime, the commercial finite element program Abaqus/Standard, Version 6.12 has been employed [102]. In the next paragraph, a brief description of the implementation of the numerical model will be given.

3.4.8.1 Implementation of the model in Abaqus

Step 1. Geometry

The three-dimensional cylindrical model is built including the two layers. The geometry is defined by the aspect ratios `Hen` = `Rm/Ri` and `Hme` = `R0/Rm` of the endoderm and of the mesoderm, respectively, with `R0` set equal to 1. In order to optimize the number of elements needed to well capture the sinusoidal component of the instability in the longitudinal direction, the initial length of the cylinder is calculated as follows. The longitudinal wavenumber is given by

$$\texttt{kz} = 2\pi * \texttt{nz}/\texttt{L}, \tag{3.105}$$

where `nz` is an integer which identifies the number of folds in the longitudinal direction, associated to the instability pattern. The value of `kz` is given by the linear stability analysis, thus as long as Eq.(3.105) is satisfied, `L` and `nz` can be chosen arbitrarily. Therefore, `nz` can be chosen equal to 1 and accordingly `L` can be calculated from Eq.(3.105).

Step 2. Constitutive model

The two layers are modeled as incompressible and hyperelastic materials. A Neo-Hookean model is used, setting the values of the shear moduli `mu_en` and `mu_me` = `mu_ratio` ∗ `mu_en` for the endoderm and the mesoderm, respectively.

Step 3. Differential Growth

The growth is implemented in the model as a thermal expansion. The Expansion and Conductivity properties of the materials are set according to Table 3.1.

	Expansion α	Conductivity
Endoderm	1.0	0.0
Mesoderm	0.0	0.0

Table 3.1: Thermal constants used in the numerical simulations in order to model the differential volumetric growth of the endodermal and mesodermal layers.

The following linear evolution law is adopted for the growth:

$$g_l = 1 + \alpha_l \cdot t, \qquad l = (en, me)\,, \tag{3.106}$$

where α_l are the expansion constants, representing the growth rates for each layer and t is the time.

Step 4. Mesh

In order to exactly model the incompressibility of the materials, tri-linear brick hybrid elements with 8 integration points (`C3D8H`) are used. The number of elements in the radial, circumferential and longitudinal directions is chosen depending on the geometry of the cylinder and on the shape of the initial perturbation, see Table 3.2.

	`Hme` = 1.8	`Hme` = 1.9	`Hme` = 2
radial En.	2	2	2
radial Me.	12	15	20
circum.	m*10	m*10	m*10
long.	100	100	100

Table 3.2: Mesh parameters in function of the geometry of the model and of the perturbation. m is the circumferential wavenumber.

Step 5. Initial imperfection

The perturbation is included in the model, introducing a small imperfection in the initial mesh, with an amplitude `Perturbation` $= 0.001$ and the form of Eq.(3.85). The circumferential and longitudinal wavenumbers `m` and `kz` respectively, are those predicted by the linear stability analysis for each combination of the initial parameters.

Step 6. Time Step

The static analysis procedure offered by Abaqus Standard is used to solve the equilibrium problem. The initial, the minimum and the maximum time steps are manually set to `InitialStep` $= 10^{-2}$, `MinStep` $= 10^{-3}$ and `MaxStep` $= 10^{-2}$.

Step 7. Boundary Conditions

A condition of zero-longitudinal displacement at the top and the bottom of the cylinder is imposed. In order to model the stress-free boundary conditions at the inner and outer surfaces, a local cylindrical reference system is defined. Then, the circumferential displacements are set to zero at the outer boundary. This allows for a more stable numerical solution and avoids unconstrained rigid body motions.

Step 8. Contact control

A contact control is set to the inner surface, in order to avoid incompatible deformations due to superposition of elements, with the tolerance option set to
`absolutePenetrationTolerance` $= 0.5$.

3.4.9 Numerical results

In this section, the numerical results from the fully nonlinear finite element analysis performed with Abaqus/Standard are summarized. First, the numerical implementation will be validated by comparing the theoretical predictions of Section 3.4.7 with the corresponding results from the numerical simulations. Second, the non-linear evolution of the instability patterns developing at the inner surface of the embryonic endoderm will be investigated.

3.4.9.1 Validation of the numerical code versus the theoretical predictions

In order to validate the finite element implementation, the critical growth ratios in the numerical simulation are compared with the theoretical predictions. The criterion

for such a comparison is based on the energy considerations. In this physical system the selected solution always minimizes the total elastic energy of the system. Before the onset of buckling, the solution with the minimal elastic energy is the basic axisymmetric deformation in Eq. (3.69). During the growth process, the stresses accumulate until a critical growth value is reached. At this point, the system bifurcates into a solution with a lower energy than the one associated with the basic axisymmetric solution, thus buckling occurs.

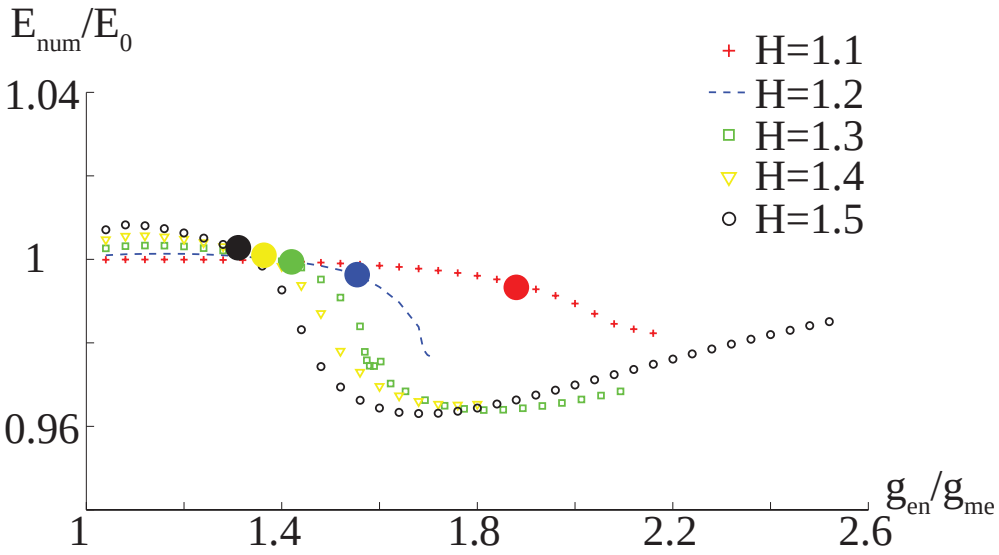

Figure 3.20: The energy ratio E_{num}/E_0 against the growth ratio g_{en}/g_{me} at $H_{me} = 1.8$, fixing $\mu_{me}/\mu_{en} = 10$ and at different $H_{en} = 1.1, 1.2, 1.3, 1.4, 1.5$. The filled colored bullets identify the critical growth values defined according to the energy criterion.

The critical growth in the numerical simulations is identified as the value of $(g_{en}/g_{me})^{cr}$ at which the ratio between the total current elastic energy and the initial elastic energy E_{num}/E_0 has decreased by more than 1% of its initial value. The total elastic energy E_0 follows from integrating Eq. (3.58), as:

$$E_0 = 2\pi \left(\int_0^L \int_{R_i}^{R_m} \psi_{0en} \cdot R_{en} \, \mathrm{d}R_{en} \, \mathrm{d}Z_{en} + \int_0^L \int_{R_m}^{R_0} \psi_{0me} \cdot R_{me} \, \mathrm{d}R_{me} \, \mathrm{d}Z_{me} \right),$$

where ψ_{0en} and ψ_{0me} are the strain energy functions of the endodermal and mesodermal layers associated with the basic deformation in Eq. (3.69). In Figure 3.20, the curves for the ratio E_{num}/E_0 are plotted for different H_{en} at fixed $H_{me} = 1.8$ for $\mu_{me}/\mu_{en} = 10$. The trend of the curves shows how the ratio E_{num}/E_0 undergoes a steep decrease right after

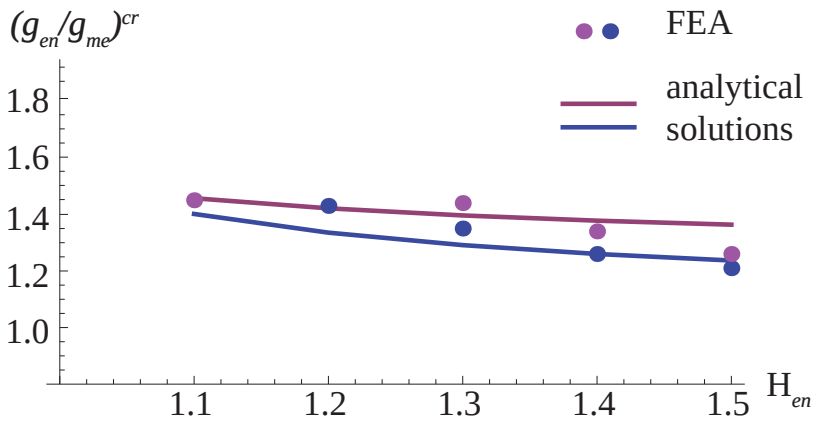

Figure 3.21: Comparison between the critical growth value $(g_{en}/g_{me})^{cr}$ from the numerical finite element solution (dots) and the analytical linear stability analysis (lines). The parameters are set as $H_{me} = 1.8$, $\mu_{me}/\mu_{en} = 10$ (blue) and $\mu_{me}/\mu_{en} = 6$ (magenta).

the bifurcation point. Furthermore, as predicted from the linear stability analysis, the critical growth ratios are higher for cylinder with small H_{en} .

Figure 3.21 shows that the critical growth values of the numerical simulations are in good agreement with the analytical predictions. The solid lines refer to the analytical solutions, whereas the markers indicate the numerical thresholds found from the simulations. This confirms the numerical implementation, which can now be employed to investigate pattern formation in the fully nonlinear regime.

3.4.9.2 Evolution of the instability pattern

Now, the aim is to analyze the morphological evolution of the instability patterns far beyond the onset of buckling. Figure 3.22 collects the resulting patterns in the (H_{en}, H_{me})-space. The phase diagram in Figure 3.22 highlights a transition from a one-dimensional circumferential pattern to a two-dimensional pattern, already indicated by the analytical curves in Fig 3.17. In particular, tissues with both thick endoderm and mesoderm select a circumferential instability pattern with $m^{cr} > 0$ and $k_z^{cr} = 0$, whereas tissues with both thin endoderm and mesoderm select a two-dimensional instability pattern with $m^{cr}, k_z^{cr} > 0$. Figure 3.23 illustrates the phase diagram of the instability patterns in the $(H_{en}, \mu_{me}/\mu_{en})$-space. In agreement with the analytical curves in Fig. 3.19, the instabil-

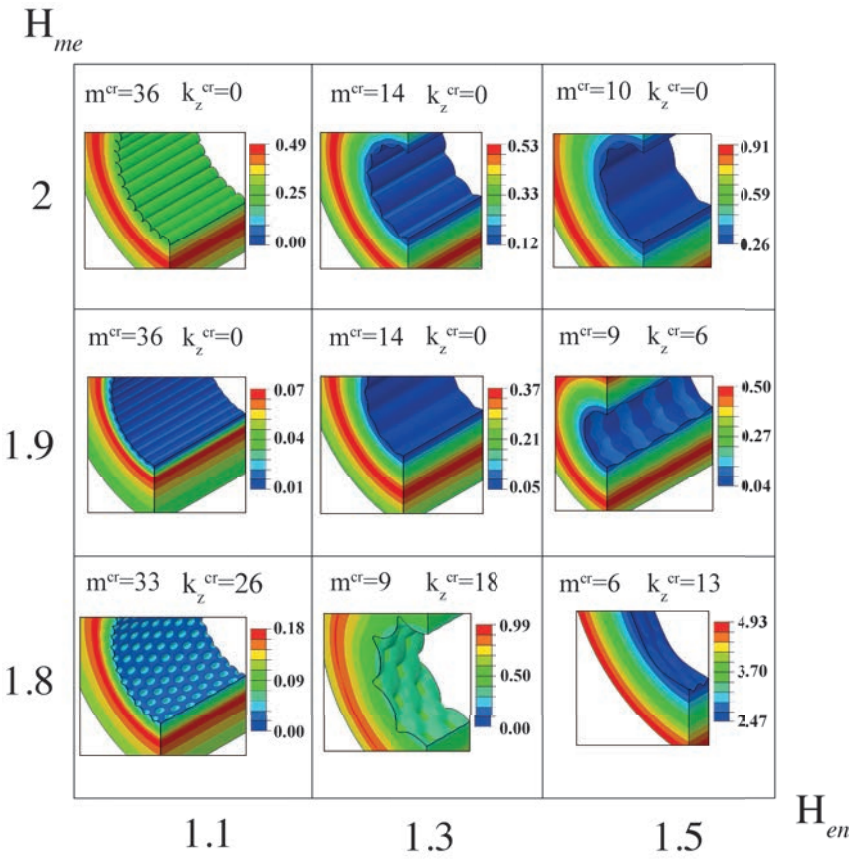

Figure 3.22: Phase diagrams in the (H_{en}, H_{me})-space at constant $\mu_{me}/\mu_{en} = 5$: Different instability patterns emerge during the numerical simulations, a one-dimensional circumferential pattern for $m^{cr} > 0$, and $k_z^{cr} = 0$ and a two-dimensional pattern for $m^{cr} > 0$ and $k_z^{cr} > 0$, where the colorbar indicates the value of the radial displacement.

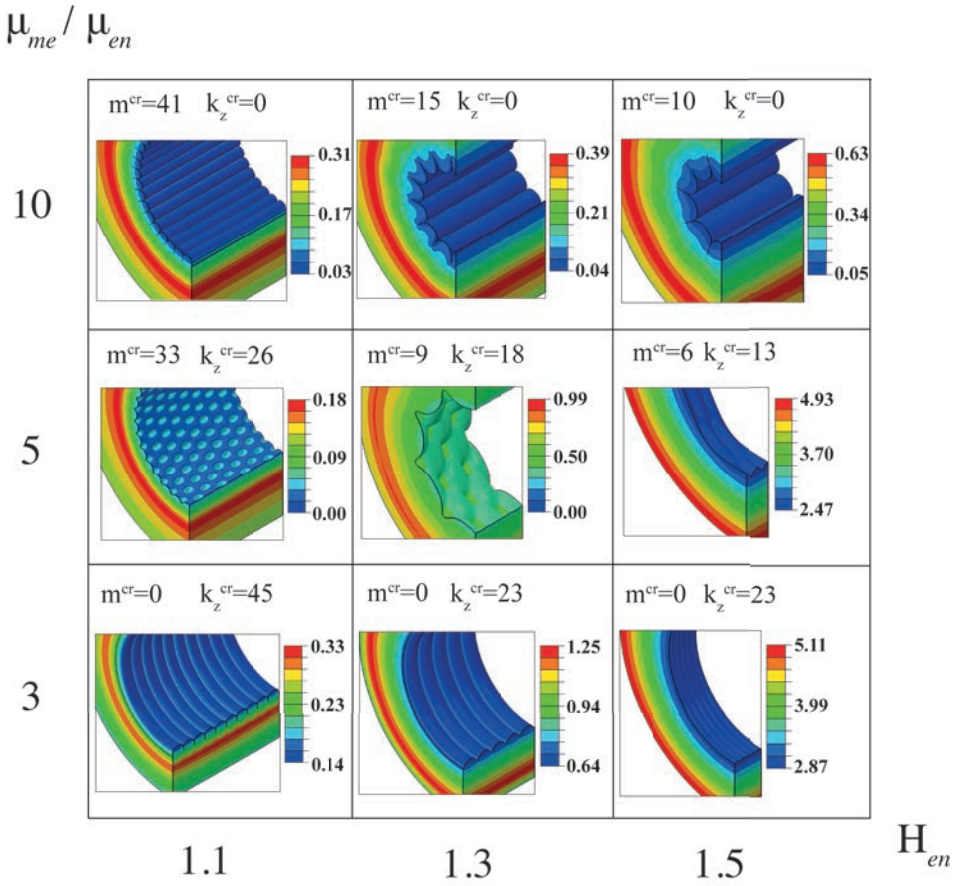

Figure 3.23: Phase diagrams in the $(H_{en}, \mu_{me}/\mu_{en})$-space at constant $H_{me} = 1.8$: Different instability patterns emerge during the numerical simulations, a one-dimensional circumferential pattern for $m^{cr} > 0$ and $k_z^{cr} = 0$, a one-dimensional longitudinal pattern for $m^{cr} = 0$ and $k_z^{cr} > 0$, and a two-dimensional pattern for $m^{cr} > 0$ and $k_z^{cr} > 0$. The colorbar indicates the value of the radial displacement.

ity pattern undergoes a transition from a one-dimensional to a two-dimensional mode in Figure 3.23. In particular, for high stiffness ratios μ_{me}/μ_{en} a circumferential pattern with $m^{cr} > 0$ and $k_z^{cr} = 0$ is selected, whereas for low stiffness ratios μ_{me}/μ_{en} a longitudinal pattern with $m^{cr} > 0$ and $k_z^{cr} = 0$ emerges. The region in which the shear moduli are of the same order is characterized by a two-dimensional pattern with $m^{cr} > 0$ and $k_z^{cr} > 0$. In the next section, the fully nonlinear evolution for each of these endodermal patterns is studied and the amplitude of the emerging surface undulations is investigated.

Case 1. One-dimensional circumferential pattern. Figure 3.24 shows the amplitudes ε_θ of the one-dimensional circumferential instability pattern, $k_z^{cr} = 0$, for varying growth factors g_{en}/g_{me}. The amplitude is normalized with respect to the average internal radius $\bar{r}_i$ such that $\varepsilon_\theta = (r_i^{max} - r_i^{min})/\bar{r}_i$, where $\bar{r}_i$ is the average of r_i for each growth multiplier g_{en}/g_{me} and r_i^{min} and r_i^{max} are the minimum and maximum radii among all the values calculated for the nodes on the inner surface. Before the critical point is reached (1), the simulations show a slow increase in the amplitude of the perturbation. The instability thresholds of Section 3.4.7 are marked with crosses in Figure 3.24. Beyond the critical point (2), the curves become steeper, reveal a fast increase in amplitude (3), then show a discontinuity which corresponds to the incipient formation of creases, whose width increases over increasing growth ratio (4-5).

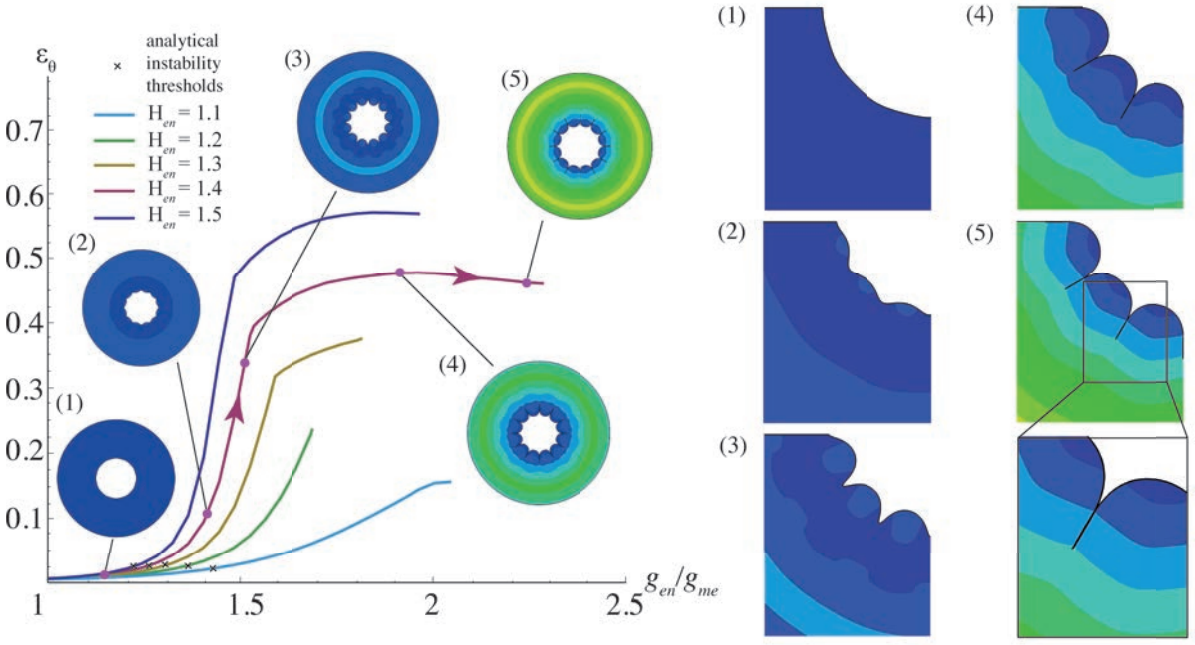

Figure 3.24: (left) Amplitudes ε_θ of the one-dimensional circumferential instability pattern, against the growth g_{en}/g_{me}. The curves are shown for constant $H_{me} = 1.8$ and $\mu_{me}/\mu_{en} = 10$ at varying $H_{en} = \{1.1, 1.2, 1.3, 1.4, 1.5\}$. (right) Zoomed views of the resulting patterns depicted in the snapshots (1-5), highlighting the creasing of the inner surface. The colorbar indicates the absolute value of the radial displacement.

Case 2. One-dimensional longitudinal pattern. Figure 3.25 illustrates the amplitudes ε_z of the one-dimensional longitudinal instability pattern for different thicknesses of the internal layer H_{en}. To calculate $\varepsilon_z = (r_i^{max} - r_i^{min})/\bar{r}_i$, the radii $\bar{r}_i$, r_i^{min}, and r_i^{max} are calculated among all nodes of the inner surface, at a fixed θ coordinate. Two characteristic trends can be observed, as depicted by the lines a and b in Figure 3.25, and the corresponding insets. Cylinders with a thinner inner layer, $H_{en} \leq 1.3$, undergo a steep increase in the amplitude of the perturbation (line a) after the critical point, with a discontinuity, which indicates the formation of creases. Conversely, cylinders with a thicker inner layer, $H_{en} > 1.3$ (line b), undergo an initial increase in the wrinkling perturbation, followed by a gradual decrease over increasing growth. Therefore, the endoderm surface is characterized by stable wrinkles.

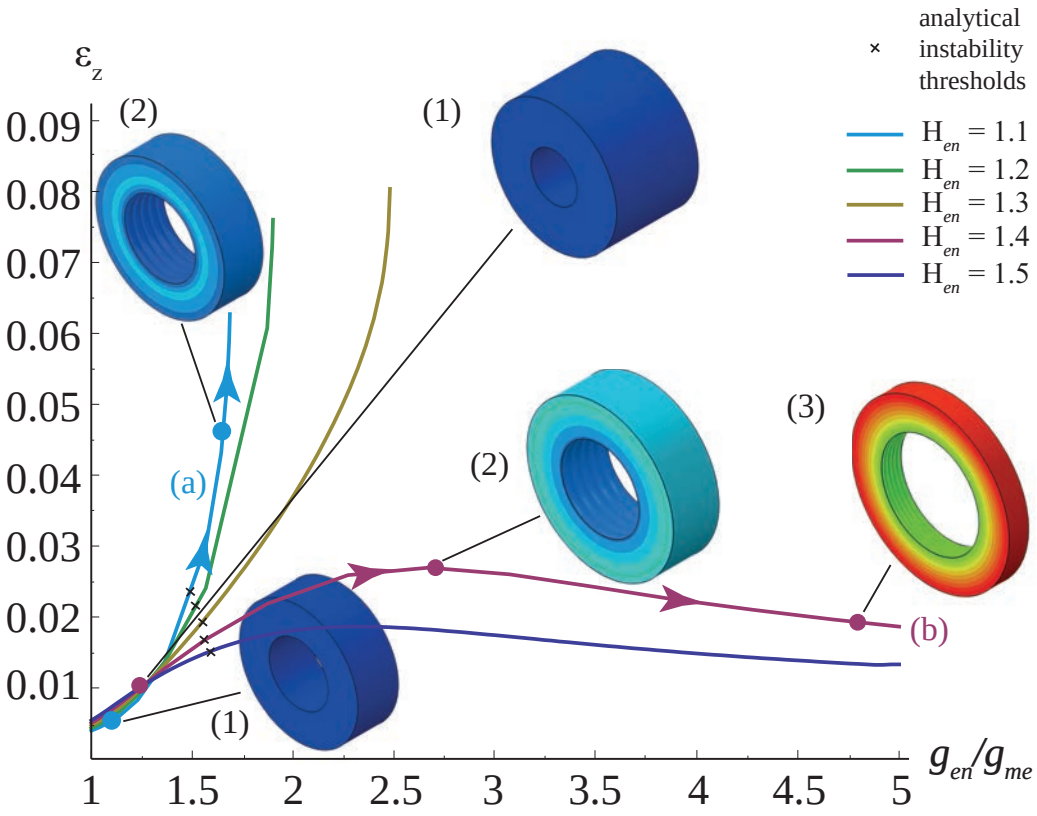

Figure 3.25: Amplitudes ε_z of the one-dimensional longitudinal instability pattern, against the growth g_{en}/g_{me}. The curves are shown for constant $H_{me} = 1.8$ and $\mu_{me}/\mu_{en} = 3$ at varying $H_{en} = \{1.1, 1.2, 1.3, 1.4, 1.5\}$.

Case 3. Two-dimensional pattern. Figure 3.26 depicts the amplitude of the two-dimensional instability pattern. In Figure 3.26, the value $\varepsilon_{2D} = (r_i^{max} - r_i^{min})/\bar{r}_i$ with $\bar{r}_i$, r_i^{min}, and r_i^{max} is evaluated among all nodes at the inner surface. Similar to the one-dimensional longitudinal pattern, the curves now display two different trends: cylinders with a thicker inner layer, $H_{en} > 1.4$, select stable wrinkles with an initially increasing amplitude later reaching a saturation value (line a), wheres cylinders with a thinner inner layer, $H_{en} \leq 1.4$, undergo a steep increase in the amplitude of the perturbation after the critical point, forming a creased surface. Moreover, both the circumferential ε_θ and the longitudinal ε_z amplitudes of the two-dimensional instability pattern have the same trend when plotted against the growth ratio g_{en}/g_{me}, as shown in Figure 3.27.

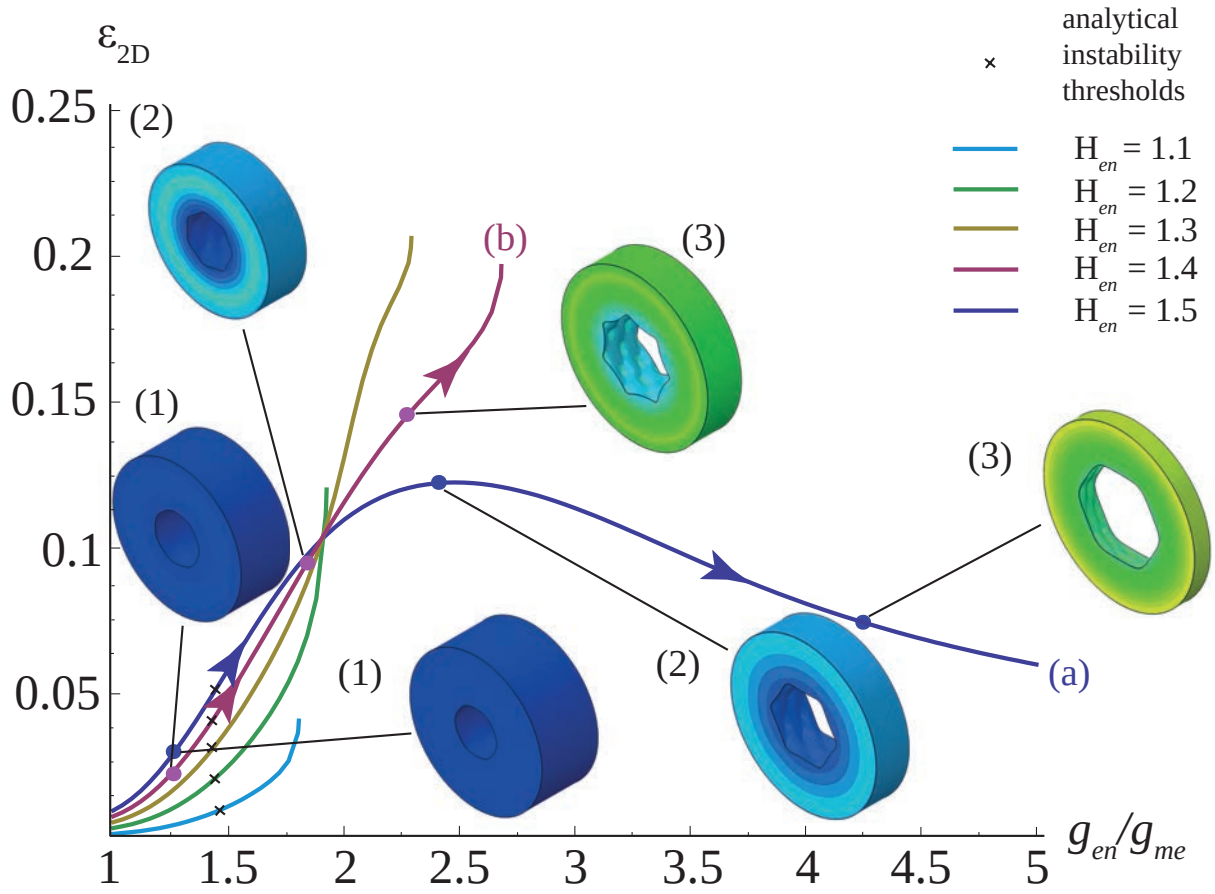

Figure 3.26: The amplitudes ε_{2D} of the two-dimensional instability pattern, against the growth g_{en}/g_{me}. The curves are shown for constant $H_{me} = 1.8$ and $\mu_{me}/\mu_{en} = 5$ at varying $H_{en} = \{1.1, 1.2, 1.3, 1.4, 1.5\}$.

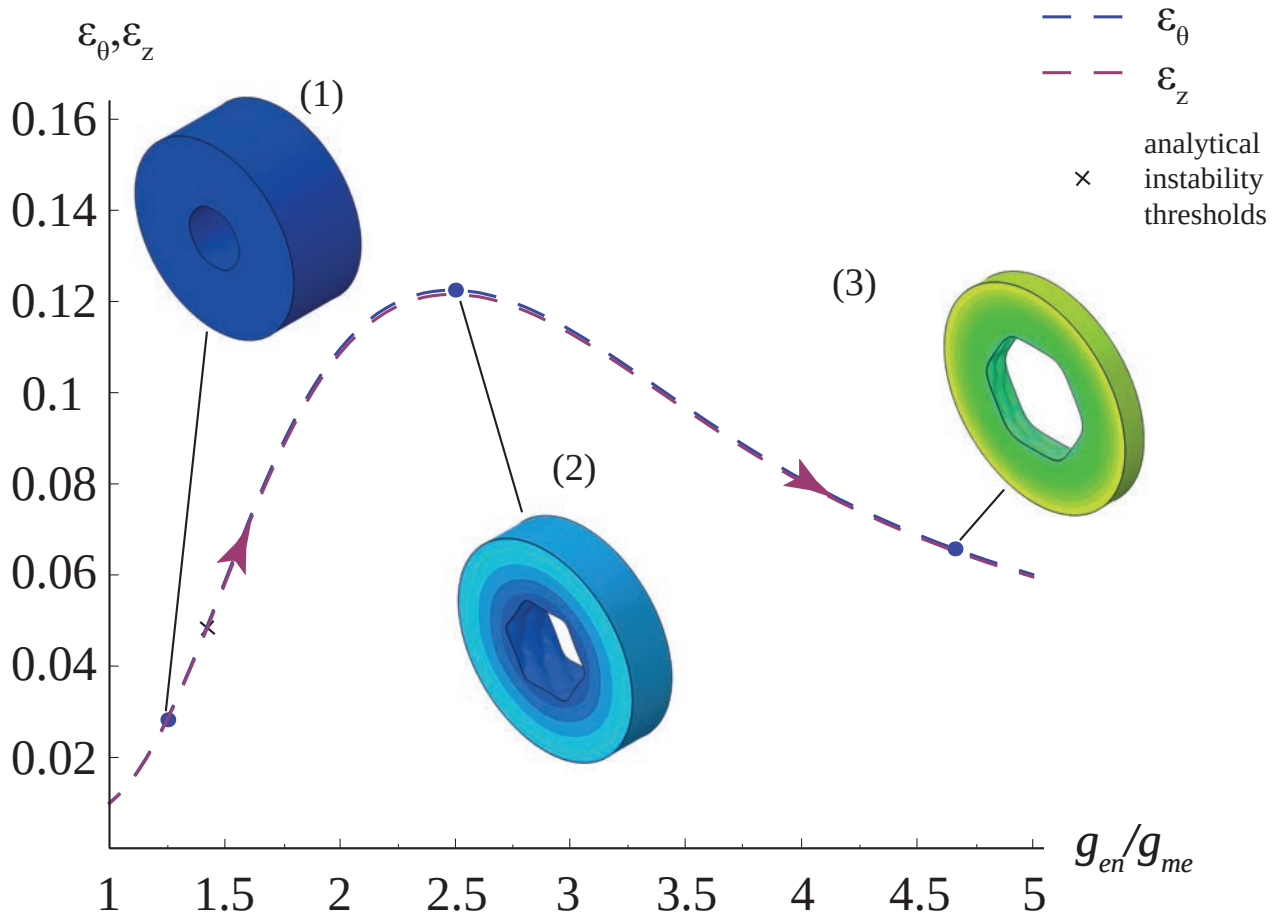

Figure 3.27: The two components ε_θ (blue) and ε_z (magenta) of the amplitude of the two-dimensional instability pattern, against the growth g_{en}/g_{me}. The curves are shown for $\mu_{me}/\mu_{en} = 5$, $H_{en} = 1.5$ at $H_{me} = 1.8$ (dotted).

3.4.9.3 Secondary bifurcations: wavelength doubling

The undulation wavelengths depicted in Figures 3.24, 3.25, and 3.26 remain unaltered for increasing values of g_{en}/g_{me}, so that the number of circumferential and longitudinal folds remains the same value selected by the linear stability analysis. Nonetheless, the numerical simulations highlight another possible scenario for the non-linear evolution of the instability.

In Figure 3.28, the instability initially begins with $m = 12$ and $n_z = 2$ as predicted by the analytical solution, but then, beyond the critical point $(g_{en}/g_{me})^{cr} = 1.44$, the number of longitudinal folds doubles. Therefore, a secondary transition from a square to

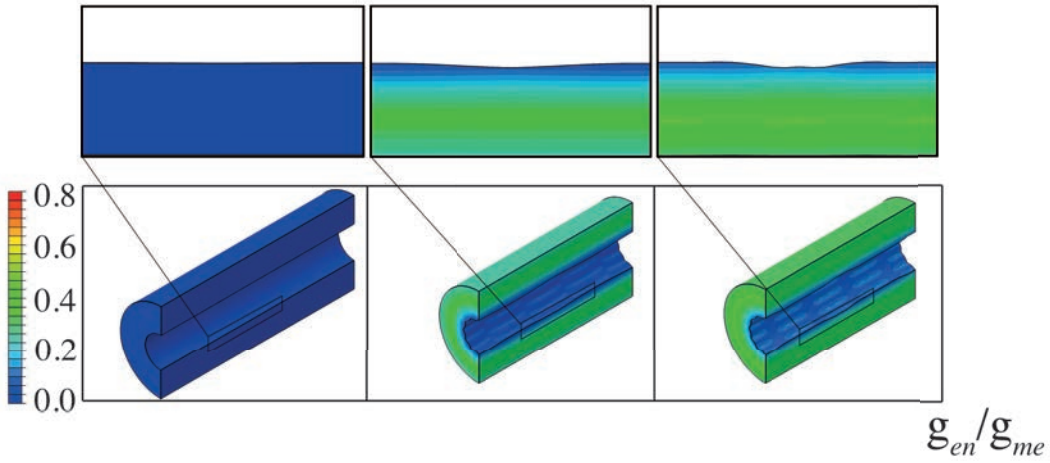

Figure 3.28: Wavelength doubling of the two-dimensional instability pattern, along the z-axes. The snapshots are taken at $g_{en}/g_{me} = \{1, 1.72, 1.81\}$ (left, middle, right), for $H_{en} = 1.35$, $H_{me} = 1.9$, and $\mu_{me}/\mu_{en} = 5$. The colorbar indicates the value of the radial displacement. The predicted critical growth ratio is $(g_{en}/g_{me})^{cr} = 1.44$.

a hexagonal surface pattern is observed far beyond the linear stability threshold. Such a wavelength doubling is very similar to the one observed for the wrinkling of a stiff elastic layer over a soft substrate [103], undergoing a secondary bifurcation driven by the subharmonic resonance. A similar behavior has also been found for the circumferential folding of core-shell soft cylinders [104].

3.4.10 Validation of the model with experimental data

The aim of this section is to discuss the theoretical predictions and the results from the numerical simulations in comparison with the few available data in the biological literature on GI embryogenesis.

From Figure 3.17, the morphoelastic model predicts the emergence of a circumferential pattern for embryonic GI tissues with thin epithelium and thick mesoderm. Conversely, a two-dimensional pattern is selected for tissues with similar aspect ratios of the layers. These results are in agreement with the experimental results from chick and mouse embryos reported in [90]. In fact, circumferential folds emerge around Day 8 after fertilization in chick embryos, which are characterized by a thin endoderm, whilst two-dimensional patterns first arise in mouse embryos. In Figure 3.29(a-b), the measurements of the area and external perimeter of the epithelium and mesenchyme of small and large intestine

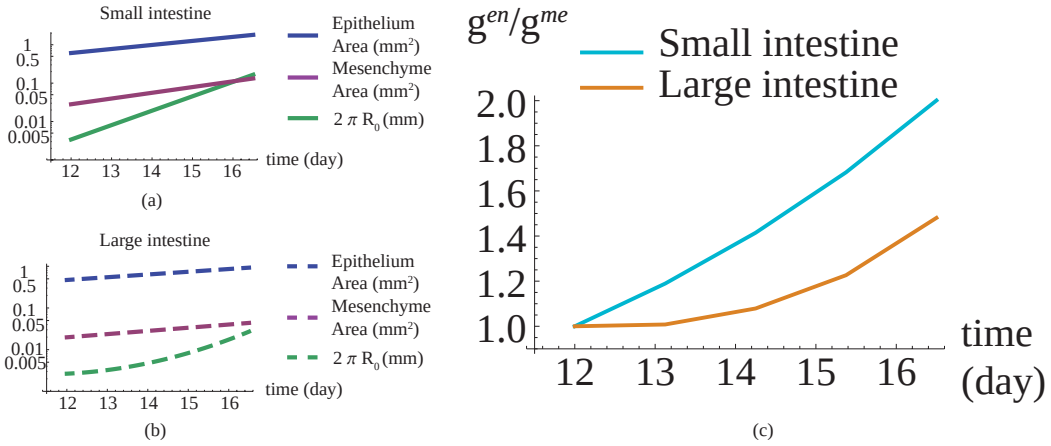

Figure 3.29: Experimentally measured geometries of embryonic mouse intestines: outer circumference (blue), mesoderm area (magenta) and endoderm area (green) in the duodenum (a) and in the large intestine (b) [9]. Analytically predicted values of volumetric growth ratios for the small intestine (cyan) and large intestine (orange) over the days after fertilization(c).

in mouse embryos are reported [9]. Assuming a stress free-configuration at the first day and an isotropic growth process, the corresponding growth ratios for the small and large intestine are calculated at different embryonic ages, as depicted in Figure 3.29(c). Our simulations indicate that the growth ratio for the small intestine is greater than the one for large intestine. In particular, a two-dimensional pattern arises in the small intestine between day $13-14$ after incubation at a growth factor $g_{en}/g_{me} = 1.2-1.4$. This value is in agreement with the analytical predictions in Figure 3.17 which predict the emergence of a two-dimensional pattern at a growth factor $g_{en}/g_{me} = 1.4$, for an initial geometry with $H_{en} = 1.4, H_{me} = 2$.

Geometrical parameter	Jejunum	Ileum	asc. colon	desc. colon
Endoderm (mucosa)	208 μm	140 μm	155 μm	115 μm
Mesoderm (muscularis+serosa)	49 μm	53 μm	66 μm	64 μm
$2R_0$	1.5 mm	1 mm	1.26 mm	1.26 mm
H_{en}	1.42	1.45	1.38	1.25
H_{me}	2.13	1.11	1.13	1.11

Table 3.3: Geometrical parameters, thicknesses and diameter, of jejunum and ileum, ascending and descending colon, measured at the first trimester of gestation of a human fetus.

In Table 3.3, the geometrical measurements of the endodermal and mesodermal layers

in different segments of the small and large intestines in human embryos are reported from [105]. In the small intestine, where both the endoderm and the mesoderm are thick, villi start forming from a two-dimensional pattern, while in the colon, characterized by a very thin mesoderm, a longitudinal pattern is observed first. This is in agreement with the analytical results presented in Section 3.4.7.1, which predict the formation of longitudinal folds in the colon with a mesodermal aspect ratio in the range of $1.15 \leq H_{me} < 1.3$. In fact, the growth thresholds and the associated modes depicted in Figure 3.18 show that a longitudinal folding pattern is selected for tissues with thin mesodermal layer $H_{me} < 1.3$. Moreover, the results predict that intestines with a thicker endoderm have lower growth thresholds, which suggests that instabilities occur earlier in intestinal tissues with a thick endoderm. This finding is in qualitative agreement with the measurements, which showed that villi first form in the upper part of the duodenum where the epithelium is thicker respect to the epithelium of the other gut segments in a human fetus [89].

3.5 Concluding remarks

In this chapter, the morphoelastic theory presented in Chapter 2 has been applied in order to model the GI morphogenesis in different species of vertebrates. A first model has been proposed, where the GI tube has been modeled as a one layered cylinder, made of hyperelastic, incompressible and anisotropic tissue, i.e. the embryonic mucosa surrounded by a much stiffer composite of tissues. The theoretical model showed that the spatially constrained growth of the embryonic mucosa, could be the mechanism driving the early formation of the intestinal villi in mouse embryos. In fact, these functional structures arise from a two-dimensional undulated pattern, which the model has been able to reproduce. Nevertheless, the model didn't allow to predict the finite wavelength of the emerging instability pattern, thus a more complex model has been proposed. The GI tube has been modeled as a two-layered cylinder, made of two hyperelastic, incompressible and isotropic tissues: the two primary matrices from which the gut originates, i.e the inner endoderm and the outer stiffer mesoderm. Note that, since the mesoderm is considered stiffer than the endoderm, the limit case $\mu_{me}/\mu_{en} \to \infty$ corresponds to the one-layer model proposed in the first part of the chapter. The mechanisms driving the onset of the instability is thus the unconstrained differential growth between the primary layers. This model not only allows for investigating the onset of different mono-dimensional patterns such as the circumferential folding in chick small intestines and the longitudinal rings observed in

the human colon, but also the emergence of the two-dimensional network of folds which precedes the formation of the intestinal villi in mouse embryos. Moreover, the model highlights that the selection of this variety of patterns relies in the geometrical and mechanical factors, characterizing the GI embryonic tissues. With the aim of investigating the evolution of the established patterns as the growth proceeds, the problem has been implemented in Abaqus and the numerical simulations in the fully nonlinear regime have been performed. The numerical results have shown that the patterns can evolve, following different paths ranging from the formation of stable wrinkles to the emergence of creases. In some cases, even a dramatic wavelength doubling can occur. Furthermore, the numerical simulations highlighted that the geometry and the mechanical properties of the two embryonic layers are crucial in determining the post-buckling evolution of the instability pattern.

In conclusion, the few experimental data available in the literature have validated the proposed model and the hypothesis according to which the differential growth between the two embryonic layers could be the underlying mechanisms which drive the formation of the diverse structures in the GI tract of vertebrates.

Chapter 4

Helical buckling of pre-stressed tubular organs

Contents

In this chapter, the morphoelastic theory illustrated in Chapter 2 will be applied to another interesting biological problem: the helical buckling of pre-stressed tubular tissues. The study is motivated by the necessity of predicting dangerous phenomena, such as the obstruction of the blood vessels. Blood vessels and in particular arteries might be subjected to torsional loads during life. For example, rotation of the head exerts a torsion load on the carotids and on the vertebral artery at the level of the atlantoaxial joint [106]. The vertebral arteries are also subjected to twist when the back rotates. Torsional instabilities in blood vessels can induce an alteration of the blood flow and an increase of the resistance of the vessel to the blood flow. Eventually, those alterations can initiate ischemic episodes and may eventually be fatal [107]. Therefore, the study of torsional instabilities in tubular tissues is a topic of utmost interest.

An introduction to the anatomy and the mechanisms which are known to govern the functionality of the arteries is first presented. Then, the morphoelastic model will be formulated following the theory presented in Chapter 2, with the aim of providing a useful tool for the prediction of the occurrence of torsional instabilities in tubular organs.

4.1 Preliminary remarks

Before formulating the morphoelastic model, some useful concepts will be introduced. In particular, the main biological phenomena regulating the physiological state of arteries will be illustrated.

4.1.1 Introduction to the anatomy and the physiology of arteries

Blood vessels constitute the vast network ensuring blood circulation in vertebrates where arteries, veins and capillaries are the main components. Precisely, arteries and veins are the sites where the macro-circulation occurs. Arteries distribute the blood (reach of oxygen) from the heart to the organs and veins transport the blood (reach of carbon dioxide) back to the heart. Micro-circulation takes place in the capillaries which are the smallest blood vessels and are embedded in organs. They directly exchange oxygen

and carbon dioxide with organs [108].
As sketched in Figure 4.1, arteries are made of three layers, the tunica intima, media and adventitia. The innermost layer, the *tunica intima* is a thin sheet of epithelial cells.

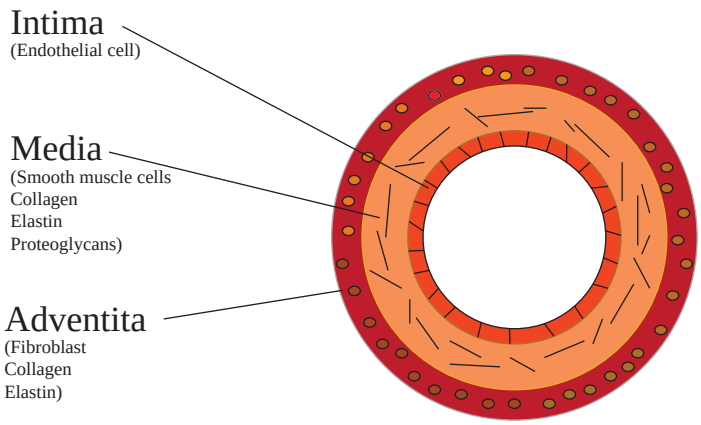

Figure 4.1: Multi-layered structure of the artery. The main components of the Tunica Intima, Media and Adventitia.

The *tunica media* is the middle layer and is made up of smooth muscle cells, few elastic layers, collagen and elastin fibrils. The outermost layer, the *tunica adventitia* contains collagen fibers, fibroblasts, ground substances and nerves. The structure of arteries varies depending on the distance from the heart. Big arteries such as the aorta have a diameter $>$ 10mm and their tunica media is mainly composed by elastic tissue, while small peripheral arteries (0.1–10mm) have a dominant muscular composition [74]. In the following the spectacular mechanism which is behind the ability of arteries to adapt in response to external stimuli, will be illustrated.

4.1.2 Principle of homeostasis

During the second half of the 19*th* Century, Claude Bernard coined the word *milieu intérieur* for describing the internal equilibrium state which characterizes all living organisms [109]. Later, Cannon extended the concept to the so-called **homeostasis principle** according to which living systems tend to maintain the internal equilibrium by cooperation of internal physiological processes [110]. Behind the homeostasis principle is the idea that a living tissue is in a physiological equilibrium steady-state. When it is perturbed from this state, it reacts by activating some internal processes aiming at restoring the original homeostatic state.

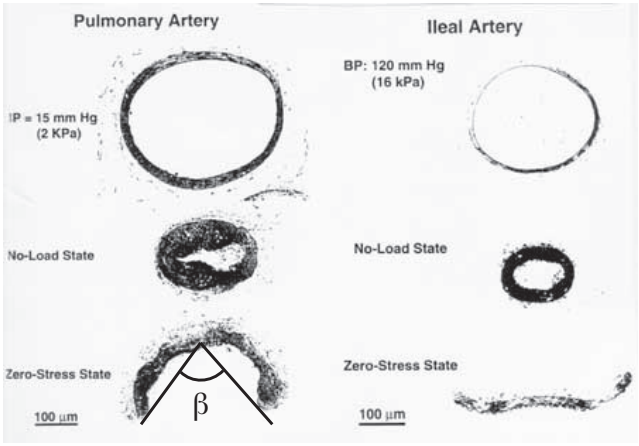

Figure 4.2: Loaded, unloaded and stress free state of pulmonary (left) and ileal (right) aorta in rats, from [10].

As all tissues exposed to mechanical cues, blood vessels are known to respond to changes in external mechanical factors, such as blood flow and pressure in order to maintain their own homeostatic state. Several hypotheses for a characterization of the homeostatic state in arteries have been proposed. According to Choung and Fung arteries adapt to external stimuli to reduce the transmural stress gradient [69]. Takamizawa et al. [111] proposed that arteries tend to maintain an optimal homeostatic state in which the tissue is characterized by a uniform circumferential strain. This is an optimal state in the sense that a uniform distribution of circumferential strain ensures a higher resistance to changes in loads. Recently, Destrade et al. proposed an extension of Takamizawa's and coworkers hypothesis, according to which arteries are in a state of *homogeneous transmural strain* under the physiological blood pressure [112]. In the following, this hypothesis will be adopted.

4.1.3 Residual stresses and stress-free state

Arteries adapt to external mechanical stimuli by growing and by reorganizing their internal architecture (remodeling). As discussed in Section 2.1.2, growth and remodeling might introduce incompatibilities in the tissue, and consequently residual stresses arise. In fact, experiments performed by Fung and co-workers [10, 33] have shown that, when removed from its anatomical environment and cut radially, a ring of artery strengthens and opens up into a cylindrical open sector, revealing the presence of residual stresses in the vessel, see Figure 4.2. The open sector, which is a stress-free natural state for the

tissue, is characterized by an opening angle β. Different values of β have been measured in arteries in physiological conditions and in those affected by hypertension (higher blood pressure), suggesting that the opening angle adjusts as a function of the internal blood pressure. Therefore, the residual stresses arising from the growth and remodeling must be taken into account when modeling torsional instabilities in arteries.

4.1.4 Remodeling process in arteries

From experiments it is known that the stress-free state of an artery is an open sector. Therefore, let $\mathcal{B}_0$ be the stress-free state where the artery is defined as an open sector (see Figure 4.3), so that the circumferential and longitudinal pre-stretches λ_θ (related to the

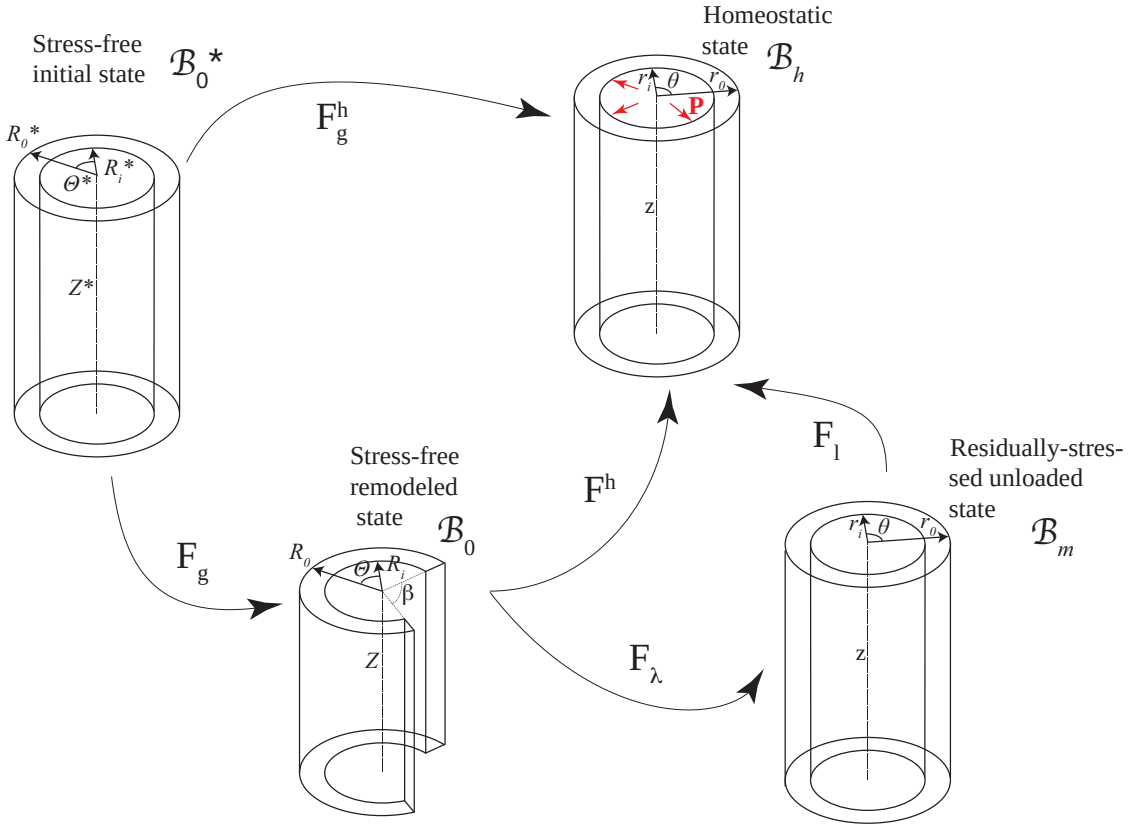

Figure 4.3: Schematic representation of the remodeling process in the artery: the initial hypothetical stress-free state $\mathcal{B}_0^*$, the stress-free remodeled state $\mathcal{B}_0$ associated to the pre-stretches $\lambda_\theta, \lambda_z$, the unloaded residually-stressed state $\mathcal{B}_m$ and the homeostatic state $\mathcal{B}_a$ where the artery is a remodeled residually-stressed cylinder subjected to the internal pressure P.

opening angle) and λ_z, respectively, are defined. The residual stresses completely depend on these two parameters. Precisely, they arise from the deformation which closes the open sector and squeezes/stretches it along its longitudinal axis into an intact unloaded residually-stressed cylinder. Let $\mathcal{B}_m$ be the unloaded residually-stress state of the artery, and χ_λ be the deformation mapping transforming the open sector into the intact cylinder in $\mathcal{B}_m$. Now, $\mathcal{B}_0$ is actually a *stress-free remodeled state*, defined by an upstream pure remodeling process which transforms the initial state $\mathcal{B}_0^*$, where the artery is a stress-free cylinder, into the geometrically incompatible open-sector. According to the approach based on the multiplicative decomposition, a tensor $\mathbf{F}_g$ (which depends on $\lambda_\theta, \lambda_z$) can be associated to the pure remodeling process. Furthermore, since during remodeling no change of mass occurs, it must be $\det \mathbf{F}_g = 1$.

Arteries are subjected to an internal pressure during their life. According to the homeostasis principle formulated in [112], $\lambda_\theta, \lambda_z$ adjust depending on the internal pressure so that the deformation $\boldsymbol{\chi}^h$ which closes and squeezes/stretches the open sector from $\mathcal{B}_0$ to the final homeostatic state (with an applied internal pressure) is homogeneous. Let $\mathcal{B}^h$ be the homeostatic state of the artery and $\mathbf{F}_h$ the gradient associated to the deformation $\boldsymbol{\chi}^h$, thus $\mathbf{F}_g^h = \mathbf{F}^h \mathbf{F}_g$.

As for the growth process, the characteristic time scale of remodeling is much bigger than the one associated to the elastic deformation and to the external loads. Therefore the considered problem is quasi-static and the dynamics which drive the remodeling from the initial state $\mathcal{B}_0^*$ to the remodeled stress-free state $\mathcal{B}_0$ can be neglected. In order to solve the elastic problem, it is essential to know the values of $\lambda_\theta, \lambda_z$ in the state $\mathcal{B}_0$, which can be easily determined from cutting experiments. According to the homeostasis principle, let $\mathcal{B}_0$ be a stationary state and let $\mathbf{F}_g^*$ and $\mathbf{F}_e^*$ be two tensors such that:

$$\dot{\mathbf{F}}_g = \mathcal{H}(\mathbf{F}_g^*, \mathbf{F}_e^*) \approx 0. \tag{4.1}$$

$\mathbf{F}_g^* = \mathbf{F}_g(t \gg \tau_g)$ and $\mathbf{F}_e^* = \mathbf{F}_e(t \gg \tau_g) = \mathbf{F}^h$ are the remodeling tensor depending on the pre-stretches $\lambda_\theta, \lambda_z$ and the homogeneous elastic deformation gradient, respectively. Consequently, following the hypothesis of homogeneous transmural strain, $\lambda_\theta, \lambda_z$ can be calculated as functions of the pressure and thus the state $\mathcal{B}_0$ is completely defined.

In the following, the morphoelastic model will be used to study torsional instabilities in pre-stressed cylinders. Three different cases will be considered, associated to three different loading scenarios: zero-traction boundary conditions, an applied internal pressure and an applied external pressure, respectively. The three considered cases covered a wide

range of biological applications. For example in the airways no pressure is acting on the surfaces, while due to the presence of surrounding tissues, the adult intestine is subjected to external pressure. Lastly, the case of internal pressure applies to the arteries. The remodeling process described above will be taken into account in all the three cases and the critical value of the torsion rate will be calculated at varying values of the pre-stretches $\lambda_\theta, \lambda_z$ in order to investigate the effects of residual stresses on the onset of torsional instabilities in hollow cylinders.

4.2 Kinematics of the elastic problem

Let $\mathcal{E} \subset \mathbb{R}^3$ be the three-dimensional Euclidean space, so that $\mathcal{B}_m, \mathcal{B}_a \subset \mathcal{E}$ are two regions occupied by a hollow circular cylinder in two different instants of time. A finite torsion rate γ is applied to the tube, which moves from the residually-stressed material configuration $\mathcal{B}_m$ to the spatial configuration $\mathcal{B}_a$. As illustrated in Section 4.1.4, let the

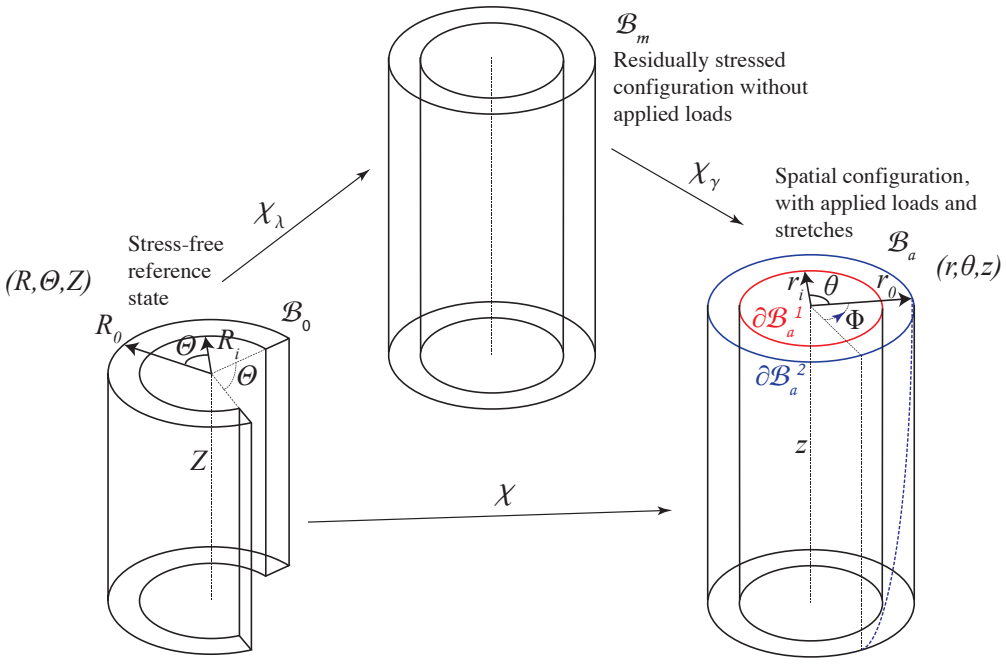

Figure 4.4: Schematic representation of the mapping $\boldsymbol{\chi}$: the component $\boldsymbol{\chi}_\lambda$ restores the geometrical compatibility mapping into the residually-stressed hollow cylinder in $\mathcal{B}_m$; while the component $\boldsymbol{\chi}_\gamma$ takes into account the finite torsion rate γ. $\Phi = \gamma\lambda_z Z$ is the twist angle associated to γ.

reference state $\mathcal{B}_0$ be identified by a cylindrical sector with:

$$R_i \leq R \leq R_0, \quad 0 \leq \Theta \leq 2\pi - \beta, \quad 0 \leq Z \leq L \tag{4.2}$$

where R_i and R_0 are the inner and outer radii, respectively, L is the axial length and $\beta < 2\pi$ is the initial opening angle, as depicted in Figure 4.4. Note that if β is negative there is an overlapping region in the reference state.
Setting the orthonormal bases $(\mathbf{E}_R, \mathbf{E}_\Theta, \mathbf{E}_Z)$ in $\mathcal{B}_0$ and $(\mathbf{e}_r, \mathbf{e}_\theta, \mathbf{e}_z)$ in $\mathcal{B}_a$, the mapping $\boldsymbol{\chi}$ which transforms the position $\mathbf{X}$ in $\mathcal{B}_0$ into its spatial counterpart $\mathbf{x}$ in $\mathcal{B}_a$ is defined as in Eq.(2.1). The mapping $\boldsymbol{\chi}$ can be split into two components as $\boldsymbol{\chi} = \boldsymbol{\chi}_\gamma \circ \boldsymbol{\chi}_\lambda$, where $\boldsymbol{\chi}_\lambda$ is the component which restores the geometrical compatibility of the tube, therefore associated with the definition of the circumferential and axial pre-stretches, and $\boldsymbol{\chi}_\gamma$ takes into account the application of a finite torsion rate, as shown in Figure 4.4.

Considering the cylindrical coordinate systems (r, θ, z) and (R, Θ, Z) in $\mathcal{B}_a$ and $\mathcal{B}_0$, respectively, the mapping $\boldsymbol{\chi}$ is defined using the following deformation fields:

$$\boldsymbol{\chi}(r, \theta, z) = \begin{cases} r(R, \Theta, Z) = r(R) \\ \theta(R, \Theta, Z) = \lambda_\theta \Theta + \lambda_z \gamma Z \\ z(R, \Theta, Z) = \lambda_z Z \end{cases} \tag{4.3}$$

where $r(R)$ is a scalar function of R, $\lambda_\theta = 2\pi/(2\pi - \beta)$ is the circumferential pre-stretch, depending on the initial angle β, and γ is the finite torsion rate. According to the definition in Eq.(2.2), the deformation gradient $\mathbf{F}$ associated to the mapping $\boldsymbol{\chi}$ is radially inhomogeneousin general and reads:

$$\mathbf{F} = \begin{pmatrix} \frac{\partial r(R)}{\partial R} & 0 & 0 \\ 0 & \dfrac{r}{R}\lambda_\theta & \lambda_z \gamma r \\ 0 & 0 & \lambda_z \end{pmatrix} \tag{4.4}$$

in the $\mathbf{e}_k \otimes \mathbf{E}_l$ basis, (l, k) spanning over $\{r, \theta, z\}$ and $\{R, \Theta, Z\}$, respectively. Furthermore, the kinematics of the elastic problem is completely defined by introducing the incompressibility constraint in Eq.(2.21) and imposing:

$$r(R) = \sqrt{\frac{R^2}{\lambda_z \lambda_\theta} + a}, \qquad \text{with} \quad a = r_\mathrm{i}^2 - R_\mathrm{i}^2/(\lambda_\mathrm{z}\lambda_\theta). \tag{4.5}$$

Using equation (4.4), the left Cauchy-Green tensor $\mathbf{B} = \mathbf{F}\mathbf{F}^T$ reads:

$$\mathbf{B} = \begin{pmatrix} \left(\dfrac{R}{r\lambda_z\lambda_\theta}\right)^2 & 0 & 0 \\ 0 & \left(\dfrac{r}{R}\lambda_\theta\right)^2 + (\lambda_z\gamma r)^2 & \lambda_z^2\gamma r \\ 0 & \lambda_z^2\gamma r & \lambda_z^2 \end{pmatrix} \tag{4.6}$$

in the $\mathbf{e}_h \otimes \mathbf{e}_k$ basis, (h, k) spanning over $\{r, \theta, z\}$. As shown by Ogden [76], the Eulerian principal axes associated to the deformation in equation (4.3) have the following unit vectors:

$$\mathbf{e}_1 = \mathbf{e}_r, \quad \mathbf{e}_2 = \mathbf{e}_\theta \cos\phi - \mathbf{e}_z \sin\phi, \quad \mathbf{e}_3 = \mathbf{e}_\theta \sin\phi + \mathbf{e}_z \cos\phi, \tag{4.7}$$

where ϕ identifies the rotation angle of the principal vectors $\mathbf{e}_2$ and $\mathbf{e}_3$ with respect to $\mathbf{e}_\theta$ and $\mathbf{e}_z$. The corresponding principal stretches λ_1, λ_2 and λ_3 can be calculated by diagonalizing $\mathbf{B}$ as follows:

$$\mathbf{Q}^T\mathbf{B}\mathbf{Q} = \mathbf{V}^2 = \mathrm{diag}(\lambda_1^2, \lambda_2^2, \lambda_3^2) \tag{4.8}$$

where $\mathbf{Q}$ is the rotation matrix associated to the change of basis in equation (4.7), diag indicates a diagonal matrix and $\mathbf{V}$ is the unique, positive-definite spatial stretch tensor arising from the polar decomposition of the deformation gradient. It follows that the principal stretch associated to the principal axis $\mathbf{e}_1$ is $\lambda_1 = \dfrac{R}{r\lambda_z\lambda_\theta}$, while the two other principal stretches are related by:

$$\begin{cases} \lambda_2^2 + \lambda_3^2 = \lambda_\theta^2 \dfrac{r^2}{R^2} + \lambda_z^2\gamma^2 r^2 + \lambda_z^2 \\ \lambda_2\lambda_3 = \dfrac{\lambda_z\lambda_\theta r}{R} \end{cases} \tag{4.9}$$

with:

$$\tan(2\phi) = \frac{2\lambda_z^2\gamma r}{\lambda_2^2 + \lambda_3^2 - 2\lambda_z^2}, \tag{4.10}$$

which is valid within the range $0 \leqslant \phi < \pi/4$.
With the final aim of applying the model to soft tubular tissues, the constitutive equations for the cylinder will be introduced in the following section.

4.3 Constitutive equations

As first proposed by Ogden et al. [113] and later adopted by Destrade et al. [112], it is assumed here that the mechanical behavior of the vessel is mainly driven by the tunica media layer, being mostly constituted by rubber-like elastin, collagen and smooth muscle cells. Therefore, the cylinder is modeled as a hyperelastic, incompressible and isotropic material. Moreover, a neo-Hookean model for the strain energy function ψ is assumed:

$$\psi = \frac{\mu}{2}(\mathrm{tr}\,\mathbf{C} - 3), \tag{4.11}$$

where μ is the shear modulus, and tr is the trace operator and $\mathbf{C} = \mathbf{F}^T\mathbf{F}$ is the right Cauchy-Green tensor. From Eq.(4.11), the constitutive relations defined in Eqs.(2.65) and (2.66) for the nominal stress $\mathbf{S}$ and the Cauchy stress $\boldsymbol{\sigma}$ respectively, can be written:

$$\mathbf{S} = \mu\mathbf{F}^T - p\mathbf{F}^{-1} \tag{4.12}$$

$$\boldsymbol{\sigma} = \mu\mathbf{B} - p\mathbf{I}. \tag{4.13}$$

Using Eqs.(4.6, 4.13), the non-null components of the Cauchy stress tensor read:

$$\begin{cases} \sigma_{rr}(r) = \mu B_{rr} - p = \mu\dfrac{(r^2 - a)}{r^2\lambda_\theta\lambda_z} - p \\ \sigma_{\theta\theta}(r) = \mu B_{\theta\theta} - p = \mu\left(\dfrac{r^2\lambda_\theta}{\lambda_z(r^2 - a)} + \lambda_z\gamma r\right) - p \\ \sigma_{\theta z}(r) = \sigma_{z\theta}(r) = \mu B_{\theta z} = \mu\lambda_z^2\gamma r \\ \sigma_{zz}(r) = \mu B_{zz} - p = \mu\lambda_z^2 - p. \end{cases} \tag{4.14}$$

It is useful to recall that, as first reported by Rivlin [114], the finite torsion of the pre-stretched cylinder can be obtained by applying surface tractions alone at the end surfaces:

$$N_\gamma = 2\pi\int_{r_i}^{r_0}\sigma_{zz}r dr; \qquad M_\gamma = 2\pi\int_{r_i}^{r_0}\sigma_{z\theta}r^2 dr \tag{4.15}$$

where N_γ is the normal force and M_γ is the torque, whose values depend on the applied boundary conditions.
In the following, the governing equations for the elastic problem will be derived and the basic solutions calculated in the three load scenarios considered.

4.4 Governing equations and basic axial-symmetric solutions

The elastic problem is governed by Eqs.(2.78) and (2.79) with Neumann boundary conditions which, according to Eqs.(2.42), write in the general form:

$$\begin{cases} \boldsymbol{\sigma}\mathbf{n} = C_1\mathbf{n} & \text{on} \quad \partial\mathcal{B}_a^1 = \{r : r = r_i\} \\ \boldsymbol{\sigma}\mathbf{n} = C_2\mathbf{n} & \text{on} \quad \partial\mathcal{B}_a^2 = \{r : r = r_0\} \end{cases} \tag{4.16}$$

where $\mathbf{n}$ is the spatial outer normal unit vector on the surface and C_1, C_2 are two scalar values describing the presence of traction loads. As depicted in Figure 4.5, three sets of

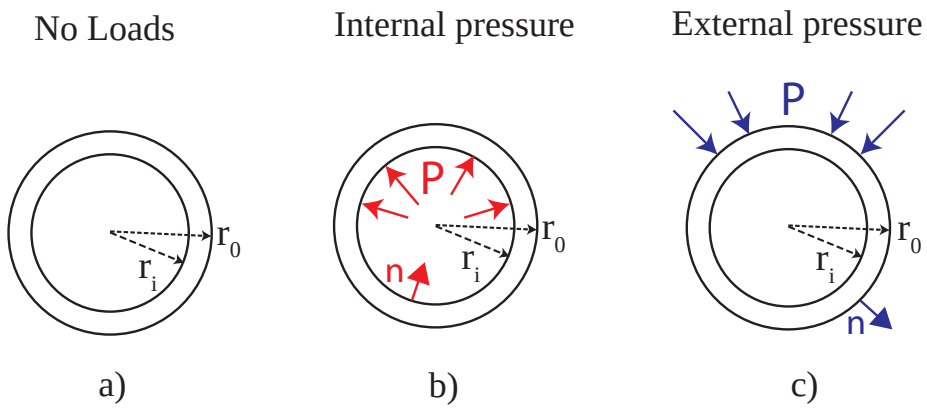

Figure 4.5: Three different boundary conditions are considered: the hollow cylinder (a) is stress-free at both surfaces, a pressure P is applied (b) at the internal surface or (c) at the external surface.

boundary conditions will be investigated in the following:

(a) no traction loads on the internal and external surfaces;

(b) a pressure of magnitude P acting on the internal surface $\partial\mathcal{B}_a^1$.

(c) a pressure of magnitude P acting on the external surface $\partial\mathcal{B}_a^2$;

whose corresponding values of the constants C_1, C_2 are collected in Table 4.1.
Therefore, substituting Eq.(4.4) with Eq.(4.3) into Eqs.(2.78) and (2.79), the governing

	on $r = r_i$	on $r = r_0$
(a) No loads	$C_1 = 0$	$C_2 = 0$
(b) Internal pressure	$C_1 = -P$	$C_2 = 0$
(c) External pressure	$C_1 = 0$	$C_2 = -P$

Table 4.1: Scalar values C_1, C_2 in equation (4.16), defining the boundary conditions of Eq.(2.78), for the three loading scenarios shown in Figure 4.5.

equations reduce to:

$$\frac{d\sigma_{rr}(r)}{dr} + \frac{1}{r}(\sigma_{rr}(r) - \sigma_{\theta\theta}(r)) = 0 \quad \text{in} \quad \mathcal{B}_a \tag{4.17}$$

$$\frac{r\, r_{,R}}{R}\lambda_\theta\lambda_z = 1 \quad \text{in} \quad \mathcal{B}_a \tag{4.18}$$

with boundary conditions in Eq.(4.16).
As discussed by Hoger [115] the distribution of residual stresses inside the material will depend on the shape of the body. According to the assumption that the pre-stretches calibrate with the pressure loads, the residual stresses will also depend on the boundary conditions, which fix the Lagrange multiplier p. Therefore, the basic solution of the elastic problem expressed by in Eqs.(4.16,4.17,4.18) is calculated for each of the three cases under consideration.

4.4.1 Case (a): stress-free internal and external surfaces

First, the basic axial-symmetric solution is derived when no traction loads are applied on both the external and the internal surfaces of the cylindrical tube. In this case, the boundary conditions in Eqs.(4.16) reduce to:

$$\begin{cases} \sigma_{rr}(r_i) = 0 \\ \sigma_{rr}(r_0) = 0 \end{cases} \tag{4.19}$$

The basic position vector $\mathbf{x}^{(0)}$ is identified by the inhomogeneous basic deformation in Eq.(4.3), with $r(R)$ defined as in Eq.(4.5). Substituting Eqs.(4.14) into Eq.(4.17), it follows that:

$$\int_{r_i}^{r_0} \frac{B_{rr}(r) - B_{\theta\theta}(r)}{r} dr = 0, \tag{4.20}$$

where the boundary conditions in Eq.(4.19) have been used. Now, the relation between the deformed external and internal radii is given by the global incompressibility constraint in Eq.(4.18), reading here as:

$$r_0 = \sqrt{\frac{R_0^2 - R_i^2}{\lambda_z \lambda_\theta} + r_i^2}. \tag{4.21}$$

By substituting r_0 from Eq.(4.21) into Eq.(4.20), it follows that:

$$\begin{aligned} &\frac{1}{H^2\lambda_\theta^2}\left(\frac{1}{r_i^2\lambda_z} - \gamma^2(H^2-1)\lambda_\theta\lambda_z^2 - \frac{H^4\lambda_\theta}{H^2 + H^2 r_i^2\lambda_\theta\lambda_z - 1}\right) + \\ &-2\lambda_\theta \log[H] + \frac{1}{\lambda_\theta}\log\left[1 + \frac{H^2-1}{H^2 r_i^2 \lambda_\theta \lambda_z}\right] = 0, \end{aligned} \tag{4.22}$$

where $H = R_0/R_i$ is the initial aspect ratio. Eq.(4.22) defines an implicit relation to derive the deformed internal radius r_i, and, consequently, r_0 from Eq.(4.21), given the initial geometry of the hollow tube H, the axial and circumferential pre-stretches $\lambda_\theta, \lambda_z$ and the finite torsion rate γ. The variation of r_i and r_0 with the initial aspect ratio is depicted in Figure 4.6 (left), showing the curves obtained by numerically solving, for a given choice of β, λ_z and γ, Eqs.(4.21, 4.22) using the software Mathematica [100]. Finally, the Lagrange multiplier p can be easily calculated from Eq.(4.17), using Eq.(4.21), and

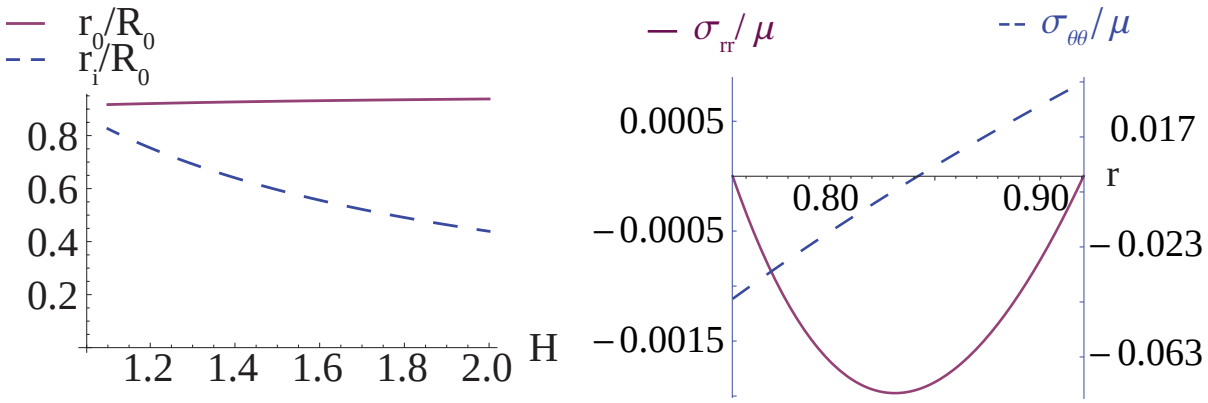

Figure 4.6: External and internal radii, r_0 (thick) and r_i (dashed), respectively, plotted against the initial aspect ratio $H = R_0/R_i$ (left); and Cauchy stress components σ_{rr} (thick) and $\sigma_{\theta\theta}$ (dashed) within a tube with initial aspect ratio $H = 1.2$ (right). The curves are obtained setting $\beta = \pi/6$, $\lambda_z = 1$, and $\gamma = 0.15$, for traction-free internal and external surfaces.

reads:

$$p = \mu B_{rr}(r) + \mu \int_r^{r_0} \frac{B_{rr}(s) - B_{\theta\theta}(s)}{s} ds, \tag{4.23}$$

which allows to calculate the distributions of the Cauchy stress components inside the tube. In Figure 4.6 (right) the distribution of the radial and circumferential components of the Cauchy stress are depicted as functions of the radius. The circumferential stress is compressive at the internal radius and tensile at the external radius, while the radial component is always compressive across the layer and it vanishes at the internal and external surfaces for the boundary conditions.

4.4.2 Case (b): Pressure load P at the internal surface

The aim of this section is to calculate the basic solution to Eqs.(4.17,4.18) when a pressure P acts on the internal surface of the cylindrical tube. Precisely, this case applies to the problem of an artery, which underwent a prior remodeling process under the effect of the internal pressure P and is now twisted. The boundary conditions in Eqs.(4.16) read:

$$\begin{cases} \sigma_{rr}(r_i) = -P \\ \sigma_{rr}(r_0) = 0. \end{cases} \tag{4.24}$$

According to the homeostasis principle, the residual strains arise in response to the applied pressure P in order to provide an optimal material behavior of the artery. Therefore, as illustrated in Section 4.1.4, in the absence of a torsion rate it is assumed that the tube undergoes a homogeneous deformation when a pressure P is applied on the external surface of the cylinder. Let the homogeneous deformation be in the following form:

$$r^h(R,\Theta,Z) = \frac{R}{\sqrt{\lambda_z \lambda_\theta}}; \quad \theta^h(R,\Theta,Z) = \lambda_\theta \Theta; \quad z^h(R,\Theta,Z) = \lambda_z Z. \tag{4.25}$$

The associated homogeneous deformation gradient writes:

$$\mathbf{F}^h = \mathrm{diag}\left(\frac{1}{\sqrt{\lambda_z \lambda_\theta}}, \sqrt{\frac{\lambda_\theta}{\lambda_z}}, \lambda_z \right). \tag{4.26}$$

The Cauchy stress related to the homogeneous deformation in Eq.(4.26) is calculated by substituting Eq.(4.26) into Eq.(4.13) and reads $\boldsymbol{\sigma}^h = \mathbf{B}^h - p^h \mathbf{I}$, where $\mathbf{B}^h = \mathbf{F}^h (\mathbf{F}^h)^T$. Its

components write:

$$\begin{cases} \sigma_{rr}(r) = \mu B^h_{rr} - p^h = \mu \dfrac{1}{\lambda_\theta \lambda_z} - p^h \\ \sigma_{\theta\theta}(r) = \mu B^h_{\theta\theta} - p^h = \mu \dfrac{\lambda_\theta}{\lambda_z} - p^h \\ \sigma_{zz}(r) = \mu B^h_{zz} - p^h = \mu \lambda_z^2 - p^h. \end{cases} \tag{4.27}$$

The relation between P and the pre-strains can now be calculated by substituting Eq.(4.27) into Eq.(4.17) and writes:

$$P = -\int_{r_i^h}^{r_0^h} \frac{{F^h_{rr}}^2(r) - {F^h_{\theta\theta}}^2(r)}{r} dr = \frac{(-1+\lambda_\theta^2)\mu \ln[H]}{\lambda_\theta \lambda_z}, \tag{4.28}$$

where $r_0^h = \dfrac{R_0}{\sqrt{\lambda_z \lambda_\theta}}$ and $r_i^h = \dfrac{R_i}{\sqrt{\lambda_z \lambda_\theta}}$. Eq.(4.28) corresponds to the pressure calculated by Destrade et al. in their Eq.(3.5) [112].

Finally, the basic position vector $\mathbf{x}^{(0)}$ is identified by the inhomogeneous basic deformation in Eq.(4.3), with $r(R)$ defined as in Eq.(4.5), thus the Lagrange multiplier p in Eqs.4.14 is obtained by solving the equilibrium equation (4.17) with boundary conditions in Eq.(4.24) where P is given by Eq.(4.28), being:

$$p = \mu B_{rr}(r) + \mu \int_{r_i}^{r} \frac{B_{rr}(r) - B_{\theta\theta}(r)}{r} dr + \frac{(-1+\lambda_\theta^2)\mu \ln[H]}{\lambda_\theta \lambda_z}. \tag{4.29}$$

The deformed internal radius r_i is calculated from Eqs.(4.17,4.24) by substituting Eqs.(4.14) and Eq.(4.28). The radial and circumferential components of the Cauchy stress for the case (b) are depicted in Figure 4.7 (left).

4.4.3 Case (c): Pressure load P at the external surface

Lastly, the case of a pressure load P applied on the external surface of the cylindrical tube is considered. In this case the boundary conditions in Eqs.(4.16) take the following form:

$$\begin{cases} \sigma_{rr}(r_i) = 0 \\ \sigma_{rr}(r_0) = -P \end{cases} \tag{4.30}$$

As done for the case b), the boundary conditions allow to derive an analytical relationship between the external pressure P and the pre-strains inside the tube:

$$P = \mu \int_{r_i}^{r_0} \frac{{F_{rr}^h}^2(r) - {F_{\theta\theta}^h}^2(r)}{r} dr = -\frac{(-1+\lambda_\theta^2)\mu \ln[H]}{\lambda_\theta \lambda_z}, \tag{4.31}$$

The Lagrange multiplier p in Eqs.4.14 can be calculated from Eq.(4.17), using the basic inhomogeneous deformation in Eq.(4.3), as follows:

$$p = \mu B_{rr}(r) - \mu \int_{r}^{r_0} \frac{B_{rr}(r) - B_{\theta\theta}(r)}{r} dr - \frac{(-1+\lambda_\theta^2)\mu \ln[H]}{\lambda_\theta \lambda_z}, \tag{4.32}$$

where r_0 is given by Eq.(4.21). As in the previous case, the internal radius r_i is implicitly calculated from the boundary conditions in Eqs.(4.30), using Eqs.(4.14, 4.17). The variations of the radial and circumferential components of the Cauchy stress with r are depicted in Figure 4.7 (right). For the given pre-stretches, the resulting circumferential stresses have the same sign for both cases. Moreover, the radial stress is tensile across the layer in the case (c), whilst it is compressive in the case (b).

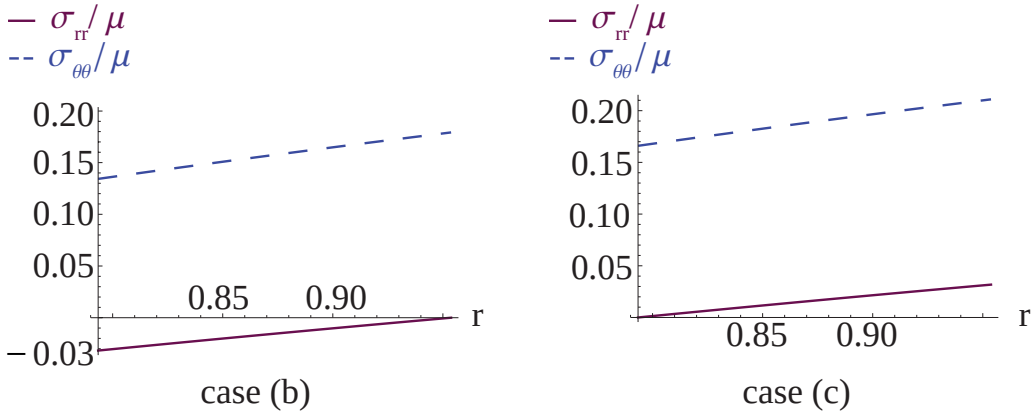

Figure 4.7: Cauchy stress components σ_{rr} (thick) and $\sigma_{\theta\theta}$ (dashed) within a tube with initial aspect ratio $H = 1.2$. The curves are obtained setting $\beta = \pi/6$, $\lambda_z = 1$, and $\gamma = 0.15$, when a pressure is applied at the internal (left) and external (right) surface.

In the following section, the linear stability analysis of the basic axial-symmetric elastic solutions will be performed in order to study the onset of torsional instabilities for the hollow cylinder in the three cases considered. The method of incremental deformations superposed on finite deformations presented in Section 2.2 will be used.

4.5 Incremental boundary value problem

Let the basic position $\mathbf{x}^{(0)}$ be perturbed superposing to the finite basic deformation in Eq.(4.3) an incremental deformation $\boldsymbol{\chi}^{(1)}$ in the following form:

$$\boldsymbol{\chi}^{(1)}(r,\theta,z) = u(r,\theta,z)\mathbf{e}_r + v(r,\theta,z)\mathbf{e}_\theta + w(r,\theta,z)\mathbf{e}_z \tag{4.33}$$

where u, v, w are three incremental displacement fields. The displacement gradient $\boldsymbol{\Gamma}$, associated to the incremental deformation has the form:

$$\boldsymbol{\Gamma} = \begin{pmatrix} u_{,r} & (u_{,\theta} - v)/r & u_{,z} \\ v_{,r} & (v_{,\theta} + u)/r & v_{,z} \\ w_{,r} & (v_{,\theta})/r & w_{,z} \end{pmatrix}, \tag{4.34}$$

According to the theory presented in Section 2.2, the perturbed deformation gradient $\bar{\mathbf{F}}$ rewrites in the form of Eq.(2.86) and the perturbed Nominal stress $\bar{\mathbf{S}}$ in the form of Eq.(2.88). The first-order increment $\hat{\mathbf{S}}$ of the Nominal stress tensor $\mathbf{S}$ is in the form of Eq.(2.89) and its push forward $\hat{\mathbf{S}}_0 = \mathbf{F}\hat{\mathbf{S}}$ is given by Eq.(2.92) and writes:

$$\hat{\mathbf{S}}_0 = \boldsymbol{\mathcal{A}}_0^1 \boldsymbol{\Gamma} + p\boldsymbol{\Gamma} - q\mathbf{I}. \tag{4.35}$$

where $\boldsymbol{\mathcal{A}}_0^1$ is the instantaneous moduli, defined in Eq.(2.93), p is the Lagrange multiplier and q its first-order increment.
The **incremental BVP** writes:

$$\operatorname{div}\hat{\mathbf{S}}_0 = \mathbf{0} \qquad \text{in} \quad \mathcal{B}_a \tag{4.36}$$

$$\operatorname{tr}\boldsymbol{\Gamma} = 0 \qquad \text{in} \quad \mathcal{B}_a \tag{4.37}$$

$$\hat{\mathbf{S}}_0^T\mathbf{n} = \delta C_1\mathbf{n} - C_1\boldsymbol{\Gamma}^T\mathbf{n} \qquad \text{at} \quad r = r_i \tag{4.38}$$

$$\hat{\mathbf{S}}_0^T\mathbf{n} = \delta C_2\mathbf{n} - C_2\boldsymbol{\Gamma}^T\mathbf{n} \qquad \text{at} \quad r = r_0 \tag{4.39}$$

where $\hat{\mathbf{S}}_0$ is given by equation (4.35) and $\delta C_1, \delta C_2$ are the increments of the boundary values C_1, C_2, respectively.

In summary, the bulk equations of the incremental BVP are given by a system of four PDEs, i.e. the three incremental equilibrium equations in Eqs.(4.36), and the first-order increment of the incompressibility constraint in Eq.(4.37), together with the increment of

the boundary conditions in Eqs.(4.38,4.39), which read in components:

$$\frac{\partial(r\hat{S}_{0rr})}{\partial r}+\frac{\partial\hat{S}_{0\theta r}}{\partial\theta}+r\frac{\partial\hat{S}_{0zr}}{\partial z}-\hat{S}_{0\theta\theta}=0 \qquad \text{in } \mathcal{B}_a \tag{4.40}$$

$$\frac{\partial(r\hat{S}_{0r\theta})}{\partial r}+\frac{\partial\hat{S}_{0\theta\theta}}{\partial\theta}+r\frac{\partial\hat{S}_{0z\theta}}{\partial z}+\hat{S}_{0\theta r}=0 \qquad \text{in } \mathcal{B}_a \tag{4.41}$$

$$\frac{\partial(r\hat{S}_{0rz})}{\partial r}+\frac{\partial\hat{S}_{0\theta z}}{\partial\theta}+r\frac{\partial\hat{S}_{0zz}}{\partial z}=0 \qquad \text{in } \mathcal{B}_a \tag{4.42}$$

$$u_{,r}+\frac{u+v_{,\theta}}{r}+w_{,z}=0 \qquad \text{in } \mathcal{B}_a \tag{4.43}$$

$$\hat{S}_{rr}(r_i)=\delta C_1-C_1\Gamma_{rr}(r_i) \qquad \text{at} \quad r=r_i \tag{4.44}$$

$$\hat{S}_{rr}(r_0)=\delta C_2-C_2\Gamma_{rr}(r_0) \qquad \text{at} \quad r=r_0 \tag{4.45}$$

The four unknowns of the problem are the three incremental displacements in Eq.(4.33) and the increment of the Lagrange multiplier q.

In the next section, the incremental elastic problem will be rewritten using the Stroh formulation.

4.6 Stroh formulation of the BVP

In order to solve the incremental BVP, Eqs.(4.40-4.45) are transformed into a system of six first-order ODEs. Assuming variable separation, the solution is sought in the following form:

$$\begin{aligned}\{u,q\}&=\{U(r),Q(r)\}\cos(k_z z-m\theta)\\ \{v,w\}&=\{V(r),W(r)\}\sin(k_z z-m\theta)\end{aligned} \tag{4.46}$$

where m is the circumferential mode and $k_z=2n\pi/L$ is the wavenumber of the tube in the longitudinal direction, with m and n being integers, and U,V,W,Q are four scalar functions of r. Such a helical perturbation deforms the hollow cylinder as illustrated in Figure 4.8. From Eq.(4.35) and Eq.(4.46), the incremental stress components must have the following form:

$$\begin{aligned}\hat{S}_{0rr}&=S_{0rr}(r)\cos(k_z z-m\theta)\\ \{\hat{S}_{0r\theta},\hat{S}_{0rz}\}&=\{S_{0r\theta}(r),S_{0rz}(r)\}\sin(k_z z-m\theta)\end{aligned} \tag{4.47}$$

where $S_{0rr},S_{0r\theta},S_{0rz}$ are three scalar functions of r. Substituting Eqs.(4.46) and (4.47) into the incremental constitutive equations in Eq.(4.35), the following equation can be

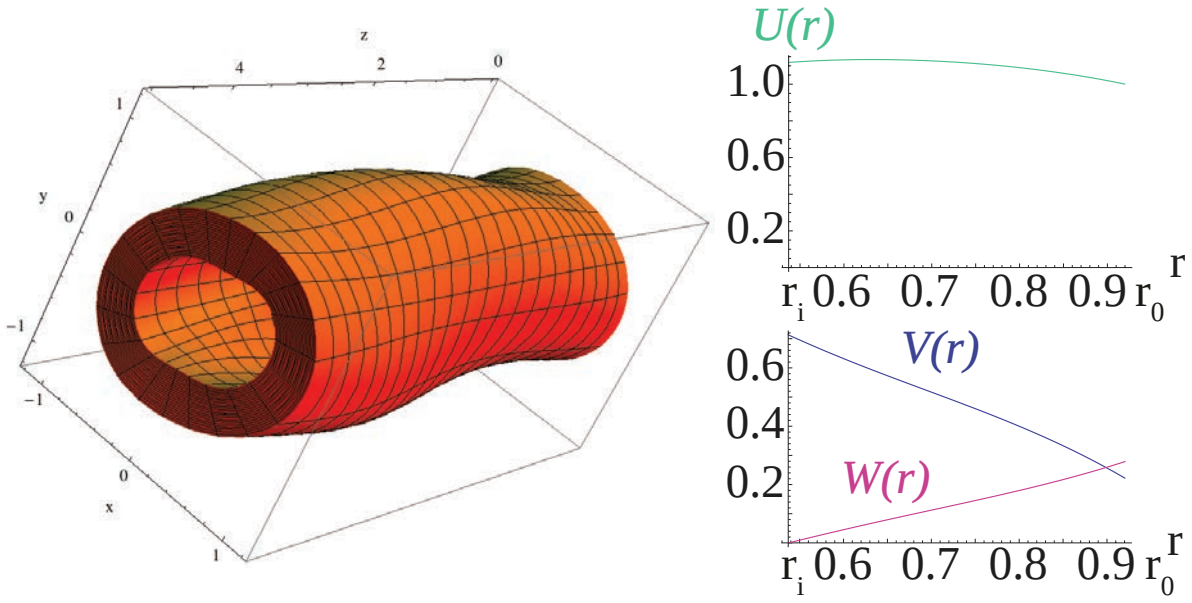

Figure 4.8: Helical buckling of a cylindrical tube obtained from the output of the numerical simulations in the case (a) for $H = 1.6$, $R_0 = 1$, $L = 5$, $U(r_0) = 0.15$ $\lambda_z = 1$ and $\beta = \pi/6$, occurring at the critical wavenumbers $m = 2$, $k_z = 1.37$ (left). Plots of the resulting incremental displacement fields $U(r)$, $V(r)$ and $W(r)$ inside the tube, setting $U(r_0) = 1$ (right). The amplitude of the linear perturbation is fixed arbitrarily for illustrative purposes.

derived:

$$Q = (\mathcal{A}^1_{0rrrr} + p)U' - S_{0rr} \tag{4.48}$$

$$V' = \frac{S_{0r\theta}}{\mathcal{A}^1_{0r\theta r\theta}} + \frac{1}{r}\frac{(V - mU)}{\mathcal{A}^1_{0r\theta r\theta}}p \tag{4.49}$$

$$W' = \frac{S_{0rz}}{\mathcal{A}^1_{0rzrz}} + \frac{k_z U}{\mathcal{A}^1_{0rzrz}}p, \tag{4.50}$$

where the prime denotes differentiation with respect to r. Moreover, the incremental incompressibility condition in equation (4.43), reads:

$$U' = \frac{mV - U}{r} - k_z W. \tag{4.51}$$

Substituting Eqs.(4.35) and (4.46) into Eqs.(4.40-4.42) and using Eq.(4.47) to replace the components $\hat{S}_{0rr}, \hat{S}_{0r\theta}, \hat{S}_{0rz}$ of the incremental stresses, it follows that:

$$\begin{aligned}
&\frac{1}{r^2}\Bigg\{-rS_{0rr}-\Big[\mathcal{A}^1_{0\theta\theta\theta\theta}+\mathcal{A}^1_{0\theta r\theta r}m^2+p+k_zr\Big(-m\mathcal{A}^1_{0\theta rzr}-m\mathcal{A}^1_{0zr\theta r}+\mathcal{A}^1_{0zrzr}k_zr\Big)\Big]U\\
&+\Big[m\Big(\mathcal{A}^1_{0\theta r\theta r}+\mathcal{A}^1_{0\theta\theta\theta\theta}+p\Big)-\Big(\mathcal{A}^1_{0\theta\theta z\theta}+\mathcal{A}^1_{0zr\theta r}\Big)k_zr\Big]V\\
&+r\Big[\Big(rS_{0rr}\Big)'+\Big(\mathcal{A}^1_{0rrrr}+p\Big)U'-mpV'\Big]+k_zpr^2W'\Bigg\}=0,
\end{aligned} \tag{4.52}$$

$$\begin{aligned}
&\frac{1}{r^2}\Bigg\{-m\Big(rS_{0rr}\Big)-\Big[m\Big(\mathcal{A}^1_{0\theta r\theta r}+\mathcal{A}^1_{0\theta\theta\theta\theta}+p\Big)-\Big(\mathcal{A}^1_{0\theta rzr}+\mathcal{A}^1_{0z\theta\theta\theta}\Big)k_zr\Big]U\\
&+\Big[\mathcal{A}^1_{0\theta r\theta r}+m^2\Big(\mathcal{A}^1_{0\theta\theta\theta\theta}+p\Big)-\Big(\mathcal{A}^1_{0\theta\theta z\theta}+\mathcal{A}^1_{0z\theta\theta\theta}\Big)k_zmr+\mathcal{A}^1_{0z\theta z\theta}k_z^2r^2\Big]V\\
&-k_zmprW-r\Big(rS_{0rt}\Big)'+\mathcal{A}^1_{0rrrr}mrU'+mprU'-prV'\Bigg\}=0,
\end{aligned} \tag{4.53}$$

$$\begin{aligned}
&\frac{1}{r^2}\Bigg\{k_zr\Big(rS_{0rr}\Big)-k_zmprV+\Big[\mathcal{A}^1_{0\theta z\theta z}m^2+k_z^2\Big(\mathcal{A}^1_{0zzzz}+p\Big)r^2-\Big(\mathcal{A}^1_{0\theta zzz}+\mathcal{A}^1_{0zz\theta z}\Big)mk_zr\Big]W\\
&-r\Big(rS_{0rz}\Big)'-k_z\Big(\mathcal{A}^1_{0rrrr}+p\Big)r^2U'\Bigg\}=0.
\end{aligned} \tag{4.54}$$

Now, let the displacement-traction vector $\boldsymbol{\eta}(r)$ be defined as follows:

$$\boldsymbol{\eta}(r)=\begin{bmatrix}\mathbf{U}(r)\\ r\,\mathbf{S}(r)\end{bmatrix}\quad\text{with}\quad\begin{aligned}\mathbf{U}\,(r)&=[\,U(r),V(r),W(r)\,]^T\\ \mathbf{S}\;(r)&=[\,s_{0rr}(r),s_{0r\theta}(r),s_{0rz}(r)\,]^T.\end{aligned} \tag{4.55}$$

Accordingly, Eqs.(4.49-4.54) rewrite:

$$\frac{d\boldsymbol{\eta}(r)}{dr}=\frac{1}{r}\mathbf{G}(r)\boldsymbol{\eta}(r), \tag{4.56}$$

where $\mathbf{G}$ is the so-called Stroh matrix, having the following block form:

$$\mathbf{G}=\begin{pmatrix}\mathbf{G}_1 & \mathbf{G}_2\\ \mathbf{G}_3 & \mathbf{G}_4\end{pmatrix}. \tag{4.57}$$

In particular, the four blocks of $\mathbf{G}$ read:

$$\mathbf{G}_1 = \begin{pmatrix} -1 & m & -k_z r \\ -m\sigma_1 & \sigma_1 & 0 \\ k_z r \sigma_2 & 0 & 0 \end{pmatrix}, \quad \mathbf{G}_2 = \begin{pmatrix} 0 & 0 & 0 \\ 0 & 1/\alpha_1 & 0 \\ 0 & 0 & 1/\alpha_2 \end{pmatrix}, \tag{4.58}$$

$$\mathbf{G}_3 = \begin{pmatrix} \kappa_{11} & \kappa_{12} & \kappa_{13} \\ \kappa_{12} & \kappa_{22} & -\kappa_{23} \\ \kappa_{13} & -\kappa_{23} & \kappa_{33} \end{pmatrix}, \quad \mathbf{G}_4 = -\mathbf{G}_1^T, \tag{4.59}$$

where:

$$\begin{aligned}
\kappa_{11} &= m^2(\nu_1 - \alpha_1\sigma_1^2) + k_z^2 r^2(\nu_2 - \alpha_2\sigma_2^2) + (\mathcal{A}^1_{0rrrr} + \mathcal{A}^1_{0\theta\theta\theta\theta}) + 2\alpha_1\sigma_1 - k_z r m(\mathcal{A}^1_{0\theta rzr} + \mathcal{A}^1_{0zr\theta r}),\\
\kappa_{12} &= m\Big\{-\mathcal{A}^1_{0rrrr} - \mathcal{A}^1_{0\theta\theta\theta} - \nu_1 + \alpha_1\big[(\sigma_1 - 1)^2 - 1\big]\Big\} + k_z r(\mathcal{A}^1_{0\theta\theta z\theta} + \mathcal{A}^1_{0zr\theta r}),\\
\kappa_{13} &= k_z r(\mathcal{A}^1_{0rrrr} + \alpha_1\sigma_1),\\
\kappa_{22} &= m^2\big[(\mathcal{A}^1_{0rrrr} + \mathcal{A}^1_{0\theta\theta\theta}) + 2\alpha_1\sigma_1\big] - k_z r m(\mathcal{A}^1_{0\theta\theta z\theta} + \mathcal{A}^1_{0z\theta\theta\theta}) + k_z^2 r^2\nu_3 + \nu_1 - \sigma_1^2\alpha_1,\\
\kappa_{23} &= m k_z r(\mathcal{A}^1_{0rrrr} + 2\alpha_1\sigma_1),\\
\kappa_{33} &= m^2\alpha_3 + k_z^2 r^2(\mathcal{A}^1_{0rrrr} + \mathcal{A}^1_{0zzzz} + 2\alpha_3\sigma_3) - k_z r m(\mathcal{A}^1_{0\theta zzz} + \mathcal{A}^1_{0zz\theta z}),
\end{aligned} \tag{4.60}$$

and:

$$\begin{aligned}
\nu_1 &= \mathcal{A}^1_{0\theta r\theta r}, \qquad \alpha_1 = \mathcal{A}^1_{0r\theta r\theta}, \qquad \sigma_1 = p/\alpha_1,\\
\nu_2 &= \mathcal{A}^1_{0zrzr}, \qquad \alpha_2 = \mathcal{A}^1_{0rzrz}, \qquad \sigma_2 = p/\alpha_2,\\
\nu_3 &= \mathcal{A}^1_{0z\theta z\theta}, \qquad \alpha_3 = \mathcal{A}^1_{0\theta z\theta z}, \qquad \sigma_3 = p/\alpha_3
\end{aligned} \tag{4.61}$$

As discussed in Section 2.3.3, the Stroh form of the incremental BVP doesn't provide the most convenient form for implementing an efficient numerical algorithm for solving the incremental problem when Neumann boundary conditions are assigned. Therefore, the surface impedance method will be used in order to obtain a compact form which will allow for the implementation of a stable numerical solving procedure.

4.7 Surface impedance method and numerical solution

Following Section 2.3.2, a set of independent solutions $\boldsymbol{\eta}_n$, $n = \{1, \ldots, 6\}$ of the system in Eq.(4.56) is defined. Then the 6×6 matricant $\mathbf{M}(r, r_i)$ is introduced as in Eq.(2.113). The matricant in Eq. (2.113), is the solution of the initial value problem:

$$\frac{d\mathbf{M}}{dr}(r, r_i) = \frac{1}{r}\mathbf{G}(r)\mathbf{M}(r, r_i) \qquad \text{with} \qquad \mathbf{M}(r_i, r_i) = \mathbf{I}_{(6)}, \tag{4.62}$$

where $\mathbf{I}_{(6)}$ is the 6×6 identity matrix. Now, since the components of the incremental deformation in Eq.(4.46) are real, the conditional impedance matrix $\mathbf{z} = \mathbf{z}(r, r_i)$ is defined as the 3×3 matrix, such that:

$$r\,\mathbf{S} = \mathbf{z}\,\mathbf{U}, \qquad \text{with} \qquad \mathbf{z} = \mathbf{M}_3\mathbf{M}_1^{-1} \tag{4.63}$$

Hence, substituting Eq.(4.55) and Eq.(4.63) in Eq.(4.56), the following set of equations is obtained:

$$\frac{d}{dr}\mathbf{U} = \frac{1}{r}\mathbf{G}_1\mathbf{U} + \frac{1}{r}\mathbf{G}_2\mathbf{z}\mathbf{U}, \tag{4.64}$$

$$\frac{d}{dr}\left(\mathbf{z}\mathbf{U}\right) = \frac{1}{r}\mathbf{G}_3\mathbf{U} - \frac{1}{r}\mathbf{G}_1^T\mathbf{z}\mathbf{U}. \tag{4.65}$$

Moreover, substituting Eq.(4.64) in Eq.(4.65), the differential matrix Riccati is derived:

$$\frac{d}{dr}\mathbf{z} = \frac{1}{r}\left(\mathbf{G}_3 - \mathbf{G}_1^T\mathbf{z} - \mathbf{z}\mathbf{G}_1 - \mathbf{z}\mathbf{G}_2\mathbf{z}\right). \tag{4.66}$$

Using equation (4.63), the boundary conditions in Eqs.(4.38,4.39) can be transformed in the initial and the stop conditions of the differential matrix Riccati equation in Eq.(4.66), as listed in Table 4.2.

The following numerical procedure is implemented in Mathematica [100], for solving the incremental problem based on the conditional impedance matrix. Fixing the initial aspect ratio H of the tube, and making outer iterations on the wavenumbers m and k_z, Eq.(4.66) is numerically integrated (using the initial conditions in the first column in Table 4.2) and the torsion rate γ is iterated until the stop condition in the second column of Table 4.2 is satisfied.

In the next section, the numerical results obtained from this procedure are presented

	initial conditions	stop conditions
a) No loads	$\mathbf{z}(r_i) = \mathbf{0}$	$\det \mathbf{z}(r_0) = 0$
c) Internal pressure	$\mathbf{z}(r_0) = \mathbf{0}$	$\det \left[\mathbf{z}(r_i) - P \begin{pmatrix} G_{11} & G_{12} & G_{13} \\ 0 & 0 & 0 \\ 0 & 0 & 0 \end{pmatrix} \right] = 0$
b) External pressure	$\mathbf{z}(r_i) = \mathbf{0}$	$\det \left[\mathbf{z}(r_0) - P \begin{pmatrix} G_{11} & G_{12} & G_{13} \\ 0 & 0 & 0 \\ 0 & 0 & 0 \end{pmatrix} \right] = 0$

Table 4.2: Initial and stop conditions used to integrate numerically equation (4.66) in order to get the bifurcation parameters of the torsional instability.

and discussed in order to investigate the role of the axial and circumferential pre-stretches on the onset of helical buckling.

4.8 Numerical results

The numerical results of the linear stability analysis are presented in the following for each of the three different load scenarios under consideration. First an illustrative example is presented to show how the critical value of torsion rate and the associated circumferential and longitudinal modes at the onset of the torsional instability are calculated. In Figure 4.9, the bifurcation parameter γ is plotted against the longitudinal mode

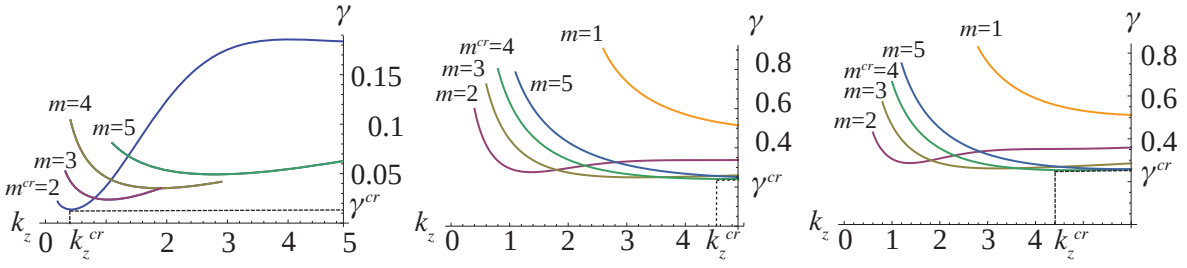

Figure 4.9: Critical torsion rates γ in function of the longitudinal mode k_z, plotted for different circumferential modes $m = 1, 2, 3, 4, 5$, obtained considering (a) a stress-free cylindrical tube, (b) a tube with an applied internal or (c) external pressure. In each case, $H = 1.05$, $R_0 = 1$, $\mu = 1$ and in case (b) and (c), the pressure is calculated from Eq.(4.28) and Eq.(4.28) respectively, using $\beta = \pi/4$ and $\lambda_z = 1$. The absolute minimum among all the curves identifies the critical values for m^{cr}, k_z^{cr} and γ^{cr}.

k_z and for different circumferential numbers m, for cylindrical tubes without external loads (Figure 4.9a), with internal pressure P given by Eq.(4.28) (Figure 4.9b) and with external pressure P given by Eq.(4.31) (Figure 4.9c), setting $H = 1.05$, $R_0 = 1$, $\mu = 1$, $\beta = \pi/4$, and $\lambda_z = 1$.

For each example, the critical value γ^{cr} corresponds to the absolute minimum among all the curves, whilst the corresponding m^{cr} and k_z^{cr} define the critical circumferential and longitudinal modes, respectively. For each class of BVPs, the results show that both the critical circumferential and longitudinal modes depend on the initial aspect ratio.

Although the pressure is the control parameter in the cases (b) and (c), the functional relationships in Eqs.(4.28, 4.31) allow to consider the pre-stretches as the order parameters of the helical buckling. In fact, the strategy of fixing P, and then calculating from Eqs.(4.28, 4.31) one pre-stretch λ_θ or λ_z at any given H whilst keeping the other fixed, would give a pre-strain varying with H, and a direct comparison with the results of the case (a) would be difficult. Furthermore, in many biological tissues the in-vivo pressure is not always known, while the geometrical data and the pre-strains are measurable from *ex-vivo* cutting experiments. Accordingly, in the following paragraphs the role played by the circumferential and axial pre-stretches λ_θ and λ_z, respectively, on the onset of the torsional instability is investigated.

4.8.1 Effect of the circumferential pre-stretch

Here, the role played by the circumferential pre-stretch λ_θ, on the onset of the torsional

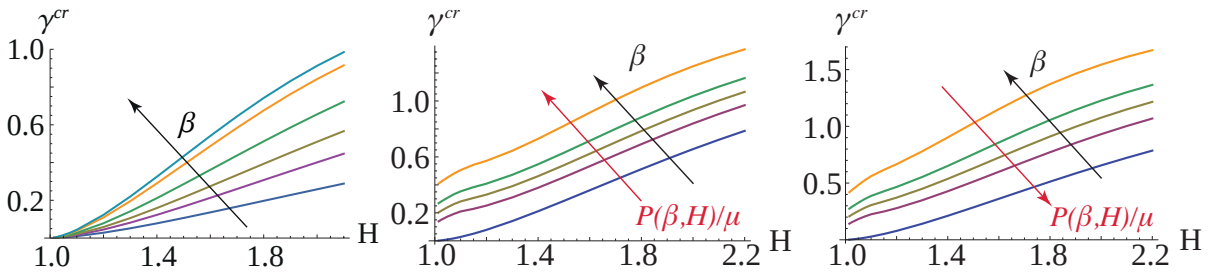

Figure 4.10: Critical values of torsion rate γ^{cr} plotted against the initial aspect ratio H at $\lambda_z = 1$, in three physical examples: traction-free (a) at $\beta = -\pi, -\pi/2, -\pi/4, 0, \pi/4, \pi/3$ applied internal (b) and external (c) pressure. In cases (b) and (c), the internal and external pressure P are calculated from Eq.(4.28) and Eq.(4.31), respectively, using $\beta = 0, \pi/6, \pi/4, \pi/3, \pi/2$.

instability is investigated. The circumferential pre-stretch depends on the initial angle $\beta < 2\pi$, as $\lambda_\theta = 2\pi/(2\pi - \beta)$. In Figure 4.10, the values of critical torsion rates γ^{cr} are plotted against the initial aspect ratio H, for different initial opening angles β and at fixed $\lambda_z = 1$.

The bifurcation parameters are shown in the case of traction-free cylindrical tubes (Figure 4.10a), tubes with applied internal pressure P given by equation (4.28) (Figure 4.10b) or applied external pressure P given by equation (4.31) (Figure 4.10c). The marginal stability curves show how, for a fixed H, an increase in the initial opening angle corresponds to an increase of the critical torsion rate. In the case of traction-free cylindrical tubes, this effect becomes more relevant for thicker tubes, while the critical torsion $\gamma^{cr} \to 0$ for $H \to 1$. When a pressure is applied on the external or the internal surface of the cylindrical tube, instead, the critical torsion rate for $H \to 1$ approaches a finite value depending on β.

In Figure 4.11, the values of the critical longitudinal mode k_z^{cr} are plotted as functions of the initial aspect ratio H at different initial opening angles and at fixed $\lambda_z = 1$, for traction-free cylindrical tubes (Figure 4.11a), tubes with applied internal pressure (Figure 4.11b) or applied external pressure (Figure 4.11c). The critical circumferential modes are also depicted at different range of H, showing that when a traction free boundary condition is considered, the circumferential mode is always $m^{cr} = 2$. The same behavior is observed in the case of applied external or internal pressure, when $\lambda_\theta = 1$. Otherwise, when $\lambda_\theta \neq 1$, tubes with $H \geq 1.2$ exhibit $m^{cr} = 2$, while thinner tubes have higher critical

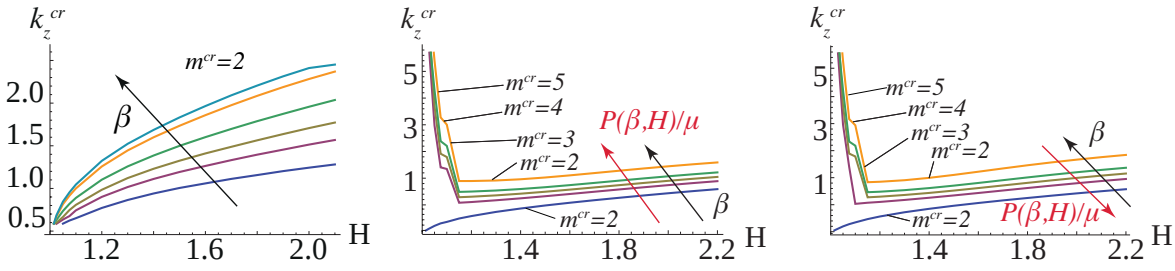

Figure 4.11: Critical values of longitudinal mode k_z^{cr} plotted against the initial aspect ratio H at $\lambda_z = 1$, in three physical examples: traction-free (a) at $\beta = -\pi, -\pi/2, -\pi/4, 0, \pi/4, \pi/3$, applied internal (b) and external (c) pressure. In the cases (b) and (c) the pressure P is calculated from Eq.(4.28) and Eq.(4.31), respectively, at $\beta = 0, \pi/6, \pi/4, \pi/3, \pi/2$. The solid black lines indicate the related value of m^{cr} for each branch of the curves.

circumferential wavenumbers.
On the other hand, for a fixed initial aspect ratio, the absolute value of the critical longitudinal mode increases as the initial opening angle increases. Moreover, thin tubes ($1 < H < 1.1$) select higher longitudinal critical wavenumbers than thick tubes.

4.8.2 Effect of the axial pre-stretch

In this section, the role played by the pre-stretch λ_z on the onset of torsional instabilities is analyzed. In Figure 4.12, the critical torsion rates γ^{cr} are plotted against the initial aspect ratio H, for different pre-stretches λ_z at fixed $\beta = \pi/6$. The marginal stability curves are depicted for traction-free cylindrical tubes (Figure 4.12a), tubes with applied internal pressure given by equation (4.28) (Figure 4.12b) and with applied external pressure given by Eq.(4.31) (Figure 4.12c). At fixed initial aspect ratio, the critical values of torsion rates increase as λ_z increases, showing how a cylindrical tube under a finite compression becomes unstable at lower torsion rates than one subjected to a finite extension. Furthermore, thin tubes have always lower values of critical torsion rate than thick tubes.

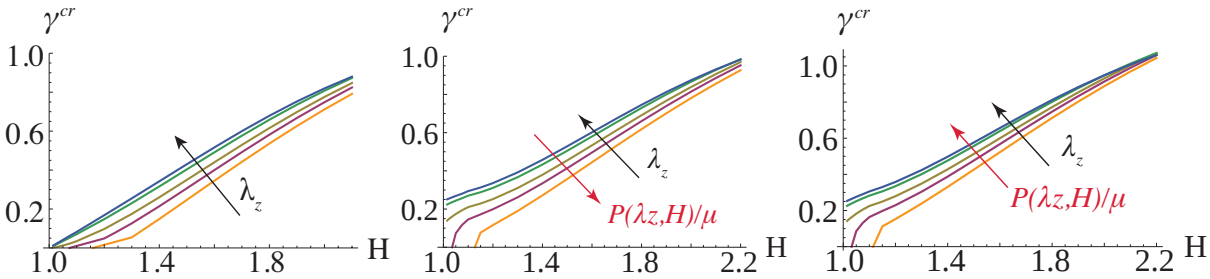

Figure 4.12: Critical values of torsion rate γ^{cr} plotted against the initial aspect ratio H for three sets of boundary conditions: traction-free tube (a), applied internal (b) or external (c) pressure for $\lambda_z = 0.9, 0.95, 1, 1.1, 1.2$, and $\beta = \pi/6$. In the cases (b) and (c), the internal and external pressure P are calculated from Eq.(4.28) and Eq.(4.31), respectively, at the given values of λ_z.

In Figure 4.13, the critical longitudinal modes are depicted for traction-free cylindrical tubes (Figure 4.13a), cylindrical tubes with applied internal (Figure 4.13b) and external (Figure 4.13c) pressure. The critical circumferential modes are also displayed for the three cases. The marginal stability curves highlight that tubes under axial compression

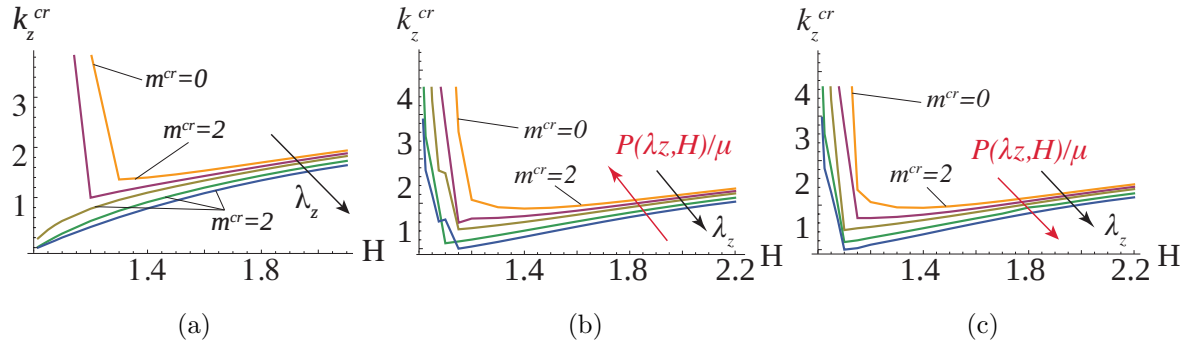

Figure 4.13: Critical values of longitudinal mode k_z^{cr} plotted against the initial aspect ratio H in three physical examples: traction-free (a), applied internal (b) and external (c) pressure at $\lambda_z = 0.9, 0.95, 1, 1.1, 1.2$, and $\beta = \pi/6$. In the cases (b) and (c) the pressure P is calculated from Eq.(4.28) and Eq.(4.31), respectively, at the given values of λ_z. The solid black lines indicate the related value of m^{cr} for each branch of the curves.

select higher longitudinal modes than tubes under axial extension, while $m^{cr} = 2$ for thick tubes. For $\lambda_z < 1$, the axial compression provokes a *barreling* instability, corresponding $m^{cr} = 0$, in thin tubes without any torsion. Although out of the scope of this work, it should be recalled that in this case other asymmetric modes can occur for the buckling of a compressed tube with guided-guided end conditions [116].

4.9 Discussion of the results

In this chapter, the torsional instabilities which can emerge when a soft, residually-stressed cylindrical tube is subjected to a finite torsion have been investigated. The model accounts for an initial opening angle β, which defines the circumferential pre-stretch $\lambda_\theta = 2\pi/(2\pi - \beta)$, and for a uniform axial pre-stretch λ_z, in order to represent the three-dimensional distribution of residual strains that is observed in living tubular tissues, such as arteries.

In Section 4.2, the geometry and the kinematics of the elastic model have been presented. Considering an incompressible neo-Hookean material, in Section 4.3, the basic axial-symmetric solutions for the three different sets of boundary conditions have been derived. As depicted in Figure 4.5, three load scenarios were considered: traction-free boundary conditions at both internal and external surfaces (a), an applied pressure load P given by Eq.(4.28) at the internal surface (b) or an applied pressure load P given by Eq.(4.31) at the external surface (c). Using the method of small deformations superposed

on finite strains, a linear stability analysis have been performed. The incremental elastic problem has been derived using the Stroh formulation. The incremental solution has been calculated using a numerical procedure based on the surface impedance method. The numerical results have been presented in Section 4.8, reporting the marginal stability curves for the critical torsion rate γ^{cr}. An illustration of the deformed tube at the onset of the torsional instability is depicted in Figure 4.8. As illustrated in Figure 4.9, the helical buckling is characterized by critical circumferential and longitudinal modes, m^{cr} and k^{cr}, respectively, depending both on the initial thickness of the tube and on the existing-pre-stretches. This confirms that the torsional instability in soft tubes strongly differs from the one for solid cylinders, which is characterized by a critical mode $m = 1$ [117, 118], with the initial formation of a kink nonlinearly evolving into a knot [119].

Moreover, the analytical results highlighted that the critical torsion rate γ^{cr} increases with an increasing initial thickness of the hollow cylinder in accordance with the experimental results of Ertepinar and Wang [120] on stress-free rubber tubes. Furthermore, when a traction-free boundary condition is considered, the circumferential mode is independent of the thickness of the tube and is always $m^{cr} = 2$ for $\lambda_z \geq 1$.

Another novel aspect of this study concerns the investigation of the effects of the circumferential and axial pre-strains on the onset of the torsional instability. The marginal stability curves in Figures 4.10-4.13 have shown that both the critical torsion rate and

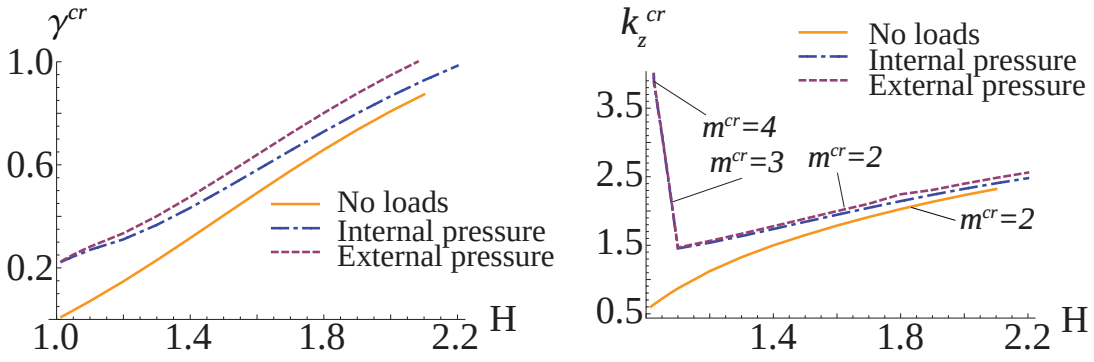

Figure 4.14: Critical values of the torsion rate γ^{cr} (left) and the longitudinal mode k_z^{cr} (right) plotted against the initial aspect ratio H, considering stress-free conditions (orange, solid), and applied external (purple, dashed) or internal (blue, dash-dot) pressure, with $\lambda_z = 1$, and $\beta = \pi/6$. The blue and purple lines are obtained by calculating the internal and external pressures from Eq.(4.28) and Eq.(4.31), respectively. The solid black lines indicate the related value of m^{cr} for each branch of the curves.

the axial wavenumber increase for increasing circumferential and axial pre-stretches. In particular, such a result on the axial wavenumber is in accordance with the results on torsional instabilities in solid cylinders [117, 121]. Finally, in Figure 4.14 the critical torsion rates and the critical circumferential and longitudinal modes have been compared for the three considered sets of boundary conditions. As expected, a tube without any loads is the most unstable configuration with respect to torsional instabilities, while the most stable configuration is always the externally pressured tube.

4.10 Validation of the model with experimental data

In this section, the critical values of the torsion rate predicted by the analytical results in Section 4.8 will be compared with the few experimental data available in the literature. A certain amount of experiments have been performed in order to investigate the effect of the twist on arteries and veins during and after anastomosis. Anastomosis is the surgical practice employed to reconnect two segments of the vessels. It is a typical operation performed when a part of the vessel is irreversibly injured and thus needs to be removed. During anastomosis, the artery can be subjected to twist, hence in order to guarantee a positive outcome of the operation, the vessel must be stable to torsional loads.
Topalan et al. studied the effect of torsion on both arteries and veins [122]. They found that arteries, which are thicker and subjected to a higher blood pressure buckle at higher twisting angles than veins. These findings are in accordance with the results obtained from the model presented here. In fact, the model predicts higher critical torsion rates for thicker cylinders in all the three load scenarios considered. Furthermore, according to the relation between pressure and pre-stretches in Eq.(4.28), the results in Figure 4.12b show that, at high values of the internal pressure, the longitudinal pre-stretch is calibrated in order to induce a tensile residual stress (as found in arteries [123, 124]). Accordingly, the critical torsion rate values are higher than for cylinder subjected to a lower pressure, such as veins where torsional buckling occurs at lower critical twisting angle [125]. Finally, as shown in Figure 4.11 and Figure 4.13, the morphoelastic model predicts critical circumferential modes $m^{cr} = 2$ for thick cylinders ($H > 1.2$). These predictions are in accordance with the pattern observed in the rat femoral aorta reported by Selvaggi et al., who measured an initial external radius $R_0 = 0.416$mm and a thickness $R_0 - R_i = 0.166$mm, corresponding to an initial aspect ratio $H = 1.664$.

4.11 Concluding remarks

In this chapter, a predictive model for helical buckling in tubular tissues has been built up following the morphoelastic theory presented in Chapter 2.
The novelties of the proposed model reside in the following main points:

- the model accounts for the physiological adaptation of soft tubular tissues to changes in applied pressure load
- the residual stresses arising from the remodeling process of the soft tissue have been taken into account
- the effects of the residual stresses on the onset of the helical instability have been investigated
- the critical values of torsion rates and the associated critical modes of the instability have been calculated as functions of biological measurable parameters.

In conclusion, the model proposed in this chapter links measurable biological parameters (blood pressure, shear modulus, initial thickness, initial opening angle and longitudinal pre-stretch) to the critical torsion at the onset of an helical instability and could be used as predictive tool for the occurrence of torsional instabilities in tubular organs.

Chapter 5

Conclusions and perspectives

Among the fundamental processes involved in the development of an organism, morphogenesis is one of the most complex. It is the result of concatenated events which occur at different (temporal and spatial) scales. During the past centuries, the experimental results collected by several scientists have improved our actual knowledge of the mechanisms that drive many morphogenetic processes in living organisms. Recently, experiments have been complemented with mathematical modeling as a tool for proving novel insights on morphogenesis in soft tissues. Few main issues must be overcome when modeling processes involving soft tissues: their nonlinear behavior, the presence of large deformations and of residual stresses. All these elements contribute to increase the complexity of the problem and require *ad hoc* theories for modeling soft tissues. In this context, this thesis aimed at developing new mathematical models for the formation of patterns and forms in biological tissues. In particular, the focus has been pointed to soft tubular organs.

A macroscopic approach has been adopted, where the tissue has been considered as a continuum body undergoing growth and remodeling. The main idea behind the proposed models is that during growth and remodeling, residual stresses can arise and once they exceed a critical value, an elastic instability can occur in the tissue and lead to a morphological change. Therefore, the morphoelastic models have been developed in the framework of the thermo-mechanics of open systems. The kinematics of finite deformations allowed for the mathematical description of the morphogenetic process. The theory of volumetric growth and remodeling, proposed by Skalak and coworkers, was used to separate the growth (remodeling) and the elastic parts of the morphogenetic process. The balance of mass and linear momentum govern the physical problem and the Clausius-

Duhem form of thermodynamics dictates the restrictions for the evolution of the growth (remodeling) and for the constitutive equations of the tissue. In order to investigate the occurrence of elastic instabilities, a linear stability analysis has been performed using the method of incremental deformations superposed on finite deformations and the critical thresholds for the onset of the instability have been determined together with the modes of the associated instability pattern.

The morphoelastic theory has been applied to the modeling of different morphogenetic processes occurring in soft tubular organs: the formation of the wide range of patterns in the gastro-intestinal system and the occurrence of torsional instabilities in pre-stressed tubular organs. In the following the main results achieved and some future perspectives will be summarized.

First, a model for the early stages of intestinal morphogenesis in vertebrate embryos has been proposed with the aim of modeling the formation of the intestinal villi from a two-dimensional undulated pattern in vertebrates species such as mouses. The embryonic intestine has been modeled as one-layered cylinder, made of hyperelastic, incompressible and anisotropic tissue, the mucosa which grows under the rigid confinement imposed by the much stiffer surrounding tissues. The spatially constrained growth introduces incompatibilities in the embryonic tissue, thus residual stresses arise and provoke the emergence of a two-dimensional pattern at the inner surface of the embryonic tissue. In this case, from the results of the linear stability analysis, the model highlighted the occurrence of a surface instability at the internal surface of the mucosal wall, in fact an increase in the perturbation modes resulted in decreasing instability thresholds. The model also allowed for investigating the effects of the structural anisotropy of the tissue on the onset of the instability, showing that both an increase in the orientation angle between fibers and in the stiffness of the tissue decrease the critical growth at which the elastic instability occurs. Moreover, both isotropic and anisotropic growth processes have been considered and compared, showing that the most unstable scenario is represented by the tissue growing only in the longitudinal direction. In conclusion, the theoretical model showed that the spatially constrained growth of the embryonic mucosa could be the mechanism driving the early formation of the intestinal villi in mouse embryos. Nevertheless, the model didn't allow to predict the finite wavelength of the emerging instability pattern, and thus a more complex model has been proposed.

In the second proposed model, the gastro-intestinal tube has been modeled as a two-

layered cylinder, made of two hyperelastic, incompressible and isotropic tissues. The two layers represent the two primary matrices from which the gut originates, i.e the inner endoderm and the outer mesoderm. The outer mesoderm is considered stiffer than the inner endoderm, so that the model allowed to account for the spatially constrained growth as the limit case where the mesoderm is infinitely stiffer than the endoderm. The mechanism driving the onset of the instability is then the spatially unconstrained differential growth between the primary layers. One of the novelty of the proposed model is that it accounts for stress-free boundary conditions at both the inner and the outer surfaces. Furthermore, the model is able to reproduce the wide range of patterns observed in the gastro-intestinal system of vertebrates. In fact, by investigating the effects of the geometrical and mechanical parameters on the onset of the instability, the model allowed to prove that these factors drive the selection of the specific pattern. Therefore, the model predicted not only the emergence of the circumferential foldings observed in the oesophagus, or the longitudinal rings which form in the jejunum but also the two-dimensional pattern which is typical of pathological states such as the feline oesophagus. The theoretical model has been supplemented with the numerical simulations performed using the finite element method in Abaqus, with the aim of investigating the fully nonlinear evolution of the linearly unstable patterns. The numerical results highlighted that those patterns can evolve following different paths which range from the formation of stable wrinkles to the emergence of creases. In some cases, even a dramatic wavelength doubling can occur. Furthermore, the numerical simulations allowed to conclude that the geometry and the mechanical properties of the two embryonic layers are also crucial in determining the post-buckling evolution of the instability pattern.

Although capturing the main macroscopic features of gastro-intestinal organogenesis, the model has the following weaknesses:

- The numerical simulations do not reproduce any transition from one pattern to another. For instance, in chick embryos, a transition from the circumferential to a zigzag pattern is observed around the 14th day after fertilization of the egg. According to the experiments performed by Shyer et al. [90], this transition is observed simultaneously to the differentiation of the mesoderm into a longitudinal oriented muscular layer, suggesting that mechanical forces might induce this transition. Therefore, both anisotropic growth and the structural anisotropy of the tissue, which have been neglected in this model, might play a role in the transition from the circumferential foldings into the zigzag pattern.

- The model doesn't account for processes occurring at the micro-scale such as signaling between endoderm and mesoderm or biochemical reactions which play an important role in the differentiation of the primary layers.

- Numerical algorithms could be developed to investigate secondary bifurcations which the present analysis have shown to occur for some combinations of the initial parameters.

Another biological problem investigated in this thesis has been the helical buckling of pre-stressed tubular tissues. This study was mainly motivated by the dangerous effects that torsional loads can have on arteries during surgical operations or even during daily life. Tubular soft tissues are known to be residually stressed. For example, when an artery is radially cut it opens into a cylindrical open sector (characterized by an opening angle) and shortens along its longitudinal axis, releasing the residual stresses. In this thesis, it has been assumed that residual stresses arise in the tubular tissues as consequence of an upstream remodeling process. The effects of remodeling have been taken into account by introducing longitudinal and circumferential (associated to the opening angle) pre-stretches. Furthermore, living tissues are known to be regulated by the homeostatic principle, i.e. they adapt to external changes in order to maintain their equilibrium stead-state. Therefore, according with the homeostatic principle, it has been assumed that the pre-stretches adjust in function of the pressure acting at the internal or external surface of the tubular organ, in order to make the strain distribution inside the tissue uniform. The tubular tissues have been modeled as one-layered hyperelastic, incompressible and isotropic materials. Three cases have been considered, associated to different load scenarios: no applied loads, an applied internal or external pressure load. Therefore the model applies to a wide range of soft tubular tissues: the intestine, where negative opening angles have been measured and which is constantly subjected to an external pressure, exerted by the surrounding tissues, but also the airways where no tractions act on their surfaces. The proposed model showed that the residual stresses arising from the remodeling process affect the critical values of torsion rate, at which the helical instability occurs in the cylinders. In particular, tissues with circumferential compressive residual stresses buckle at lower values of the torsion rate than tissues exhibiting circumferential tensile residual stresses. The model also highlighted that thin cylinders are more unstable to torsional loads than thick tubes.
The residual stresses also affect the critical modes associated with the emerging helical pattern. In particular, thin cylinders with higher initial opening angle have higher critical

circumferential and longitudinal modes, in both the cases of applied external or internal pressure. Interestingly, the model showed that in all the three load scenarios considered, thin cylinders buckled under the effect of compressive longitudinal pre-stretch developing a barreling instability. In conclusion, the proposed model could be used as a predictive tool for torsional instability in hollow cylinders. It has the novel feature of linking initial geometrical and mechanical parameters (such as the aspect ratio, the shear modulus of the cylinder and the applied pressure) with the order parameter associated to the onset of the helical instability, i.e. the critical torsion rate and the associated circumferential and longitudinal modes of the instability.

However, the following improvements could be considered for future investigations:

- The heterogeneous composition of the soft tubular tissues and their multi-layered structures have been neglected in the present study, but could play an important role in determining the onset of the helical instability in the tubular tissues.

- Numerical simulations could be performed in the nonlinear regime in order to investigate vessel occlusion. In particular, the values of torsion rate at which a complete occlusion occurs in the vessel can be calculated as a function of the residual stresses and of the blood pressure.

- In this study, it has been assumed that $L \gg R_0$; numerical simulations could be performed to investigate the boundary effects at $L = 0, L$ on the onset of the instability.

In conclusion, the modeling of morphogenesis in living tissues has been approached from a theoretical and numerical viewpoint. The task is characterized by a complexity which derives from the intrinsic complex nature of living tissues. A morphoelastic theory has been adopted, where the modern theories of growth and remodeling, the thermomechanics of open systems, the theories and methods for solving problems in nonlinear elasticity have been combined to address the complexity of the problem. The morphoelastic theory has provided the bases for useful insights in two interesting biological problems such as the gastro-intestinal organogenesis and the torsional instabilities of pre-stressed tubular organs. The results of these studies have been published in four peer-review journals.

Related Publications

- V. Balbi, P. Ciarletta. Morpho-elasticity of intestinal villi. doi:10.1098/rsif.2013.0109, *J Roy Soc Interface* 10 (2013) 20130109
- V. Balbi, E. Kuhl, P. Ciarletta. Morphoelastic control of gastro-intestinal organogenesis: Theoretical predictions and numerical insights. doi: 10.1016/j.jmps.2015.02.016, *J Mech Phys Solids*, 78 (2015) 493-510.
- V. Balbi, P. Ciarletta. Helical buckling of thick-walled, pre-stressed, cylindrical tubes under a finite torsion. doi:10.1177/1081286514550570, *Math Mech Solids*, 20 (2014) 625-642.
- P. Ciarletta, V. Balbi, E. Kuhl. Pattern selection in growing tubular tissues. doi: 10.1103/PhysRevLett.113.248101, *Phys Rev Letters*, 113 (2014) 248101.

Bibliography

[1] A Ascenzi. Biomechanics and Galileo Galilei. *J Biomech*, 26(2):95–100, 1993.

[2] J Bard. *Morphogenesis: The cellular and molecular processes of developmental anatomy*. Cambridge University Press, 1992.

[3] L Wolpert, R Beddington, J Brockets, T Jessel, P Lawrence, and E Meyerowitz. *Principles of Development*. Oxford University Press, 2002.

[4] C Cohen. Gould et D'Arcy Thompson. *Comptes Rendus Palevol*, 3(5):421–431, 2004.

[5] S Kondo and T Miura. Reaction-diffusion model as a framework for understanding biological pattern formation. *Science*, 329(5999):1616–1620, 2010.

[6] LV Beloussov, NN Luchinskaya, AS Ermakov, and NS Glagoleva. Gastrulation in amphibian embryos, regarded as a succession of biomechanical feedback events. *Int J Dev Biol*, 50(2/3):113, 2006.

[7] DV Bohórquez, NE Bohórquez, and PR Ferket. Ultrastructural development of the small intestinal mucosa in the embryo and turkey poult: a light and electron microscopy study. *Poultry Sci*, 90(4):842–855, 2011.

[8] P Ciarletta and M Ben Amar. Growth instabilities and folding in tubular organs: A variational method in non-linear elasticity. *Int J Nonlin Mech*, 47(2):248–257, 2012.

[9] R Sbarbati. Morphogenesis of the intestinal villi of the mouse embryo: chance and spatial necessity. *J Anat*, 135(3):477, 1982.

[10] SQ Liu and YC Fung. Zero-stress states of arteries. *J Biomech Eng-T ASME*, 110(1):82–84, 1988.

[11] LA Taber. Biomechanics of growth, remodeling, and morphogenesis. *Appl Mech Rev*, 48(8):487–545, 1995.

[12] EH Haeckel. *Generelle Morphologie der Organismen allgemeine Grundzuge der organischen Formen-Wissenschaft, mechanisch begrundet durch die von Charles Darwin reformirte Descendenz-Theorie von Ernst Haeckel: Allgemeine Entwickelungsgeschichte der Organismen kritische Grundzuge der mechanischen Wissenschaft von den entstehenden Formen der Organismen, begrundet durch die Descendenz-Theorie*. Verlag von Georg Reimer, 1866.

[13] S Pivar. *On the origin of form: evolution by self-organization*. North Atlantic Books, 2009.

[14] V Hamburger. Wilhelm Roux: visionary with a blind spot. *J Hist Biol*, 30(2):229–238, 1997.

[15] H Spemann and H Mangold. Induction of embryonic primordia by implantation of organizers from a different species (1923). *Int J Dev Biol*, 45(1):13, 2001.

[16] F Pauwels. *Biomechanics of the locomotor apparatus: contributions on the functional anatomy of the locomotor apparatus*. Springer Science & Business Media, 2012.

[17] W D'Arcy Thompson. On growth and form. *Cambridge Univ. Press*, 1917.

[18] MA Ulett. On growth and form (1917), by Sir D'Arcy Thompson. *Embryo Project Encyclopedia*, 2012.

[19] JS Huxley. Problems of relative growth. *Smith I*, 1932.

[20] SJ Gould. *Ontogeny and phylogeny*. Harvard University Press, 1977.

[21] AM Turing. The chemical basis of morphogenesis. *Philos T Roy Soc B*, 237(641):37–72, 1952.

[22] M Cross. Notes on the turing instability and chemical instabilities, 2006.

[23] A Gierer and H Meinhardt. A theory of biological pattern formation. *Kybernetik*, 12(1):30–39, 1972.

[24] S Kondo and R Asai. A reaction-diffusion wave on the skin of the marine angelfish pomacanthus. *Nature*, 376(6543):765–768, 1995.

[25] MP Harris, S Williamson, JF Fallon, H Meinhardt, and RO Prum. Molecular evidence for an activator–inhibitor mechanism in development of embryonic feather branching. *P Natl Acad Sci*, 102(33):11734–11739, 2005.

[26] P Prusinkiewicz, DR Fowler, and H Meinhardt. *The algorithmic beauty of sea shells*. Springer Science & Business Media, 2009.

[27] RS Smith, S Guyomarc'h, T Mandel, D Reinhardt, C Kuhlemeier, and P Prusinkiewicz. A plausible model of phyllotaxis. *P Natl Acad Sci*, 103(5):1301–1306, 2006.

[28] L Wolpert. Positional information and the spatial pattern of cellular differentiation. *J Theor Biol*, 25(1):1–47, 1969.

[29] J Jaeger, S Surkova, M Blagov, H Janssens, D Kosman, KN Kozlov, E Myasnikova, CE Vanario-Alonso, M Samsonova, DH Sharp, et al. Dynamic control of positional information in the early drosophila embryo. *Nature*, 430(6997):368–371, 2004.

[30] JBA Green and J Sharpe. Positional information and reaction-diffusion: two big ideas in developmental biology combine. *Development*, 142(7):1203–1211, 2015.

[31] R Skalak, G Dasgupta, M Moss, E Otten, P Dullemeijer, and H Vilmann. Analytical description of growth. *J Theor Biol*, 94(3):555–577, 1982.

[32] R Skalak. Growth as a finite displacement field. In *Proceedings of the IUTAM Symposium on Finite Elasticity*, pages 347–355. Springer, 1982.

[33] YC Fung and SQ Liu. Strain distribution in small blood vessels with zero-stress state taken into consideration. *Am J Physiol-Heart C*, 262(2):H544–H552, 1992.

[34] JP Xie, SQ Liu, RF Yang, and YC Fung. The zero-stress state of rat veins and vena cava. *J Biomech Eng-T ASME*, 113(1):36–41, 1991.

[35] JH Omens and YC Fung. Residual strain in rat left ventricle. *Circ Res*, 66(1):37–45, 1990.

[36] HC Han and YC Fung. Residual strains in porcine and canine trachea. *J Biomech*, 24(5):307–315, 1991.

[37] EK Rodriguez, A Hoger, and AD McCulloch. Stress-dependent finite growth in soft elastic tissues. *J Biomech*, 27(4):455–467, 1994.

[38] D Ambrosi, GA Ateshian, EM Arruda, SC Cowin, J Dumais, A Goriely, Gerhard A Holzapfel, JD Humphrey, R Kemkemer, E Kuhl, et al. Perspectives on biological growth and remodeling. *Journal of the Mechanics and Physics of Solids*, 59(4):863–883, 2011.

[39] E Kröner. Allgemeine kontinuumstheorie der versetzungen und eigenspannungen. *Arch Ration Mech An*, 4(1):273–334, 1959.

[40] EH Lee. Elastic-plastic deformation at finite strains. *J Appl Mech*, 36(1):1–6, 1969.

[41] M Epstein and GA Maugin. Thermomechanics of volumetric growth in uniform bodies. *Int J Plasticity*, 16(7):951–978, 2000.

[42] JF Ganghoffer. Mechanical modeling of growth considering domain variationpart ii: Volumetric and surface growth involving eshelby tensors. *J Mech Phys Solids*, 58(9):1434–1459, 2010.

[43] A DiCarlo and S Quiligotti. Growth and balance. *Mech Res Commun*, 29(6):449–456, 2002.

[44] D Ambrosi and F Guana. Stress-modulated growth. *Math Mech Solids*, 12(3):319–342, 2007.

[45] M Ben Amar and A Goriely. Growth and instability in elastic tissues. *J Mech Phys Solids*, 53(10):2284–2319, 2005.

[46] B Li, YP Cao, and XQ Feng. Growth and surface folding of esophageal mucosa: a biomechanical model. *J Biomech*, 44(1):182–188, 2011.

[47] DE Moulton and A Goriely. Possible role of differential growth in airway wall remodeling in asthma. *J Appl Physiol*, 110(4):1003–1012, 2011.

[48] RM Bowen. Toward a thermodynamics and mechanics of mixtures. *Arch Ration Mech An*, 24(5):370–403, 1967.

[49] SC Cowin. Bone poroelasticity. *J Biomech*, 32(3):217–238, 1999.

[50] JD Humphrey and KR Rajagopal. A constrained mixture model for growth and remodeling of soft tissues. *Math Mod Meth Appl S*, 12(03):407–430, 2002.

[51] B Loret and FMF Simões. A framework for deformation, generalized diffusion, mass transfer and growth in multi-species multi-phase biological tissues. *Eur J Mech A-Solid*, 24(5):757–781, 2005.

[52] K Garikipati, EM Arruda, K Grosh, H Narayanan, and S Calve. A continuum treatment of growth in biological tissue: the coupling of mass transport and mechanics. *J Mech Phys Solids*, 52(7):1595–1625, 2004.

[53] S Baek, KR Rajagopal, and JD Humphrey. A theoretical model of enlarging intracranial fusiform aneurysms. *J Biomech Eng-T ASME*, 128(1):142–149, 2006.

[54] D Ambrosi, L Preziosi, and G Vitale. The insight of mixtures theory for growth and remodeling. *Zeitschrift für angewandte Mathematik und Physik*, 61(1):177–191, 2010.

[55] H Byrne and L Preziosi. Modelling solid tumour growth using the theory of mixtures. *Math Med Biol*, 20(4):341–366, 2003.

[56] D Ambrosi and L Preziosi. On the closure of mass balance models for tumor growth. *Math Mod Meth Appl S*, 12(05):737–754, 2002.

[57] GA Ateshian. On the theory of reactive mixtures for modeling biological growth. *Biomech Mod Mechan*, 6(6):423–445, 2007.

[58] LV Beloussov, JG Dorfman, and VG Cherdantzev. Mechanical stresses and morphological patterns in amphibian embryos. *J Embryol Exp Morph*, 34(3):559–574, 1975.

[59] LV Beloussov. The role of tensile fields and contact cell polarization in the morphogenesis of amphibian axial rudiments. *Roux Arch Dev Biol*, 188(1):1–7, 1980.

[60] LV Beloussov and VI Grabovsky. Morphomechanics: goals, basic experiments and models. *Int J Dev Biol*, 50(2/3):81, 2006.

[61] CC DuFort, MJ Paszek, and VM Weaver. Balancing forces: architectural control of mechanotransduction. *Nat Rev Mol Cell Bio*, 12(5):308–319, 2011.

[62] S Nonaka, H Shiratori, Y Saijoh, and H Hamada. Determination of left–right patterning of the mouse embryo by artificial nodal flow. *Nature*, 418(6893):96–99, 2002.

[63] JR Hove, RW Köster, AS Forouhar, G Acevedo-Bolton, SE Fraser, and M Gharib. Intracardiac fluid forces are an essential epigenetic factor for embryonic cardiogenesis. *Nature*, 421(6919):172–177, 2003.

[64] AW Orr, BP Helmke, BR Blackman, and MA Schwartz. Mechanisms of mechanotransduction. *Dev Cell*, 10(1):11–20, 2006.

[65] MJ Paszek, N Zahir, KR Johnson, JN Lakins, GI Rozenberg, A Gefen, CA Reinhart-King, SS Margulies, M Dembo, D Boettiger, et al. Tensional homeostasis and the malignant phenotype. *Cancer cell*, 8(3):241–254, 2005.

[66] P Ciarletta, D Ambrosi, GA Maugin, and L Preziosi. Mechano-transduction in tumour growth modelling. *Eur Phys J E*, 36(3):1–9, 2013.

[67] MJ Paszek, D Boettiger, VM Weaver, and DA Hammer. Integrin clustering is driven by mechanical resistance from the glycocalyx and the substrate. *Plos Comput Biol*, 5(12):e1000604, 2009.

[68] MJ Mitchell and MR King. Computational and experimental models of cancer cell response to fluid shear stress. *Fron Oncol*, 3, 2013.

[69] CJ Chuong and YC Fung. Residual stress in arteries. In *Front Biomech*, pages 117–129. Springer, 1986.

[70] RN Vaishnav and J Vossoughi. Residual stress and strain in aortic segments. *J Biomech*, 20(3):235–239, 1987.

[71] KO McKay, BR Wiggs, PD Paré, and RD Kamm. Zero-stress state of intra-and extraparenchymal airways from human, pig, rabbit, and sheep lung. *J Appl Physiol*, 92(3):1261–1266, 2002.

[72] H Gregersen, GS Kassab, and YC Fung. Review: The zero-stress state of the gastrointestinal tract. *Digest Dis Sci*, 45(12):2271–2281, 2000.

[73] H Gregersen, TC Lee, S Chien, R Skalak, and YC Fung. Strain distribution in the layered wall of the esophagus. *J Biomech Eng-T ASME*, 121(5):442–448, 1999.

[74] YC Fung. *Biomechanics: mechanical properties of living tissues*. Springer Science & Business Media, 2013.

[75] A Goriely and M Ben Amar. On the definition and modeling of incremental, cumulative, and continuous growth laws in morphoelasticity. *Biomech Mod Mechan*, 6(5):289–296, 2007.

[76] RW Ogden. *Non-linear elastic deformations*. Courier Corporation, 1997.

[77] AN Stroh. Steady state problems in anisotropic elasticity. *J Math Phys*, 41(2):77–103, 1962.

[78] AL Shuvalov. A sextic formalism for three–dimensional elastodynamics of cylindrically anisotropic radially inhomogeneous materials. 459(2035):1611–1639, 2003.

[79] TCT Ting and CO Horgan. Anisotropic elasticity: theory and applications. *J Appl Mech*, 63:1056, 1996.

[80] YB Fu. Existence and uniqueness of edge waves in a generally anisotropic elastic plate. *Q J Mech Appl Math*, 56(4):605–616, 2003.

[81] YB Fu and DW Brookes. Edge waves in asymmetrically laminated plates. *J Mech Phys Solids*, 54(1):1–21, 2006.

[82] SV Biryukov. Impedance method in the theory of elastic surface waves. *Sov Phys Acoust*, 1985.

[83] M Destrade, A Ni Annaidh, and CD Coman. Bending instabilities of soft biological tissues. *Int J Solids Struct*, 46(25):4322–4330, 2009.

[84] AN Norris and AL Shuvalov. Wave impedance matrices for cylindrically anisotropic radially inhomogeneous elastic solids. *Q J Mech Appl Math*, 63(4):401–435, 2010.

[85] P Ciarletta and M Ben Amar. Pattern formation in fiber-reinforced tubular tissues: folding and segmentation during epithelial growth. *J Mech Phys Solids*, 60(3):525–537, 2012.

[86] S Yasugi. Role of epithelial-mesenchymal interactions in differentiation of epithelium of vertebrate digestive organs. *Dev Growth Differ*, 35(1):1–9, 1993.

[87] VA McLin, SJ Henning, and M Jamrich. The role of the visceral mesoderm in the development of the gastrointestinal tract. *Gastroenterology*, 136(7):2074–2091, 2009.

[88] WA Hilton. The morphology and development of intestinal folds and villi in vertebrates. *Am J Anat*, 1(4):459–505, 1902.

[89] FP Johnson. The development of the mucous membrane of the oesophagus, stomach and small intestine in the human embryo. *Am J Anat*, 10(1):521–575, 1910.

[90] AE Shyer, T Tallinen, NL Nerurkar, Z Wei, ES Gil, DL Kaplan, CJ Tabin, and L Mahadevan. Villification: How the gut gets its villi. *Science*, 342(6155):212–218, 2013.

[91] DE Moulton and A Goriely. Circumferential buckling instability of a growing cylindrical tube. *J Mech Phys Solids*, 59(3):525–537, 2011.

[92] M Ben Amar and F Jia. Anisotropic growth shapes intestinal tissues during embryogenesis. *P Natl Acad Sci*, 110(26):10525–10530, 2013.

[93] B Li, YP Cao, XQ Feng, and H Gao. Surface wrinkling of mucosa induced by volumetric growth: theory, simulation and experiment. *J Mech Phys Solids*, 59(4):758–774, 2011.

[94] A Papastavrou, P Steinmann, and E Kuhl. On the mechanics of continua with boundary energies and growing surfaces. *J Mech Phys Solids*, 61(6):1446–1463, 2013.

[95] M Eskandari, MR Pfaller, and E Kuhl. On the role of mechanics in chronic lung disease. *Materials*, 6(12):5639–5658, 2013.

[96] T Savin, NA Kurpios, AE Shyer, P Florescu, H Liang, L Mahadevan, and CJ Tabin. On the growth and form of the gut. *Nature*, 476(7358):57–62, 2011.

[97] GA Holzapfel and RW Ogden. Constitutive modelling of arteries. 466(2118):1551–1597, 2010.

[98] P Ciarletta, I Izzo, S Micera, and F Tendick. Stiffening by fiber reinforcement in soft materials: a hyperelastic theory at large strains and its application. *J Mech Behav Biomed*, 4(7):1359–1368, 2011.

[99] P Chadwick and RW Ogden. On the definition of elastic moduli. *Arch Ration Mech An*, 44(1):41–53, 1971.

[100] S Wolfram. *Mathematica: a system for doing mathematics by computer*. Addison Wesley Longman Publishing Co., Inc., 1991.

[101] M Ben Amar and P Ciarletta. Swelling instability of surface-attached gels as a model of soft tissue growth under geometric constraints. *J Mech Phys Solids*, 58(7):935–954, 2010.

[102] Dassault Systemes Simulia. Abaqus 6.12 documentation. *Providence, Rhode Island, US*, 2012.

[103] F Brau, H Vandeparre, A Sabbah, C Poulard, A Boudaoud, and P Damman. Multiple-length-scale elastic instability mimics parametric resonance of nonlinear oscillators. *Nat Phys*, 7(1):56–60, 2011.

[104] YP Cao, B Li, and XQ Feng. Surface wrinkling and folding of core–shell soft cylinders. *Soft Matter*, 8(2):556–562, 2012.

[105] MA Malas, R Aslankoc, B Ungor, O Sulak, and O Candir. The development of jejunum and ileum during the fetal period. *Early Hum Dev*, 74(2):109 – 124, 2003.

[106] JW Norris, V Beletsky, ZG Nadareishvili, et al. Sudden neck movement and cervical artery dissection. *Can Med Assoc J*, 163(1):38–40, 2000.

[107] JW Barton and MT Margolis. Rotational obstruction of the vertebral artery at the atlantoaxial joint. *Neuroradiology*, 9(3):117–120, 1975.

[108] KV Kardong. *Vertebrates: comparative anatomy, function, evolution*. McGraw-Hill Boston, 2006.

[109] C Bernanrd. Leçon sur les phénomènes de la vie. *Bailliere, Paris*, 1878.

[110] WB Cannon. Organization for physiological homeostasis. *Physiol Rev*, 9(3), 1929.

[111] K Takamizawa and K Hayashi. Strain energy density function and uniform strain hypothesis for arterial mechanics. *J Biomech*, 20(1):7–17, 1987.

[112] M Destrade, Y Liu, JG Murphy, and GS Kassab. Uniform transmural strain in pre-stressed arteries occurs at physiological pressure. *J Theor Biol*, 303:93–97, 2012.

[113] RW Ogden and CAJ Schulze-Bauer. Phenomenological and structural aspects of the mechanical response of arteries. *ASME Applied Mechanics Division-Publications-AMD*, 242:125–140, 2000.

[114] RS Rivlin. Large elastic deformations of isotropic materials. IV. Further developments of the general theory. *Philos T Roy Soc A*, 241(835):379–397, 1948.

[115] A Hoger. On the residual stress possible in an elastic body with material symmetry. *Arch Ration Mech An*, 88(3):271–289, 1985.

[116] R De Pascalis, M Destrade, and A Goriely. Nonlinear correction to the euler buckling formula for compressed cylinders with guided-guided end conditions. *J Elasticity*, 102(2):191–200, 2011.

[117] AE Green and AJM Spencer. *The stability of a circular cylinder under finite extension and torsion*. Division of Applied Mathematics, Brown University, 1957.

[118] P Ciarletta, M Destrade, and AL Gower. Shear instability in skin tissue. *Q J Mech Appl Math*, 66(2):273–288, 2013.

[119] AN Gent and K-C Hua. Torsional instability of stretched rubber cylinders. *Int J Nonlin Mech*, 39(3):483–489, 2004.

[120] A Ertepinar and ASD Wang. Torsional buckling of an elastic thick-walled tube made of rubber-like material. *Int J Solids Struct*, 11(3):329–337, 1975.

[121] ED Duka, AH England, and AJM Spencer. Bifurcation of a solid circular elastic cylinder under finite extension and torsion. *Acta Mech*, 98(1-4):107–121, 1993.

[122] M Topalan, SS Bilgin, WY Ip, and SP Chow. Effect of torsion on microarterial anastomosis patency. *Microsurg*, 23(1):56–59, 2003.

[123] A Rachev and SE Greenwald. Residual strains in conduit arteries. *J Biomech*, 36(5):661–670, 2003.

[124] L Cardamone, A Valentin, JF Eberth, and JD Humphrey. Origin of axial prestretch and residual stress in arteries. *Biomech Model Mechan*, 8(6):431–446, 2009.

[125] M Salgarello, P Lahoud, G Selvaggi, S Gentileschi, Ma Sturla, and E Farallo. The effect of twisting on microanastomotic patency of arteries and veins in a rat model. *Ann Plas Surg*, 47(6):643–646, 2001.